THESIS
2008
LIBRARY
Michigan State
University

This is to certify that the
dissertation entitled

MECHANICAL CHARACTERIZATION AND POWDER PROCESSING OF LEAD TELLURIDE BASED THERMOELECTRIC MATERIALS

presented by

FEI REN

has been accepted towards fulfillment
of the requirements for the

Ph. D degree in Materials Science and Engineering

Elton D. Case
Major Professor's Signature

December 5, 2007
Date

MSU is an Affirmative Action/Equal Opportunity Institution

PLACE IN RETURN BOX to remove this checkout from your record.
TO AVOID FINES return on or before date due.
MAY BE RECALLED with earlier due date if requested.

DATE DUE	DATE DUE	DATE DUE
MAR 04 2009		
012805		
MAY 24 2013		

6/07 p:/CIRC/DateDue.indd-p.1

MECHANICAL CHARACTERIZATION AND POWDER PROCESSING OF LEAD TELLURIDE BASED THERMOELECTRIC MATERIALS

VOLUME I

By

Fei Ren

A DISSERTATION

Submitted to
Michigan State University
in partial fulfillment of the requirements
for the degree of

DOCTOR OF PHILOSOPHY.

Materials Science and Engineering

2007

ABSTRACT

MECHANICAL CHARACTERIZATION AND POWDER PROCESSING OF LEAD TELLURIDE BASED THERMOELECTRIC MATERIALS

By

Fei Ren

LAST (Pb-Sb-Ag-Te) and LASTT (Pb-Sb-Ag-Te-Sn) PbTe-based materials exhibit good thermoelectric (TE) properties and have potential applications as thermoelectric generators (TEGs). However, to fully characterize the thermo-mechanical behavior of LAST and LASTT materials under in-service conditions, one must have knowledge of the mechanical and thermal properties of LAST and LASTT materials at both room temperature and high temperatures.

In this study, elastic moduli, including Young's modulus, shear modulus, and Poisson's ratio, were measured dynamically using Resonant Ultrasound Spectroscopy as a function of temperature between room temperature and about 500°C. In addition, Vickers, Knoop and nanoindentation were used to determine the effects of composition on elasticity and hardness at room temperature for 14 different LAST compositions.

The fracture strength of a p-type ingot LASTT was measured using biaxial flexure testing and the strength distribution was analyzed by Weibull analysis. Also, a preliminary study of the fracture strength for n-type ingots and hot pressed specimens were carried out.

In addition to elastic moduli, strength and hardness, the thermal expansion and

thermal diffusivity are important for the mechanical response of a material to a thermal gradient or a thermal transient. Therefore, the coefficient of thermal expansion as a function of temperature was studied by thermomechanical analysis, while room temperature thermal diffusivity was measured by flash method. In addition, preliminary thermal fatigue study was conducted using an infrared system.

In order to improve the fracture strength, powder processing study was conducted. Milled powders were characterized in terms of particle size distribution, particle morphology, and phase(s) present. Problems during the hot pressing of milled powders were also addressed.

Dedicated to my parents and SX with love.

very

rece

this

Prof

the

in

inclu

in Pr

group

Hanju

give t

this pr

Th

Tampe

Edgar I

and Dr.

Laura R

Ms Rob

ACKNOWLEDGEMENT

I am greatly grateful to Prof. Eldon Case, my Ph. D advisor and friend, who has been very supportive both academically and scholarly. During the writing of this dissertation, I received many helpful advices and insightful suggestions from Prof. Case, which made this dissertation possible. I also thank Prof. Hogan, Prof. Subramanian, Prof. Crimp, and Prof. Schock of my Ph. D committee for their helpful discussions and suggestions during the completion of my degree.

In my five years of Ph. D studies, I received countless help from many colleagues, including Ms. Jennifer Ni and Mr. Bradley Hall in Prof. Case's group, Mr. Edward Timm in Prof. Schock's group, Dr. Chun-I Wu and Mr. Jonathan D'Angelo in Prof. Hogan's group, Mr. Joe Sootsman in Prof. Kanatzidis group at Northwestern University, Ms. Huijun Kong in Prof. Uher's group at University of Michigan. In addition, credits should give to Mr. Adam Pilchak, Ms. Stacey Schroeder, and Mr. Jason Johnson, who worked in this project as undergraduate assistants, for their help with powder processing.

The author very much appreciates the help from the research staff at the High Temperature Materials Laboratory of Oak Ridge National Laboratory, including Dr. Edgar Lara-Curzio, who offered the precious collaborative opportunity; Ms. Rosa Trejo and Dr. Amit Shyam, who had been supportive in every aspect of the experiments; Ms. Laura Riester, Dr. Ke An, Dr. Harry Meyer, Dr. Andrew Payzant, Dr. Tom Watkins, and Ms. Roberta Meisner, who provided help technical supports and suggestive discussions.

In addition, I would like to thank Dr. Hazel-Ann Hosein, Ms. Carol Flegler, Mr. Kim Johnson, and Mr. Bryan Crawford for their technical supports in various instruments; Prof. Morelli and Prof. Sakamoto for their insightful discussions; Dr. Jun Sun for his help with computer-related issues.

Finally, I feel greatly in debt to my parents and my girlfriend SX, who have been continuously encouraging and supportive on my road pursuing the Ph. D degree.

LIS

LIS

PAR

1.

1

1

1

2.

2.

2.

2.

3.

Refer

PART

1. O

2.

2.1

TABLE OF CONTENTS

LIST OF TABLES xiv

LIST OF FIGURES xix

PART I INTRODUCTION 1
1. Thermoelectricity 1
   1.1. Thermoelectric effects 1
   1.2. Thermoelectric materials 5
   1.3. Applications of thermoelectric materials 14
2. Thermo-mechanical characterization of brittle materials 16
   2.1. Thermal stress 16
   2.2. Fracture strength and Weibull modulus 18
   2.3. Elastic properties 21
      2.3.1. Elasticity as a function of temperature 23
      2.3.2. Elasticity as a function of composition 24
      2.3.3. Elasticity as a function of the microcrack damage state 27
      2.3.4. Elasticity as a function of microstructure 28
      2.3.5. Resonant ultrasound spectroscopy 30
3. Scope of current research 36
References 38

PART II EXPERIMENTAL PROCEDURES 45
1. Overview of experimental procedures 45
2. Material fabrication and specimen preparation 46
   2.1. LAST and LASTT materials 46
      2.1.1. Ingot casting 46
      2.1.2. Powder processing 46
      2.1.3. Hot pressing 49
         2.1.3.1. Hot pressing using the University of Michigan facility 50
         2.1.3.2. Hot pressing using other facilities 52
      2.1.4. Specimen mounting, cutting, polishing, and etching 54
         2.1.4.1. Specimen mounting 54
         2.1.4.2. Cutting the ingot and hot pressed specimens 55
         2.1.4.3. Specimen polishing 56

2.1.4.4. Thermal etching 57
2.1.4.5. Chemical etching 57
2.2. Other PbTe and doped PbTe specimens 58
3. Mechanical property characterization 59
3.1. Microindentation 59
3.2. Nanoindentation 60
3.3. Biaxial flexure testing 62
3.4. Resonant ultrasound spectroscopy 65
3.5. Thermal fatigue 67
3.5.1. Thermocouple calibration 67
3.5.2. Thermal cycling 69
4. Powder characterization 73
4.1. Characterizing particle size distribution 73
4.2. Analysis of particle morphology 73
4.3. Powder X-ray diffraction (XRD) analysis 74
5. Phase and composition analysis 74
5.1. SEM and EDS 74
5.2. Auger electron spectroscopy 76
6. Thermal property characterization 76
6.1. Coefficient of thermal expansion measurements 76
6.1.1. Thermal mechanical analyzer (TMA) 76
6.1.2. High temperature X-ray diffraction 77
6.2. Room temperature thermal diffusivity measurement 79
References 82

PART III RESULTS AND DISCUSSIONS

CHAPTER 1
HARDNESS AS A FUNCTION OF COMPOSITION FOR N-TYPE LAST THERMOELECTRIC MATERIAL 83
1. Introduction 86
2. Background 88
3. Experimental procedure 89
3.1. Specimen preparation 89
3.2. Microindentation and nanoindentation 90
4. Results and discussion 93
4.1. Hardness, H, as a parabolic function of chemical composition 93
4.2. Comparison of observed scatter for hardness in this study with scatter for H reported in literature 100
5. Summary and conclusions 103

References 104

CHAPTER 2: YOUNG'S MODULUS AS A FUNCTION OF COMPOSITION FOR AN N-TYPE LEAD-ANTIMONY-SILVER-TELLURIDE (LAST) THERMOELECTRIC MATERIAL 107
1. Introduction 109
2. Experimental procedure 110
2.1. Specimen preparation 110
2.2. Measurement of Young's modulus by microindentation 112
2.3. Measurement of Young's modulus by nanoindentation 113
2.4. Microstructural analysis 113
3. Results and discussion 114
3.1. Comparison and statistical analysis of Young's modulus determined by microindentation and nanoindentation 114
3.2. Linear and parabolic models for elastic modulus as a function of composition 126
3.3. Extension of quadratic model to a paraboloid in four composition variables 128
3.4. A comparison of this study's modulus versus composition results with the literature 144
3.5. Microcracking as an additional source of variation in the elastic modulus 148
4. Summary and conclusions 149
Appendix A. Statistical inferences concerning the data 151
A.1. Test for normality of the data 152
A.2. Test for equivalence of sample means 154
A.3. Test for equivalence of sample variances 157
References 158

CHAPTER 3: WEIBULL ANALYSIS OF THE BIAXIAL FRACTURE STRENGTH OF A CAST P-TYPE LAST-T THERMOELECTRIC MATERIAL 162
1. Introduction 164
2. Background 165
3. Experimental procedure 166
3.1. Materials and specimen preparation 166
3.2. Biaxial flexure testing 167
3.3. Microstructural characterization 169
4. Results and discussion 170
4.1. Microstructure of the cast specimens 170

4.2. Biaxial flexure tests 172
5. Summary and conclusions 178
References 179

CHAPTER 4: THE YOUNG'S MODULUS AND POISSON'S RATIO OF LEAD-TELLURIDE BASED THERMOELECTRIC MATERIALS AS A FUNCTION OF TEMPERATURE 181
1. Introduction 184
2. Background 185
2.1. Requirement for temperature-dependent elastic moduli 185
2.2. Resonant Ultrasound Spectroscopy 188
2.3. The temperature dependence of Young's modulus 191
3. Experimental procedure 195
3.1. Specimen preparation 195
3.2. Energy Dispersive X-Ray Spectroscopy measurements of specimen composition 197
3.3. Nanoindentation 198
3.4. Resonant Ultrasound Spectroscopy (RUS) measurements 200
4. Data analysis 202
4.1. Elasticity calculations 202
4.2. Error calculation for Young's modulus, E, and Poisson's ratio, ν 203
5. Results and discussion 204
5.1. EDS results 204
5.2. Nanoindentation results 206
5.2.1. Nanoindentation measurements to provide initial guesses for RUS modulus calculations 206
5.2.2. Nanoindentation measurements to assess the elastic isotropy of the specimens included in this study 208
5.3. Elastic moduli measured via RUS 208
5.3.1. Room temperature Young's modulus as a function of porosity ... 208
5.3.2. Young's modulus and Poisson's ration as a function of temperature 210
6. Summary and conclusions 222
References 224

CHAPTER 5: THE HIGH TEMPERATURE ELASTIC MODULI OF POLYCRYSTALLINE PBTE MEASURED BY RESONANT ULTRASOUND SPECTROSCOPY 232
1. Introduction 232

1.1. Temperature dependent Young's modulus and shear modulus for polycrystalline brittle materials 232
1.2. Studies of temperature dependent elasticity of PbTe in literature 233
2. Materials and methods 236
3. Results and discussion 239
3.1. Pure polycrystalline PbTe 239
3.2. PbI_2-doped PbTe 242
3.3. Comparison between the polycrystalline pure PbTe specimen and the PbI_2-doped PbTe specimen included in this study 242
3.4. Comparison between this study and literature data 245
References 252

CHAPTER 6: MICROSTRUCTURAL AND MECHANICAL CHARACTERIZATION OF LAST (PB-AG-SB-TE) THERMOELECTRIC MATERIALS FABRICATED VIA SLOW-COOL CASTING 254
1. Microstructures of LAST materials 254
2. LAST materials grown from melt 257
3. Microstructure of slow cooled ingots 259
4. Room temperature mechanical properties 266
4.1. Biaxial flexure strength 266
4.2. Indentation hardness and Young's modulus 268
4.3. Dynamic elastic moduli 271
5. Temperature dependent elastic moduli 273
5.1. Phase(s) changes 277
5.2. Electron-elastic wave coupling 279
5.3. Point defect relaxation 281
6. Conclusions 288
References 289

CHAPTER 7: CHARACTERIZATION OF DRY MILLED POWDERS OF LAST (LEAD – ANTIMONY – SILVER – TELLURIUM) THERMOELECTRIC MATERIAL 293
1. Introduction 296
2. Background 298
3. Experimental procedure 300
3.1. Materials 300
3.2. Ingot preparation 302
3.3. Pre-milling treatment 302
3.3.1. Crushing and grinding without sieving (CG) 304

3.3.2. Crushing, Grinding, Sieving and Re-grinding (CGSR) 304
3.4. Milling (CGM-t and CGSRM-t) 304
3.5. X-ray diffraction analysis 305
3.6. SEM analysis 307
3.7. Particle size analysis 307
3.8. Analysis of Impurities in the as-ground powder 308
4. Results and discussion 309
4.1. X-ray diffraction characterization of the milled powders 309
4.2. SEM characterization of particle shape of the ground and the milled powders 313
4.3. Particle size analysis 316
4.3.1. Particle size distribution as a function of the milling time 317
4.3.2. Evolution of the mean particle size 322
4.4. Analysis of impurities in the as-milled powders 323
5. Summary and conclusions 332
References 335

CHAPTER 8: BLOATING OF HOT PRESSED SPECIMENS DURING ANNEALING 339
1. Bloating phenomena in hot pressed specimens upon annealing 339
1.1. Hot pressed specimens at University of Michigan (UMHP) 339
1.2. Hot pressed specimens at ORNL 349
1.3. Hot pressed specimen at JPL (JPLHP) 356
1.4. Hot pressed specimen at Michigan State University 356
2. Thermogravity – Mass spectroscopy (TG-MS) analysis 356
3. Auger electron spectroscopy (AES) 364
References 367

CHAPTER 9: THERMAL EXPANSION, THERMAL DIFFUSIVITY, AND THERMAL FATIGUE PROPERTIES OF LAST AND LASTT MATERIALS 368
1. Coefficient of thermal expansion (CTE) 368
1.1. Thermomechanical analysis (TMA) of LAST and LASTT materials 368
1.2. High temperature X-ray diffraction of ingot and hot pressed LAST specimens 382
2. Room temperature thermal diffusivity 387
3. Thermal fatigue study 390
4. Summary 394
References 395

CONCLUSIONS 397

BIBLIOGRAPHY 402

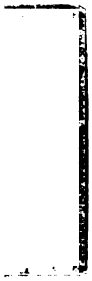

LIST OF TABLES

Table 2.1 70
Two point calibration results for the two k-type thermocouples used in the IR heating apparatus. The voltage and temperature reading from the thermocouples were recorded at the ice-water mixture temperature and the boiling water temperature.

Table 3.1.1 87
For the 17 n-type quaternary thermoelectric compounds, $Ag_aPb_bSb_cTe_d$, included in this study, the values of mole fractions a, b, c and d, along with the mean H value, H_{mean}, the standard deviation, H_{stdev}. All H_{mean} values were computed from 20 indentations per specimen, with a load of 2.94 N and a loading time of 10 seconds.

Table 3.1.2 91
Processing histories of ingots N33, N43, and N58, which were processed differently than the other 14 n-type ingots.

Table 3.2.1 115
For the LAST ingot specimens $Ag_aPb_bSb_cTe_d$ included in this study, the composition, the mean values of the Young's modulus, E_{mean}, and the standard deviation of Young's modulus, E_{std}, as determined by (a) microindentation and (b) nanoindentation.

Table 3.2.2 133
Parabolic and linear compositional dependence of Young's modulus, E, and Bulk modulus, B, for various material systems in literature. Note that in each case, the literature data is in terms of a single compositional variable, x.

Table 3.2.3 146
Room temperature Young's modulus, E, for PbTe and for LAST compositions. The three LAST compositions from Kosuga are compared to three similar compositions from this study.

Table 3.2.4 147
Ratio of maximum to minimum Young's modulus (E_{max}/E_{min}) or bulk modulus (B_{max}/B_{min}) for a number of solid solution systems from the literature.

Table 3.2.A1 156
The coefficient of determination, r^2, for the linear least-square fit of the Nano-*E*, Micro-*H*, and Micro-*H/E* data in the normal probability plots (Figure 3.2.A1).

Table 3.4.1 194
Non-linear least-squares fit parameters b_1/E_0 and T_0/θ_D in the normalized Wachtman equation (Eq. (2b)), and number of data points, N, used in least squares fit over a given temperature range. The non-linear least-squares fit to Eq. (2b) yielded a coefficient of determination, r^2, of at least 0.999 for each material. In addition, Debye temperature, θ_D, from literature for each material is also included.

Table 3.4.2 194
(a) Processing method, composition, dimensions, and mass for the specimens tested in high temperature RUS experiments. All specimens were rectangular parallelepipeds.
(b) Additional specimens included in the room temperature RUS measurements of modulus versus porosity. Specimens UMHP6 and MSUHP6 (Table 3.4.2a) were also included in the room temperature modulus measurements.

Table 3.4.3 205
Comparison between nominal composition and measured composition obtained from EDS.

Table 3.4.4 207
Values of Young's modulus obtained from the nanoindentation measurements that were used to generate the "initial guesses" for the RUS calculations.

Table 3.4.5 207
Young's modulus measured by nanoindentation as a function of indent locations (Figure 3.4.5).

Table 3.4.6 212
For three hot pressed n-type LAST specimens, room temperature Young's modulus measurement via RUS as a function of volume fraction porosity. All three specimens have the identical composition ($Ag_{0.43}Pb_{18}Sb_{1.2}Te_{20}$) and processing technique as UMHP6 (Table 3.4.2).

Table 3.4.7 212
Linear temperature dependence of Young's modulus for specimens L145, N138, UMHP6, and MSUHP6 as determined by linear least-squares fitting to Eq. (2c)

over the given temperature range.

Table 3.5.1 238
(a) Fitting results of linear least-squares fitting of Young's modulus as a function temperature to Eq. (3).
(b) Fitting results of linear least-squares fitting of shear modulus as a function temperature to Eq. (5).
(c) Fitting results of non-linear least-squares fitting of Poisson's ratio as a function temperature to Eq. (6).

Table 3.5.2 251
Comparison of measurement techniques and frequency between this study and literature.

Table 3.5.3 251
Room temperature carrier concentration of the pure and doped PbTe specimens in this study and in literature.

Table 3.6.1 258
Composition and cooling rate between the maximum temperature of the melt and solidus temperature for the LAST ingot specimens included in this study.

Table 3.6.2 263
As determining using EDS, the composition in terms of atomic percentage for the plate-like inclusions observed specimen N155 (Figure 3.6.3d).

Table 3.6.3 267
For the ingot specimens included in this study (Table 3.6.1) the (a) Biaxial flexure strength and (b) hardness and Young's modulus as determined by indentation.

Table 3.6.4 282
Regression results for Young's modulus values of specimen N155-B measured with a heating/cooling rate of 2 K/min fit to the linear temperature-modulus relation given by Eq. (4) and the non-linear least-squares fit to Eq. (5).

Table 3.7.1 301
Concentration of impurity elements in the raw materials used to cast LAST ingots in this study.

Table 3.7.2 303
Powder size reduction methods used in this study.

Table 3.7.3 306
Composition (in percentage) of Retsch Milling jar and Glen Mills milling media used in this study.

Table 3.7.4 311
Comparison of the Miller indices, 2θ, and relative peak intensities among LAST powders in this study and pure PbTe in literature.

Table 3.7.5 327
(a) As determined by ICP-MS analysis, the impurity levels in batch 1 of a dry milled LAST powder (ground and then planetary milled for three hours at 100 rpm). Note the high concentrations of Si compared to a similarly processed powder shown in Table 3.7.5b.
(b) As determined by ICP-MS analysis, the impurity levels in batch 2 of dry milled LAST powders (ground and then planetary milled for three hours at 100 rpm). The analysis was done for the elements exceeding 10 ppm in Table 3.7.5a. Compared to the results shown in Table 3.7.5a, the impurity concentrations shown here are in much better agreement with the EDS results discussed in Section 4.4.

Table 3.8.1 340
(a) Processing conditions of the hot pressed specimens included in this chapter.
(b) Thermal annealing conditions of the specimens involved in this chapter.

Table 3.8.2 360
Nominal composition, processing technique, and mass loss due to heating for the specimens analyzed by TG-MS at Netzsch Inc.

Table 3.8.3 360
Elemental concentration as indicated by atomic percentage measured by AES at five different point locations on the fracture surface of MSUHP6 (Figure 3.8.17).

Table 3.8.4 360
Elemental concentration as indicated by atomic percentage measured by AES at two different point locations on the fracture surface of MSUHP6 (Figure 3.8.18).

Table 3.9.1 369
Composition, processing technique, and the TMA measurement conditions including the temperature range, heating/cooling rate and gas environment for the LAST and LASTT specimens included in this study.

Table 3.9.2 371
Comparison of coefficient of thermal expansion values for pure alumina between this study and literature.

Table 3.9.3 378
(a) Coefficient of thermal expansion obtained by linear least-squares fitting of the TMA data to Eq. (1).
(b) Coefficient of thermal expansion obtained by linear least-squares fitting of the temperature dependent lattice parameter (determined by high temperature X-ray diffraction) to Eq. (1).

Table 3.9.4 379
For specimen MSUHP18, the dimensional change with respect to the original length, ΔL, the accumulated permanent strain, ε_{perm}, the relative strain with respect to the previous thermal cycle, ε_{rel}, the accumulated relative volumetric change with respect to the original volume which was calculated from the permanent strain, $\Delta V/V_{orig}$, and the accumulated volumetric porosity, P, as a function of thermal cycle number during the TMA measurement.

Table 3.9.5 389
Room temperature thermal diffusivity values for n-type ingot and hot pressed LAST specimens, as well as a PbTe specimen and an AgSbTe2 specimen included in this study.

Table 3.9.6 392
For the thermal fatigue experiments performed at ORNL, the average cooling rates during heating and cooling segments for the slow heating/natural cooling profile and the fast heating/natural cooling profile.

Table 3.9.7 392
Young's modulus and Poisson's ratio as a function of thermal cycling for specimens L145, N138, and P20-HP1. The temperature change as a function of time is illustrated in Figure 3.9.11 and summarized in Table 3.9.6.

LIST OF FIGURES

Figure 1.1 2
Schematics of TE couples used in (a) generator mode and (b) refrigerator mode.

Figure 1.2 6
Dimensionless figure of merit, ZT, as a function of temperature for several established and novel TE materials (after [Androulakis 2006, Hsu 2004, Tritt 2006]).

Figure 1.3 8
Illustrations of the crystal structures for (a) perovskite-type $BaTiO_3$ (after [Barsoum 1997]) and (b) $CoSb_3$-based skutterudite (after [Nolas 2001]). The "rattling ions" are Ti^{4+} in $BaTiO_3$ and the guest atom(s) in the skutterudite structure.

Figure 1.4 10
Thermoelectric properties of LAST and LASTT materials, including (a) Seebeck coefficient, (b) electrical conductivity, (c) thermal conductivity, and (d) ZT (after [Androulakis 2006, Hsu 2004]).

Figure 1.5 13
Electron density of states (DOS) as a function of energy (E) for (a) bulk materials (3-D), (b) quantum wells and thin films (2-D), (c) quantum/nano-wires (1-D), and (d) quantum dots (0-D) (after [Dresselhaus 2006]). The sharp DOS in low dimension materials can potentially enhance thermoelectric properties by increasing the magnitude of the Seebeck coefficient (Eq. (1.8').

Figure 1.6 20
Schematic of a TE module in which the individual legs are electrically connected in series and thermally connected in parallel.

Figure 1.7 22
(a) Schematics of two TE modulus with the same mean strength of 65 MPa but different strength distributions. (b) Weibull plot illustrating the difference in strength distribution between the two modules. Module B with a higher Weibull modulus has a smaller scatter in strength values than Module A.

Figure 1.8 25

Temperature dependent (a) Young's modulus and (b) Poisson's ratio for PbTe and SnTe below room temperature.

Figure 1.9.....26
Schematic of temperature dependent Young's modulus for polycrystalline materials. Young's modulus versus temperature deviates from linear relationship at elevated temperatures due to grain boundary sliding, which is a function of grain size. The onset temperature of grain boundary sliding is lower for materials with smaller grain sizes.

Figure 1.10.....29
Reduction in Young's modulus as a function of indentation-induced crack density as well as crack size (after [Kim 1993b]).

Figure 1.11.....29
Young's modulus of polycrystalline alumina as a function of volumetric porosity measured by nanoindentation and RUS techniques, where RUS has a higher sensitivity to porosity (after [Radovic 2004]). Measurements made by 4-point bend and impulse excitation are also illustrated.

Figure 1.12.....37
Schematics of vibrational patterns (Chldani figures) for thin plates with (a)-(b) square geometry and (c)-(d) circular geometry. Nodal positions, which have minimum vibration amplitude, are illustrated by the heavy dots and dotted lines. For a given specimen, the nodal pattern is a function of vibrational frequency. For example, (a) and (c) are patterns obtained at lower frequencies than (b) and (d), respectively.

Figure 2.1.....47
Powder processing techniques to produce micron sized powders from cast ingots. The crushing, grinding, and sieving stages, which will be replaced by hammer milling, ensured the particle size of input powders to ball milling is less than 53 micron.

Figure 2.2.....51
Schematic (left) and digital photograph (right) of a graphite die set used with the Astro HP4560-20 hot press to fabricate 12.7 mm diameter hot pressed specimens.

Figure 2.3.....53
Temperature-pressure-time profile during the hot pressing of specimen UMHP6 processed using the hot press facility at the University of Michigan.

Figure 2.4.....61
Schematics of indentation impressions and associated cracks for Vickers indentation and Knoop indentations.

Figure 2.5.....64
Schematics of (a) side view and (b) top view of biaxial flexure test fixture with a ball-on-ring configuration.

Figure 2.6.....66
(a) Schematic of the RUS apparatus used in this study and (b) a typical vibrational spectrum obtained from RUS scan.

Figure 2.7.....68
Thermocouple calibration configuration used to calibrate the thermal couples for the thermal fatigue apparatus.

Figure 2.8.....72
(a) Thermal cycling apparatus which utilized the infrared heating apparatus at Oak Ridge National Laboratory. (b) Side view of the specimen stage configuration with two thermocouples placed on the specimen.

Figure 2.9.....78
Schematic configuration for coefficient of thermal expansion (CTE) measurement via thermomechanical analyzer (TMA).

Figure 2.10.....80
(a) Configuration of the laboratory-built room temperature thermal diffusivity measurement system. (b) Sample holder used in the room temperature thermal diffusivity measurement system.

Figure 3.1.1 94
For six of the 17 ingot specimens, a comparison of the hardness values obtained by Vickers indentation (this study) with the hardness obtained via nanoindentation (also in this study).

Figure 3.1.2 96
The variation in H as a function of composition for the chalcogenide system $Cd_{1-x}Zn_xTe$ (after [3]).

Figure 3.1.3 98

Plot of mean values of the experimentally determined hardness, H_{exper}, versus H_{pred} for the 14 identically processed specimens of the 17 specimens in this study (Table 1), excluding N33, N43, and N58 that were processed with different cooling rates (Table 2). The H_{pred} values are computed based on the least-squares fitting of the data to Eq. (5). The resulting slope of 1.00003 and intercept of -2.1×10^{-5} GPa with a correlation coefficient of 0.95 indicate that the regression of the H data to Eq. (5) yields a good description of the hardness data. The error bars represent the standard deviation of the hardness values (Table 1) based on 20 Vickers indentations per specimen.

Figure 3.1.4 102
Schematic depicting the relative size of the indenter tip compared to the specimen's grain size. The relative size is important with respect to the relative scatter of the hardness values.

Figure 3.2.1 111
Temperature-time profiles for the processing of the 17 cast ingot specimens included in this study.

Figure 3.2.2 117
Comparison of Young's modulus measured by microindentation (Vickers and Knoop) and nanoindentation. (a) Young's modulus determined from microindentation and nanoindentation in subgroup A (six specimens that span the range of moduli determined in this study), (b) composition replicates N35 and N54 in subgroup B, where the two specimens also have the same processing history (figure 1 and table 1), (c) Three compositional replicates (ingots N42, N43, and N58) with differing processing histories. The lower Young's modulus for microindentation on N58 is likely due to the macrocracking in the specimen.

Figure 3.2.3 120
SEM micrograph showing the polished surface of specimen N58. Nearly-parallel macrocracks were observed across the entire specimen surface with spacing between ~ 200 μm and 2000 μm which likely resulted from biaxial testing prior to indentation on this particular specimen. None of the other specimens in this study showed such cracks.

Figure 3.2.4 130
For ternary and quaternary compositions from the literature, Young's modulus (solid symbols) and bulk modulus (open symbols) that are (a) and (b) parabolic functions of composition (equation (4)) or a (c) linear functions of composition (equation (4) with b = 0). In (a), (b) and (c) the curves shown were obtained by

the present authors via linear regression. The regression parameters are given in table 2.

Figure 3.2.5 137
Experimentally determined Young's modulus (E_{expr}) *versus* Young's modulus predicted from equation (5) (E_{pred}) and regression line obtained from nonlinear least-squares fitting for (a) the 16 specimens (table 1a) tested using microindentation (except N58) fit to equation (5a), (b) the 10 specimens measured by nanoindentation (table 1b) fit to equation (5b), and (c) for the 16 specimens tested using microindentation (except N58) fit to equation (5b). In each figure, the error bars represent the standard deviation of the indentation data (20 measurements per specimen for microindentation; 16 measurements per specimen for nanoindentation).

Figure 3.2.6 142
Pseudo-ternary diagrams depicting the compositions (a) the Ag-Sb-Pb plane, and (b) the Ag-Sb-Te plane for the 17 LAST cast ingot specimens included in this study along with three hot pressed LAST specimens studied by Kosuga *et al.* [5]. K_0, K_1, and K_2 indicate hot pressed specimens with compositions of $AgSbPb_{18}Te_{20}$, $Ag_{0.9}SbPb_{18}Te_{20}$, and $Ag_{0.7}SbPb_{18}Te_{20}$, respectively from Kosuga's study [5]. The grey scale for the plotting symbols corresponds to the Young's modulus values with the darker symbols indicating higher Young's modulus. Note that Kosuga's data [5] is clustered near the center of both diagrams.

Figure 3.2.A1 153
Normal probability plots of (a) Young's modulus, E, obtained via nanoindentation for specimen N53, and (b) hardness to modulus ratio, H/E, obtained via microindentation for specimen N50. Linear regression yields coefficients of determination, r^2, of 0.94 for (a) and 0.98 for (b), indicating that the indentation data are approximately normally distributed which in turn implies that it is acceptable to use the t-test and F-test on these data sets.

Figure 3.3.1 168
Schematic of the ball-on-ring load fixture used for biaxial flexure testing of cast ingots in this study.

Figure 3.3.2 171
For the cast LAST-T specimens included in this study, (a) a chemically etched specimen surface showing approximately equiaxed grains and (b) an as-polished surface showing isolated surface pores.

Fi
Fl
an
tet
fra

Fig
We
tes

Fig
The
Bio

Fig
Sch

Figu
Sch
the
grai

Figu
(a) T
195
squa
mod
temp
[Bri
Eq.

Figu
Nan
(a) sp

Figu
A ty
to m

Figu

Figure 3.3.3 173
Flaws associated with the LAST-T specimens included in this study, including (a) an elliptical surface flaw, (b) subsurface microcracking and (c) a tetrahedrally-shaped surface flaw that may be associated with microcracking and fractional grain pullout during cutting and polishing.

Figure 3.3.4 175
Weibull plot of biaxial strength data obtained from ball-on-ring biaxial flexure testing for disk-shaped specimens cut from cast p-type ingot of LAST-T material.

Figure 3.4.1 186
The maximum normalized thermal stress, $\sigma_{TH\text{-}MAX}/(E\alpha\Delta T/(1-\nu))$, as a function of Biot modulus, B1.

Figure 3.4.2 190
Schematic of equipment configuration during a typical RUS experiment.

Figure 3.4.3 190
Schematic of temperature dependent Young's modulus including four regions: (1) the cryogenic region, (2) unrelaxed modulus region, (3) viscoelastic region due to grain boundary sliding, and (4) relaxed modulus region.

Figure 3.4.4 193
(a) The aggregate Young's modulus as a function of temperature for Cu [Overton 1955], LiF [Briscoe 1957], and PbTe [Houston 1968], with non-linear least squares fitting to the Wachtman's equation (Eq. (2a)). (b) The aggregate Young's modulus normalized to the Young's modulus at 0 K, E_0, as a function of temperature normalized to the Debye temperature, θ_D, for Cu [Overton 1955], LiF [Briscoe 1957], and PbTe [Houston 1968], with non-linear least squares fitting to Eq. (2b).

Figure 3.4.5 199
Nanoindent locations selected to examine the anisotropy of Young's modulus for (a) specimen L145, N138, and UMHP6, and (b) MSUHP6.

Figure 3.4.6 199
A typical spectrum obtained from the RUS measurement, where peaks correspond to mechanical vibrational modes.

Figure 3.4.7 209

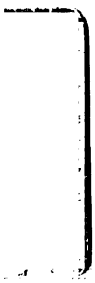

Young's modulus measured by nanoindentation as a function of indent location (Figure 5) on specimens (a) MSUHP6, (b) UMHP6, (c) N138, and (d) L145. No significant anisotropy was observed for all four specimens. The dash lines indicate the mean values of the Young's modulus for each specimen.

Figure 3.4.8 211
Room temperature RUS measurement of Young's modulus as a function of porosity for hot pressed LAST ($Ag_{0.43}Pb_{18}Sb_{1.2}Te_{20}$) specimens MSUHP5, MSUHP6, and MSUHP7 as determined from non-linear least-squares fitting to Eq. (6). A Young's modulus of about 27 GPa was extrapolated to the volumetric fraction porosity of about 0.16, which was used as the initial guess in RUS fitting program for specimen UMHP6.

Figure 3.4.9 213
Young's modulus as a function of temperature with linear least-squares fitting to Eq. (2c) for specimens (a) L145, (b) N138, (c) UMHP6, and (d) MSUHP6 included in this study.

Figure 3.4.10 216
Temperature dependent Poisson's ratio for specimens (a) L145, (b) N138, (c) UMHP6, and (d) MSUHP6 included in this study.

Figure 3.4.11 219
Comparison between literature data of pure PbTe [Houston 1968, Einspruch 1963] with TE materials included in the current study in terms of (a) Young's modulus as a function of temperature, (b) temperature dependent Poisson's ratio, and (c) the effective modulus, E/(1-v), as a function of temperature.

Figure 3.5.1 234
Temperature dependent elastic moduli of pure and doped PbTe in literature: (a) the aggregate Young's modulus, (b) the aggregate shear modulus, (c) the aggregate Poisson's ratio for pure PbTe [Houston 1968, Simmons 1971], and (d) the relative shear modulus of pure and Cr-doped PbTe [Salamov 2006].

Figure 3.5.2 240
Temperature dependent (a) Young's modulus, (b) shear modulus, and (c) Poisson's ratio for the pure PbTe specimen in this study.

Figure 3.5.3 243
Temperature dependent (a) Young's modulus, (b) shear modulus, and (c) Poisson's ratio for the PbI_2-doped PbTe specimen in this study.

Figure 3.5.4 247
Comparison of temperature dependent elastic moduli between this study and literature [Houston 1968, Simmons 1971, Salamov 2006] for (a) the Young's modulus, (b) the Poisson's ration, and (c) the relative shear modulus.

Figure 3.6.1 255
Pseudo-binary phase diagram of the PbTe-$AgSbTe_2$ where $\alpha = \alpha$-Ag_2Te, $\beta = \beta$-Ag_2Te, and $\gamma = Sb_2Te_3$ (after [Maier 1963]). For non-stoichiometric LAST compounds $Ag_{0.86}Pb_{18}Sb_{1.0}Te_{20}$, which can be approximated as $(AgSbTe_2)\cdot 9(2PbTe)$ for temperature below about 750°C, the nominal composition is located in the solid solution region near PbTe end as indicated by the dotted line.

Figure 3.6.2 258
Temperature versus time profiles for the ingot specimens included in this study.

Figure 3.6.3 260
SEM micrographs of inclusions observed in the slow cooled LAST materials: (a) fracture surface of N159 (Table 1), (b) spherical inclusion observed in N159, (c) needle-shaped inclusions observed in N155, and (d) plate-like inclusions observed in N155 (Table 1).

Figure 3.6.4 264
(a) SEM micrograph of a spherical inclusion observed in specimen N159 (Table 1) and (b) the corresponding elemental mapping for Pb, Te, Sb, and Ag for the inclusion.

Figure 3.6.5 269
The effect of ingot cooling rate on (a) fracture strength, (b) microindentation hardness, (c) nanoindentation hardness, and (d) Young's modulus for ingot LAST specimens (Table 1).

Figure 3.6.6 272
Room temperature dynamic elastic moduli including (a) Young's modulus, (b) shear modulus, and (c) Poisson's ration, for six slow cooled ingot specimens with identical composition (Table 1) and processing history (Figure 1).

Figure 3.6.7 275
Young's modulus of slow cooled ingot specimens N155A and B as a function of temperature: (a) specimen N155B measured with a 5 K/min heating/cooling rate,

(b) specimen N155B measured with a 2 K/min heating/cooling rate, and (c) comparison of N155A measured with 5 K/min heating/cooling rate to the two measurements on N155B ((a) and (b)). Specimens N155A and B were cut from a single cast ingot.

Figure 3.6.8 282
Young's modulus versus temperature data from specimen N155-B with the 2 K/min heating/cooling rate fit to Eq. (4) with linear least-squares regression between room temperature and about 500 K and a non-linear least-squares regression to Eq. (5) between room temperature and about 800 K.

Figure 3.6.9 287
Young's modulus or elastic constant c_{11} as a function of temperature, where the moduli and temperature are normalized with respect to E_{kink} and T_{kink}, the modulus and temperature at the kink, respectively, for the LAST specimen N155-B in this study, $Tb_2Hf_2O_7$ and $Tb_2Zr_2O_7$ [Dole 1983], and FeSi [Mandrus 1995, Sarrao 1994].

Figure 3.7.1 303
The time-temperature profile for the cast ingots used in this study.

Figure 3.7.2 312
X-ray diffraction patterns of powders milled in this study. Table 2 lists the acronyms for the various powder processing techniques used in this study.

Figure 3.7.3 315
SEM micrographs showing particle morphology of powders received various milling treatments, (a) particle morphology of CGSR (crushing, grinding, sieving, and re-grinding) powder, (b) cleavage steps indicated by arrows for CGM-3 (milled) powder, (c)-(f) particle morphology for CGM-3, CGM-180, CGM-420, and CGSRM-420 milled powders.

Figure 3.7.4 318
For CGM (crushed, ground and milled powders) the particle size distribution as a function of milling time. Figure 6a gives the mean particle size as a function of milling time.

Figure 3.7.5 319
The particle size distribution for (a) the CGSR (crushed, ground, sieved and reground to pass through a 53 micron sieve) (b) - (e) the particle size distribution as a function of milling time for the CGSR powders. Figure 6b gives the mean

particle size as a function of milling time.

Figure 3.7.6 320
a) Mean particle size versus milling time for CGM (crushed, ground and milled) LAST powders. The particle size reaches a steady state (grindability limit) at approximately 7 microns. b) Mean particle size versus milling time for CGSRM (crushed, ground, sieved, reground and milled) LAST powders. Although the sieving and regrind (via mortar and pestle) steps reduced the mean size of the powders that were subsequently milled, the grindability limit was about 5 microns.

Figure 3.7.7 324
The mass of the alumina milling media (table 3) as a function of milling time, depicting the wear rate of the milling media. The mass lost from the media represents a milling-induced alumina contamination of the milled powder batch.

Figure 3.7.8 330
For the EDS measurements of the LAST powders (a) a "background" spectrum for the carbon tape itself mounted on an aluminum stub, (b) results for powder batch 3 and (c) results for powder batch 4.

Figure 3.8.1 341
SEM micrographs of UMHP1 showing (a) fracture surface of the as hot pressed specimen, and (b) fracture surface after annealing at 898 K for 2hr. The mean grain size is ~ 4 micron as determined by linear intercept method.

Figure 3.8.2 343
SEM micrographs of as hot pressed UMHP3 specimen showing (a) the cut surface and (b) the fracture surface.

Figure 3.8.3 344
SEM micrographs of UMHP3 after annealing at 773 K for 1hr showing (a) the macroscopic porosity and (b) the micro-porosity on the fracture surface.

Figure 3.8.4 345
SEM micrographs of the polished surfaces of UMHP5 after thermal annealing (a) at 773 K for 1hr, and (b) at 873 K for 1hr.

Figure 3.8.5 346
(a) Low magnification and (b) high magnification SEM images showing polished surfaces of UMHP6 after thermal annealing at 673 K for 1hr.

Figure 3.8.6 347
(a) Low magnification and (b) high magnification SEM images showing polished surfaces of UMHP6 after thermal annealing at 773 K for 1hr.

Figure 3.8.7 348
(a) Low magnification and (b) high magnification SEM images showing polished surfaces of UMHP6 after thermal annealing at 873 K for 1hr.

Figure 3.8.8 350
(a) lenticular pores and (b) quasi-spherical pores observed in ETP20-HP1 annealed at 773 K for 1hr.

Figure 3.8.9 351
(a) macropores and (b) micropores observed in ETP20-HP1 annealed at 823 K for 1hr.

Figure 3.8.10 353
SEM micrographs of (a) the fracture surface of as ORHP2, and free surfaces after annealing at 823 K for 2hr depicting (b) macropores and (c) micropores.

Figure 3.8.11 355
SEM micrographs showing free surfaces of (a) the as-cut ORHP4, and (b) the specimen thermally annealed at 823 K for 1hr.

Figure 3.8.12 357
SEM micrographs of (a) the fracture surface of the hot pressed JPL-HP specimen, and (b) macro- and (c) micropores observed on the polished surface after annealing at 773 K for 1hr.

Figure 3.8.13 359
SEM micrographs of fracture surfaces of specimens (a) MSUHP3 and (b) MSUHP4 hot pressed at Michigan State University specimens after annealing at 973 K for 1 hr.

Figure 3.8.14 362
Relative mass changes as a function of temperature for the n-type ingot specimen ETN174 (straight line), the p-type ingot specimen ETP40 (dashed line), the n-type hot pressed specimen MSUHP10 (dash-dot line), and the p-type hot pressed specimen MSUHP4 (dotted line), as determined from TG-MS analysis.

Figure 3.8.15 363
Ion current intensity of CO_2 (amu = 44) as a function of temperature for the n-type hot pressed specimen MSUHP10 (straight line), and the p-type hot pressed specimen MSUHP4 (dashed line), as determined from TG-MS analysis.

Figure 3.8.16 363
Ion current intensity of Te (amu = 128) and Te_2 (amu = 256) as a function of temperature for the n-type hot pressed specimen MSUHP10 and the p-type hot pressed specimen MSUHP4, as determined from TG-MS analysis.

Figure 3.8.17 366
SEM micrograph depicting needle-shaped inclusions observed on the fracture surface of MSUHP6 during AES analysis.

Figure 3.8.18 366
SEM micrographs showing need-shaped inclusions and the surrounding matrix observed on the fracture surface of specimen MSUHP6.

Figure 3.9.1 371
Dimension change as a function of temperature as determined by TMA for a pure polycrystalline alumina specimen.

Figure 3.9.2 373
Dimensional change as a function of temperature as determined by TMA for the n-type ingot specimen N155.

Figure 3.9.3 373
Dimensional change as a function of temperature as determined by TMA for the n-type hot pressed specimen MSUHP6.

Figure 3.9.4 376
Dimensional change as a function of temperature as determined by TMA for the p-type ingot specimen P45. Note the specimen length decreases after the first cycle, which may indicate mass loss due to sublimation. A discontinuity occurred at about 630 K during the first heating cycle, which was likely an artifact.

Figure 3.9.5 376
Dimensional change as a function of temperature as determined by TMA for the p-type hot pressed specimen MSUHP18.

Figure 3.9.6 381

Temperature dependent CTE of n-type ingot LAST specimen N155 calculated from Eq. (2). The open symbols represent the mean CTE values from the four heating and cooling cycles, while the error bars indicates the standard deviation among the heating and cooling cycles.

Figure 3.9.7 381
Temperature dependent CTE of n-type hot pressed LAST specimen MSUHP6 calculated from Eq. (2). The open symbols represent the mean CTE values from the four heating and cooling cycles, while the error bars indicates the standard deviation among the heating and cooling cycles.

Figure 3.9.8 383
Series of high temperature X-ray diffraction patterns as a function of temperature for (a) N155 and (b) MSUHP6 between room temperature and 623 K.

Figure 3.9.9 384
Temperature dependent lattice parameter as calculated from high temperature XRD patterns for n-type specimens N155 and MSUHP6.

Figure 3.9.10 385
Comparison of relative dimensional change with respect to the room temperature value between high temperature XRD measurements and TMA measurements for (a) specimen N155, and (b) specimen MSUHP6.

Figure 3.9.11 391
Temperature profiles during thermal fatigue cycling for (a) the slow heating/natural cooling thermal cycles, and (b) the fast heating/natural cooling thermal cycles.

PART I. INTRODUCTION

1. Thermoelectricity

1.1. Thermoelectric effects

The thermoelectric (TE) effect refers to the direct conversion between a temperature differential and electricity, including the Seebeck effect (the direct TE effect) and the Peltier effect (the reverse TE effect) [Nolas 2001].

In the Seebeck effect, when a temperature difference is applied to TE devices, which consist of p-n junctions, charge carriers (electrons or holes) will migrate along the temperature gradient and result in a voltage difference in open circuit or a current in closed circuits (Figure 1.1). In the Peltier effect, when a current is driven through TE materials, heat will be absorbed at one of the junctions between two dissimilar materials and rejected at the other junction (Figure 1.1). The Seebeck effect and the Peltier effect are the basis for both TE generation and refrigeration, respectively [Nolas 2001].

The efficiency of TE materials is related to the dimensionless figure of merit, ZT, which is defined as [Nolas 2001, Rowe 1995]

$$ZT = \frac{S^2 \sigma T}{k} \tag{1.1}$$

where σ = electrical conductivity, k = thermal conductivity, T = temperature, and S = the Seebeck coefficient or thermopower.

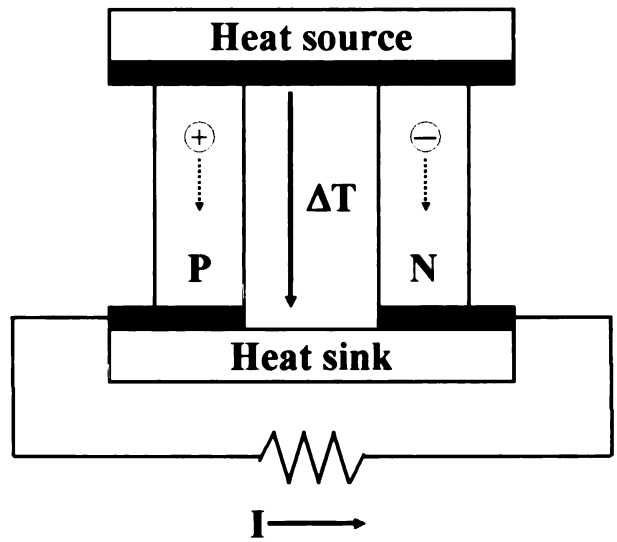

(a)

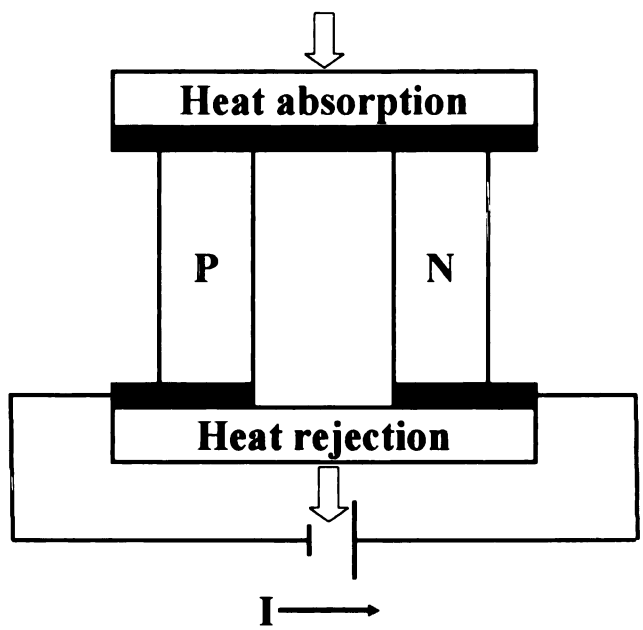

(b)

Figure 1.1. Schematics of TE couples used in (a) generator mode and (b) refrigerator mode.

The numerator of the right hand side of Eq. (1.1), $S^2\sigma$, is defined as the power factor. A higher ZT value corresponds to higher energy conversion efficiency, η, such that [Yang 2006]:

$$\eta = \frac{T_H - T_C}{T_H} \frac{\sqrt{1+ZT}-1}{\sqrt{1+ZT}+\frac{T_C}{T_H}} \tag{1.2}$$

where $(T_H - T_C)/T_H$ is the Carnot efficiency [Nolas 2001].

The Seebeck coefficient is defined as the ratio of the voltage difference (ΔV) developed to the temperature difference (ΔT), $S = \Delta V/\Delta T$ [Nolas 2001, Rowe 1995].

Consider a single parabolic band, where the electron energy as a function of the wave vector **k** is proportional to $(\mathbf{k} - \mathbf{k}_0)^2$ ($\mathbf{k}_0$ is the wave vector at the band extremum). If only one type of carrier is present, and the effects of magnetic field and phonon/electron interaction are negligible, the Seebeck coefficient, S, can be expressed as [Nolas 2001]:

$$S = \pm\frac{1}{eT}\left(\zeta - \frac{K_1}{K_0}\right) \tag{1.3}$$

where e is the electron charge, ζ is the Fermi energy, K_0 and K_1 are transport integrals defined by [Nolas 2001]

$$K_0 = \frac{8\pi}{3}\left(\frac{2}{h^2}\right)^{3/2}(m^*)^{1/2}T\tau_0\left(r+\frac{3}{2}\right)(k_BT)^{r+3/2}F_{r+1/2}(\xi) \tag{1.4a}$$

and

$$K_1 = \frac{8\pi}{3}\left(\frac{2}{h^2}\right)^{3/2}(m^*)^{1/2}T\tau_0\left(r+\frac{5}{2}\right)(k_BT)^{r+5/2}F_{r+3/2}(\xi) \tag{1.4b}$$

In Eq. (1.4), h is the Planck's constant, k_B is the Boltzmann constant, m* is the effective

electron mass, τ_0 and r are constants related to the electron relaxation time, τ_0 ($\tau_e = \tau_0 E^r$), E is the electron energy, ξ is equal to $E/(k_B T)$, and $F_n(\xi)$ are the Fermi-Dirac integrals [Goldsmid 1960]:

$$F_n(\xi) = \int_0^\infty \xi^n \frac{1}{\exp\left(\frac{\xi - \zeta}{k_B T}\right) + 1} d\xi \tag{1.5}$$

For degenerate semiconductors where $\zeta/k_B T >> 0$, it can be shown that Eq. (1.3) can be simplified to [Ziman 1979]

$$S = \frac{\pi^2}{3} \frac{k_B^2 T}{e} \left(\frac{\partial \ln \sigma(E)}{\partial E} \right)_{E=\zeta} \tag{1.6}$$

where the electrical conductivity as a function of energy, $\sigma(E)$, can be related to the electron density of states, N(E), and the electron relaxation time, $\tau(E)$, such that [Ziman 1979]:

$$\sigma(E) \propto N(E)\tau(E) \tag{1.7}$$

Thus, the Seebeck coefficient, S, is proportional to the differentials of the density of states, N(E), and the relaxation time, $\tau(E)$, with respect to the electron energy at the Fermi energy:

$$S = \frac{\pi^2}{3} \frac{k_B^2 T}{e} \left(\frac{\partial \ln N(E)}{\partial E} + \frac{\partial \ln \tau(E)}{\partial E} \right)_{E=\zeta} \tag{1.8}$$

When more than one type of charge carriers is present, the Seebeck coefficient, S, can be expressed as [Nolas 2001]:

$$S = \frac{\sum_{i=1}^{n} S_i \sigma_i}{\sum_{i=1}^{n} \sigma_i} \tag{1.9}$$

where S_i and σ_i are the Seebeck coefficient and electrical conductivity for the i^{th} type carrier.

It can be shown [Goldsmid 1960, Nolas 2001, Rowe 1995] that Eq. (3) can be modified to describe the Seebeck coefficient under conditions of a non-parabolic band, a magnetic field, or electron/phonon interaction.

1.2. Thermoelectric materials

The common TE materials currently used in TE devices are heavily doped semiconductors, including Bi_2Te_3-based alloys [Scherrer 1995], PbTe-based alloys [Fano 1995], and SiGe compounds [Vining 1995]. However, these materials (alloys based on Bi_2Te_3, PbTe, and SiGe) exhibit peak ZT values less than one (Figure 1.2), which corresponds to an efficiency that is less than 30 percent of the Carnot limit in TE power generation mode (Eq. (1.2)). If the ZT value can be improved to 1.7, the power generation efficiency is then increased to about 40 percent of the Carnot limit (Eq. (1.2)).

Since the 1990's, a great deal of effort has been made to search for novel materials possessing better TE properties. One approach to increase ZT is to decrease the thermal conductivity (Eq. 1) by introducing "rattling ions" [Nolas 2006, Nolas 2001] or through nanostructuring [Androulakis 2006, Androulakis 2007, Hsu 2004].

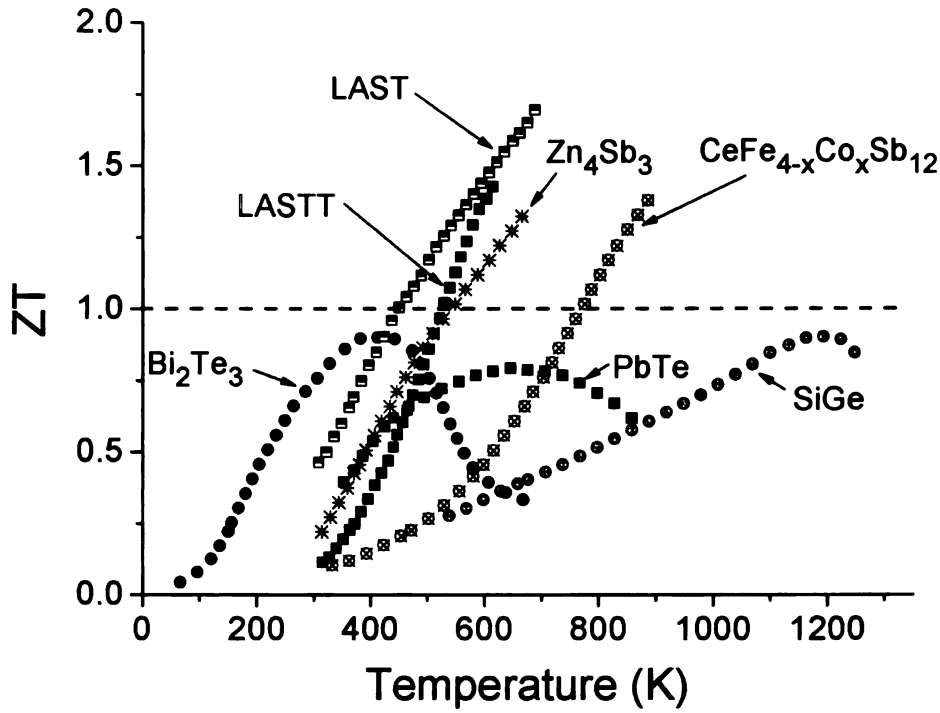

Figure 1.2. Dimensionless figure of merit, ZT, as a function of temperature for several established and novel TE materials (after [Androulakis 2006, Hsu 2004, Tritt 2006]).

The "rattling ion" theory was first introduced by Slater [Slater 1950] to study the ferroelectric behavior of $BaTiO_3$, where under an external applied electric field the displacement of the small Ti^{4+} ion with respect to the center of the O^{2-} octahedral cage results in a large polarization of in $BaTiO_3$ [Slater 1950] (Figure 1.3a). In addition, the "rattling ion" theory has been applied to dielectric and piezoelectric behaviors [Barsoum 1997, Kingery 1976].

Skutterudites use "rattling ions" to reduce the thermal conductivity of TE materials [Nolas 2006, Nolas 2001, Uher 2006] and clathrates [Nolas 2006, Nolas 2001]. Skutterudites, such as $CoSb_3$ based materials, have a cubic structure with a void site at the body center position in the cubic lattice [Uher 2006] (Figure 1.3b). Introducing foreign atoms into the vacant sites decreases thermal conductivity due to phonon scattering, resulting in increase in ZT (Figure 1.2) [Nolas 2006]. Similarly clathrate materials such as $Sr_8Ga_{16}Ge_{30}$ have cage structures that can host guest atoms as rattlers. Consequently, the thermal conductivity can be reduced to improve TE performance [Nolas 2006].

An alternative approach to reduce the thermal conductivity is to incorporate nano-structures in the bulk materials, which was successfully demonstrated in Ag, Sb, and Sn doped PbTe systems, i.e. n-type LAST (Pb-Sb-Ag-Te) [Hsu 2004] and p-type LASTT (Pb-Sb-Ag-Te-Sn) [Androulakis 2006]. The reduction of thermal conductivity in LAST and LASTT materials was attributed to the phonon scattering by the nano-sized regions.

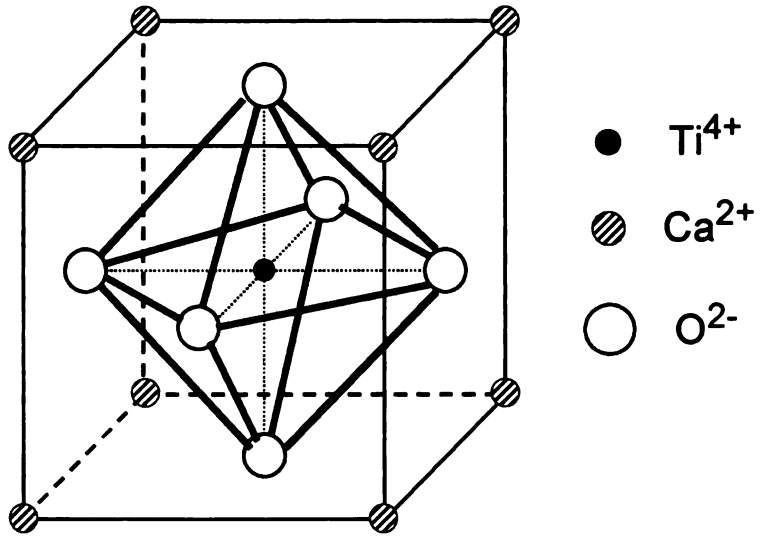

(a)

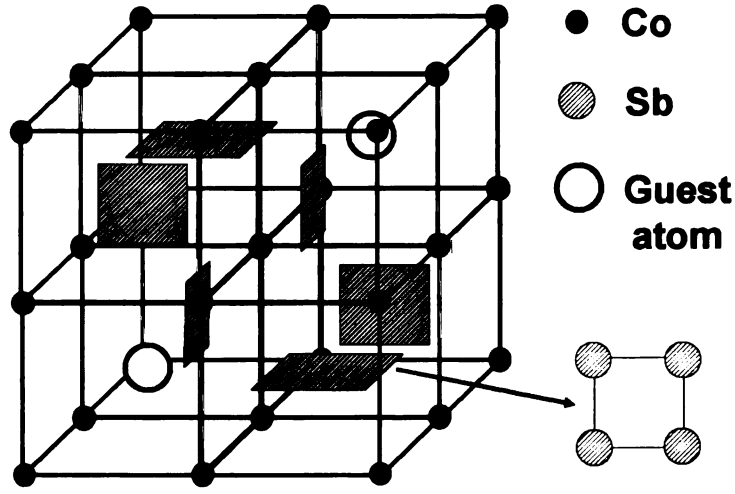

(b)

Figure 1.3. Illustrations of the crystal structures for (a) perovskite-type $BaTiO_3$ (after [Barsoum 1997]) and (b) $CoSb_3$-based skutterudite (after [Nolas 2001]). The "rattling ions" are Ti^{4+} in $BaTiO_3$ and the guest atom(s) in the skutterudite structure.

LAST and LASTT materials have high values of the Seebeck coefficient (Figure 1.4a) and electrical conductivity (Figure 1.4b) with low thermal conductivities (Figure 1.4c), resulting in high ZT values (Figure 1.4d) [Androulakis 2006, Hsu 2004]. The LAST material with the composition of $AgPb_{18}SbTe_{20}$ has a the peak ZT value reaching 1.7 at 700 K (Figure 1.4d) [Hsu 2004], while the LASTT material with the composition of $Ag_{0.5}Pb_6Sn_2Sb_{0.2}Te_{10}$ exhibits ZT values as high as 1.45 at 600 K (Figure 1.4d) [Androulakis 2006].

The good thermoelectric properties of LAST and LASTT materials are believed to originate from Ag and Sb rich nanostructures with dimensions ranging from several nanometers to tens of nanometers [Androulakis 2006, Hsu 2004, Quarez 2005]. It has been proposed that the nano regions in LAST and LASTT materials strongly scatter phonons, which in turn significantly reduces the thermal conductivity [Androulakis 2006, Hsu 2004, Quarez 2005]. The origin of these nanostructures is possibly due to spinodal decomposition [Porter 1990]. For example, in a similar system PbTe-PbS, 2-nm wide alternating strips of PbTe and PbS due to spinodal decomposition were observed by high resolution TEM [Androulakis 2007].

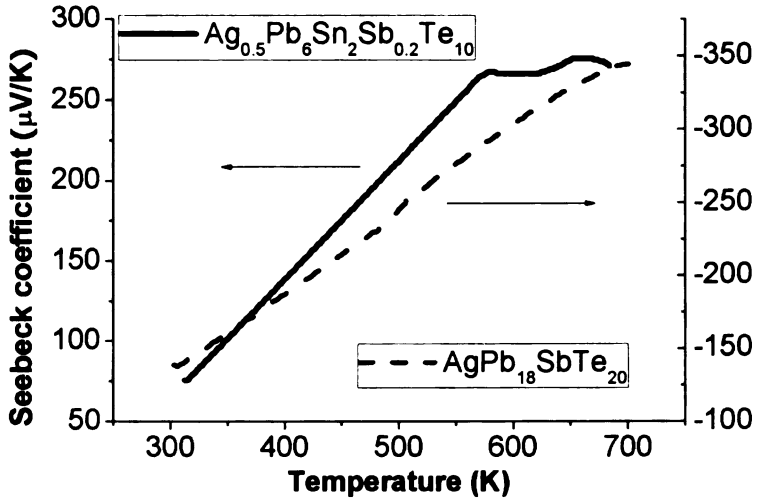

(a)

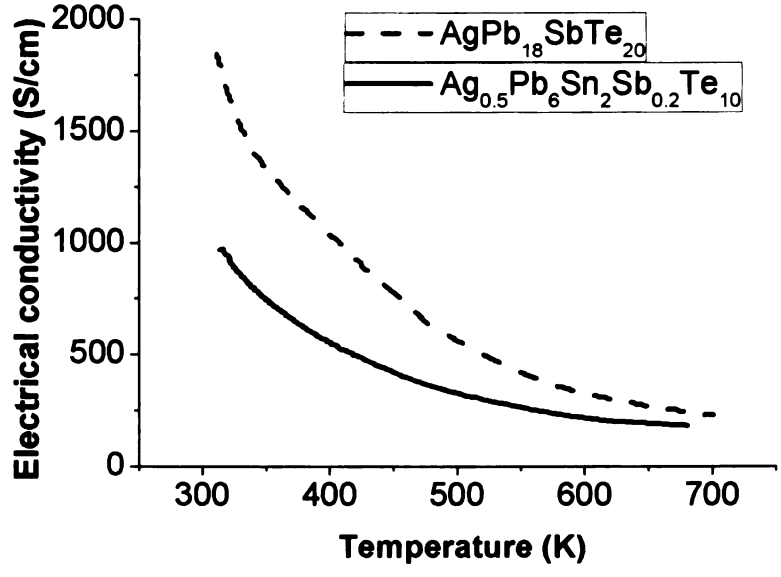

(b)

Figure 1.4. Thermoelectric properties of LAST and LASTT materials, including (a) Seebeck coefficient, (b) electrical conductivity, (c) thermal conductivity, and (d) ZT (after [Androulakis 2006, Hsu 2004]).

Figure 1.4 continued.

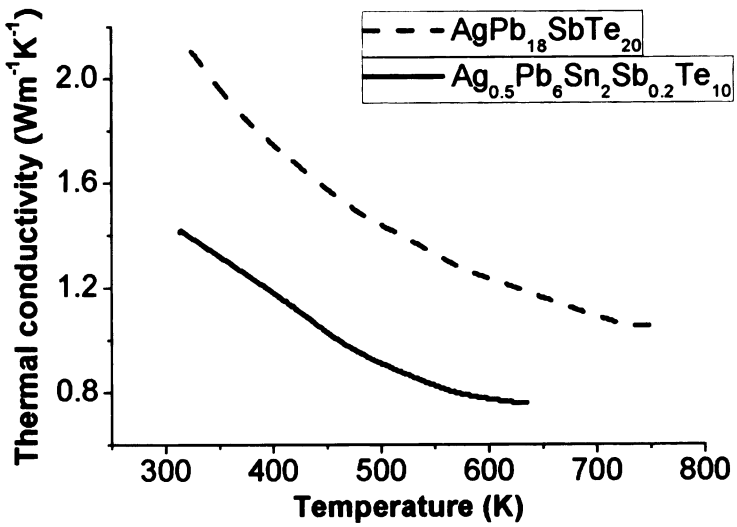

(c)

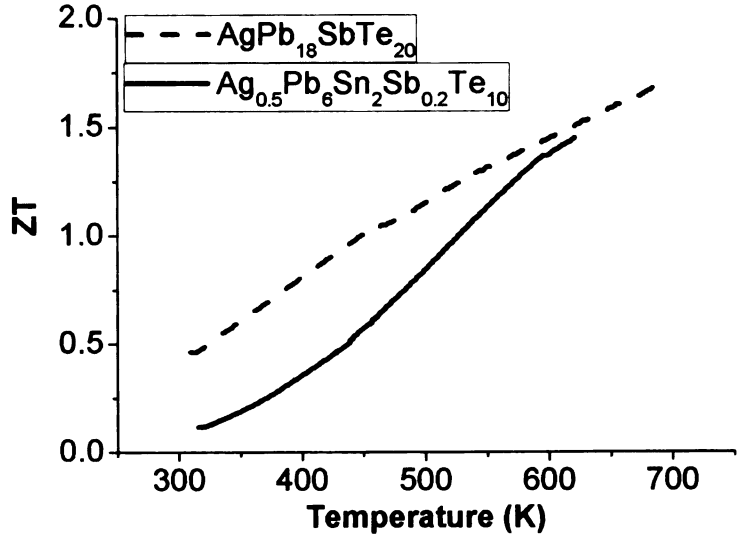

(d)

The second approach to enhance ZT is to increase the Seebeck coefficient (Eq. (1)), which has been demonstrated in low-dimensional TE materials, including 2-dimensional thin films [Bottner 2006, Venkatasubramanian 2001], 1-dimensional nano wires [Rao 2006], and 0- dimensional quantum dots [Harman 2002].

From Eq. (1.8), the Seebeck coefficient, S, is related to the electron density of states, N(E), and the relaxation time, $\tau(E)$, near the Fermi energy, ζ, such that

$$S \propto \left(\frac{\partial \ln N(E)}{\partial E} + \frac{\partial \ln \tau(E)}{\partial E} \right)_{E=\zeta} \qquad (1.8')$$

For bulk materials, N(E) is proportional to $E^{1/2}$ [Nolas 2001], thus $\partial \ln N(E)/\partial E = 1/2$. However due to the quantum confinement in low dimensional materials, a sharp density of states as a function of E can be achieved (Figure 1.5, after [Dresselhaus 2006]), which in turn yields an enhanced Seebeck coefficient [Dresselhaus 2006].

In addition to the ZT enhancement by the quantum confinement effect on N(E), the Seebeck coefficient can also be improved by changing the electron scattering mechanism, thus increasing $\partial \ln \tau(E)/\partial E$ (Eq. 1.8') [Heremans 2004, 2005]. For example, in a PbTe material with Pb nanostructures, Heremans and coworkers found that the Seebeck coefficient could be increased by up to about 90 percent due to selective scattering of electrons whose wave length is comparable to the dimensions of the Pb nanostructures (about 30 to 50 nm) [Heremans 2004, 2005].

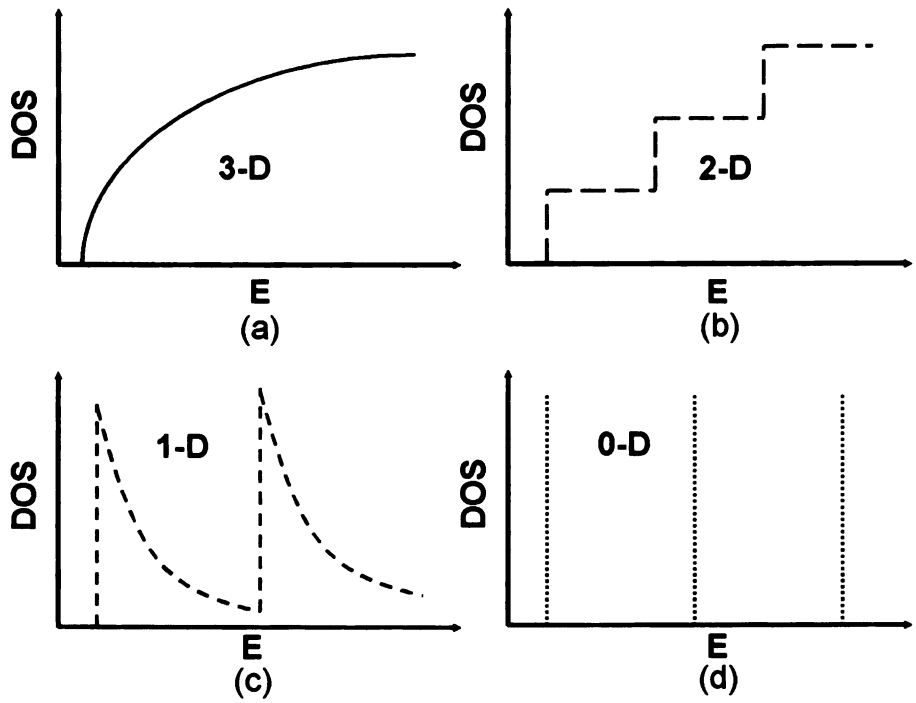

Figure 1.5. Electron density of states (DOS) as a function of energy (E) for (a) bulk materials (3-D), (b) quantum wells and thin films (2-D), (c) quantum/nano-wires (1-D), and (d) quantum dots (0-D) (after [Dresselhaus 2006]). The sharp DOS in low dimension materials can potentially enhance thermoelectric properties by increasing the magnitude of the Seebeck coefficient (Eq. (1.8').

1.3. Applications of thermoelectric materials

The application of TE materials can be classified into two categories: (i) power generation and (ii) refrigeration [Rowe 1995]. TE refrigeration units commonly utilize Bi_2Te_3 while PbTe and SiGe are often used for power generation [Rowe 1995]. Due to the low thermoelectric efficiency of Bi_2Te_3, PbTe and SiGe, these thermoelectric materials are limited to applications where efficiency and/or cost are a secondary consideration [Rowe 1995].

While TE generators (TEG) are used in limited terrestrial applications, such as weather stations and navigation aids [Hall 1995], radioisotope thermoelectric generators (RTG) are widely used in deep space missions, where solar energy is limited. For deep space probes, RTGs are used to convert radioisotope-generated heat into electricity as the power source. Early RTGs employed telluride alloys such as PbTe, while SiGe compounds, which have a better performance at higher temperature and a better resistance to sublimation, have been utilized in recent RTGs [Bennett 1995, Yang 2006].

Although TE cooling devices have so far found limited application in large domestic or industrial refrigerators, they are popular in the small refrigerator markets, such as portable picnic boxes and coolers in automobiles [Goldsmid 1995, Riffat 2003].

Using TE materials (i) to cool electronic components and (ii) for temperature control in scientific instruments [Goldsmid 1995], TE coolers (TEC) have shown many advantages, including [Riffat 2003]: vibration-free operation, small size, high reliability, and precise temperature control. For example, TECs currently are used to cool IR

detectors, laser diodes, X-ray detectors, as well as charge-coupled devices [Riffat 2003].

Recently, due to concern about improving fuel efficiency and reducing green-house gases, a particularly active research area in TE community has been the recovery of waste heat energy from both industrial waste heat [Kajikawa 2006] and vehicle engine waste heat [Matsubara 2006].

In a typical gasoline-fueled internal-combustion engine, only ~ 25% of the total energy is used in vehicle operation, while the other 75% of energy is lost due to radiation from the radiator and cooling system, and engine exhaust [Yang 2006]. The basic idea of waste heat recovery in automobiles is to utilize TEGs to convert waste heat energy into useful electricity [Yang 2006].

There are several major challenges to overcome in the development of TEGs for waste heat recovery applications [Matsubara 2006, Riffat 2003, Yang 2006]. For example, the improvement of energy conversion efficiency requires TE materials with high ZT values as well as good thermal stability. In addition the TE performance at the module level and techniques for integrating TE devices into vehicles are challenges that are unmet.

In addition, since TEGs components will be subject to mechanical vibration and thermal cycling in waste heat recovery applications, it is particularly important to consider the effects of thermo-mechanical stress and thermal fatigue upon the physical properties of TE materials and TE modules. Due to mechanical and/or thermal fatigue, the TE modules may degrade or even fail over time.

2. Thermo-mechanical characterization of brittle materials

2.1. Thermal stress

Thermal stress induced in a solid body due to a temperature gradient is a function of a material's elastic moduli, such as Young's modulus and Poisson's ratio for isotropic materials, the constraint conditions [Wachtman 1996], and the specimen geometry [Kingery 1976].

For a TE leg with a rigid axial constrain subject to a temperature gradient of $\Delta T = T_H - T_C$, the thermal stress, σ_{th}, in the axial direction is [Wachtman 1996]

$$\sigma_{th} = E\varepsilon_{th} = \frac{1}{2}E\alpha\Delta T \tag{1.10}$$

where ε_{th} is the thermal strain, α is the coefficient of thermal expansion (CTE), and E is the Young's modulus.

The Young's modulus of LAST materials ranges from about 24 GPa to 68 GPa [Ren 2007b], while the CTE of LAST materials is approximately 20×10^{-6} K^{-1} (see **Part III, Chapter 9**). Thus for a LAST material with E = 50 GPa, $\alpha = 20 \times 10^{-6}$ K^{-1}, the thermal stress induced by a ΔT of 500 K is approximately 250 MPa. This stress will be in compression during heating ($T_{init} = T_C$) while in tension during cooling ($T_{init} = T_H$), which could be a considerable challenge for TE materials, since most brittle materials are much weaker in tension than in compression [Kingery 1976].

Even if the TE components are not rigidly constrained, thermal stress will arise due to self-constraint within the materials [Kingery 1976], such that

$$\sigma_{th} = \alpha f(E,\upsilon)\Delta T \tag{1.11}$$

where f(E, ν) is a function of Young's modulus and Poisson's ratio. For example, for a long solid cylinder, the maximum thermal stress in the directions transverse to the cylinder axis is given by:

$$\sigma_{th} = \alpha \frac{E}{2(1-\upsilon)} \Delta T \tag{1.12a}$$

while the maximum thermal stress for a infinite plate is

$$\sigma_{th} = \alpha \frac{E}{1-\upsilon} \Delta T \tag{1.12b}$$

When the materials are subject to temperature transients, the thermal stresses are a function of the Biot modulus, Bi, in addition to α, E, ν, and ΔT [Case 2002, Cheng 1951, Zhao 2000]. The Biot modulus, Bi, is defined as [Case 2002, Manson 1966]:

$$Bi = ah/k \tag{1.13}$$

where h is the surface heat transfer coefficient, k is the thermal conductivity, and r is the distance from the specimen's centerline to the interface between the quench medium and the specimen outer surface [Case 2002]. The surface heat transfer coefficient, h, is a sensitive function of the material that makes up the quench medium, the temperature of the quench medium, the temperature of the specimen, the specimen material, and the surface roughness of the specimen [Case 2002, Kim 1991, Lee 1993].

For the quenching of a flat plate, the maximum stress state at the surface of the plate, σ_{max}, can be estimated as [Case 2002, Cheng 1951, Lu 1998]:

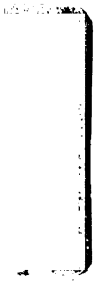

$$\sigma_{max} = \frac{E\alpha\Delta T}{1-\nu}\left[\frac{1}{1.5+3.25/Bi}\right] \text{ for } 0 < Bi < 5 \quad (1.14a)$$

or

$$\sigma_{max} = \frac{E\alpha\Delta T}{1-\nu}\left[\frac{1}{1.5+3.25/Bi-0.5\exp(-16/Bi)}\right] \text{ for } 0 < Bi < 20 \quad (1.14b)$$

Thus to fully characterize the thermo-mechanical behavior of TE materials, one must have knowledge of not only the fracture strength, but also the elastic and thermal properties, such as thermal expansion and thermal conductivity. Also, the details of the temperature and time (during the quench) dependence of h must be known.

2.2. Fracture strength and Weibull modulus

Techniques to determine the fracture strength of brittle materials can be classified into two categories, i.e. uniaxial bending and biaxial flexure [Wachtman 1996]. Compared to uniaxial techniques, such as three-point bending and four-point bending, biaxial testing has several advantages [Shetty 1980]: flexible specimen geometry, insensitivity to specimen edge flaws that are usually introduced during specimen preparation, and easier specimen preparation. In addition, since the in-service stress state is typically multiaxial, data obtained from biaxial testing may be more useful in device design [Ren 2006].

From the TE device design point of view, knowledge of the scatter in fracture strength is of equal importance to the mean of fracture strength. In commonly adapted TE module designs, TE elements (usually in the forms of "legs") are connected so that they

are thermally in parallel and electrically in series (Figure 1.6). Since the functionality of the entire module is determined by the weakest leg, it is extremely important to know the distribution of fracture strength.

The fracture strength of a polycrystalline brittle material is determined by the largest flaw [Wachtman 1996]. If there is only one type of flaw population, the fracture strength may obey the Weibull distribution, which is a special case of extremal value statistics, a sub-category of the order statistics [Castillo 1988]. The r-th order statistic of a given sample refers to the r-th member in the ordered sequence of the sample. Extremal value statistics considers the distribution of either the maximum or the minimum values [Castillo 1988].

The distribution of the fracture strength of polycrystalline materials can be expressed in terms of Weibull distribution [Wachtman 1996]:

$$\ln\ln\left(\frac{1}{1-P_f}\right) = m\ln\left(\frac{\sigma}{\sigma_0}\right) \tag{1.15}$$

where P_f is the probability of failure, m is the Weibull modulus, σ and σ_0 are sample strength and characteristic strength, respectively.

When the failure strength, σ, equals the characteristic strength, σ_0, then $m\ln(\sigma/\sigma_0) = 0$ and the failure probability $P_f \approx 0.632$. Thus, the characteristic strength is a measure of the "average" strength of the tested group, while the Weibull modulus characterizes the strength distribution, where a higher value of m indicates a small degree of scatter in the data. Also, the Weibull distribution may be viewed as a "skewed Gaussian" distribution

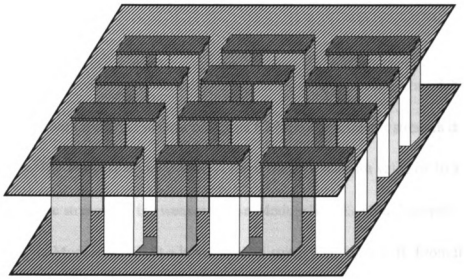

Figure 1.6. Schematic of a TE module in which the individual legs are electrically connected in series and thermally connected in parallel.

with σ_0 as a location parameter and m as a shape parameter.

The Weibull analysis can be interpreted graphically by Weibull plots, in which $\ln\ln(1/(1- P_f))$ is plotted against $\ln(\sigma)$. Data obtained from a group of samples that obey the Weibull distribution can be represented by a straight line (Figure 1.7), whose slope is the Weibull modulus, and the characteristic strength is the σ value that corresponds to $\ln\ln(1/(1- P_f)) = 0$.

To illustrate the concept of Weibull analysis in TE module design, consider two 10-leg modules with the same mean strength of 65 MPa but different strength distribution (Figure 1.7a). The weakest leg in Module A has a fracture strength value of 30 MPa, while the fracture strength of the weakest leg in Module B is 53 MPa. Naturally one would infer that Module A fails at a lower applied stress than Module B. From the corresponding Weibull plots (Figure 1.7b), it is clear that the strength distributions of both modules obey a Weibull distribution, as indicated by the straight line fit through each data set. Module B with a higher Weibull modulus value (m = 10) shows a smaller scatter in the fracture strength than Module A (m = 3), although the characteristic strength values, σ_0, are 72 MPa for Module A and 68 MPa for module B, which are comparable (Figure 1.7b).

2.3. Elastic properties

Elastic moduli are an important aspect of the study of the thermo-mechanical behavior of TE materials subjected to thermal and mechanical loading. However,

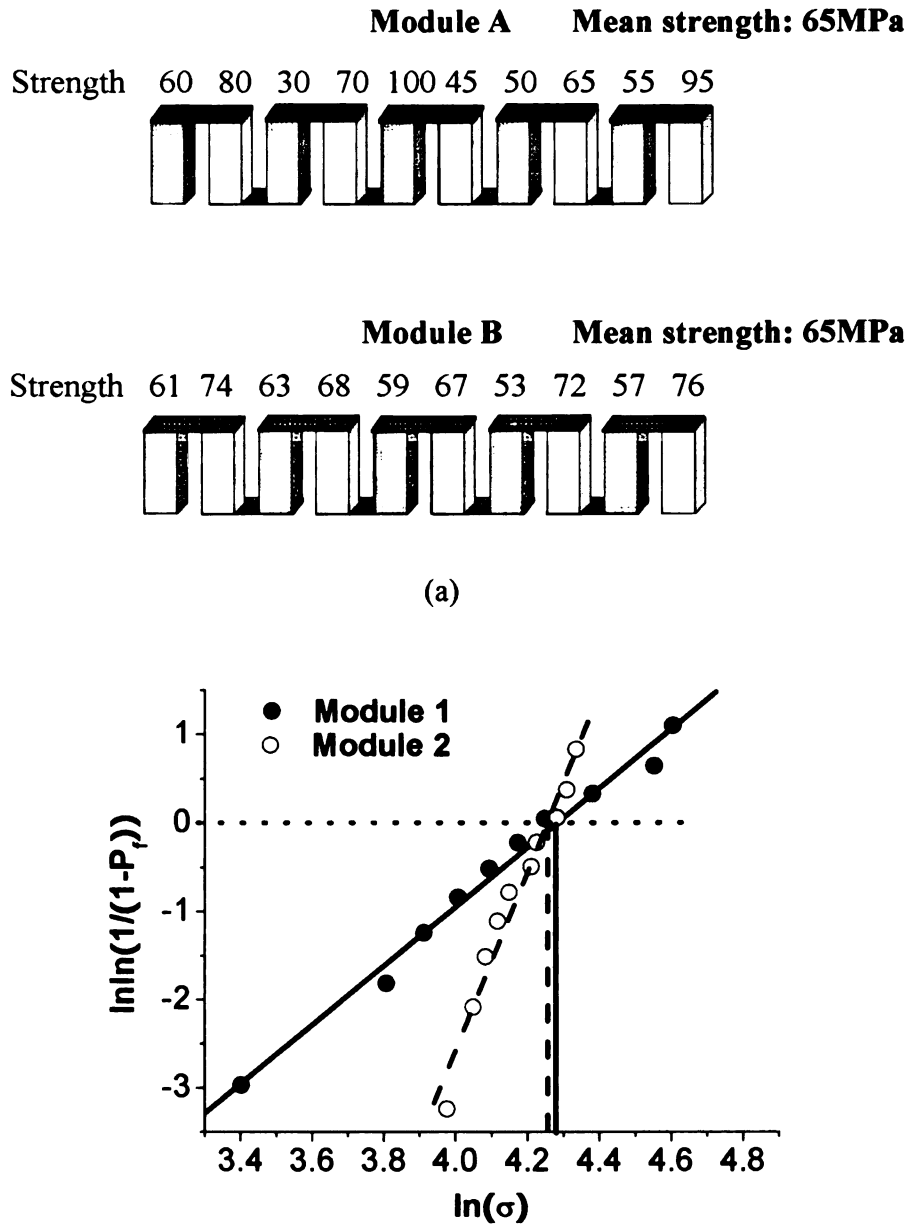

Figure 1.7. (a) Schematics of two TE modulus with the same mean strength of 65 MPa but different strength distributions. (b) Weibull plot illustrating the difference in strength distribution between the two modules. Module B with a higher Weibull modulus has a smaller scatter in strength values than Module A.

elasticity is a complex subject, not only because the elastic constants are fourth rank tensors [Nye 1967] but also because the elastic constants can be affected by many factors, including temperature [Simmons 1971], damage state [Case 1993], microstructure [Radovic 2004], and composition [Ren 2007a].

2.3.1. Elasticity as a function of temperature

For brittle polycrystalline materials, Young's modulus usually decreases with increasing temperature, which has been described by several empirical equations, including the Wachtman equation [Wachtman 1961]:

$$E(T) = E_0 - bT\exp\left(-\frac{T_0}{T}\right) \tag{1.16}$$

where E(T) is the temperature dependent Young's modulus, E_0 is the Young's modulus at 0 K, b and T_0 are empirical constants, and T_0 is a constant related to Debye temperature. Anderson later provided a justification to Wachtman equation [Anderson 1966] by relating Young's modulus to temperature dependent bulk modulus. Anderson demonstrated that b is related to Gruneisen parameters and T_0 approaches 1/2 of Debye temperature at high temperatures [Anderson 1966]. When Wachtman's equation is applied to an elastic modulus versus temperature data set, parameters b and T_0 are usually determined by a least-squares fit of Eq. (1.16) to the data.

The temperature dependence of the elastic moduli for many material systems can be described by the Wachtman relationship. For example, the aggregate Young's modulus

values of PbTe and SnTe calculated from single crystal data [Simmons 1971] is described well by the Wachtman equation (Figure 1.8a). Figure 1.8b also gives the aggregate Poisson's ratio [Simmons 1971] as a function of temperature for PbTe and SnTe, which can not be described by a simple function.

At temperatures $T >> T_0$, Wachtman equation simplifies to [Case 1983]

$$E(T) = E_{RT}(1 - b_E T) \tag{1.17}$$

where E_{RT} is the Young's modulus at room temperature and b_E is a fitting parameter.

For polycrystalline materials, grain boundary sliding occurs at elevated temperatures, thus Young's modulus versus temperature behavior deviates from a linear relationship (Eq. (1.17)) (Figure 1.9). The onset temperature of grain boundary sliding is a function of impurities or second phases at grain boundaries as well as grain size, such that grain boundary sliding starts at a lower temperature for smaller grain sizes (Figure 1.9) [Wachtman 1996].

2.3.2. Elasticity as a function of composition

The elastic moduli are proportional to the second derivative of the binding energy with respect to strain. Since alloying can change the binding energy, the elasticity thus can be greatly altered by alloying. For binary solid solutions, A_XB_{1-X}, or pseudo-binary within ternary or quaternary compounds, $A_XB_{1-X}C$, or $A_XB_{1-X}CD$, the elasticity is a function of the composition parameter, x, such that [Ren 2007b]:

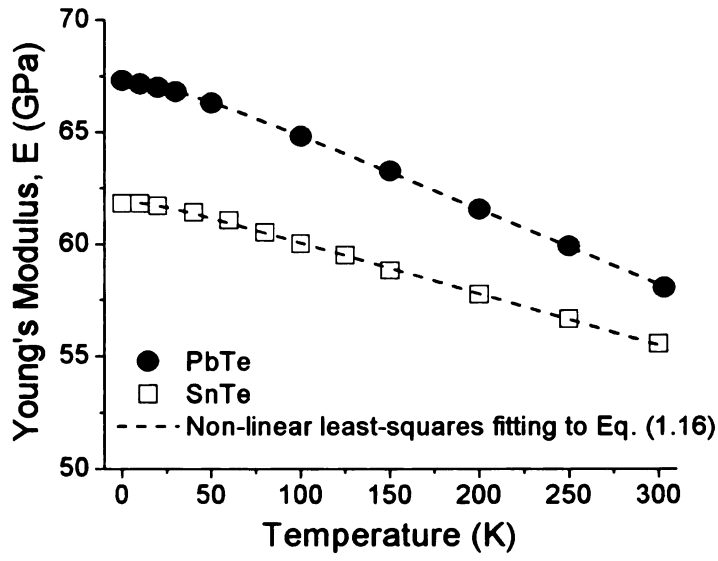

(a)

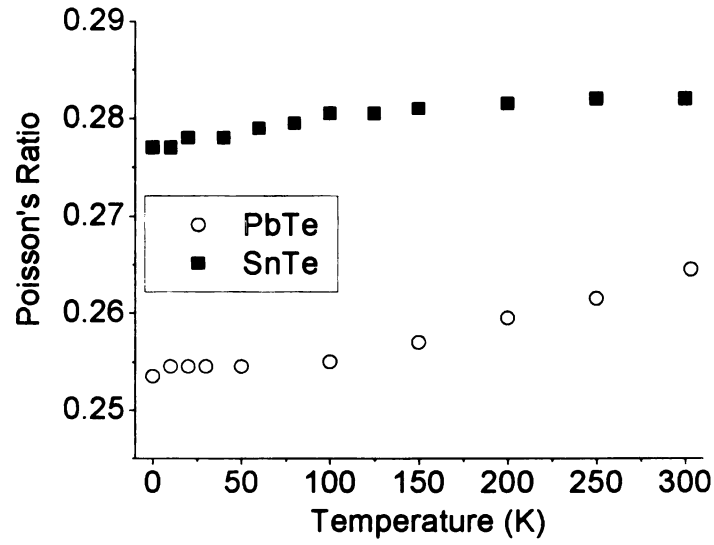

(b)

Figure 1.8. Temperature dependent (a) Young's modulus and (b) Poisson's ratio for PbTe and SnTe below room temperature.

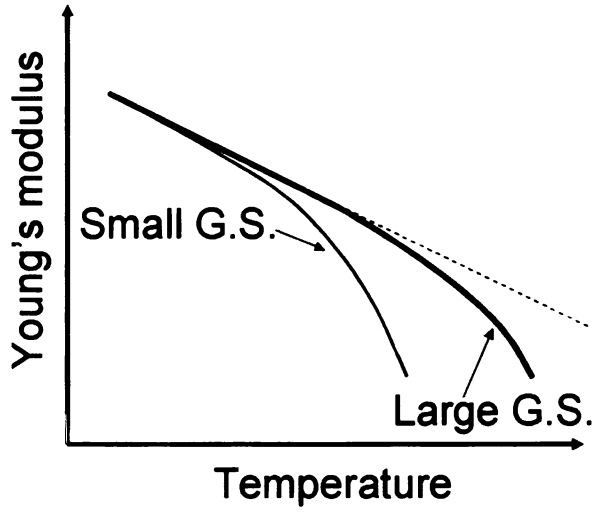

Figure 1.9. Schematic of temperature dependent Young's modulus for polycrystalline materials. Young's modulus versus temperature deviates from linear relationship at elevated temperatures due to grain boundary sliding, which is a function of grain size. The onset temperature of grain boundary sliding is lower for materials with smaller grain sizes.

$$E(x) = xE_A + (1-x)E_B - Bx(1-x) \tag{1.18}$$

where E_A and E_B are Young's modulus of the end members, and B is usually referred as bowing parameter. The bowing parameter may be interpreted in terms of the degree of lattice mismatch. When b approaches zero, the system obeys Vegard's law, where the elasticity of the system is a linear combination of the end-member's values. Detailed discussion of bowing parameters is given in **Part III Chapter 2**.

2.3.3. Elasticity as a function of the microcrack damage state

The effect of the microcracking damage state on Young's modulus is a function of the crack damage parameter, ε, such that [Case 2002]:

$$E(\varepsilon) = E_{un}[1 - f(\upsilon)\varepsilon] \tag{1.19}$$

where E_{un} is the Young's modulus of the un-damaged material, the function f(ν) depends on the microcrack orientation and Poisson's ratio. The crack damage parameter, ε, is a function of the mean square of the crack surface area, $\langle A^2 \rangle$, mean crack perimeter, $\langle P \rangle$, and the crack density, N, which may be described by [Case 2002]:

$$\varepsilon = \frac{2}{\pi}\frac{\langle A^2 \rangle}{\langle P \rangle}N \tag{1.20}$$

A model study on alumina by Case and Kim *et al.* [Case 1993, Kim 1993a, Kim 1993b] demonstrated that the reduction in Young's modulus due to surface limited cracks induced by indentation was a function of the volumetric number density of microcracks as well as the crack size [Kim 1993b].

Case and coworkers [Case 1993] treated the alumina specimens with surface cracks as a composite material, which consisted of crack-damaged surface layers and undamaged bulk material. Kim and Case [Kim 1993a] then modified the dynamic beam vibration theory to accommodate the damaged/undamaged alumina composites [Case 1993] with crack shape correction [Kim 1993a]. The experimental values of Young's modulus for surface-cracked alumina [Kim 1993b] agreed well with the model developed by Case and Kim (Figure 1.10) [Case 1993, Kim 1993a].

2.3.4. Elasticity as a function of microstructure

In addition to temperature, composition, and damage state, elasticity is also a function of microstructure, including porosity and second phases. Young's modulus is decreased by porosity, P, which can be described by [Wachtman 1996]:

$$E(P) = E_d \exp(-b_P P) \tag{1.21}$$

where E_d is the Young's modulus of the dense materials and b_P is an empirical constant.

For modulus – porosity relationships, the value b_P is about 4 for many ceramics [Wachtman 1996]. An experimental study on polycrystalline alumina showed Young's modulus decreased from > 380 GPa to ~ 350 GPa when volumetric porosity increased from 1.5% to about 4% (Figure 1.11) [Radovic 2004]. The same study by Radovic *et. al.* [Radovic 2004] demonstrated the reduction in Young's modulus due to a small volume fraction porosity was detectible by resonant ultrasound spectroscopy (RUS) but not detected by in nanoindentation. The difference in the nanoindentation technique and RUS

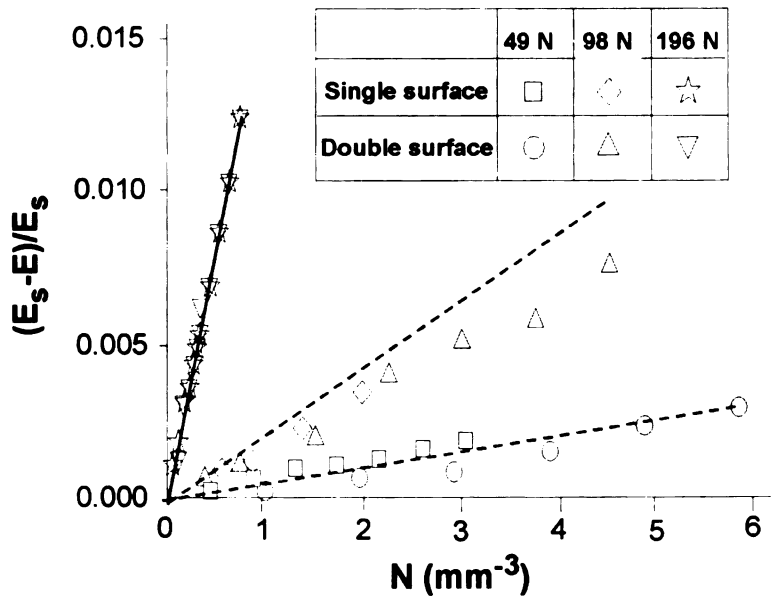

Figure 1.10. Reduction in Young's modulus as a function of indentation-induced crack density as well as crack size (after [Kim 1993b]).

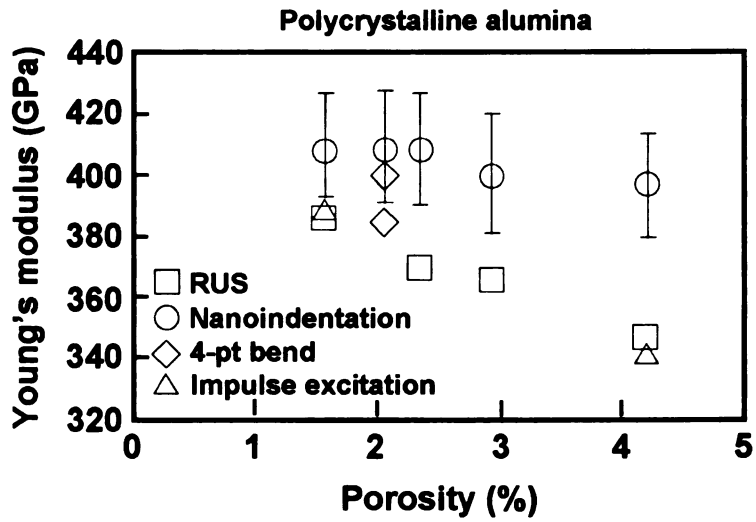

Figure 1.11. Young's modulus of polycrystalline alumina as a function of volumetric porosity measured by nanoindentation and RUS techniques, where RUS has a higher sensitivity to porosity (after [Radovic 2004]). Measurements made by 4-point bend and impulse excitation are also illustrated.

in terms of sensitivity to defects such as pores and cracks will be discussed in detail in **Part III Chapter 2**.

2.3.5. Resonant ultrasound spectroscopy

As discussed in **Section 2.1**, the elastic moduli are critical to evaluate the stress/strain in the TE devices under in-service conditions. The elastic constants of solids can be determined by static or dynamic methods. Static or quasi-static methods of determining the elastic moduli include bending tests [Radovic 2004, Wachtman 1996] and indentation [Marshall 1982, Radovic 2004, Ren 2007b]. Dynamic methods, including wave propagation techniques and resonant techniques, have much higher accuracy [Wachtman 1996]. In addition the stresses/strains involved in dynamic tests are far below the elastic limit of the material. The low values of stress imposed by dynamic measurement techniques are important for measurements at elevated temperatures because the possibility of time-dependent deformation or rate dependency in the measurements is minimized. Thus, the same test specimens can be used for repeated measurements as a function of temperature. Therefore the dynamic methods for determining elastic moduli are considered as non-destructive testing [Migliori 1997].

Amongst various resonant techniques, RUS is one of the more accurate and popular test methods to determine the elastic properties of solids [Leisure 1997, Migliori 1997, Migliori 1993, Radovic 2004, Ulrich 2002, Zadler 2004]. The RUS technique is based on the principle that the vibrational modes induced in a mechanically driven specimen are a

function of the elasticity, geometry, dimensions, and mass density of the specimens [Leisure 1997, Migliori 1997, Migliori 1993, Zadler 2004].

The elasticity calculations in RUS are linked to the concepts of "direct" and "inverse" problems in mathematical physics [Dulikravich 1999]. The direct problem consists of calculating the resonant frequencies, given the elastic moduli as well as the mass and dimensions of the specimens. The inverse problem is the determination of the elastic moduli and/or specimen dimensions when the resonant frequencies are known, for example, from the RUS spectra [Leisure 1997, Migliori 1993, Zadler 2004].

Mechanical vibrations in solid crystalline materials can be described by [Leisure 1997]:

$$C_{ijkl}\frac{\partial^2 u_k}{\partial x_j \partial x_i} = \rho\frac{\partial^2 u_i}{\partial^2 t} \tag{1.22}$$

where the C_{ijkl} are the elastic constants, u_i are the displacements, x_i are the spatial coordinates, t is time, and i, j, k = 1, 2, 3.

A general analytical solution to Eq. (1.22) is usually unavailable. A commonly used approach to solving Eq. (1.22) is to find the extremum of the elastic Lagrangian function [Whittaker 1944], L, which is given by [Leisure 1997, Migliori 1997, Migliori 1993]:

$$L = \frac{1}{2}\int_V (KE - PE)dV \tag{1.23}$$

where V is the specimen volume. The kinetic energy, KE, and the potential energy, PE, are given as:

$$KE = \frac{1}{2}\rho\omega^2 u_i^2$$

where ρ is the mass density and ω is the angular frequency of the vibrational mode. The potential energy PE may be written as:

$$PE = \frac{1}{2}C_{ijkl}u_{i,j}u_{k,l} \tag{1.24}$$

Following the Rayleigh-Ritz technique, the displacement vector can be expanded into a complete set of functions [Leisure 1997, Migliori 1993], such that:

$$u_i = a_{i\alpha}\Phi_\alpha \tag{1.25}$$

where $a_{i\alpha}$ are expansion coefficients and Φ_α are the basis functions. The Lagrangian can be written in terms of the following matrix form [Leisure 1997, Migliori 1993]:

$$L = \frac{1}{2}\left(\left(\rho\omega^2\right)\mathbf{a}^T\mathbf{E}\mathbf{a} - \mathbf{a}^T\mathbf{\Gamma}\mathbf{a}\right) \tag{1.26}$$

In Eq. (1.26), the expansion coefficients $a_{i\alpha}$ are expressed in terms of vector $\mathbf{a}$ and its transpose $\mathbf{a}^\mathbf{T}$. The vectors subsume the material parameters including elastic moduli and dimensions. Matrices $\mathbf{E}$ and Γ are constructed from the basis functions, Φ_α. Equating the derivative of L to zero yields:

$$\mathbf{\Gamma}\mathbf{a} = \left(\rho\omega^2\right)\mathbf{E}\mathbf{a} \tag{1.27}$$

Thus, solving Eq. (1.27) is the solution of the direct problem, where the resonant frequencies for a 3-D elastic body are computed from the eigenvalues $\rho\omega^2$ [Leisure 1997, Migliori 1993].

For rectangular parallelepipeds (RP), Legendre polynomials are often used as the basis functions, while powers of Cartesian coordinates are used for a solid body of an arbitrary geometry [Leisure 1997, Migliori 1997]. In addition, symmetry conditions are

often applied to reduce the size of matrices **E** and Γ [Leisure 1997, Migliori 1993].

For the inverse problem, one is interested in calculating the elastic moduli and/or specimen dimensions from measured frequencies, i.e. calculation of the eigenvectors, **a**, Eq. (1.27). A common strategy used to solve the inverse problem (which in this case is determining the elastic moduli from the RUS data) is to minimize the error relationship, χ, defined as [Leisure 1997, Migliori 1993]:

$$\chi = \sum_n w_n \frac{(f_n - g_n)^2}{g_n^2} \tag{1.28}$$

where w_n are the weighing parameters, f_n and g_n are the calculated and measured specimen resonant frequencies, respectively. To minimize χ one uses a non-linear least-squares fitting procedure, which requires an initial set of parameters.

A frequently used non-linear least-squares scheme is the Levenberg-Marquardt (LM) algorithm [Leisure 1997, Migliori 1993, Ulrich 2002], where the Taylor's expansion [Wylie 1982] is used to linearize the error relationship $\chi(\mathbf{a})$ (Eq. (1.28)):

$$\chi(\mathbf{a}) = \chi(\mathbf{a}_0) + \left(\partial\chi / \partial \mathbf{a}_\alpha\right)_{\mathbf{a}_{\alpha 0}} \left(\mathbf{a}_\alpha - \mathbf{a}_{\alpha 0}\right)$$

$$+ \frac{1}{2}\left(\partial^2 \chi / \left(\partial \mathbf{a}_\alpha \partial \mathbf{a}_\beta\right)_{\mathbf{a}_{\alpha 0}\mathbf{a}_{\beta 0}} \left(\mathbf{a}_\alpha - \mathbf{a}_{\alpha 0}\right)\left(\mathbf{a}_\beta - \mathbf{a}_{\beta 0}\right)\right) + \cdots \tag{1.29}$$

where the error χ is expressed as a linear function of the expansion coefficients vector **a**.

If the initial guess, $\mathbf{a}_{\alpha 0}$, closely approximates the solution, then the higher order terms of Eq. (1.29) become small, thus Eq. (1.29) becomes:

$$\partial\chi / \partial \mathbf{a}_\alpha = \left(\partial\chi / \partial \mathbf{a}_\alpha\right)_{\mathbf{a}_{\alpha 0}} + \left(\partial^2 \chi / \left(\partial \mathbf{a}_\alpha \partial \mathbf{a}_\beta\right)_{\mathbf{a}_{\alpha 0}\mathbf{a}_{\beta 0}} \left(\mathbf{a}_\beta - \mathbf{a}_{\beta 0}\right)\right) \tag{1.30}$$

In order to find the minimum of the error, χ, (Eq. (1.30)), one sets the derivative $\partial\chi/\partial\mathbf{a}_\alpha$ to zero and solves for the local extremum of Eq. (1.30) with non-linear least-squares techniques, which gives:

$$\mathbf{a}_\alpha = \mathbf{a}_{\alpha 0} - \mathbf{A}^{-1}_{\alpha\beta}\mathbf{B}_\beta \tag{1.31}$$

Substituting $\mathbf{a}_\alpha$ into Eq. (1.27) yields a new set of f_n, which gives a smaller error, χ (Eq. (1.28)), than the initial guess. The computation continues in an iterative manner until the error function is no longer reduced.

Commercial software is now available to analyze RUS data. For example, the RP Model (Quasar, Inc., Albuquerque NM) utilizes the scheme described above and performs the non-linear least-squares fitting. However, due to the nature of the LM algorithm and other non-linear least-squares procedures, the initial guesses need to be relatively close to the true values, otherwise the fitting can be easily trapped at a local minimum rather than converging to the solution (the global minimum) [Migliori 1993].

When considering the error estimation, it is difficult to trace the error to individual elastic constants, but instead the error can be related to the linear combinations of the elastic constants [Migliori 1993]. Usually, to characterize the overall fit of the data to the model, an overall goodness-of-fit parameter, the root mean square (RMS) error is used. A smaller RMS error indicates a better fit of the data to the model. In some software, such as RP Model (Quasar, Inc., Albuquerque NM), a realistic error for individual parameters is estimated as the value that corresponds to a 2 percent increase in χ^2 [Migliori 1993].

There are several considerations in the application of RUS technique [Migliori 1993].

First, (as discussed previously), in order for the RUS software to converge to a solution, it is very important to provide a close initial guess for each of the fitted parameters, that is, for each of the elastic moduli [Migliori 1993]. Secondly, since the specimen dimensions are included in the vector **a** and the initial guess $\mathbf{a}_{\alpha 0}$, an accurate determination of the specimen dimensions is required in RUS technique [Migliori 1993]. Last but not least, missing peaks (resonant vibrational modes) during RUS scan can cause dramatic difference in fitting results. Thus, for a given specimen one should take more than one spectrum by shifting the specimen location on the RUS transducers [Migliori 1993].

Missing peaks usually result from specimen placement on the excitation and pickup transducers of the RUS apparatus (**Part II**). If the excitation transducer is placed on one of the nodal positions for a vibrational mode, the specimen will not be excited. In addition, if one or two of the pickup transducers are placed at the anti-nodes, the detected vibrational intensity will be attenuated. Thus, certain modes of vibration have low amplitude due to the physical constraint resulting from the dead weight loading of the specimen onto the transducers. The previously discussed RUS scheme assumed free vibrations; however in practice the specimen must be in physical contact with the transducers. Thus, by shifting the specimen location with respect to transducers, the missing resonant peaks in one specimen's placement will likely appear with a different placement [Migliori 1993].

To visualize mechanical vibrations in solid bodies, one can refer to the Chladni patterns (Figure 1.12), which illustrate the nodal lines for vibrating thin plates [Rossing

1982]. Chladni patterns are functions of plate geometry as well as frequency (Figure 1.10). In addition, Chladni patterns can be visualized by sprinkling sand or powder onto a mechanically driven thin plate, such that the sand particles are collected at the nodal lines where the vibration amplitude is minimal. It is worthwhile noting that even for a thin plate with simple geometry, the nodal patterns for the vibrational modes can be quite complicated as the frequency increases (Figure 1.12). Thus, for thick plates such as those used in the RUS experiments, the vibrational modes will be extremely complex.

3. Scope of current research

This dissertation focuses on the effects of temperature and composition on elasticity of PbTe-related thermoelectric materials including pure PbTe, LAST and LASTT. In addition, composition dependence of hardness is evaluated. The fracture strength of a p-type ingot LASTT was measured using biaxial flexure testing while the strength distribution was analyzed by Weibull analysis. Also, preliminary study of the fracture strength for n-type ingot and hot pressed specimens were carried out. In addition, effort to improve the fracture strength by powder processing is included.

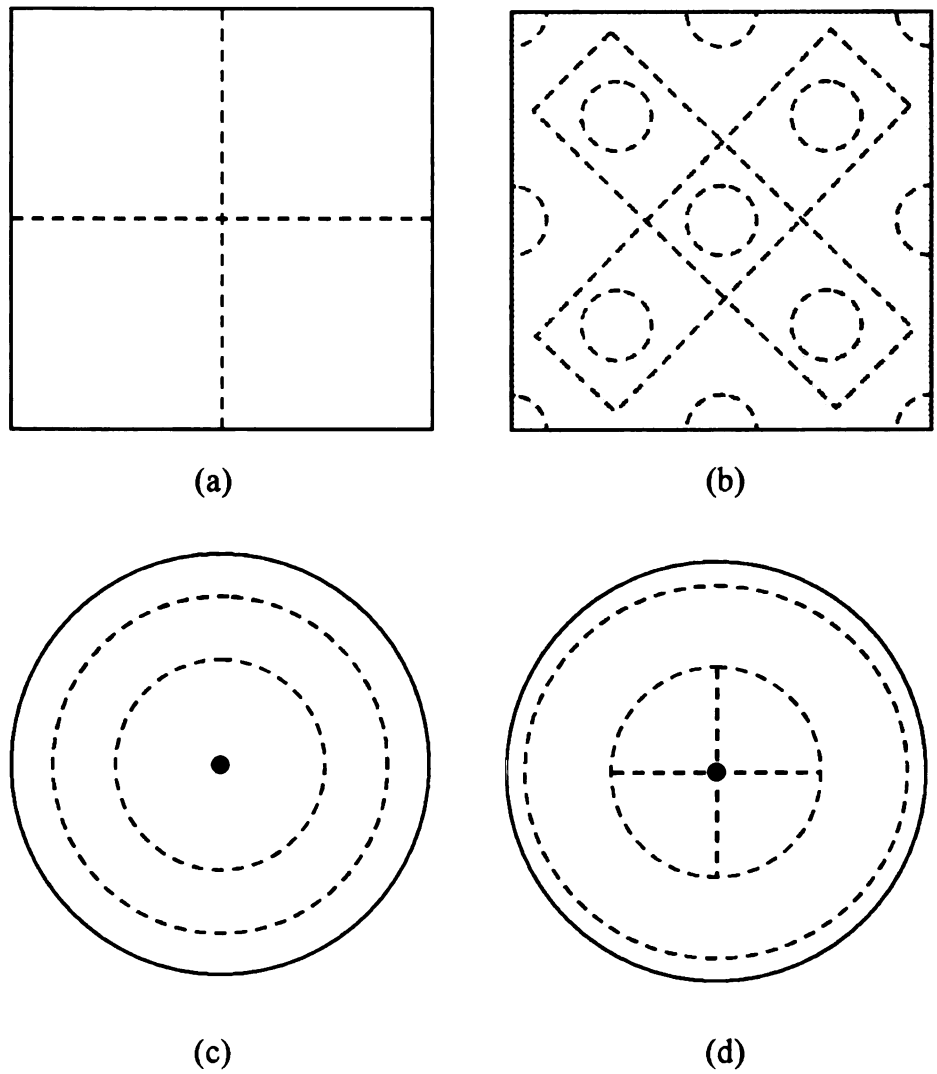

Figure 1.12. Schematics of vibrational patterns (Chldani figures) for thin plates with (a)-(b) square geometry and (c)-(d) circular geometry. Nodal positions, which have minimum vibration amplitude, are illustrated by the heavy dots and dotted lines. For a given specimen, the nodal pattern is a function of vibrational frequency. For example, (a) and (c) are patterns obtained at lower frequencies than (b) and (d), respectively.

References

[Anderson 1966] O. L. Anderson, "Derivation of Wachtman's Equation for Temperature Dependence of Elastic Moduli of Oxide Compounds", *Physical Review*, **144**: 553-557 (1966).

[Androulakis 2006] J. Androulakis, K. F. Hsu, R. Pcionek, H. Kong, C. Uher, J. J. DAngelo, A. Downey, T. Hogan and M. G Kanatzidis, "Nanostructuring and high thermoelectric efficiency in p-type Ag(Pb1-ySny)(m)SbTe2+m", *Advanced Materials*, **18**: 1170-1173 (2006).

[Androulakis 2007] J. Androulakis, C. H. Lin, H. Kong, C. Uher, C. I. Wu, T. Hogan, B. A. Cook, T. Caillat and M. G Kanatzidis, "Spinodal Decomposition and Nucleation and Growth as a Means to Bulk Nanostructured Thermoelectrics: Enhanced Performance in Pb1-xSnxTe-PbS", *Journal of the American Chemical Society*, **129**: 9780-9788 (2007).

[Barsoum 1997] M. W. Barsoum, *Fundamentals of ceramics*, (McGraw-Hill Cc., Inc., New York, 1997), pp. 70-71, 410-415.

[Bennett 1995] G L. Bennett, "Space applications", in *CRC handbook of thermoelectrics*, edited by D. M. Rowe (CRC Press, Inc., New York, 1995), 515-537.

[Bottner 2006] H. Bottner, G Chen and R. Venkatasubramanian, "Aspects of thin-film superlattice thermoelectric materials, devices, and applications", *MRS Bulletin*, **31**: 211-217 (2006).

[Case 2002] E. D. Case, "The Saturation of Thermomechanical Fatigue in Brittle Materials", in *Thermo-Mechanical Fatigue and Fracture*, edited by M. H. Alibadi (WIT Press, Southampton, UK, 2002), pp. 137-208.

[Case 1993] E. D. Case and Y. Kim, "The Effect of Surface-Limited Microcracks on the Effective Youngs Modulus of Ceramics .1. Analysis", *Journal of Materials Science*, **28**: 1885-1900 (1993).

[Castillo 1988] E. Castillo, *Extreme value theory in engineering*, (Academic Press, Inc., Boston, 1988), pp. 24, 198-203.

[Cheng 1951] C. M. Cheng, "Resistance to thermal shock", *J. Am. Rocket Soc.*, **21**: 147-153 (1951).

[Dresselhaus 2006] M. S. Dresselhaus and J. P. Heremans, "Recent developments in low-dimensional thermoelectric materials", in *Thermoelectric handbook: macro to nano*, edited by D. M. Rowe (Taylor and Francis, New York, 2006), 39/1- 39/24.

[Dulikravich 1999] G. S. Dulikravich, T. J. Martin and B. H. Dennis, "Multidisciplinary inverse problems", in *Inverse problems in engineering: theory and practice*, edited by K. A. Woodbury (The American society of mechanical engineers, New York, 1999), 1-8.

[Fano 1995] V. Fano, "Lead telluride and its alloys", in *CRC handbook of thermoelectrics*, edited by D. M. Rowe (CRC Press, Inc., New York, 1995), 257-266.

[Goldsmid 1960] H. J. Goldsmid, *Applications of thermoelectricity*, (John Wiley and Sons, Inc., New York, 1960), pp. 23-39.

[Goldsmid 1995] H. J. Goldsmid, "Applications of thermoelectric cooling", in *CRC handbook of thermoelectrics*, edited by D. M. Rowe (CRC Press, Inc., New York, 1995), 617-619.

[Hall 1995] W. C. Hall, "Terrestrial applications of thermoelectric generators", in *CRC handbook of thermoelectrics*, edited by D. M. Rowe (CRC Press, Inc., New York, 1995), 503-513.

[Harman 2002] T. C. Harman, P. J. Taylor, M. P. Walsh and B. E. LaForge, "Quantum dot superlattice thermoelectric materials and devices", *Science*, **297**: 2229-2232 (2002).

[Heremans 2004] J. P. Heremans, C. M. Thrush and D. T. Morelli, "Thermopower enhancement in lead telluride nanostructures", *Physical Review B*, **70**: (2004).

[Heremans 2005] J. P. Heremans, C. M. Thrush and D. T. Morelli, "Thermopower enhancement in PbTe with pb precipitates", *Journal of Applied Physics*, **98**: (2005).

[Hsu 2004] K. F. Hsu, S. Loo, F. Guo, W. Chen, J. S. Dyck, C. Uher, T. Hogan, E. K. Polychroniadis and M. G. Kanatzidis, "Cubic AgPbmSbTe2+m: Bulk thermoelectric

materials with high figure of merit", *Science*, **303**: 818-821 (2004).

[Kajikawa 2006] T. Kajikawa, "Thermoelectric power generation system recovering industrial waste heat", in *Thermoelectric handbook: macro to nano*, edited by D. M. Rowe (Taylor and Francis, New York, 2006), 50/1-50/28.

[Kim 1993a] Y. Kim and E. D. Case, "The Effect of Surface-Limited Microcracks on the Effective Young's Modulus of Ceramics .2. Application of Analysis to Particular Microcrack Geometries", *Journal of Materials Science*, **28**: 1901-1909 (1993a).

[Kim 1993b] Y. Kim, E. D. Case and S. Gaynor, "The Effect of Surface-Limited Microcracks on the Effective Young's Modulus of Ceramics .3. Experiments", *Journal of Materials Science*, **28**: 1910-1918 (1993b).

[Kim 1991] Y. Kim, W. J. Lee and E. D. Case, "The measurement of the surface heat transfer coefficient of ceramics quenched into a water bath", *Mater. Sci. and Eng. A*, **132**: 29-47 (1991).

[Kingery 1976] W. D. Kingery, H. K. Bowen and D. R. Uhlmann, *Introduction to ceramics (2nd edition)*, (Wiley-Interscience, New York, 1976), pp. 816-819.

[Lee 1993] W. J. Lee, Y. Kim and E. D. Case, "The effect of quenching media on the heat transfer coefficient of polycrystalline alumina", *J. Mater. Sci.*, **31**: 2079-2083 (1993).

[Leisure 1997] R. G Leisure and F. A. Willis, "Resonant ultrasound spectroscopy", *Journal of Physics-Condensed Matter*, **9**: 6001-6029 (1997).

[Lu 1998] T. J. Lu and N. A. Fleck, "The thermal shock resistance of solids", *Acta Mater.*, **46**: 4755-4768 (1998).

[Manson 1966] S. S. Manson, *Thermal Stress and Low Cycle Fatigue*, (McGraw-Hill, New York, 1966), Chapter 7.

[Marshall 1982] D. B. Marshall, T. Noma and A. G Evans, "A Simple Method for Determining Elastic-Modulus-to-Hardness Ratios Using Knoop Indentation Measurements", *Journal of the American Ceramic Society*, **65**: C175-C176 (1982).

[Matsubara 2006] K. Matsubara and M. Matsuura, "A thermoelectric application to vehicles", in *Thermoelectric handbook: macro to nano*, edited by D. M. Rowe (Taylor and Francis, New York, 2006), 52/1-52/11.

[Migliori 1997] A. Migliori and J. L. Sarrao, *Resonant Ultrasound Spectroscopy: Applications to Physics, Materials Measurements, and Nondestructive Evaluation*, (Academic Press, New York, 1997),

[Migliori 1993] A. Migliori, J. L. Sarrao, W. M. Visscher, T. M. Bell, M. Lei, Z. Fisk and R. G. Leisure, "Resonant Ultrasound Spectroscopic Techniques for Measurement of the Elastic-Moduli of Solids", *Physica B*, **183**: 1-24 (1993).

[Nolas 2006] G. S. Nolas, J. Poon and M. Kanatzidis, "Recent developments in bulk thermoelectric materials", *MRS Bulletin*, **31**: 199-205 (2006).

[Nolas 2001] G. S. Nolas, J. Sharp and H. J. Goldsmid, *Thermoelectrics: basic principles and new materials developments*, (Springer, Berlin; New York, 2001), pp. 28-57, 151-159, 178-207.

[Nye 1967] J. F. Nye, *Physical Properties of Crystals* (Oxford University Press, London, 1967),

[Porter 1990] W. D. Porter and K. E. Easterling, *Phase transformation in metals and alloys*, (Campman and Hill, New York, 1990), pp. 1-4, 208-222, 308-314.

[Quarez 2005] E. Quarez, K. F. Hsu, R. Pcionek, N. Frangis, E. K. Polychroniadis and M. G. Kanatzidis, "Nanostructuring, compositional fluctuations, and atomic ordering in the thermoelectric materials AgPbmSbTe2+m. The myth of solid solutions", *Journal of the American Chemical Society*, **127**: 9177-9190 (2005).

[Radovic 2004] M. Radovic, E. Lara-Curzio and L. Riester, "Comparison of different experimental techniques for determination of elastic properties of solids", *Materials Science and Engineering a-Structural Materials Properties Microstructure and Processing*, **368**: 56-70 (2004).

[Rao 2006] A. M. Rao, X. H. Ji and T. M. Tritt, "Properties of nanostructured

one-dimensional and composite thermoelectric materials", *MRS Bulletin*, **31**: 218-223 (2006).

[Ren 2006] F. Ren, E. D. Case, E. J. Timm, M. D. Jacobs and H. J. Schock, "Weibull analysis of the biaxial fracture strength of a cast p-type LAST-T thermoelectric material", *Philosophical Magazine Letters*, **86**: 673-682 (2006).

[Ren 2007a] F. Ren, E. D. Case, E. J. Timm and H. Schock, "Hardness as a function of composition for n-type LAST thermoelectric material", *Journal of Alloys and Compounds*, available online at doi:10.1016/j.jallcom.2007.01.086 (2007a).

[Ren 2007b] F. Ren, E. D. Case, E. J. Timm and H. Schock, "Young's modulus as a function of composition for an n-type lead-antimony-silver-telluride (LAST) thermoelectric material", *Philosophical Magazine*, **87**: 4907-4934 (2007b).

[Riffat 2003] S. B. Riffat and X. L. Ma, "Thermoelectrics: a review of present and potential applications", *Applied Thermal Engineering*, **23**: 913-935 (2003).

[Rossing 1982] T. D. Rossing, "Chladni's law for vibrating plates", *American Journal of Physics*, **50**: 271-274 (1982).

[Rowe 1995] D. M. Rowe, *CRC handbook of thermoelectrics*, (CRC Press, Boca Raton, FL, 1995), edited by D.M. Rowe, pp. 7-42.

[Scherrer 1995] H. Scherrer and S. Scherrer, "Bismuth telluride, antimony telluride, and their solid solutions", in *CRC handbook of thermoelectrics*, edited by D. M. Rowe (CRC Press, Inc., New York, 1995), pp. 211-237.

[Shetty 1980] D. K. Shetty, A. R. Rosenfield, P. McGuire, G. K. Bansal and W. H. Duckworth, "Biaxial Flexure Tests for Ceramics", *American Ceramic Society Bulletin*, **59**: 1193-1197 (1980).

[Simmons 1971] G. Simmons and H. Wang, *Single Crystal Elastic Constants and Calculated Aggregate Properties: a Handbook* (the MIT Press, Cambridge, MA, 1971), pp. ix-x, 200.

[Slater 1950] J. C. Slater, "The Lorentz correction in barium titanate", *Phys. Rev.* , **78**: 748-761 (1950).

[Tritt 2006] T. M. Tritt and M. A. Subramanian, "Thermoelectric materials, phenomena, and applications: A bird's eye view", *MRS Bulletin*, **31**: 188-194 (2006).

[Uher 2006] C. Uher, "Skutterudite-based thermoelectrics", in *Thermoelectric handbook: macro to nano*, edited by D. M. Rowe (Taylor and Francis, New York, 2006), 34/1-34/17.

[Ulrich 2002] T. J. Ulrich, K. R. McCall and R. A. Guyer, "Determination of elastic moduli of rock samples using resonant ultrasound spectroscopy", *Journal of the Acoustical Society of America*, **111**: 1667-1674 (2002).

[Venkatasubramanian 2001] R. Venkatasubramanian, E. Siivola, T. Colpitts and B. O'Quinn, "Thin-film thermoelectric devices with high room-temperature figures of merit", *Nature*, **413**: 597-602 (2001).

[Vining 1995] C. B. Vining, "Silicon germanium", in *CRC handbook of thermoelectrics*, edited by D. M. Rowe (CRC Press, Inc., New York, 1995), 329-337.

[Wachtman 1996] J. B. Wachtman, *Mechanical Properties of Ceramics*, (Wiley Interscience, New York, 1996), pp. 33-35, 72-80, 92-100.

[Wachtman 1961] J. B. Wachtman, W. E. Tefft, D. G. Lam and C. S. Apstein, "Exponential Temperature Dependence of Youngs Modulus for Several Oxides", *Physical Review*, **122**: 1754-& (1961).

[Whittaker 1944] E. T. Whittaker, *Analytical dynamics of particles and rigid bodies*, (Dover Publications, New York, 1944), pp. 38-39.

[Wylie 1982] C. R. Wylie and L. C. Barrett, *Advanced engineering mathematics*, 4th edition, (McGraw-Hill, Inc., New York, 1982), pp. 934-938.

[Yang 2006] J. H. Yang and T. Caillat, "Thermoelectric materials for space and automotive power generation", *MRS Bulletin*, **31**: 224-229 (2006).

[Zadler 2004] B. J. Zadler, J. H. L. Le Rousseau, J. A. Scales and M. L. Smith, "Resonant Ultrasound Spectroscopy: theory and application", *Geophysical Journal International*, **156**: 154-169 (2004).

[Zhao 2000] L. T. Zhao, T. J. Lu and N. A. Fleck, "Crack channeling and spalling in a plate due to thermal shock loading", *J. Mech. Phys. Solids*, **48**: 867-897 (2000).

[Ziman 1979] J. M. Ziman, *Electrons and phonons*, (Oxford University Press, London, 1979), pp. 258, 396-403.

Part II. Experimental Procedures

1. Overview of experimental procedures

This section explains the experimental procedures in detail, including mechanical characterization, powder processing, microstructure analysis, and thermal characterization, along with the specimen preparation procedures.

Room temperature hardness, H, and Young's modulus, E, were measured by both microindentation (Vickers and Knoop) and nanoindentation. The fracture strength, σ_f, was obtained from biaxial flexure testing (BFT). Resonant ultrasound spectroscopy (RUS) was utilized to examine the temperature dependence of the elastic moduli, including Young's modulus, E, shear modulus, G, and Poisson's ratio, ν. The thermal fatigue study was conducted using an infrared (IR) heating apparatus and the RUS.

Powder processing includes pre-milling treatments, ball milling, and hot pressing of milled powders. The Coulter Counter® technique was used to determine the powder particle size distribution, scanning electron microscopy (SEM) to examine the powder particle morphology, and X-ray diffraction (XRD) to detect the crystalline and amorphous phase(s).

The microstructure of bulk materials fabricated by casting and hot pressing were studied using SEM. Energy dispersive X-ray spectroscopy (EDS) and Auger electron spectroscopy (AES) were utilized to examine the composition of cast and hot pressed materials. Thermal mechanical analysis (TMA) and high temperature XRD were used to

determine the coefficient of thermal expansion. In addition, room temperature diffusivity was measured using the facility at the High Temperature Materials Laboratory of Oak Ridge National Laboratory.

2. Material fabrication and specimen preparation

2.1. LAST and LASTT materials

2.1.1. Ingot casting

The cast specimens included in this study were fabricated using a 3-zone split tube-rocking furnace (Applied Test Systems, Inc. Butler, PA). High-purity elemental materials (> 99.99 percent pure) were weighed and then sealed into 25-mm-diameter fused silica ampoules under a 0.01 Pa vacuum. The temperature-time profiles during ingot casting are discussed in detail in **Part III** (Results and discussions).

2.1.2. Powder processing

Figure 2.1 illustrates the powder processing procedures, which includes pre-milling treatment and milling. The hot pressing is discussed in Section 2.3 and the details of powder characterization techniques are described in Section 4.

The pre-milling treatments were performed with mortars and pestles (#60317, CoorsTek, Golden, CO). Two types of pre-milling treatments were applied, namely (i) crushing and grinding without sieving (CG) and (ii) crushing, grinding, sieving and re-grinding (CGSR).

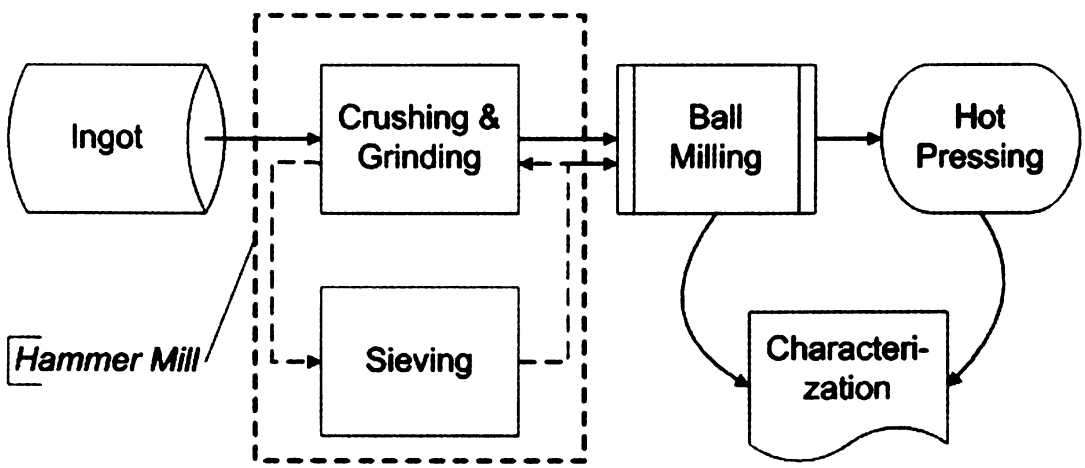

Figure 2.1. Powder processing techniques to produce micron sized powders from cast ingots. The crushing, grinding, and sieving stages, which will be replaced by hammer milling, ensured the particle size of input powders to ball milling is less than 53 microns.

During the CG pre-milling treatment, the as-cast ingots were wrapped between two pieces of weighing paper. A hammer was used to break the ingots into centimeter-sized pieces by slowly applying pressure to the ingots. The ingot pieces were then placed in a mortar and ground with a pestle for about 5 minutes.

For CGSR treatment, the ingots were first processed using the CG treatment. Then the ground powders were sieved with a series of sieves with mesh sizes ranging from 250 microns to 53 microns (AS 200, Retsch Inc., Germany). Powders with particles larger than 53 microns were then re-ground and sieved. The grinding and sieving steps were repeated until all particles were passed through the 53-micron sieves.

The CG and CGSR pre-milling treatments of the powder specimens included in the particle size distribution analysis (**section 4.1**), the particle morphology observation (**section 4.2**), and the powder X-ray diffraction study (**section 4.3**) were conducted in air. Both CG and CGSR treated powders were then milled with a planetary ball mill (PM100, Retsch Inc., Germany). In each milling run, about 20 to 25 grams of CG or CGSR pre-milled powders were loaded into an alumina milling jar (250 mm capacity, Part number 01.462.0221, Retsch Inc., Germany). Ten spherical high-purity alumina milling media that were approximately 20 mm in diameter (Part number 7250-020000-5, Glen Mills, Clifton, NJ) were used. Milling was conducted in air with a speed of 100 rpm for a milling time between 3 min and 420 min.

Hot pressed specimens fabricated using the hot press facilities at University of Michigan (**section 2.1.3.1**), at the High Temperature Materials Laboratory of Oak Ridge

National Laboratory (**section 2.1.3.2**), and the Jet Propulsion Laboratory (**section 2.1.3.2**) were first treated with the CGSR technique in air and then milled for 180 minutes with a speed of 100 rpm.

In order to minimize the oxidation of the powders during pre-milling treatments, powders used for hot pressing at Michigan State University (**section 2.1.3.2**) were first treated with the CGSR technique in an Ar-filled glove box (VAC controlled atmosphere systems, Vacuum Atmosphere Co.). Pre-milled powders were then loaded into the milling jar inside the glove box and milled for 180 minutes in air. The milled powders were removed from the milling jar inside the glove box and stored in glass vials.

Acetone was used to clean the mortar and pestle, as well as the milling jar and media after each milling experiment. In addition, after every four milling runs, the milling jar and media were thoroughly cleaned by milling with 50 mL of glass beads approximately 0.6 to 0.85 mm in diameter (Potter's Industries Ballotini Glass Impact Media, Valley Forge, PA) at 130 rpm for 8 minutes.

2.1.3. Hot pressing

Due to the initial unavailability of hot press facilities at Michigan State University, milled LAST and LASTT powders were hot pressed using four facilities: (1) the facility (Astro HP4560-20, Astro Industries Inc. Santa Barbara, CA) located in the Naval Architecture and Marine Science Building at University of Michigan (Ann Arbor, MI), (2) hot pressing facility at the High Temperature Materials Laboratory of Oak Ridge National

Laboratory (Oak Ridge, TN), (3) the hot pressing facility at the Jet Propulsion Laboratory (Pasadena, CA), and finally (4) the hot pressing facility (Model HP200-14020-23G, Thermal Technology Inc., Santa Rosa, CA) at the Energy and Automotive Research Laboratories (EARL) of Michigan State University (East Lansing, MI).

2.1.3.1. Hot pressing using the University of Michigan facility

Hot pressing using the facility at University of Michigan (denoted as UMHP) was conducted in collaboration with Mr. Edward Timm. Graphite dies with 12.7 mm (1/2 inch) inner diameter were used (Figure 2.2). About 10 grams of powder was used for each specimen. Prior to loading powders into the die, graphite sheets 0.015 mm thick were cut from the as-received Grafoil® sheets (GTA grade GRAFOIL, Advanced Energy Technology, Inc., Cleveland, OH) using scissors. The cut Grafoil® pieces were then lined on the inner wall of the die cylinder as well as the plunger surfaces to reduce the sticking of specimens to the inner wall of the die cavity. The die set was then loaded into the furnace, which was evacuated for about 10 minutes and back filled with N_2. The evacuation and filling was repeated three times before heating or applying pressure to the die.

The maximum sintering temperatures for UMHP specimens were between 330°C and 420°C with a holding time of about 90 minutes at maximum temperature and a heating/cooling rate of approximately 5°C/min to 10°C/min. Pressure ranging from approximately 30 MPa to 100 MPa was applied manually by increasing the force of the

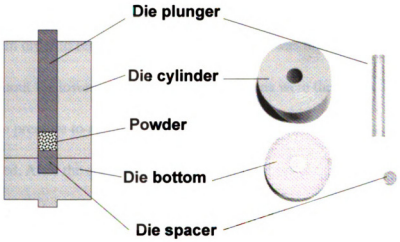

Figure 2.2. Schematic (left) and digital photograph (right) of a graphite die set used with the Astro HP4560-20 hot press (located at the University of Michigan) to fabricate 12.7 mm diameter hot pressed specimens.

hydraulic press at the start of the isothermal hold. The pressure was removed at the end of the isothermal hold segment. During the entire hot pressing period, an N_2 flow of about 40 mL/min was used to reduce possible oxidation. A typical temperature-time profile during hot pressing is illustrated in Figure 2.3.

Specimens hot pressed at 400°C and 420°C became stuck to the inner wall of the graphite die. In order to remove the specimens, the die was inverted and reloaded into the hot press without the lower die plunger. The specimens were then forced out by slowly increasing the pressure to approximately 5.5 MPa. Specimens hot pressed at 330°C were easily removed. After the specimen was removed from the die, a razor blade was used to separate the graphite sheet from specimens. The final pressed specimens were cylinders that were 12.7 mm (0.5 inch) in diameter and 10 mm thick.

2.1.3.2. Hot pressing using other facilities

Hot pressing using the facility at the High Temperature Materials Laboratory of Oak Ridge National Laboratory (denoted as ORHP) was carried out by Mr. Edward Timm. The specimens were hot pressed under a continuous N_2 flow of approximately 101 kPa (1 atm). The maximum temperature was between approximately 410°C and 520°C, while the pressure ranged from 24.4 MPa to 41.3 MPa.

Hot pressing at the Energy and Automotive Research Laboratories (EARL) of Michigan State University (denoted as MSUHP) was also performed by Mr. Edward Timm. Graphite die sets with an inner diameter of 31.1 mm (1.225 inch) were used.

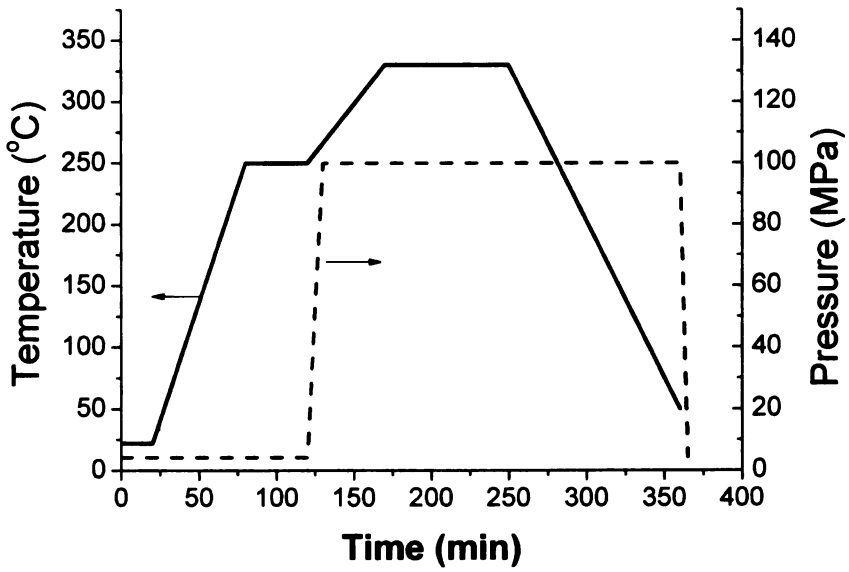

Figure 2.3. Temperature-pressure-time profile during the hot pressing of specimen UMHP6 processed using the hot press facility at the University of Michigan.

Approximately 45 grams of powders was used to press each specimen. The maximum hot pressing temperatures varied between 300°C and 550°C, while the pressure ranged between 60 to 100 MPa. A continuous Ar flow of approximately 13.8 kPa (2 psi) was maintained during the hot pressing.

In addition, two 10-gram batches of milled LAST powder was submitted to the Jet Propulsion Laboratory (JPL) and hot pressed at 550°C. One of the two JPL-pressed specimens was included in this study (**Part III, Chapter 8**).

2.1.4. Specimen mounting, cutting, polishing, and etching

2.1.4.1. Specimen mounting

Two types of mounting techniques were used in this study: (i) hot mounting with thermoplastic and (ii) cold mounting in epoxy resin. For hot mounting, specimens and aluminum stubs 25.4 mm (1 inch) in diameter (SPI Supplies, West Chester, PA) were placed on a hot plate (Model 4658, Cole-Parmer Instrument Co., Chicago, IL). After the hot plate was heated, thermoplastic (Lakeside 70, Buehler Ltd., Lake Bluff, IL.) was applied to the aluminum stub. The specimens were placed on top of the thermoplastic. A uniform pressure was applied to the specimens to create a tight bond between the stubs and specimens. The hot plate was then turned off and the specimens were allowed to cool naturally.

For cold mounting, the epoxy and hardener (Epoxicure® Resin/hardener, Buehler Ltd., Lake Bluff, IL.) were thoroughly mixed in 30-mL plastic cups with a weight ratio of

epoxy to hardener of 5:1. Specimens were set in phenolic mounting rings 25.4 mm (1 inch) in diameter (PN 811-221, Leco Corp., St. Joseph MI), which were placed on a flat steel board sprayed using mold release (Crown 3470, North American Professional Products, Woodstock, IL) prior to mounting. After the epoxy/hardener mixture was slowly poured into the mounting rings, a steel block was placed on top of the mounting rings in order to provide a compression pressure to minimize the leakage of the epoxy/hardener from underneath the phenolic mounting rings. The epoxy resin was cured in air at room temperature for about 24 hours. After the epoxy had cured, the mounted specimens were trimmed with a razor blade to remove the residual epoxy outside the mounting rings.

2.1.4.2. Cutting the ingot and hot pressed specimens

To cut the ingot and hot pressed specimens to desired dimensions, the specimens were first hot mounted onto glass microscope slides using thermoplastic (Section 2.4.1). The hot-mounted specimens were then cut using a low speed diamond saw (IsoMet®, Buehler Ltd., Lake Bluff, IL.) with the lowest speed setting (1 on the dial). To make multiple parallel cuts, the specimen holder was first raised after each cut was completed and the specimen position was adjusted using the micrometer. The specimen holder was then lowered to make the next cut.

After cutting, the specimens were removed from the glass slides by reheating with the hot plate. Specimens were then cleaned by placing them into a 100-mL glass beaker

containing approximately 30 mL of ethanol. The beaker containing the specimens and the ethanol was then placed in the water bath of an ultrasonic cleaner (UltraMet® III, Buehler Ltd., Lake Bluff, IL) for about 5 to 10 minutes.

2.1.4.3. Specimen polishing

In this study, two automatic polishers were used for polishing, namely a Leco polisher (AP-50/VP-50, Leco Corp., St. Joseph, MI) and a Buehler polisher (EcoMet® 3, Buehler Ltd., Lake Bluff, IL.). For polishing on the Leco polisher, polishing wheels approximately 30 cm (12 inch) in diameter and diamond paste with grit size ranging from 67 microns down to 1 micron (MUS, Warren Diamond Powder Co. Olyphant, PA) were used. In addition, a polishing compound (PN 811-004, Leco Corp., St. Joseph, MI) was used as the lubricant during polishing. Polishing time varied between 10 minutes and 90 minutes per grit size depending on the number of specimens. The specimens and the mounting plate were cleaned using running water after the polishing with each grit size was completed. After polishing was finished, the specimens were unmounted and cleaned ultrasonically (see **section 2.4.2**) and dried with a stream of compressed air (Dust-Off, Falcon Safety Products, Inc., Branchburg, NJ).

The Buehler polisher used 20-cm (8 inch) polishing wheels. The coarse polishing was performed on abrasive paper with grit size between 400 and 1500 (BarbiMet paper discs, Buehler Ltd., Lake Bluff, IL). The fine polishing was conducted on polishing cloth (TexMet polishing cloth, Buehler Ltd., Lake Bluff, IL) with diamond suspensions with

grit sizes ranging from 9 microns to 1 micron (Metadi supreme polycrystalline diamond suspension, Buehler Ltd., Lake Bluff, IL). The specimens were thoroughly washed with tap water between different grits. After the final polishing with 1 micron grit, the specimens were cleaned ultrasonically with detergent water.

2.1.4.4. Thermal etching

Thermal etching of polished ingot specimens and hot pressed specimens was performed by Mr. Jonathan D'Angelo using a three-zone tube furnace (Applied Test Systems Inc. Butler, PA) located in Professor Timothy Hogan's laboratory (Engineering Research Complex, Michigan State University). The specimens were placed on fused silica plates near the center of the furnace, then the furnace was evacuated and back filled with 99.995 percent pure Ar at a pressure of about 40 kPa (300 torr) at room temperature. The etching temperatures used ranged between 300°C and 400°C for hot pressed specimens while ingot specimens were etched between 600°C and 650°C.

2.1.4.5. Chemical etching

The etchant consisted of 1.0 M KOH and 0.7 M $K_3(Fe(CN)_6)$ [Robozerov 2000]. In order to formulate the chemical etchant, 5.61 ± 0.001 g of KOH pellets (4325AL, Columbus Chemical Industries, Inc. Columbus, WI) and 23.03 ± 0.001 g of $K_3(Fe(CN)_6)$ powder (P1285, Spectrum Chemical MFG. Corp. New Brunswick, NJ) were weighed with an electronic balance and added to a 250 mL beaker containing about 90 mL

deionized water. The mixture was stirred magnetically until all the KOH pellets and $K_3(Fe(CN)_6)$ powder were dissolved into a yellow and transparent solution. The etching solution was then transported into a narrow neck flask for storage.

All specimens that were etched were first polished down to a one micron surface finish. Prior to etching, specimens were placed in a petri dish with polished surfaces facing up. Cotton-tipped applicators were dipped into the etching solution and then swept across the polished surfaces of the specimens so that the specimen surfaces were covered by the etching solution. Every 10 minutes the specimen surfaces were swept by applicators with etching solution in order to keep the specimen surfaces from drying. The total etching time was in the range of 70 to 120 minutes.

After the desired time duration of etching, the specimens were thoroughly rinsed with tap water and then rinsed with deionized water. The specimens were dried in a high speed air stream.

2.2. Other PbTe and doped PbTe specimens

In addition to LAST and LASTT specimens, pure PbTe, PbI_2-doped PbTe, and PbS-doped PbTe specimens included in this study were prepared by Joe Sootsman of Prof. Mercouri Kanatzidis's group at Northwestern University (Evanston, IL).

The pure PbTe and PbI_2-doped PbTe specimens were fabricated by the Bridgman method while the PbS-doped PbTe specimen was cast.

3. Mechanical property characterization

3.1. Microindentation

In this study, Vickers indentation was utilized to measure the hardness, H, while the room temperature Young's modulus, E, was calculated from the Vickers indentation hardness and the hardness to Young's modulus ratio, H/E, as determined by Knoop indentation.

Vickers indentation was performed on a semi-micro hardness tester (Buehler Ltd. Lake Bluff, IL). Prior to indenting the specimens, the Vickers indenter was calibrated with a standard hardness block (Yamamoto Scientific Tools, Chiba, Japan). The calibration was performed under indentation loads ranging between 2.94 N and 49 N with a loading rate of 70 micron/sec, and a loading time of 10 seconds.

Vickers indentation measurements of LAST and LASTT specimens included in this study used a load of 2.94 N, a loading rate of 70 micron/sec, and a loading time of 10 seconds. After each indent, the two diagonal lengths of the indentation impression, $2a_1$ and $2a_2$, were measured with a microscope mounted on the indenter (Figure 2.4). The average of the two diagonal lengths, 2a, was used to calculate the hardness using the relationship:

$$H = 1.8544P/(2a)^2 \qquad (2.1)$$

where P is the indentation load [Wachtman 1996].

To determine the H/E ratio, Knoop indentation was performed using a commercial indenter (HMV-2000, Shimadzu, Japan) with a load of 0.49 N and a loading time of 10

seconds. For materials that undergo entirely plastic deformation during Knoop indentation, the ratio of the length of the longer diagonal, a, to the length of the shorter diagonal, b, is approximately 0.14 [Marshall 1982]. However, for materials that exhibit elastic recovery after the removal of indentation load, the lengths of the longer diagonal, a', and the shorter diagonal, b', of the indentation impression (Figure 2.4) after the load is removed differ from a and b, such that a'/b' is smaller than $a/b = 0.14$ [Marshall 1982]. The H/E ratio of the material with elastic recovery behavior is then determined from [Marshall 1982]:

$$H/E = [0.14 - (b'/a')]/0.45 \qquad (2.2)$$

3.2. Nanoindentation

In addition to microindentation, nanoindentation was utilized in this study. The indent impression size was about 5 microns for nanoindentation, while the size of the microindentation impressions was between 70 microns and 300 microns. Thus nanoindentation data was the representation from a much smaller specimen surface area than the microindentation values.

Nanoindentation was performed using two nanoindenters: (i) a Nanoindenter XP (Nano Instrument, Oak Ridge, TN) at the Composite Materials and Structures Center at Michigan State University and (ii) a TriboIndenter (Hysitron Inc., Minneapolis, MN) at the High Temperature Materials Laboratory of Oak Ridge National Laboratory. The Nanoindenter XP was operated under the "CSM XP Standard Hardness, Modulus, Tip

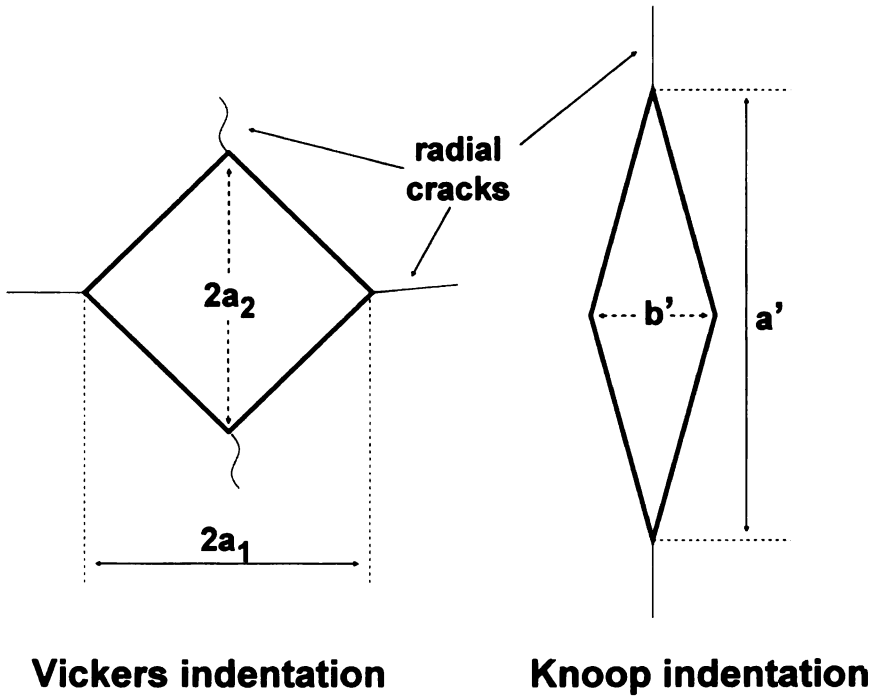

Figure 2.4. Schematics of indentation impressions and associated cracks for Vickers indentation and Knoop indentations.

Cal" mode with a Berkovich indenter tip. A maximum penetration depth of 2000 nm and a thermal drift threshold of 0.05 nm/sec were used for all the nanoindentation experiments. Nanoindentation on the TriboIndenter was performed using a peak load of 2000 micro-N, a loading/unloading rate of 200 micro-N/sec, and a holding time of 10 sec at the peak load.

For both nanoindenters, H was calculated from the maximum load during the indentation, P_{MAX}, and the corresponding projected area of the indenter tip, A, using the following equation [Oliver 1992],

$$H = P_{MAX} / A \tag{2.3}$$

For the NanoIndenter XP, the Young's modulus was calculated from the unloading curve using a commercial software package (TestWorks®, Nano Instrument, Oak Ridge, TN). For the TriboIndenter, the Young's modulus was calculated from the load versus displacement curve ranging between the peak load and 10 percent of the peak load according to the method developed by Oliver and Pharr [Oliver 1992].

3.3. Biaxial flexure testing

The biaxial flexure fixture utilized a ball-on-ring (BOR) configuration (Figure 2.5). The top section of the fixture is a cylindrical bar with a length of 76.2 mm (3 inch) and a diameter of 33.8 mm (1 1/3 inch). The loading ball of the fixture (Figure 2.5a) was made from a hard steel sphere 6.35 mm (0.25 inch) in diameter which was glued into a hemispherical pit at the end of the bar. The bottom section of the fixture consisted of a

plate that is 76.2 mm (3 inch) in diameter and 25.4 mm (1 inch) thick, and a cylindrical bar that is 31.75 mm (1.25 inch) in diameter and 50.8 mm (2 inch) long. A circular groove with an inner diameter of 12.7 mm (0.5 inch) and an outer diameter of 19.05 mm (0.75 inch) was machined into the top surface of the plate. The cross section of the groove is hemispherical with a diameter of 3.175 mm (1/8 inch). Fifteen steel spheres 3.175 mm (1/8 inch) in diameter placed in the groove formed the supporting ring for the specimen. The spheres in the machined groove were not fixed and could move freely in order to reduce the friction between the specimens and the supporting ring during the fracture tests.

The specimens tested with biaxial flexure fixture were disks that were approximately 3 mm thick and either 22 mm or 32 mm in diameter. The tensile surfaces of all specimens were polished with diamond paste (see section 2.4.3) down to a one-micron finish.

The BFT fixture was used on a commercial testing machine (Model 4206, Instron, Norwood, MA). The axis of the crossheads was aligned such that the center of the loading ball and the center of supporting ring were aligned vertically. The crosshead speed used was 0.5 mm/min. Only the specimens fractured into three or more "pie-shaped" sections were considered as valid specimens [Shetty 1980] and included in the strength calculation. For the valid fracture tests, the maximum load, P, was used to calculate the biaxial flexure strength according to [Shetty 1980]:

$$\sigma = \frac{3P(1+\nu)}{4\pi t^2}\left[1+2\ln\left(\frac{a}{b}\right)+\left(\frac{1-\nu}{1+\nu}\right)\left(1-\frac{b^2}{2a^2}\right)\frac{a^2}{R^2}\right] \qquad (2.4)$$

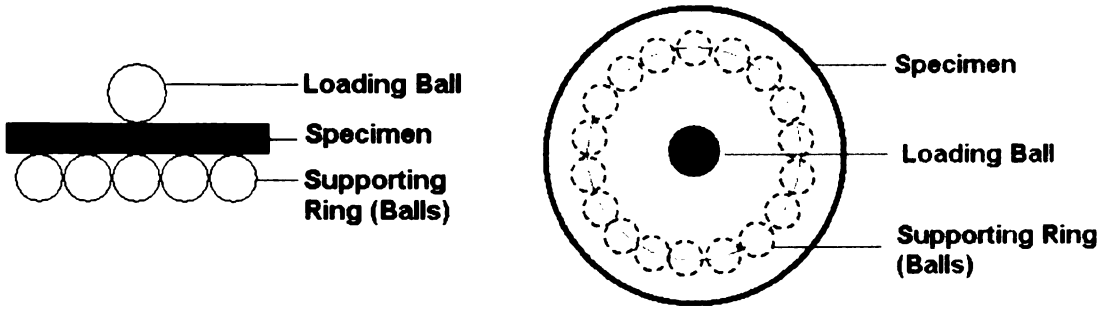

(a) (b)

Figure 2.5. Schematics of (a) side view and (b) top view of biaxial flexure test fixture with a ball-on-ring configuration.

In Eq. (2.4), ν is the Poisson's ratio, a is the radius of the supporting ring, b is the radius of the uniform loading area at the center (estimated as 1/3 of the specimen thickness [Shetty 1980], and R is the radius of the disc-shaped specimens.

3.4. Resonant ultrasound spectroscopy

High temperature mechanical characterization is very important since the LAST and LASTT TE legs that are used in TEGs are designed to serve at elevated temperatures, for example ~ 700 to 800 K. In the current research, the elastic moduli including E, G, and ν, were determined as a function of temperature via resonant ultrasound spectroscopy (RUS).

The RUS technique is based on the principle that the vibrational resonance spectrum induced in a mechanically driven specimen is a function of the geometry, dimensions, and mass density of the specimen [Migliori 1997]. Cylinders, disks, and rectangular parallelepipeds are typically used as test specimens. The test specimen is placed on a tripod arrangement of three piezoelectric transducers. One "driver" transducer generates the mechanical vibration and the other two "pickup" transducers sense the mechanical vibrations in the specimen (Figure 2.6a). For high temperature RUS measurements, the specimens and transducers were placed inside an enclosed chamber that was equipped with a furnace. For the PbTe-based materials included in this study, the chamber was filled with Ar gas to minimize specimen oxidation.

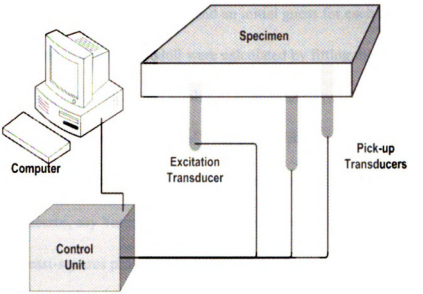

(a)

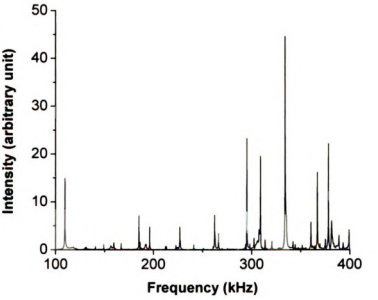

(b)

Figure 2.6. (a) Schematic of the RUS apparatus used in this study and (b) a typical vibrational spectrum obtained from RUS scan.

Given the specimen mass, dimensions, and an initial guess for each of the elastic moduli to be measured, the elastic moduli were calculated by fitting the RUS resonant frequency spectra (Figure 2.6b) using a nonlinear least-squares program (RPModel, Quasar International, Inc. Albuquerque, NM). For polycrystalline specimens with randomly oriented grains, there are only two independent elastic constants [Nye 1967]. Thus two initial guesses, say Young's modulus and Poisson's ratio, are required as input to the non-linear least-squares program.

3.5. Thermal fatigue

3.5.1. Thermocouple calibration

The two k-type thermocouples used in the infrared temperature cycling system were calibrated using the two-point calibration method, i.e. ice point and water boiling point (Figure 2.7).

To calibrate thermocouples at the ice point, about 300 ml of crushed ice and 300 ml of water were mixed in a 1000 ml glass beaker. A thermocouple to be calibrated was immersed into the beaker after about 10 min when the water-ice mixture reached thermal equilibrium. The tip of the thermocouple was held about 5 cm below the surface while attention was paid not to touch the sidewall and the bottom of the beaker. A digital temperature meter (UP550, Yokogawa Electric Corp. Tokyo, Japan) connected to the thermocouple and was used as the temperature reading device. The temperature was recorded approximately 3 min after thermal equilibrium was achieved, indicated by a

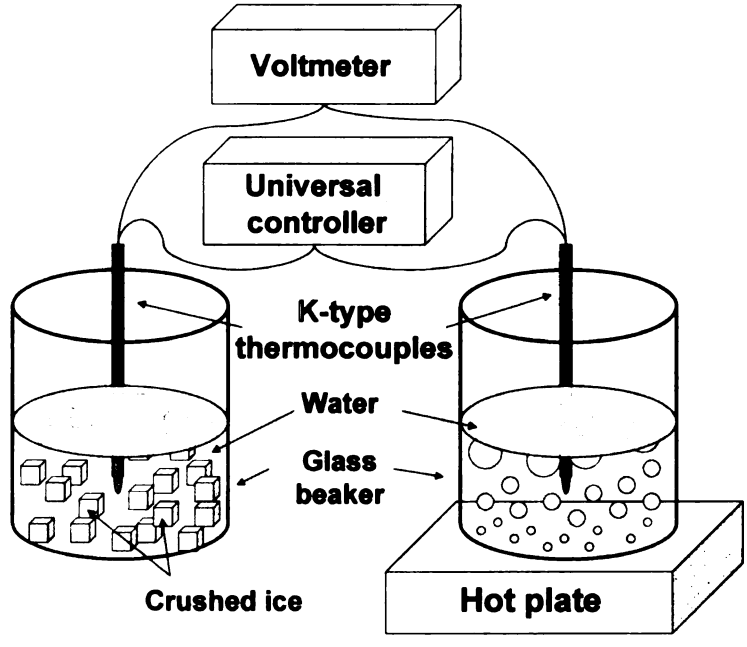

Figure 2.7. Thermocouple calibration configuration used to calibrate the thermal couples for the thermal fatigue apparatus.

steady reading on the digital temperature meter. Meanwhile, the voltage of the thermocouple was recorded using a multi-meter (DM-4400A, Sperry Instruments, Milwaukee, WI).

A water boiling point temperature calibration was conducted in a boiling water bath. About 500 ml of water in a glass beaker was heated by a hot plate. Temperature and voltage readings were recorded after equilibrium was reached.

Calibration results of the two thermocouples, namely thermocouple 1 and thermocouple 2, are summarized in Table 2.1. For both thermocouples, the differences between the set points and the digital readouts were less than 1°C at both the ice point and the water boiling point. The maximum voltage difference between thermocouple 1 and 2 was 0.1 mV at a given set point.

3.5.2. Thermal cycling

The thermal cycling experiments were performed in a sealed Plexiglas box. A stainless steel frame inside the box hosted an infrared (IR) lamp, a specimen stage, and an IR camera (Figure 2.8a). The IR lamp (PN 5194-02-1000, Research Inc. Eden Prairie, MN) was the heat source which was connected to a power supply (PN 5620-11-SP34, Research Inc. Eden Prairie, MN). The IR heater was controlled by a universal controller (UP550-20, Yokogawa Corp. of America, Newnan, GA). The specimen stage consisted of a SiC plate and surrounding insulation blocks (Figure 2.8b). The two thermal couples used to monitor the specimen temperature were connected to a computer via a data

Table 2.1. Two point calibration results for the two k-type thermocouples used in the IR heating apparatus. The voltage and temperature reading from the thermocouples were recorded at the ice-water mixture temperature and the boiling water temperature.

	Ice-water mixture		Boiling water	
Thermocouple	Temperature (°C)	Voltage (mV)	Temperature (°C)	Voltage (mV)
1	0.2	-1.0	99.5	3.0
2	-0.2	-1.0	100.7	3.1

acquisition card (SCXI 1300, National Instrument, Austin, TX) placed outside the plastic box. The IR camera was focused on the top of the specimen through an observation port in the top insulating block. The IR camera was connected to a computer that captured the video data (Figure 2.8a).

Prior to beginning the heating cycle, specimens were placed on the SiC plate. The two thermal couples were placed on the top surface of the specimen symmetrically with respect to the axis of the SiC plate. The top insulation block was placed above the specimen and centered in such a way that the specimen and the thermal couples were within the field of view of the IR camera (Figure 2.8b).

After the two openings aside the Plexiglas box were sealed (Figure 2.8a), a vacuum pump evacuated the air inside the box for about five minutes. The chamber was then back filled of 99.99 percent pure Ar for about 10 minutes. The Ar pressure was about 34.5 kPa (5 psi) as indicated by the gas regulator. The above pumping and back filling was performed twice. An Ar flow was maintained after the second back filling through out the entire heating/cooling cycle. To avoid overheating, the IR lamp was water cooled during the entire test.

For one heating and cooling cycle, 21 percent of full power was initially applied to the IR lamp. After about 30 minutes, the specimen reached the thermal equilibrium at a temperature of about 300°C. The power to the IR lamp was then turned off, allowing the specimen to cool freely. The time required for free cooling of the specimen from 300°C to 50°C was about 30 minutes.

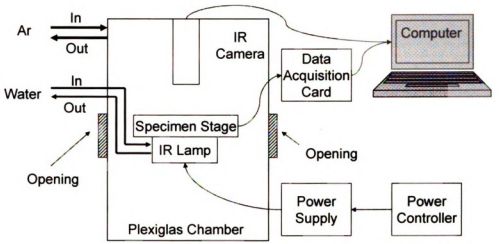

(a)

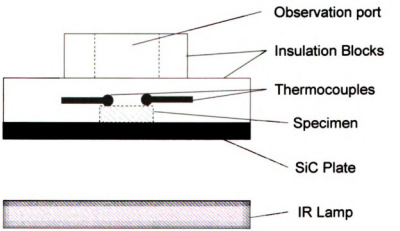

(b)

Figure 2.8. (a) Thermal cycling apparatus which utilized the infrared heating apparatus at Oak Ridge National Laboratory. (b) Side view of the specimen stage configuration with two thermocouples placed on the specimen.

During the heating/cooling cycles, the temperature of the specimen was monitored by the IR camera as well as the thermocouples.

4. Powder characterization

In this study the milled powders were analyzed using the following techniques Coulter Counter to measure the particle size distribution, Scanning Electron Microscopy (SEM) to examine the particle morphology, and X-ray diffraction (XRD) to study phases present in the powders.

4.1. Characterizing particle size distribution

Powder particle size distributions were studied using a Multisizer^{TM} 3 Coulter Counter (Beckman Coulter, Fullerton, CA). For each specimen, about 3 to 5 grams of powders were submitted to CCE Technologies (Cottage Grove, MN). The powders were suspended in a 0.9 percent NaCl electrolyte (Beckman Coulter, ISOTON® II) with a density of 1.01 g/cm^3 and a viscosity of 0.01 g/(cm·s). The suspension was then drawn through an aperture 100 to 400 microns in diameter. Using currents ranging from 1600 to 3200 μA, the impedance of the suspension was measured. The particle size was calculated based on the impedance change induced by the particles.

4.2. Analysis of particle morphology

In this study, the powder particle morphology was examined by an SEM (JEOL 6400,

JEOL Ltd. Tokyo, Japan) using an acceleration voltage of 20 kV, a working distance of 15 mm, and a condenser lens setting of 9 to 10. Carbon tape (SPI Supplies, West Chester, PA) was first applied to cylindrical aluminum stubs that were 12 mm thick and 12 mm in diameter (SPI Supplies, West Chester, PA). About 0.1 gram of powder was placed onto the carbon tape and gently spread with a spatula. The loose particles were then removed by a compressed air stream to prevent possible contamination to SEM chamber.

4.3. Powder X-ray diffraction (XRD) analysis

The XRD study of milled powders was performed on a rotating anode diffractometer (Rigaku 20B, Rigaku Corp, Japan) with Cu K_α radiation, a scan step size of 0.02 deg/step, and a scan rate of 2 to 3 deg/min. The tube current was 100mA and the voltage was 45 kV, while the scan range was between 20 to 80 deg for 2θ. The mass of each XRD powder specimen was about 1 to 2 grams.

5. Phase and composition analysis

5.1. SEM and EDS

In addition to the examination of powder morphology (**section 4.2**), SEM and Energy Dispersive X-ray Spectroscopy (EDS) were utilized to study the phases present and composition of the ingot and hot pressed specimens. Two SEMs were involved in this study: a JEOL 6400 SEM located at the Advanced Microscopy Center of Michigan State University and a Hitachi S-3400N environmental SEM (Hitachi Ltd., Japan) located in

the High Temperature Materials Laboratory at Oak Ridge National Laboratory.

Specimens used in the JEOL SEM were attached to either 12 mm or 25 mm diameter aluminum stubs (SPI Supplies, West Chester, PA) using carbon tape. All of the specimens had sufficiently high electrical conductivity that no additional coating was used on the specimens. A 20 kV accelerating voltage was used for all analysis, while the working distance was 39 mm for low magnification observations. For the high magnification SEM observations and EDS studies, a working distance of 15 mm was used.

The EDS analysis on the JEOL SEM was performed using an INCA X-ray microanalysis system (Oxford Instruments, UK). Prior to each EDS experiment, a pure copper specimen with a processing rate of 6 and a collection time of 120 seconds was used to calibrate the EDS. For the EDS X-ray analysis using the INCA system, a processing rate of 6 was used for all specimens in this study, while the collection time varied between 120 and 240 seconds. A processing rate of 2 was used in the elemental mapping analysis with four to eight frames (approximately 30 to 60 minutes) per specimen.

Specimens used in the Hitachi environmental SEM (ESEM) were mounted to 12 mm aluminum stubs (SPI Supplies, West Chester, PA) with carbon tapes. The ESEM was operated in the vacuum mode (~ 10^{-6} Pa) without inert gas. The EDS analysis was performed using an EDAX detector (Genesis, EDAX Inc. Mahwah, NJ). The working distance was around 10 mm and the acceleration voltage was 15 kV.

5.2. Auger electron spectroscopy

The Auger electron spectroscopy (AES) was performed using the facility (PHI680 Auger Nanoprobe, Physical Electronics Inc. Chanhassen, MN) at the High Temperature Materials Laboratory of Oak Ridge National Laboratory with the assistance of Dr. Harry Meyer III.

A hot pressed specimen, MSUHP6, approximately 30 mm x 3 mm x 3 mm in dimension, was fractured in the Auger microscope chamber, under a vacuum of about 10^{-8} Pa. The fracture surface was then analyzed by AES. The accelerating voltage used was 20 kV, and the magnification ranged between 500 and 2000.

In the AES analysis, the measured intensity was corrected by the standard sensitivity factors of each element determined by the instrument manufacturer.

6. Thermal property characterization

6.1. Coefficient of thermal expansion measurements

In this study, the coefficient of thermal expansion (CTE) was measured using a thermal mechanical analyzer (Q400, TA Instruments, New Castle, DE), and by high temperature XRD.

6.1.1. Thermal mechanical analyzer (TMA)

The TMA measurements were performed at Oak Ridge National Laboratory (Oak Ridge, TN). For the TMA measurements, the specimen was placed between a silica

specimen stage and a silica probe. The relative dimensional change in the specimen due to thermal expansion is measured by the probe. A thermocouple near the specimen was used to monitor the temperature (Figure 2.9).

Surrounding the specimen stage, an enclosed cylindrical furnace was used to heat the specimen. For PbTe-based materials, the temperature ranges were between room temperature and 300°C or 400°C with heating rates of either 2°C/min or 3°C/min.

In order to minimize oxidation at elevated temperature, prior to any experiment a 30-min Ar flush was used to fill the gas reservoir inside the TMA. In addition, a continuous Ar flow of either 50 or 100 μL/min was supplied during the measurement.

The mass and dimensions were recorded before and after each TMA measurement.

6.1.2. High temperature X-ray diffraction

In addition to the powder XRD (see **section 4.3**), a powder specimen and a hot pressed specimen were analyzed as a function of temperature using facilities at the High Temperature Materials Laboratory of Oak Ridge National Laboratory. The powder specimen was obtained by grinding a piece of ETN155 ingot with mortar and pestle. About 0.2 gram of ETN155 powder was used for XRD analysis. The hot pressed specimen was MSUHP6, which was approximately 10 mm x 7 mm x 2 mm in dimension.

For both ETN155 powder and MSUHP6, XRD was performed both at room temperature (PANalytical, Philips Ltd., Netherlands) and at high temperature (X'Pert, Philips Ltd., Netherlands). For both the room temperature and the high temperature XRD

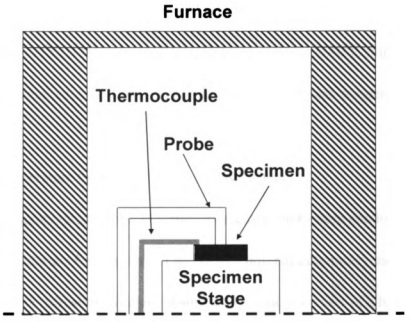

Figure 2.9. Schematic configuration for coefficient of thermal expansion (CTE) measurement via thermomechanical analyzer (TMA).

analysis, the scan step size was 0.017 degree, the scan rate was approximately 0.07 degree/sec and the 2θ range scanned was from 20 to 80 degree. The tube current and voltage were 40 mA and 45 kV, respectively.

The temperature dependent XRD analysis was conducted in an N_2 environment at the following nine temperatures: room temperature (~ 25°C), 100°C, 200°C, 225°C, 250°C, 275°C, 300°C, 325°C, and 350°C. The heating rate was 40°C/min with a one-minute thermal equilibrium hold prior to X-ray scan at each temperature.

6.2. Room temperature thermal diffusivity measurement

The room temperature thermal diffusivity measurement were conducted at the High Temperature Materials Laboratory at Oak Ridge National Laboratory using a room temperature flash diffusivity system [Wang 2003], which consists of a high power Xenon flash lamp enclosed in a dark box and an IR window about 25.4 mm (1 inch) in diameter on the side of the dark box. The specimens were mounted in a sample holder that was positioned next to the IR window. An InSb IR detector was attached to the back of the sample holder. The IR detector was cooled by liquid N_2 during the operation. Both the flash lamp and the IR detector are controlled by a computer (Figure 2.10a).

Six ingot specimens approximately 15 mm x 10 mm x 1.5 mm in dimension were used for the room temperature thermal diffusivity measurements. Before the test, the thicknesses of the specimens were measured with a micrometer and entered into the computer program for thermal diffusivity calculation. To mount a specimen, a sample

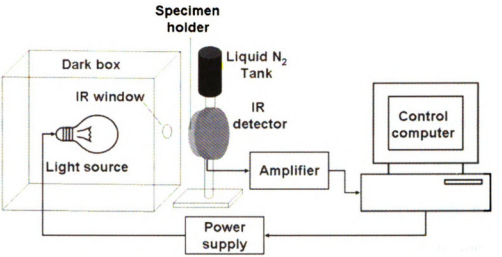

(a)

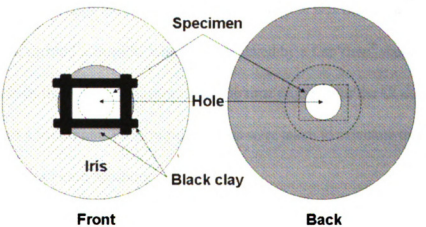

(b)

Figure 2.10. (a) Configuration of the laboratory-built room temperature thermal diffusivity measurement system. (b) Sample holder used in the room temperature thermal diffusivity measurement system.

holder with a proper size was selected, such that the specimen was large enough to cover the hole in the sample holder. Carbon clay attached the specimen to the holder as well as to seal the gaps between the specimen and the edge of the hole. The iris on the sample holder was then closed to prevent light leakage (Figure 2.10b).

To start the test, the sample holder was attached to the IR detector and positioned such that the specimen was directly facing the IR window. A black blanket was put around the sample holder and the IR detector to block ambient light. A computer was used for control and data collection. After the program was started, the electric voltage signal converted from the IR detector was continuously monitored. When the voltage drift was less than 0.001 V, the lamp fired a flash light onto the specimen surface facing the IR window. The voltage change induced by the heat flow was then measured by the IR detector. The thermal diffusivity was then calculated by a LabView® -based software [Wang 2003] from the specimen thickness and the time required for the IR detector voltage to reach a maximum. Three measurements were taken to calculate the average thermal diffusivity of each specimen.

References

[Marshall 1982] D. B. Marshall, T. Noma and A. G. Evans, "A Simple Method for Determining Elastic-Modulus-to-Hardness Ratios Using Knoop Indentation Measurements", *Journal of the American Ceramic Society*, **65**: C175-C176 (1982).

[Migliori 1997] A. Migliori and J. L. Sarrao, *Resonant Ultrasound Spectroscopy: Applications to Physics, Materials Measurements, and Nondestructive Evaluation*, (Academic Press, New York, 1997).

[Nye 1967] J. F. Nye, *Physical Properties of Crystals* (Oxford University Press, London, 1967).

[Oliver 1992] W. C. Oliver and G. M. Pharr, "An Improved Technique for Determining Hardness and Elastic-Modulus Using Load and Displacement Sensing Indentation Experiments", *Journal of Materials Research*, **7**: 1564-1583 (1992).

[Robozerov 2000] V. V. Robozerov, V. A. Zykov and T. A. Gavrikova, "Chemical etching of lead chalcogenides", *Inorganic Materials*, **36**: 127-131 (2000).

[Shetty 1980] D. K. Shetty, A. R. Rosenfield, P. McGuire, G. K. Bansal and W. H. Duckworth, "Biaxial Flexure Tests for Ceramics", *American Ceramic Society Bulletin*, **59**: 1193-1197 (1980).

[Wachtman 1996] J. B. Wachtman, *Mechanical Properties of Ceramics*, (Wiley Interscience, New York, 1996).

[Wang 2003] H. Wang and R. B. Dinwiddie, "Development of a LabView based portable thermal diffusivity system", *Proceedings of The 27th International Thermal Conductivity Conference and the 15th International Thermal Expansion Symposium*, edited by H. Wang and W. D. Porter, DEStech Publichations, Inc., pp 484-492, (2003).

PART III RESULTS AND DISCUSSION

Chapter 1

F. Ren, E. D. Case, E. J. Timm and H. Schock, "Hardness as a function of composition for n-type LAST thermoelectric material", *Journal of Alloys and Compounds*, available online at doi:10.1016/j.jallcom.2007.01.086 (2007).

Hardness as a function of composition for n-type LAST thermoelectric material

F. Ren[a], E. D. Case[a, *], E. J. Timm[b], H. J. Schock[b]

[a] Chemical Engineering and Materials Science Department, Michigan State University, East Lansing, MI 48824 USA

[b] Mechanical Engineering Department, Michigan State University, East Lansing, MI 48824 USA

Abstract

Compositional changes (alloying) in metals, ceramics, and semiconductors lead to changes in microstructure and mechanical properties that range from subtle to dramatic. In particular, hardness measurements have been widely used to track changes in mechanical properties as a function of composition. In this study, composition dependence of the Vickers indentation hardness, H, is examined for 17 specimens that include 15 different n-type compositions within the quaternary chalcogenide family of LAST (Lead-Antimony-Silver-Tellurium) high-temperature thermoelectric materials. In addition, nanoindentation measurements were made on six of the 17 specimens that were indented via Vickers indentation. The H values obtained independently by the microindentation (Vickers indentation) and nanoindentation techniques agreed very well.

In this study, relationships from the literature for the parabolic dependence of H on the single compositional variable x for pseudo binaries $AB_{1-x}C_x$ is successfully extended to describe the composition dependence of H for a true quaternary system. Possible implications of hardness change on fabrication and in-service reliability are also discussed.

Keywords: A. Thermoelectric materials; C. Composition fluctuations; C. Mechanical properties.

*Corresponding author. Tel.: +1 (517)-353-6715; fax: +1 (517)-432-1105. E-mail address: casee@egr.msu.edu

1. Introduction

Hardness, H, as measured by indentation testing, has been widely used as a tool to characterize mechanical property changes as a function of alloying composition. For example, indentation testing has been performed to determine H as a function of composition for both bulk materials [1-5] as well as thin films [6-8]. For bulk materials often Vickers indentation is used to determine hardness [1-5] while nanoindentation is used for bulk materials as well as coatings and thin films [6, 7]. The types of materials examined via hardness testing (microindentation and nanoindentation) include metal alloys [4, 6], ceramics [5, 9], bioceramics [10], and glassy specimens [11].

In this study, Vickers indentation hardness was measured for as-cast ingots consisting of 17 specimens (15 different n-type compositions) in the LAST (Lead – Antimony – Silver – Tellurium) family of high temperature thermoelectric materials [12, 13]. Promising candidates for thermoelectric waste heat recovery applications, the quaternary compounds of LAST family are silver and antimony doped PbTe materials that have exhibited a ZT (dimensionless figure of merit) of 1.7 at 700 K [12]. In particular, the indented specimens included the compositions $Ag_aPb_bSb_cTe_d$, where mole fraction ranges in this quaternary system were $0.006 < a < 0.043$, $0.417 < b < 0.480$, $0.011 < c < 0.050$, and $0.496 < d < 0.517$ (Table 3.1.1). This study demonstrates that the observed changes in hardness in this quaternary system can be described as parabolic functions of the individual mole fractions of the Ag, Pb, Sb, and Te. In addition, comparison between Vickers hardness and nanoindentation hardness for six selected compositions shows good

Table 3.1. For the 17 n-type quaternary thermoelectric compounds, $Ag_aPb_bSb_cTe_d$, included in this study, the values of mole fractions a, b, c and d, along with the mean H value, H_{mean}, the standard deviation, H_{stdev}. All H_{mean} values were computed from 20 indentations per specimen, with a load of 2.94 N and a loading time of 10 seconds.

Spec. ID	Ag a	Pb b	Sb c	Te d	H_{mean} (GPa)	H_{stdev} (GPa)
N33	0.030	0.422	0.042	0.506	0.922	0.174
N35	0.043	0.427	0.034	0.496	0.798	0.068
N37	0.017	0.427	0.043	0.513	0.727	0.107
N39	0.015	0.467	0.017	0.501	0.740	0.126
N40	0.006	0.480	0.011	0.503	0.526	0.063
N41	0.008	0.464	0.021	0.506	0.592	0.057
N42	0.011	0.454	0.030	0.505	0.855	0.186
N43	0.011	0.454	0.030	0.505	0.641	0.071
N48	0.025	0.446	0.028	0.501	0.768	0.053
N49	0.020	0.455	0.024	0.502	0.687	0.060
N50	0.009	0.472	0.016	0.503	0.578	0.039
N51	0.016	0.442	0.034	0.509	0.652	0.095
N52	0.021	0.450	0.026	0.502	0.660	0.061
N53	0.015	0.468	0.016	0.501	0.645	0.073
N54	0.043	0.427	0.034	0.496	0.743	0.102
N55	0.017	0.417	0.050	0.517	0.772	0.108
N58	0.011	0.454	0.030	0.505	0.548	0.075

agreement.

2. Background

One reason for the wide interest in hardness testing is that the microstructure (and hardness) of materials can change dramatically with alloying. Thus, there are many microstructurally-based mechanisms that lead to hardness changes as a function of composition, including solid solution hardening [1-3], inclusions and nanoinclusions [6, 7], and spinodal decomposition [14, 15].

In addition to the often-observed correlation between hardness and composition [1 - 8], a number of material properties are functions of hardness, H. The mechanical properties linked to hardness include compressive strength [16, 17], fracture toughness [18], and Young's modulus [19]. For example, an upper limit for the compressive fracture strength, σ_c, can be estimated from the relationship σ_c (upper bound) $\approx$ H/3 [16, 17]. Thus, for a fine-grained, brittle material processed in an optimal manner (minimal defects), σ_c approaches roughly H/3 [16, 17].

The hardness, H, is associated with processes such as machinability and wear that are crucial to the fabrication and reliability of a wide variety of materials. For example, extensive wear of a component subject to sliding contact under in-service conditions may lead to serious failures. Zeng *et al.* [20] recently found that wear resistance of artificial teeth correlates well with the Vickers hardness. In addition, Krakhmalev and Bergstrom used the brittleness index, K_C /H, to predict the wear of $MoSi_2$-based ceramic composites

sliding against a metallic alloy at elevated temperatures where K_C is the fracture toughness [21].

The machinability of brittle materials also has been correlated with hardness. For a series of compositions in a family of yttria-aluminosilicate machinable glass ceramic materials, the residual surface roughness following machining is a strong function of hardness [22]. In addition, Kamboj et al. [23] found that the grinding force during machining of green (unfired) gelcast ceramics correlates well with the hardness of the work piece. In a machining study of hot pressed, functionally-graded silicon nitride/hexagonal boron nitride composites, Wang et al. found that the machinability of the dense composites correlates well with both the hardness and Young's modulus of the composites [24].

Thus the compositional dependence of H is significant since H is linked to other mechanical properties. For LAST, the fabrication of thermoelectric (TE) modules for waste heat recovery will require the machining of perhaps several hundred (or more) individual TE legs. Since machinability and wear resistance are functions of H for other brittle materials [20-24], it is likely that H will be an important factor in the successful machining of TE legs.

3. Experimental procedure

3.1 Specimen preparation

All specimens included in this study were cast from a melt using a 3-zone split-tube rocking furnace. A total of 100 grams of Ag, Pb, Sb, and Te granules with purities ranging from 99.99% to 99.999% were sealed in a fused silica ampoule. For the 14 specimens except N33, N43, and N58, the ampoules were heated from room temperature to 1020°C at 50°C/hr, and rocked for 8 hours during an isothermal hold at 1020°C. The rocking was then stopped and the specimens were cooled in the following steps: (1) to 850°C at 85°C/hr, (2) to 750°C at 5°C/hr, (3) to 50°C at 30°C/hr. For specimens N33, N43, and N58, the cooling rates were different than the cooling rate for the other 14 specimens (Table 3.1.2). In addition, the maximum temperature for specimen N43 was 980°C rather than 1020°C (Table 3.1.2).

The as-cast ingots were first cut into disks that were 22 mm in diameter and 7 mm thick. The disks were then cut into individual 5 mm X 5 mm X 7 mm prismatic legs that were indented on the 5 mm X 7 mm specimen faces. After cutting and prior to indentation testing, all of the specimens were polished with an automatic polishing system (AP-50, Leco Corp., St. Joseph, MI) using a series of diamond paste grits range from 35 microns down to a minimum grit size of 1 micron.

3.2 Microindentation and nanoindentation

Each specimen included in this study was microindented via Vickers indentation. In addition, six of the Vickers-indented specimens were also nanoindented. Prior to the Vickers indentation testing, the indenter was calibrated using a standard hardness calibration block (Yamamoto Scientific Tools, Chiba, Japan).

Table 3.1.2. Processing histories of ingots N33, N43, and N58, which were processed differently than the other 14 n-type ingots.

Specimen ID	Ingot processing history
N33	(1) heated from room temperature to 1020°C at 50°C/hr, (2) rocked at 1020°C for 8 hr, (3) cooled to 860°C at 160°C/hr, (5) cooled to 600°C at 4°C/hr, (6) cooled to 50°C at 275°C/hr.
N43	(1) heated from room temperature to 980°C at 50°C/hr, (2) rocked at 980°C for 8 hr, (3) cooled to 850°C at 70°C/hr, (4) cooled to 750°C at 5°C/hr, (5) cooled to 50°C at 30°C/hr.
N58	(1) heated from room temperature to 1020°C at 50°C/hr, (2) rocked at 1020°C for 8 hr, (3) cooled to 900°C at 60°C/hr, (4) cooled to 850°C at 10°C/hr, (5) cooled to 750°C at 5°C/hr, (6) cooled to 50°C at 30°C/hr.

To determine the hardness as a function of composition, 20 Vickers indentations were made in each of the 17 specimens at a 2.94 N load, with a loading time of 10 seconds and a loading rate of 70 μm/sec. The hardness, H, was calculated from the diagonal length, 2a, of the indentation impression such that

$$H = 1.8544P/(2a)^2, \quad (1)$$

where P is the indentation load [25].

After the Vickers indentation was complete, nanoindentation was performed on six specimens (Nano Indenter XP, MTS Systems Corporation, Oak Ridge, TN) with a Berkovich indenter tip. The maximum penetration depth was fixed at 2000 nm with a loading rate of 10 nm/s, and a thermal drift threshold of 0.05 nm/s. Sixteen nanoindentations (a 4 X 4 array with 50 μm spacing between the indent centres) were made on each of the six specimens, where each indentation impression was about 5 μm across. After the indentation load was removed, the hardness, H, was calculated from a commercial software package [26] such that

$$H = \frac{P_{MAX}}{A} \quad (2)$$

where P_{MAX} is the maximum load and A is the projected area of the indent impression at P_{MAX}. The area A is determined from a pre-calibrated tip shape function and the indentation depth based on Oliver-Pharr method [27].

After indentation, specimens were repolished and thermally etched at temperatures ranging from 615°C and 675°C for 1 hr in an atmosphere of 95% Ar + 5% H_2 with a pressure of 300 torr. The etched specimen surfaces were examined by SEM (6400V,

JEOL Corporation, Japan). The LAST specimens were sufficiently conductive to allow SEM examination to be performed without sputtering an electrically conductive coating onto the specimen surface. Grain sizes were calculated from the SEM images using the linear intercept method with about 200 intercepts for each specimen.

4. Results and discussion

To minimize chipping and cracks near the indentation impressions, we chose to use a Vickers indentation load of 2.94 N in this study. Another advantage of using an indentation load of 2.94 N is that it corresponds to the load levels used in the literature to study the effect of composition on microhardness [1-3, 28].

The goal of the nanoindentation work included in this study was to provide an independent check of the Vickers hardness data. The six specimens included in the nanoindentation study were selected such that the measured Vickers indentation values on those particular specimens were relatively uniformly distributed between the maximum and minimum of the Vickers hardness values measured for the 17 specimens included in this study. The measured Vickers hardness agrees well with the hardness measured by nanoindentation (Fig .1).

4.1 Hardness, H, as a parabolic function of chemical composition

The central focus of this study is the hardness versus composition behaviour of LAST thermoelectric materials. In the literature, for solid solution hardening of ternary

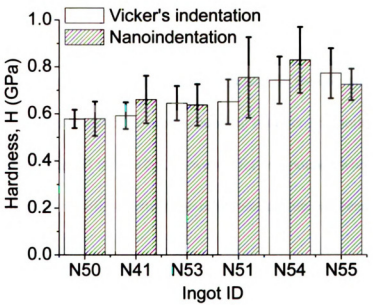

Figure 3.1.1. For six of the 17 ingot specimens, a comparison of the hardness values obtained by Vickers indentation (this study) with the hardness obtained via nanoindentation (also in this study).

metallic and ionic compounds with composition $A_{1-x}B_xC$, the hardness H as a function of the composition variable x has been written in terms of the empirical parabolic function [3]

$$H(x) = H_{AC} + (H_{BC} - H_{AC})x + kx(1-x), \quad (3)$$

where H_{AC} and H_{BC} are the hardness values of the binary compounds AC and BC, respectively (assuming that $H_{AC} < H_{BC}$). Also k is a positive constant that is (ideally) independent of x.

As discussed by Schenk *et al.*[3], Eq. (3) holds relatively well for solid solution hardening in compounds for which the atomic bonding is either predominantly ionic or metallic, giving a maximum H for $x \approx 0.5$. However, for compounds whose bonding is at least partially covalent, a modified form of the H(x) relationship has been used [1-3], namely

$$H(x) = H_{AC} + (H_{BC} - H_{AC})x + K(x)x(1-x) \quad (4)$$

where K is a function of composition, x. Shchennikov *et al.*[1] and Schenk *et al.* [2, 3] demonstrate that Eq. (4) can describe (i) the dependence of H on the compositional variable x and (ii) the shift in the maximum in H toward the harder of the two binary compounds (Figure 3.1.2).

Using Vickers indentation, the hardness as a function of composition has been investigated for a number of chalcogenide compounds, including the ternary mercury chalcogenides $Hg_{1-x}Cd_xSe$, $HgSe_{1-x}S_x$, $HgTe_{1-x}S_x$ [1] as well as the ternary cadmium chalcogenides $CdTe_{1-x}Se_x$ [2] and $Cd_{1-x}Zn_xTe$ [3]. Also, an earlier study of polycrystalline

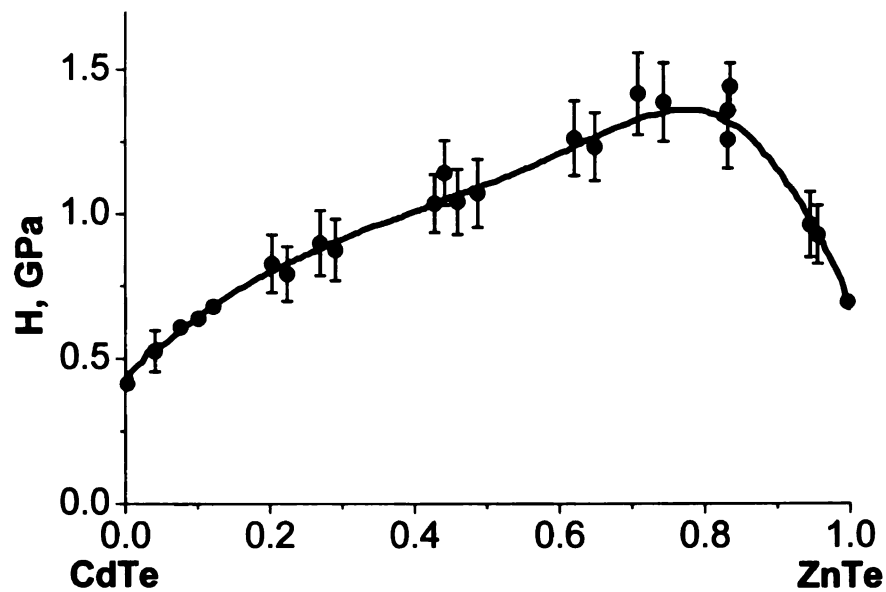

Figure 3.1.2. The variation in H as a function of composition for the chalcogenide system $Cd_{1-x}Zn_xTe$ (after [3]).

$PbTe_{1-x}S_x$, $PbTe_{1-x}Se_x$ and $PbS_{1-x}Se_x$ shows a similar quasi-parabolic dependence of hardness as a function of composition [28].

In order to determine if the H values for the LAST specimens included in this study can be described by a systematic function of composition, the hardness data for specimens in the system $Ag_aPb_bSb_cTe_d$ (Table 3.1.1) were fit to a relationship similar to Eq. (3), but as a function of the individual mole fractions of the Ag, Pb, Sb and Te (a, b, c, and d respectively) such that

$$H_{pred}(a,b,c,d) = g_0 + g_1a + g_2a^2 + g_3b + g_4b^2 + g_5c + g_6c^2 + g_7d + g_8d^2 \qquad (5)$$

For the 14 specimens except N33, N43, and N58, (Table 3.1.1) included in this study, a plot of the experimentally-determined hardness, $H_{exper,}$ versus the predicted hardness, H_{pred}, (predicted from Eq. (5)) yields a straight line with a slope of 1.00003 and intercept of $-2.1x10^{-5}$ GPa, which is very near the "ideal" values of one and zero respectively (Figure 3.1.3). The correlation coefficient for the regression is 0.95. As discussed in section 3, specimens N33, N43, and N58 had different cooling rates than the other 14 specimens (Table 3.1.2). If all 17 specimens are included in the regression, then the slope and intercept of H_{exper} versus H_{pred} are 1.00001 and $1.2x10^{-4}$ respectively, with a correlation coefficient of 0.80.

In this study, the minimum and maximum average H values were 0.526 GPa and 0.922 GPa, respectively (Table 3.1.1). However, a number of other material systems show similar or even larger variations in H as a function for composition. For example, for ternary systems, the value of H can change by a factor of three or more as the

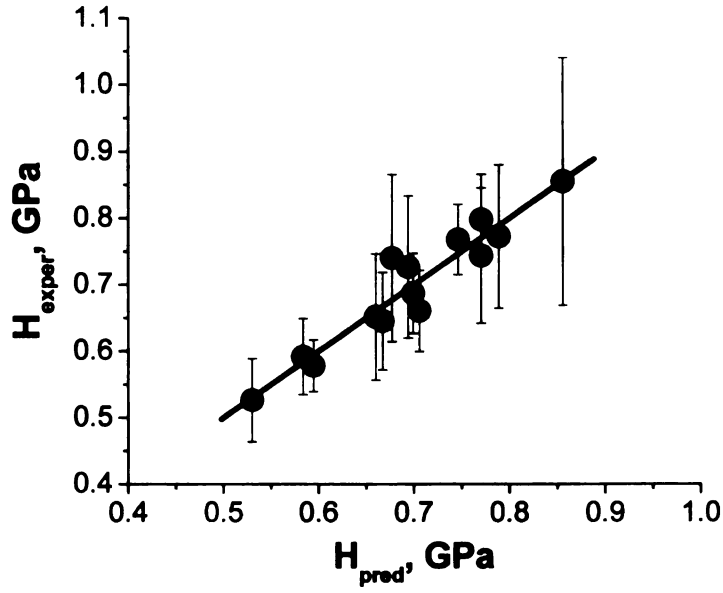

Figure 3.1.3. Plot of mean values of the experimentally determined hardness, H_{exper}, versus H_{pred} for the 14 identically processed specimens of the 17 specimens in this study (Table 3.1.1), excluding N33, N43, and N58 that were processed with different cooling rates (Table 3.1.2). The H_{pred} values are computed based on the least-squares fitting of the data to Eq. (5). The resulting slope of 1.00003 and intercept of -2.1×10^{-5} GPa with a correlation coefficient of 0.95 indicate that the regression of the H data to Eq. (5) yields a good description of the hardness data. The error bars represent the standard deviation of the hardness values (Table 3.1.1) based on 20 Vickers indentations per specimen.

composition changes along a binary or pseudo-binary system within the ternary. For example, in the system $Cd_{1-x}Zn_xTe$, for $0 \leq x \leq 1$, the Vickers indentation hardness, H, rises from about 0.41 GPa for pure CdTe to a maximum of roughly 1.4 GPa at $x \approx 0.7$ [3] (Figure 3.1.2). As x increases from 0.7 to 1, H decreases to about 0.7 GPa for pure ZnTe [3]. In addition, for the system $PbTe_{1-x}Se_x$, H increases from 0.396 GPa for pure PbTe to a maximum of 0.964 GPa at 30 mol% PbTe, and then decreases to 0.571 GPa for pure PbSe [28]. Shchennikov *et al.* [1] found that for $HgTe_{1-x}S_x$, H was approximately 0.240 GPa for $x = 0$, increased to a maximum of 0.804 GPa at $x \approx 0.5$ and decreased to 0.243 GPa at $x = 1$. Thus, for the various ternary chalcogenide systems studied by Darrow *et al.* [28], Schnek *et al.* [3] and Shchennikov *et al.* [1], the magnitude of the composition-induced changes in the Vickers indentation hardness, H, are roughly comparable to the H changes observed for the quaternary compounds included in this study.

In the literature, a number of chalcogenide compounds, including PbTe, SnTe, and GeTe, were believed to form solid solutions with $AgSbTe_2$ [29]. These compounds obey Vegard's law (a linear change in lattice parameter as a function of composition) and X-ray powder diffraction revealed no second phases. However, using electron diffraction, high resolution transmission electron microscopy as well as single crystal X-ray diffraction studies, Quarez *et al.* [29] recently demonstrated $Ag_aPb_bSb_cTe_d$ (LAST) includes coherently embedded nanocrystals (consisting of Ag-Sb rich spinodally decomposed regions) dispersed within a Pb-Te rich (Ag-Sb poor) matrix. Thus, while the function used

to describe the hardness data (Eq. (5)) is similar to that used for solid solutions of ternary compounds [1-3] (Eqs. (3) and (4)), the LAST material includes nanocrystals [29] that may also contribute to the composition dependence of hardness.

4.2 Comparison of observed scatter for hardness in this study with scatter for H reported in literature.

The scatter in H values observed in this study (Table 3.1.1) may be related to hardness anisotropy that occurs in many materials. For example, in $MgSO_4 \cdot 7H_2O$ single crystals, H varies from approximately 0.24 GPa to 0.4 GPa as a function of azimuthal angle on the (010) specimen faces and roughly from 0.29 to 0.42 GPa on (100) faces for Vickers indentations at a 0.39 N load [30]. For $LiNbO_3$ single crystals indented via a Berkovich indenter, the hardness changes by a factor of up to 1.4 as a function of azimuthal angle [31]. In general, scatter in the measured H values is expected to be the most pronounced for polycrystalline specimens having a grain size that is significantly larger than the dimensions of the indentation impression. (Indentations made across the surface of a large-grained polycrystalline specimen will approximate the results obtained by indenting single crystals on differing crystallographic planes over a range of azimuthal angles). In this study, the grain sizes of the cast LAST specimens determined from the linear intercept method range from ~ 490 to 720 microns, while the Vickers indentation impression dimensions are roughly 80 to 100 microns. The disparity in the relative dimensions of indentation impression and grain size is conducive to anisotropy-based

scatter in the measured H values (Figure 3.1.4).

Another source of comparison for the relative scatter of the H data is the study by Darrow *et al.* [28]. To evaluate H for their series of polycrystalline $PbTe_{1-x}Se_x$ specimens with varying composition, Darrow *et al.* [28] placed 10 Vickers indentations in each of their nine specimens. Although Darrow *et al.* [28] did not report standard deviation for their data, they plotted the range of the H measurements for each specimen. Using the maximum and minimum H values (H_{max} and H_{min}, respectively), the normalized range $R_N = (H_{max} - H_{min})/H_{mean}$ varied from ~ 0.21 to 0.69 for Darrow *et al.*'s nine $PbTe_{1-x}Se_x$ specimens [28] while for the 17 LAST specimens (this study) R_N ranged from ~ 0.24 to 0.62, with 14 of the 17 specimens having an $R_N < 0.5$. Thus, the magnitude of the scatter in Darrow *et al.*'s [28] Vickers H values for $PbTe_{1-x}Se_x$ is comparable to that observed in this study. (The Darrow *et al.* [28] $PbTe_{1-x}Se_x$ study is a relatively good source of comparison data, since the LAST specimens are essentially Ag and Sb-doped PbTe materials). Note for range ($H_{max} - H_{min}$) and the standard deviation H_{std}, $H_{std} \sim (0.6(H_{max} - H_{min})/2)$. In addition, the coefficient of variation, CV, is given by the standard deviation/mean. Thus, in the study by Darrow *et al.* [28] the normalized range of ~ 0.21 to 0.69 should correspond to a CV range of roughly 0.06 to 0.20, which is comparable to the CV values for the LAST data included in this study.

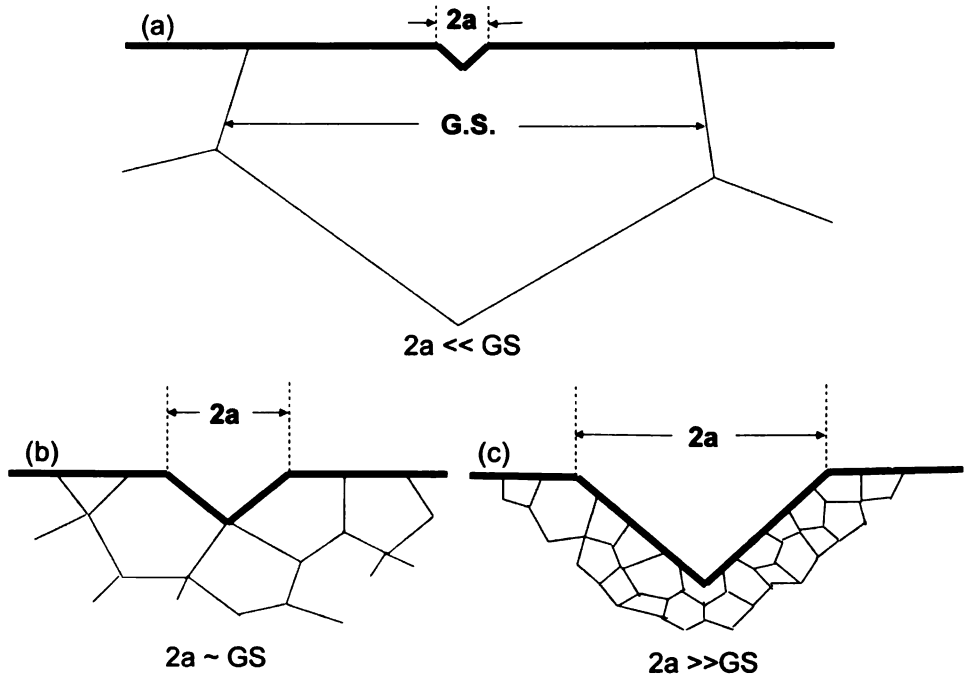

Figure 3.1.4. Schematic depicting the relative size of the indenter tip compared to the specimen's grain size. The relative size is important with respect to the relative scatter of the hardness values.

5. Summary and Conclusions

This study reports the dependence of hardness, H, upon chemical composition for 17 n-type quaternary LAST [12, 13, 29] thermoelectric specimens (Table 3.1.1). Measurements were made on the entire set of 17 specimens via Vickers indentation. As an independent check on the microindentation (Vickers) measurements, nanoindentation was performed on six of the 17 specimens. The values of H found by nanoindentation agreed very well with the values measured by microindentation (Figure 3.1.1).

The parabolic model of H versus composition (Eq. (3)) that has been used previously to model binary joins within ternary systems [1 - 3] is extended here to include true quaternary systems (Eq. (5)). This study is the first to treat the compositional dependence of hardness in a true quaternary system in which the compositions of each of the four elements vary independently over a section of the quaternary system. We demonstrated that the compositional dependence hardness of the LAST system is well characterized by a parabolic function (Eq. (5)), which is an extension of Eq. (3). The scatter observed in the H data (Table 3.1.1 and Figure 3.1.3) is likely due, at least in part, to the crystallographic anisotropy of hardness [28, 30, 31] in our large-grained polycrystalline LAST specimens.

As discussed in the Background (Section 2), a number of researchers have found that hardness correlates well with a number of properties for brittle materials, including wear and machinability [20-24]. In order to produce thermoelectric devices, especially in waste heat conversion applications, wear and machinability will impact the fabrication and in-service reliability of thermoelectric components. In addition, H has also been observed

to correlate with the compressive strength of brittle, fine-grained materials [16, 17], which also is a significant property in terms of the construction of thermoelectric devices from brittle thermoelectric materials.

Acknowledgements

The authors acknowledge the financial assistance of the U. S. Department of Energy Grant DE-FC26-04NT42281 and Office of Naval Research MURI Grant number N000140310789.

References

[1] V. V. Shchennikov, S. V. Ovsyannikov, and N. Y. Frolova, J. Phys. D-Appl. Phys. 36 (2003) 2021.

[2] M. Schenk and C. Silber, J. Mater. Sci.-Mater. Electron. 9 (1998) 295.

[3] M. Schenk and T. H. D. Le, Semicond. Sci. Technol. 13 (1998) 335.

[4] K. C. Chen, F. M. Chu, P. G. Kotula, and D. Thoma, Intermetallics 9 (2001) 785.

[5] D. Asthana and A. K. Shrivastava, Mater. Sci. Forum 223 (1996) 453.

[6] M. A. Baker, P. J. Kench, C. Tsotsos, P. N. Gibson, A. Leyland, and A. Matthews, J. Vac. Sci. Technol. 23 (2005) 423.

[7] J. Almer, M. Oden, and G. Hakansson, Thin Solid Films 385 (2001) 190.

[8] L. Zajickova, V. Bursikova, V. Perina, A. Mackova, and J. Janca, Surf. Coat. Technol. 174 (2003) 281.

[9] M. M. Korsukova, V. N. Gurin, S. Otani, and Y. Ishizawa, Solid State Commun. 99 (1996) 215.

[10] I. M. Low, J. Am. Ceram. Soc. 87 (2004) 2125.

[11] D. de Graaf, M. Braciszewicz, H. T. Hintzen, M. Sopicka-Lizer, and G. de With, J. Mater. Sci. 39 (2004) 2145.

[12] K. F. Hsu, S. Loo, F. Guo, W. Chen, J. S. Dyck, C. Uher, T. Hogan, E. K. Polychroniadis, and M. G. Kanatzidis, Science 303 (2004) 818.

[13] D. Bilc, S. D. Mahanti, K. F. Hsu, E. Quarez, R. Pcionek, and M. G. Kanatzidis, Phys. Rev. Lett. 93 (2004) Art. No. 146403.

[14] P. H. Mayrhofer, A. Horling, L. Karlsson, J. Sjolen, T. Larsson, C. Mitterer, and L. Hultman, Appl. Phys. Lett. 83 (2003) 2049.

[15] J. Chao and J. L. Gonzalez-Carrasco, Scripta Mater. 47 (2002) 423.

[16] R. W. Rice, Mechanical Properties of Ceramics and Composites, Marcel Dekker, New York, 2000, pp. 308 - 312.

[17] J. Langford, J. Hard Mat. 2 (1991) 55.

[18] B. R. Lawn, Fracture of Brittle Solids, second ed., Cambridge University Press, New York, 1993, pp. 258 - 263.

[19] D. B. Marshall, T. Noma, and A. G. Evans, Am. Ceram. Soc. Bull. 65 (1982) C175.

[20] J. Y. Zeng, Y. Sato, C. Ohkubo, and T. Hosoi, J. Prosthet. Dent. 94 (2005) 453.

[21] P. V. Krakhmalev and J. Bergstrom, Wear 260 (2006) 450.

[22] K. Morita, A. Umenzawa, S. Yamato, and A. Makishima, J. Am. Ceram. Soc. 76

(1993) 1861.

[23] R. K. Kamboj, S. Dhara, and P. Bhargava, J. Eur. Ceram. Soc. 23 (2003) 1005.

[24] G. Wang, W. Pan, M. N. Jiang, J. Chen, and Y. M. Luo, Mater. Sci. Eng. B 90 (2002) 261.

[25] J. B. Wachtman, Mechanical Properties of Ceramics, Wiley and Sons, New York, 1996.

[26] "XP CSM standard hardness, modulus, and tip cal", TestWorks® 4, Nano Instruments, Oak Ridge, TN

[27] W. C. Oliver and G. M. Pharr, J. Mater. Res. 7 (1992) 1564.

[28] M. S. Darrow, W. B. White and R. Roy, J. Mater. Sci. 4 (1969) 313.

[29] E. Quarez, K. F. Hsu, R. Pcionek, N. Frangis, E. K. Polychroniadis and M. G. Kanatzidis, J. Am. Chem. Soc. 127 (2005) 9177.

[30] S. Karan and G. Sen, Mater. Sci. Eng. A 398 (2005) 198.

[31] S. Bhagavat and I. Kao, Mater. Sci. Eng. A 393 (2005) 327.

Chapter 2

F. Ren, E. D. Case, E. J. Timm and H. Schock, "Young's modulus as a function of composition for an n-type lead-antimony-silver-telluride (LAST) thermoelectric material", *Philosophical Magazine*, **87**: 4907-4934 (2007).

Young's modulus as a function of composition for an n-type Lead-antimony-silver-telluride (LAST) thermoelectric material

F. REN†, E. D. CASE*†, E. J. TIMM‡, and H. J. SCHOCK‡

†Chemical Engineering and Materials Science Department,
Michigan State University, East Lansing, MI 48824 USA

‡Mechanical Engineering Department,
Michigan State University, East Lansing, MI 48824 USA

For 17 cast lead-antimony-silver-telluride (LAST) thermoelectric specimens (representing 14 different chemical compositions), a combination of Vickers and Knoop microindentation techniques were used to determine the composition dependent Young's modulus, E, which ranged from 24 GPa to 68 GPa. Following microindentation, independent nanoindentation measurements also were performed on 10 of the 17 specimens. In the literature, for pseudobinary joins in ternary or quaternary compounds (with the compositions $A_xB_{1-x}C$ or $A_XB_{1-X}CD$, respectively), changes in the Young's modulus have been expressed as quadratic functions of the compositional parameter x. In this study we extend the quadratic functional form to a paraboloid in four composition variables to describe composition-dependent changes in E for the LAST compounds. Also, the composition dependent changes in LAST are compared to the trends observed in the literature for E and bulk modulus for systems described by a single compositional variable.

Keywords: Semiconductors; Microindentation; Nanoindentation; Elastic properties

1. Introduction

Thermoelectric materials with high *ZT* values (figure of merit) have been developed recently [1-4]. The family of quaternary thermoelectric materials Ag-Pb-Sb-Te (LAST) exhibit a *ZT* value of up to 1.7 at 700K [1, 5-6], showing promise for thermoelectric power generation applications [1]. For LAST compounds, studies of fracture strength [7] and hardness [8] appear in the literature, but the data on room temperature elastic moduli is limited to one study involving three specimens [5].

Since thermoelectric materials are typically brittle semiconductors, they are subject to crack and microcrack damage during mechanical or thermal loading [9]. For waste heat conversion applications, mechanically and thermally imposed stresses will act in concert on the TE elements. Fundamental to the characterization of the response of a material to an imposed strain is the Young's modulus, E, where for elastically isotropic material subjected to strain, ε, the stress, σ, generated in the body is given by

$$\sigma = E' \varepsilon \tag{1}$$

such that $E' = E$ for plane stress and $E' = E/(1-\nu)$ for plain strain, where ν is Poisson's ratio [10]. For geometrically complex TE modules with realistic physical constraints, detailed calculations of the mechanically and thermally imposed stresses can be performed by Finite Element Analysis (FEA), but the elastic modulus is still required in order to construct the stiffness matrix for FEA [11, 12].

In this study, the room temperature Young's modulus of 17 LAST specimens (representing 14 different compositions) was measured by microindentation. For 10 of the 17 specimens, separate and independent measurements of the Young's modulus also were obtained using nanoindentation.

This study shows that the functional form of the compositional dependence of Young's modulus of our LAST ingot specimens can be described by a paraboloid function that is a quadratic in each of the four elemental constituents. This paraboloid form is an extension of relationships given in the literature where the Young's modulus [13-15] and bulk modulus [16-18] of ternary and quaternary solid solutions of composition $A_xB_{1-x}C$ and $A_xB_{1-x}CD$ are functions of a single compositional parameter x.

2. Experimental procedure

2.1 *Specimen preparation*

All specimens used in this study were 5 mm × 5 mm × 7 mm legs that were cut from the cast LAST ingots. For each composition, high purity (99.99% to 99.999% pure) Pb, Ag, Sb, and Te granules were sealed into a fused silica ampoule. The ampoule was then placed in a 3-zone split tube-rock furnace and processed using the time-temperature profiles shown in Figure 3.2.1. The as-cut legs were then polished with a series of diamond grit down to 1 μm. All microindentations and nanoindentations were made on the 5 mm × 7 mm specimen faces.

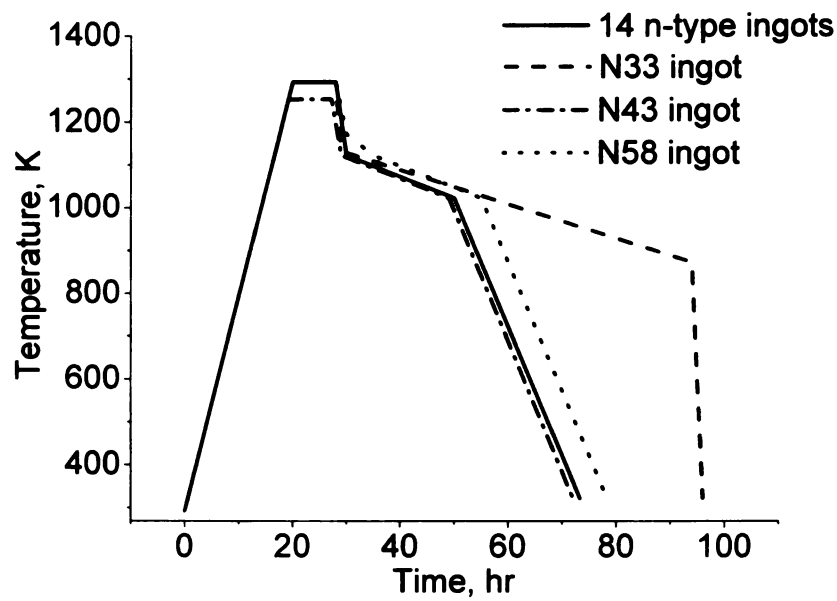

Figure 3.2.1. Temperature-time profiles for the processing of the 17 cast ingot specimens included in this study.

2.2 *Measurement of Young's modulus by microindentation*

Following a procedure developed by Marshall *et. al.* [19], a combination of Knoop and Vickers microindentation was used to evaluate Young's modulus. Knoop indentation impressions were used to estimate the ratio of hardness, H, to Young's modulus, E, [19]

$$\frac{H}{E} = \frac{0.14 - \frac{b'}{a'}}{0.45} \tag{2}$$

where b' and a' are, respectively, the lengths of the short and long diagonals of the Knoop indentation impressions after the load is removed [19]. In order to compute E from equation (2) [19], we measured the hardness, H, by Vickers indentation using the relationship [20]

$$H = \frac{1.8544P}{(2a)^2} \tag{3}$$

where P is the applied indentation load and $2a$ is the diagonal length of the Vickers indentation impression.

Knoop indentations were performed on a commercial indenter (HMV-2000, Shimadzu, Japan) with a load of 0.49 N and a loading time of 10 seconds. Vickers indentations were made using a semi-micro hardness tester (Buehler Ltd. Lake Bluff, IL.) at a constant load of 2.94 N with a loading rate of 70 μm/sec and a loading time of 10 seconds. For each of the 17 specimens included in this study, 20 Vickers microindentations and 20 Knoop microindentations were performed on each specimen, for a total of 680 microindentations. The centers of neighboring microindentations were

placed approximately 500 to 1000 microns apart.

2.3 *Measurement of Young's modulus by nanoindentation*

In order to provide a second, independent measure of the elastic modulus of the LAST material, the elastic modulus of 10 of the 17 specimens included in this study was measured via nanoindentation (Nano Indenter XP, MTS Systems Corporation, Oak Ridge, TN). As will be discussed in Section 3.1, the nanoindentation measurements also provided a Young's modulus determination with a spatial sampling of the specimen on the size scale of microns while the microindentation measurements sampled the elastic modulus with a spatial resolution of hundreds of microns.

A 4 x 4 array of nanoindentations was made on each of the 10 specimens using a Berkovich indenter tip with a loading rate of 10 nm/sec and a maximum penetration depth of approximately 2000 nm. Thus, a total of 160 nanoindentations were included in this study. The elastic moduli were calculated from the nanoindentation load and the indenter tip displacement via the Continuous Stiffness Measurement technique (TestWorks® 4, Nano Instruments, Oak Ridge, TN) based on the Oliver-Pharr method [21].

2.4 *Microstructural analysis*

After the microindentation and nanoindentation procedures were complete, the specimen

surfaces were thermally etched between 888 K and 948 K for 1 hr in a reducing atmosphere that consisted of 95% Ar and 5% H_2 under a pressure of approximately 300 torr. The thermally etched specimen surfaces were examined using a Scanning Electron Microscope (SEM, JEOL 6400V, JEOL Corp. Japan) with an accelerating voltage of 20 kV and a working distance of 39 mm. SEM images were used to calculate the grain size based on the linear intercept method using about 200 intercepts per micrograph.

3. Results and Discussion

Table 3.2.1 lists the chemical compositions, $Ag_aPb_bSb_cTe_d$, of the 17 cast LAST ingot specimens included in this study.

3.1 Comparison and statistical analysis of Young's modulus determined by microindentation and nanoindentation

Microindentation was used to determine the Young's modulus as a function of composition for each of the 17 LAST specimens included in this study. After the microindentation measurements had been completed, the Young's modulus of 10 of the 17 specimens also was independently measured by nanoindentation. The 10 specimens selected for nanoindentation can be divided into three subgroups, where each subgroup focuses on a different aspect of the comparison between the two measurement techniques.

Table 3.2.1. For the LAST ingot specimens $Ag_aPb_bSb_cTe_d$ included in this study, the composition, the mean values of the Young's modulus, E_{mean}, and the standard deviation of Young's modulus, E_{std}, as determined by (a) microindentation and (b) nanoindentation.

Table 3.2.1a.

Spec.ID	Ag (a)	Pb (b)	Sb (c)	Te (d)	E_{mean} (GPa)	E_{std} (GPa)
N33	0.030	0.422	0.042	0.506	31.8	8.33
N35	0.043	0.427	0.034	0.496	42.2	9.94
N37	0.017	0.427	0.043	0.513	43.4	14.1
N39	0.015	0.467	0.017	0.501	40.3	17.9
N40	0.006	0.480	0.011	0.503	24.2	11.1
N41	0.008	0.464	0.021	0.506	36.9	10.9
N42	0.011	0.454	0.030	0.505	63.0	20.4
N43	0.011	0.454	0.030	0.505	56.0	21.0
N48	0.025	0.446	0.028	0.501	65.9	14.6
N49	0.020	0.455	0.024	0.502	58.9	15.2
N50	0.009	0.472	0.016	0.503	50.3	19.4
N51	0.016	0.442	0.034	0.509	44.7	16.0
N52	0.021	0.450	0.026	0.502	62.0	22.9
N53	0.015	0.468	0.016	0.501	68.5	22.0
N54	0.043	0.427	0.034	0.496	44.6	15.9
N55	0.017	0.417	0.050	0.517	24.5	7.48
N58	0.011	0.454	0.030	0.505	24.7	10.0

Table 3.2.1b.

Spec.ID	Ag (a)	Pb (b)	Sb (c)	Te (d)	E_{mean} (GPa)	E_{std} (GPa)
N35	0.043	0.427	0.034	0.496	49.5	3.5
N41	0.008	0.464	0.021	0.506	42.0	3.8
N42	0.011	0.454	0.030	0.505	59.1	1.8
N43	0.011	0.454	0.030	0.505	56.3	1.2
N50	0.009	0.472	0.016	0.503	51.0	3.8
N51	0.016	0.442	0.034	0.509	49.7	8.1
N53	0.015	0.465	0.016	0.501	71.3	6.0
N54	0.043	0.427	0.034	0.496	51.3	0.7
N55	0.017	0.417	0.050	0.517	25.8	1.4
N58	0.011	0.454	0.030	0.505	58.2	1.0

The six specimens included in nanoindentation subgroup A were selected such that their Young's moduli were approximately evenly distributed over the full range of Young's modulus values (68 GPa to 24 GPa) measured by microindentation (Figure 3.2.2a). For the six specimens included in subgroup A, the mean values of the elastic moduli measured by the two techniques, i. e. microindentation and nanoindentation, agreed to within $\pm$ 13 % (Figure 3.2.2a). In addition, for each of the six specimens in subgroup A, the t-test showed no statistically significant difference between the mean modulus value determined by microindentation and the average modulus measured by nanoindentation (Figure 3.2.2a and Appendix A). In contrast, for each specimen the standard deviation of the microindentation data for each specimen was larger than that for the corresponding nanoindentation data, as determined by the F-test (Appendix A). For the nanoindentation and microindentation measurements performed on the six specimens of group A (which span the entire range of modulus values included in this study) the mean values are statistically equivalent while the scatter in the nanoindentation data is significantly lower than the scatter in the microindentation data (Appendix A).

Subgroup B includes two specimens; N35 and N53 that were cut from two separately cast ingots having identical composition (Table 3.2.1) and identical processing history (Figure 3.2.1). The modulus results for subgroup B (Figure 3.2.2b and Appendix A) demonstrate that for the LAST ingots with same composition and processing history, (i) there are no statistically significant differences between the mean values of the Young's modulus for these composition replicates, and (ii) as was the case for subgroup A,

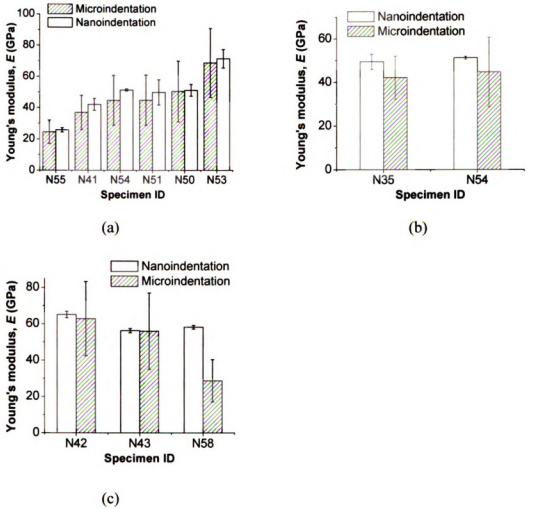

Figure 3.2.2. Comparison of Young's modulus measured by microindentation (Vickers and Knoop) and nanoindentation. (a) Young's modulus determined from microindentation and nanoindentation in subgroup A (six specimens that span the range of moduli determined in this study), (b) composition replicates N35 and N54 in subgroup B, where the two specimens also have the same processing history (Figure 3.2.1 and Table 3.2. 1), (c) Three compositional replicates (ingots N42, N43, and N58) with differing processing histories. The lower Young's modulus for microindentation on N58 is likely due to the macrocracking in the specimen.

the scatter in nanoindentation data in subgroup B is considerably less than the scatter in the microindentation data (Appendix A).

Subgroup C included three specimens, i.e. N58, N42 and N43 (Figure 3.2.2c). Each of these three specimens was extracted from a different cast ingot, where the composition of each ingot was identical within Subgroup C. However, the composition of the Subgroup C specimens was different than the composition of the two replicates in Subgroup B (Table 3.2.1). For Subgroup C the processing conditions differed slightly among the three specimens in the group such that (i) the maximum processing temperatures were 1253 K for N43 and 1293 K for N42 and N58, and (ii) the cooling rates between the maximum temperature and 1123 K were 85 K/hr for N42 and 70 K/hr for N43 while N58 was first cooled from 1293 K to 1173 K at 60 K/hr and then cooled to 1123 K at 10K/hr (Figure 3.2.1). The mean modulus values measured via microindentation and nanoindentation were comparable for specimens N42 and N43 (Figure 3.2.2c) and again the scatter in the microindentation data greatly exceeded the scatter in the nanoindentation data. The measured Young's moduli were 59.1 ± 1.8 GPa, 56.3 ± 1.2 GPa and 58.2 ± 1.0 GPa for the nanoindentation tests on specimens N42, N43 and N58 respectively (Table 3.2.1a) while the measured microindentation moduli were 62.9 ± 20.4 GPa, 56.0 ± 21 GPa and 28.7 ± 11.6 GPa, respectively for the same three specimens. (Statistical inferences obtained from comparing the means and variances of the subgroup C specimens are discussed in Appendix A). While the modulus measurements on the three replicates were comparable in most instances, the Young's

modulus measured for specimen N58 via microindentation was ~ 50% lower than the modulus measured by nanoindentation (Figure 3.2.2c).

Within subgroup C, the difference in the Young's modulus for specimen N58 is likely a function of the specimen history. Specimen N58 was the only one of the 17 specimens included in this study that had been subjected to significant stress prior to the modulus testing, in that specimen N58 was cut from a disc-shaped biaxial flexure specimen that had been included in a Weibull analysis of the fracture strength [17]. Macrocracks likely induced by fracture testing were observed on the surface of specimen N58 (Figure 3.2.3), but were not observed for other specimens in the study, which was expected since the other specimens had not been subjected to similar stresses. The cracks observed in specimen N58 ran across the width of the specimen surface and were nearly parallel with spacing of ~ 200 μm to 2000 μm between any two adjacent cracks (Figure 3.2.3).

The decrement in microindentation-measured Young's modulus values can be understood in terms of a crack induced drop in modulus, since in the literature there are many instances in which macrocracking and/or microcracking result in a decrease in the elastic modulus [9, 22-26]. However this does not explain why the Young's modulus measured from specimen N58 via nanoindentation was apparently unaffected by the cracking, since the nanoindentation moduli are quite similar for the composition replicate specimens N58, N42 and N43 (Figure 3.2.2c).

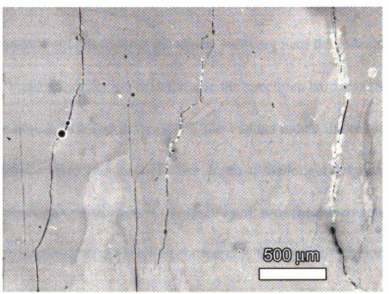

Figure 3.2.3. SEM micrograph showing the polished surface of specimen N58. Nearly-parallel macrocracks were observed across the entire specimen surface with spacing between ~ 200 µm and 2000 µm which likely resulted from biaxial testing prior to indentation on this particular specimen. None of the other specimens in this study showed such cracks.

Both the sensitivity of the microindentation technique to cracks and the lack of sensitivity of the nanoindentation technique to cracks in specimen N58 are consistent with the differing size scales for the indentation impressions for the two techniques.

Recall that the microindentation technique developed by Marshall *et al.* [19] employs both Knoop indentations to determine the elastic recovery near the indentation impression and Vickers indentation to determine the specimen hardness (Section 2.2). For the set of 17 specimens included in this study, the Vickers indent impression diagonal lengths varied from ~ 70 to 120 μm while the length of the longer diagonal of Knoop indentation impressions ranged from ~ 130 to 290 μm; thus the dimensions of the microindentation impressions are roughly comparable to the spacing among the macrocracks in N58. In contrast, the nanoindentation impressions (generated by a Berkovich tip) were approximately 5 μm across, which is smaller than the inter-crack spacing by a factor of up to two orders of magnitude or more.

The dimensions of the indentation impression are critical, since the stress and strain fields near an indentation typically scale with the indentation dimension. For example, the stress near a Berkovich indentation falls off by more than a factor of 10 outside a hemispherical region of the specimen centered at the indentation impression and having a radius equal to three times the indentation dimension [27]. Likewise, stress fields for other indenter geometries such as Vickers and Knoop also fall off very rapidly at a few diagonal lengths from the indentation impression center [28, 29].

The local nature of the measurement of elastic modulus by nanoindentation is

underscored by the fact that nanoindentation is widely considered to be the preferred method to determine the modulus and hardness of thin films [30-32]. For a thin film of thickness t_0, if the Berkovich tip penetrates to a depth less than ≈ 0.1 to $0.2\ t_0$, then the elastic modulus determined from the nanoindentation test is representative of the film itself, without perturbations from the underlying substrate [30-32]. While modulus measurements of ultra thin films (films less than 100 - 200 nm thick) often employ spherical indentation tips [31], nanoindenters with Berkovich tips have been used very widely to measure the mechanical properties of thin films of thickness of several microns down to less than one micron [33, 34].

Since the nanoindentation depth in this study was limited to 2 microns or less, then the criteria discussed above for thin film testing (in terms of the relative depth of the nanoindentation impression required for the measured modulus to be entirely unperturbed by the substrate [30, 32]) implies that the "sampling volume" for nanoindentation should be a quasi-spherical volume of roughly 10 to 20 microns, centered on the indentation impression; that is, the modulus measured by nanoindentation in this study should be insensitive to defects (say, pores and cracks) and other microstructural inhomogeneities that are more than roughly 10 to 20 microns distant from the indent center. Following the arguments by Giannakopoulos *et al.* [28] and Chiang *et al.* [29], modulus determinations by microindentation (Knoop and Vickers) would be insensitive to defects for distances of more than roughly 400 to 500 microns (or more) from the center of the microindentation impression.

A study by Guelorget *et al.* of tensile-fracture-induced damage in a semi-hard copper sheet provides a further experimental demonstration of the local nature of Young's modulus measurements made by the nanoindentation technique [35]. As a series of nanoindentations were made progressively closer to a fracture surface in the copper sheet, Guelorget *et al.* [35] measured a simultaneous increase in hardness (due to an increase in dislocation number density) and a decrease in modulus (presumably due to a microcrack zone local to the macroscopic fracture surface). The measured changes in modulus were assumed to exceed those due to free-surface effects [35]. Using a Berkovich tip with an indentation depth of 500 nm and a indent impression dimension of roughly 3.5 microns, Guelorget *et al.* observed the Young's modulus to steadily drop by a total of about 10 percent over the interval between roughly 250 microns and 25 microns from the fracture [35], while the increase in hardness commenced at about 1.5 mm from the fracture, presumably indicating different length scales for the microcrack damage zone near the tensile fracture site and the increase in dislocation density as one approached the deformed region of the copper sheet.

While the nanoindentation and microindentation techniques used in this study provide a local measure of the Young's modulus, it is important to note that (in the absence of defects such as microcracks, cracks and pores), the literature shows that nanoindentation values agree well with more "global" measurements of Young's modulus, such as resonant ultrasound spectroscopy and impulse excitation. (In both the resonant ultrasound spectroscopy (RUS) and the impulse excitation (IE) techniques, the entire

specimen is subjected to acoustic vibrations and thus the specimen modulus reflects the global mechanical response of the specimen [36, 37]). For example, Radovic and co-workers compared the Young's modulus measurements obtained from four different measurement techniques, RUS, IE, four-point bend testing and nanoindentation [38]. For dense materials such as 4140 steel and Pyrex glass, Radovic *et al.* found that the Young's modulus obtained via nanoindentation compared well with RUS, IE, and four-point bending [38]. For 7075 aluminum, the nanoindentation modulus was about 8% higher than modulus obtained by the other three techniques [38]. For pure alumina specimens with volume fraction porosities between 1.57% and 4.27%, the slope of the modulus versus porosity curve was lower for nanoindentation than were the modulus-porosity slopes for RUS, IE and four-point bending, but when extrapolated to zero porosity, the Young's modulus predicted for pure, dense Al_2O_3 varied little among the four techniques [38]. This implies that the nanoindentation-determined moduli were somewhat less sensitive to the porosity in the alumina specimen than the other techniques.

As a whole, the work by Radovic *et al.* [38] shows that for a variety of materials, the modulus determined by nanoindentation agrees relatively well with the global or macroscopically determined modulus, except when defects are present. Therefore, we would expect a similar behavior in our study, in that the Young's modulus determined by nanoindentation should be comparable to the Young's modulus of the specimens on a global scale. In addition, this is also consistent with the fact that the 20 Vickers microindentations and 20 Knoop microindentations per specimen were placed about 500

to 1000 microns apart, thus on each specimen surface the microindentation array sampled a significant fraction of the specimen surface.

Therefore, in addition to providing two independent measures of the Young's modulus, the nano- and micro- indentation measurements included in this study serve to probe the spatial homogeneity of the elastic modulus by measuring the modulus on the microscale (via nanoindentation) and the mesoscale (by Knoop/Vickers indentation). A departure from a spatial homogeneity in elastic modulus can stem from a departure from homogeneity in the material structure via, say, defects (cracks, microcracks and pores) or localized differences in crystalline phases. It is significant to note that in this study, the measured moduli for both techniques are similar for the two sets of compositional replicates (Figure 3.2.2b, Figure 3.2.2c and Appendix A), while the moduli measured by the two techniques change by up to nearly a factor of three for the full range of compositions shown in Table 3.2.1a and Figure 3.2.2a.

The changes in modulus as a function of composition (as measured by nanoindentation and microindentation) track well together the LAST specimens in this study which implies that the physical mechanism for the modulus change is linked to changes in the material that occur at a size scale smaller than the micron level. As will be discussed in the next section, this is consistent with composition-dependent changes in elastic moduli reported in the literature for solid-solution systems, where the modulus changes have been interpreted in terms of relaxations in the atomic lattice and redistributions of charge, bond length and bond angle.

3.2 *Linear and parabolic models for elastic modulus as a function of composition*

For binary solid solution systems, A_XB_{1-X} (or a binary join in a ternary system such as $A_XB_{1-X}C$ or a quaternary system $A_XB_{1-X}CD$), compositional variation can lead to changes in various physical properties, *P*, that can be described by the empirical relationship [16, 39-44]

$$P(x) = xP_A + (1-x)P_B - bx(1-x) \qquad (4)$$

where *x* is the compositional parameter in the binary system AB with end members A and B and *b* is a constant that is sometimes referred to as the bowing parameter [16, 17, 40, 42, 43, 45, 46]. Alternatively, some researchers have expressed equation (4) in the form $A_0 + A_1x + A_2x^2$ where $A_0 = P_B$, $A_1 = (P_A - P_B - b)$, $A_2 = b$ [17,18]. The bowing parameter, b, is a measure of the departure of *P* versus composition from Vegard's linear relationship (when $b = 0$, equation (4) becomes Vegard's law). The properties, *P*, that change as a parabolic function of composition include lattice parameter [16, 17, 47, 48], bond length [16], band gap [16, 17, 47], elastic modulus [13-18, 48] and hardness [8, 49-51].

A number of researchers have interpreted the bowing parameter as a function of the lattice mismatch strain [16, 17, 40, 43-46]. In particular, for semiconductor alloys, Zunger and co-workers [46] proposed that the bowing parameter, *b*, could be modeled in terms of three physically distinct contributions; namely (i) a volume deformation term, b_{VD}, (ii) a charge exchange term b_{CE} and (iii) a structural relaxation term, b_{SR}. (The

b_{VD} term is envisioned as resulting from a hydrostatic deformation in which the lattice with the larger lattice parameter is compressed and the lattice with the smaller lattice parameter is expanded. The charge exchange refers to a redistribution of electron density in the deformed lattice and the structural relaxation is associated with subsequent changes in bond length and bond angle [40, 45, 46]). The total bowing parameter b is then given by $b = b_{VD} + b_{CE} + b_{SR}$ [40, 45, 46]. Other researchers also have adopted this physical interpretation of the bowing parameter [17, 43].

Many studies have demonstrated the compositional dependence of elastic moduli can be expressed as parabolic functions of composition [13, 14, 16, 17] (figures 4a and 4b), while other systems obey Vegard's law and yield a linear compositional dependence of elastic moduli [15, 17] (Figure 3.2.4c). In order to facilitate the intercomparison of the modulus versus composition data (Table 3.2.2 and Figure 3.2.4), the moduli in each data set were normalized with respect to the maximum modulus, (E_{max} or B_{max}), that occurred in the indicated composition range [13, 15-18].

In Figure 3.2.4 and in Table 3.2.2, the compositional dependence of bulk modulus as a function of x in the literature has often been computed using full potential linearized augmented plane wave (fp-lapw) calculations [16, 43, 44, 52]. Typically, after the cohesive energy is computed for the material as a function of cell volume, the Murnaghan equation of state [53] is used to calculate the bulk modulus as a function of cell volume (composition). Then, in the literature, an expression for bulk modulus as a function of composition is often obtained via a least-squares best fit of the calculated bulk modulus

versus composition to equation 4, where the bowing parameter is the adjustable parameter in the fitting procedure [16, 43, 44, 52].

Thus, in the literature there are many examples of the elastic modulus (Young's modulus, bulk modulus, or single crystal elastic constants) changing either linearly or quadratically as a function of the compositional parameter x.

3.3 *Extension of quadratic model to a paraboloid in four composition variables*

A parabolic function of a single compositional parameter x (equation (4)) is not adequate to describe our specimens (Table 3.2.1), since the four composition variables (Pb, Te, Sb, and Ag) were allowed to vary independently when our quaternary thermoelectric specimens were fabricated for this study. The subsystems within the quaternary LAST system include four possible ternary systems and possible six binary systems. However, as discussed by Quarez *et al.* [26], the LAST system has been viewed in terms of solid solutions in the systems PbTe and $AgSbTe_2$ with a family of compositions $AgPb_mSbTe_{m+2}$ being made up of $AgSbTe_2$ plus m(PbTe), although nanostructures observed in LAST are likely critical to its function as a thermoelectric material. Nevertheless, given the manner in which the four elements (Pb, Sb, Ag and Te) vary, the full range of LAST compositions included in this study (Table 3.2.1a) can not be represented in terms of linear combinations of the two potential end member compositions PbTe and $AgSbTe_2$. Also, there is no data in the literature on the elastic

properties of $AgSbTe_2$.

Therefore, since for this study it was not feasible to use PbTe and $AgSbTe_2$ as the end-member compositions, alternative functional forms needed to be found in order to attempt to construct four-component analogues to equation (4). We employed two differential functional forms (equations (5a) and (5b) below) as candidate functions to describe the composition-related changes in the Young's modulus of LAST.

As a first attempt, a paraboloid (a quadratic in each of the four composition variables) was employed, where the coefficient of the linear terms was the Young's modulus of the elemental components such that

$$E_{\text{pred}}(a,b,c,d) = p_0 + E_{\text{Ag}}a + p_{\text{Ag}}a^2 + E_{\text{Pb}}b + p_{\text{Pb}}b^2 + E_{\text{Sb}}c + p_{\text{Sb}}b^2 + E_{\text{Te}}d + p_{\text{Te}}d^2 \quad (5a)$$

In equation (5a), a, b, c and d are the mole fractions Ag, Pb, Sb and Te, respectively (Table 3.2.1a), where the compositions are normalized such that $a + b + c + d = 1$. (The normalization is a means of imposing a reasonable set of "boundary conditions" on these composition parameters, for example with this normalization PbTe would be represented by a = 0, b = 0.5, c = 0 and d = 0.5). The parameters p_{Ag}, p_{Pb}, p_{Sb} and p_{Te} are the bowing parameters for Ag, Pb, Sb and Te, respectively. The five adjustable parameters in equation (5a) (the four bowing parameters and the constant p_0) were determined by a nonlinear least-squares best-fit procedure.

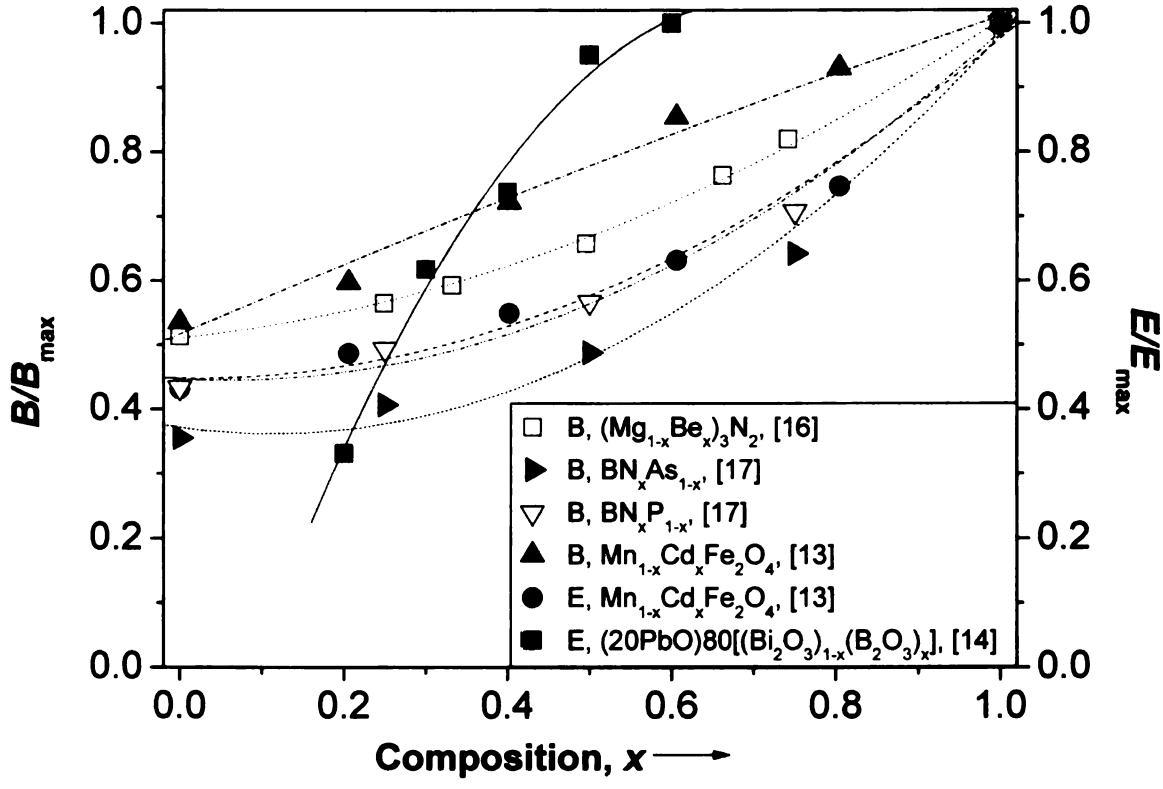

(a)

Figure 3.2.4. For ternary and quaternary compositions from the literature, Young's modulus (solid symbols) and bulk modulus (open symbols) that are (a) and (b) parabolic functions of composition (equation (4)) or a (c) linear functions of composition (equation (4) with b = 0). In (a), (b) and (c) the curves shown were obtained by the present authors via linear regression. The regression parameters are given in Table 3.2.2.

Figure 3.2.4 continued.

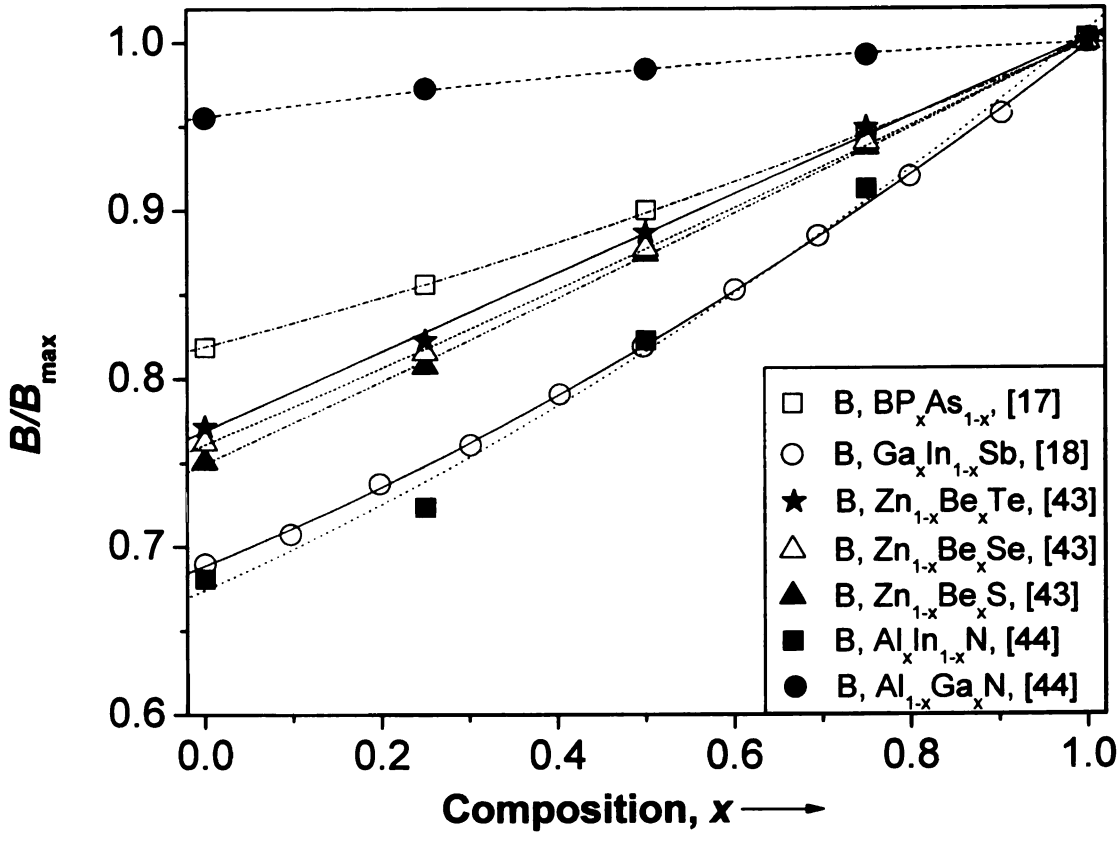

(b)

Figure 3.2.4 continued.

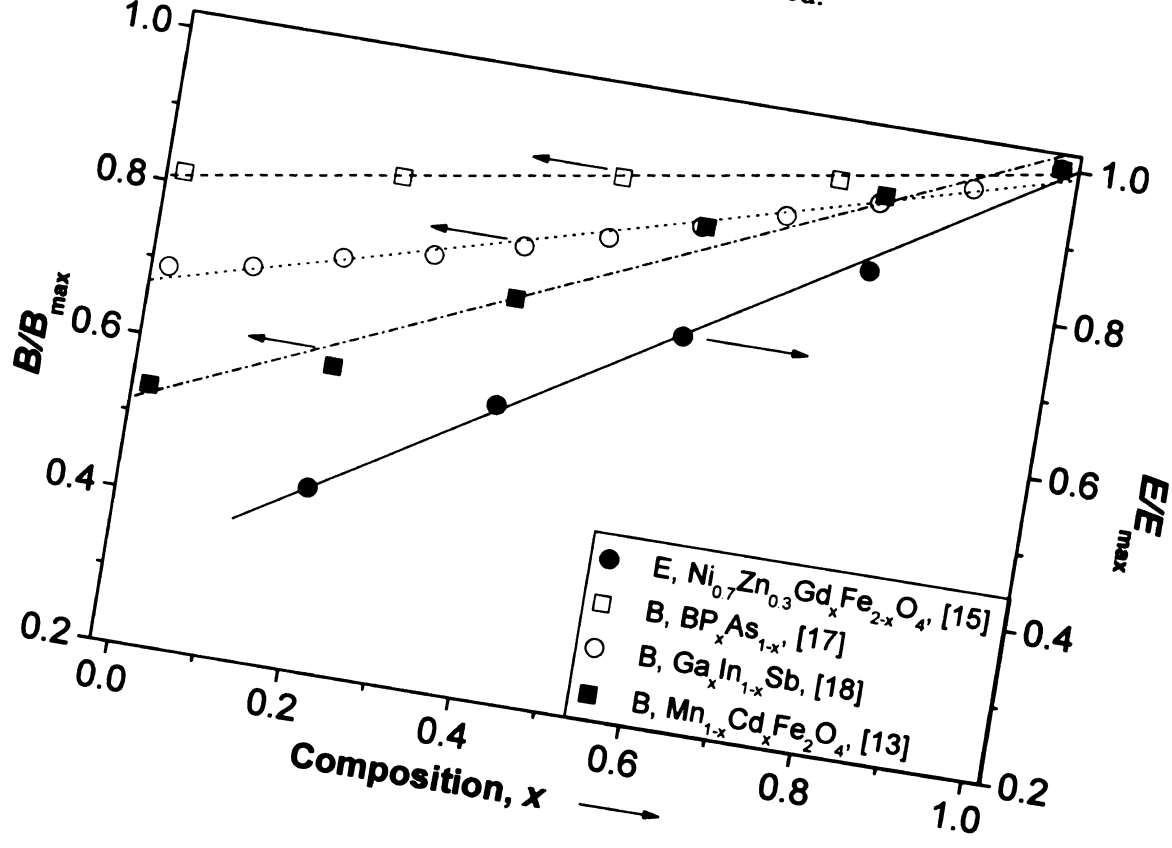

(c)

Table 3.2.2. Parabolic and linear compositional dependence of Young's modulus, E, and Bulk modulus, B, for various material systems in literature. Note that in each case, the literature data is in terms of a single compositional variable, x.

Parabolic dependence between moduli and composition

Material	$B(x = 0)$ (GPa)	$B\ (x = 1)$ (GPa)	b (GPa)	r^2	Data type	Ref.
$Mn_{1-x}Cd_xFe_2O_4$	77	144	-6.1[†]	0.99[†]	experiment	[13]
$(Mg_{1-x}Be_x)_3N_2$	217.8	111.0	80.2[‡]	0.99[†]	calculation	[16]
BN_xP_{1-x}	160	369	227[§]	0.99[†]	calculation	[17]
BN_xAs_{1-x}	131	369	289[§]	0.98[†]	calculation	[17]
BP_xAs_{1-x}	131	160	63[§]	0.99[†]	calculation	[17]
$Ga_xIn_{1-x}Sb$	38.9	56.4	5.0[‡]	0.99[†]	calculation	[18]
$Zn_{1-x}Be_xS$	69.4	92.4	0.86[§]	0.99[†]	calculation	[43]
$Zn_{1-x}Be_xSe$	56.8	74.6	1.18[§]	0.99[†]	calculation	[43]
$Zn_{1-x}Be_xTe$	43.3	56.2	-0.34[§]	0.99[†]	calculation	[43]
$Al_xGa_{1-x}N$	211.8	202	-5[‡]	0.99[†]	calculation	[44]
$Al_xIn_{1-x}N$	211.8	144	19.1[‡]	0.99[†]	calculation	[44]

Material	$E\ (x = 0)$ (GPa)	$E\ (x = 1)$ (GPa)	b (GPa)	r^2	Data type	Ref.
$Mn_{1-x}Cd_xFe_2O_4$	149	352	220.9[†]	0.98[†]	experiment	[13]
$(20PbO)\cdot80[(Bi_2O_3)_{1-x}\cdot(B_2O_3)_x]$	72.6 (x=0.6)	24.2 (x=0.2)	-205[†]	0.99[†]	experiment	[14]

Table 3.2.2 continued.

Linear dependence between moduli and composition $P(x) = A_0 + A_1 x$ ($P = E, B$)						
Material	A_0 (GPa)	A_1 (GPa)	Modulus	r^2	Data type	Ref.
$Mn_{1-x}Cd_xFe_2O_4$	74.9 ± 2.9	70.5 ± 4.3	*B*	0.99†	experiment	[13]
$Ni_{0.7}Zn_{0.3}Gd_xFe_{2-x}O_4$	12.3 ± 0.4	28.2 ± 0.8	*E*	0.99†	experiment	[15]
BP_xAs_{1-x}	129.6 ± 0.7	30.4 ± 1.7	*B*	0.99†	calculation	[17]
$Ga_xIn_{1-x}Sb$	37.8 ± 0.3	17.5 ± 0.6	*B*	0.99†	calculation	[18]

† From regression performed in this study

‡ Bowing parameters reported in references [16], [18] and [44] were obtained from a least-squares fit to quadratic function forms, but r^2 values were not reported.

§ In references [17] and [43], bowing parameters were given without specifying the function forms.

The Young's modulus values E_{Pb}, E_{Te}, E_{Sb} and E_{Ag} used in equation (5a) were the aggregate (polycrystalline) moduli calculated from single crystal elasticity data for the four elemental constituents (Pb, Te, Sb, and Ag respectively). Bounds for macroscopically isotropic elastic moduli of polycrystalline specimens composed of randomly oriented grains can be computed from single crystal elastic constants [54].

The Voigt and Reuss bounds apply to any crystalline symmetry [54] while the Hashin and Shtrikman bounds can be calculated only for cubic crystals [54-56]. An estimate of the effective Young's modulus for a randomly oriented polycrystalline body then can be obtained from the mean of the bounds, that is either Voigt-Reuss-Hill mean [57] or the mean of the Hashin and Shtrikman bounds [54 – 56]. For the cubic crystals lead and silver, the Young's moduli were calculated from the mean of the Hashin and Shtrikman bounds (E_{Pb} = 24.3 GPa [54, 58] and E_{Ag} = 81.7 GPa [54, 59]). For trigonal antimony, the polycrystalline aggregate value of E_{Sb} = 67.8 GPa was calculated from the mean of the Voigt and Reuss bounds [54, 60]. For trigonal Te, no Voigt bound or Reuss bound was available in the literature, so a polycrystalline aggregate value of E_{Te} = 40.5 GPa was calculated based on the Voigt and Reuss bounds [54, 57, 61, 62], where the bounds were computed from the elastic stiffness and elastic compliance data for single crystal Te [54, 62-64].

Excluding specimen N58 due to its macrocracks, the Young's modulus versus composition data obtained from microindentation (Table 3.2.1a) for the remaining 16 LAST specimens was fit via a least-squares technique to equation (5a). Since the

experimentally determined Young's modulus, E_{exper}, is a function of four compositional variables (Pb, Te, Sb, and Ag), one could attempt to use a five-dimensional space to plot E_{exper} directly as a function of composition. Within this plot, one could then construct a surface representing E_{pred}, the moduli as a function of composition as calculated by equation (5a).

To circumvent the difficulties of attempting to depict points and surfaces within a five-dimensional space, in this study we instead plot the experimentally determined Young's modulus, E_{exper}, versus the predicted modulus, E_{pred}, which yields a linear plot with a slope of 0.999, an intercept of 0.012 GPa and a coefficient of determination, r^2, of 0.73. (A perfect correspondence between E_{exper} and E_{pred} would result in a straight-line plot of slope 1 and intercept zero). For the fit to the 16 data points, the bowing parameters p_{Ag}, p_{Pb}, p_{Sb} and p_{Te} (for Ag, Pb, Sb and Te, respectively) and the constant p_0 were determined by the least-squares best-fit procedure, were p_0 = 2272 GPa, and p_{Ag} = -79167 GPa, p_{Pb} = -2506 GPa, p_{Sb} = -14172 GPa and p_{Te} = -6698 GPa. When we also excluded specimens N33 and N43 that were processed differently than the other 14 specimens (Figure 3.2.1), the regression of the 14 identically processed specimens yielded an r^2 = 0.79, with a slope of 0.9999 and an intercept of 0.0049 GPa (Figure 3.2.5a). The error bars in Figure 3.2.5a represent the standard deviation of the 20 microindentation measurements performed on each specimen. Although the value of r^2 increased slightly when the 14 identically processed specimens were considered, there is not sufficient data in this study to determine whether or not small difference in processing

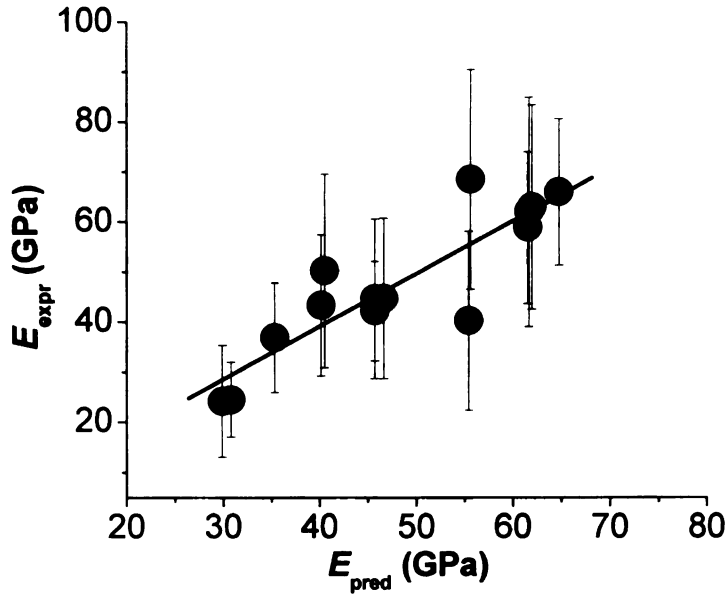

(a)

Figure 3.2.5 Experimentally determined Young's modulus (E_{expr}) *versus* Young's modulus predicted from equation (5) (E_{pred}) and regression line obtained from nonlinear least-squares fitting for (a) the 16 specimens (Table 3.2.1a) tested using microindentation (except N58) fit to equation (5a), (b) the 10 specimens measured by nanoindentation (Table 3.2.1b) fit to equation (5b), and (c) for the 16 specimens tested using microindentation (except N58) fit to equation (5b). In each figure, the error bars represent the standard deviation of the indentation data (20 measurements per specimen for microindentation; 16 measurements per specimen for nanoindentation).

Figure 3.2.5 continued.

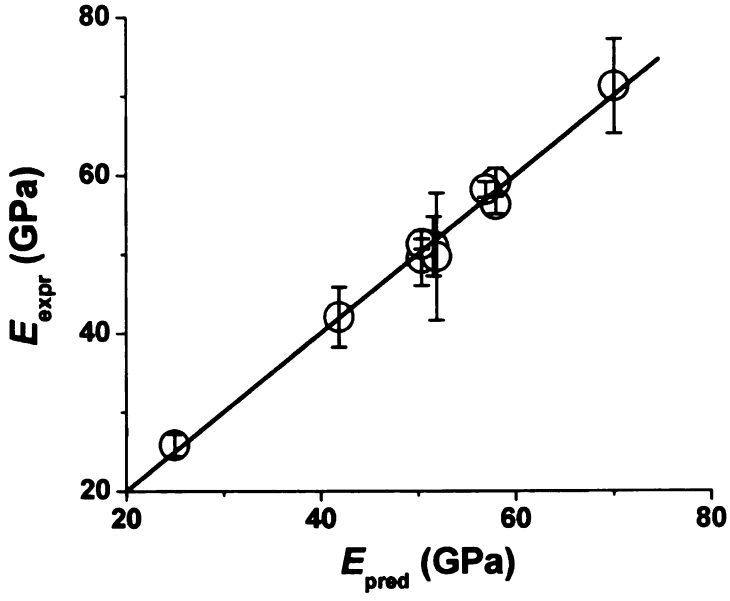

(b)

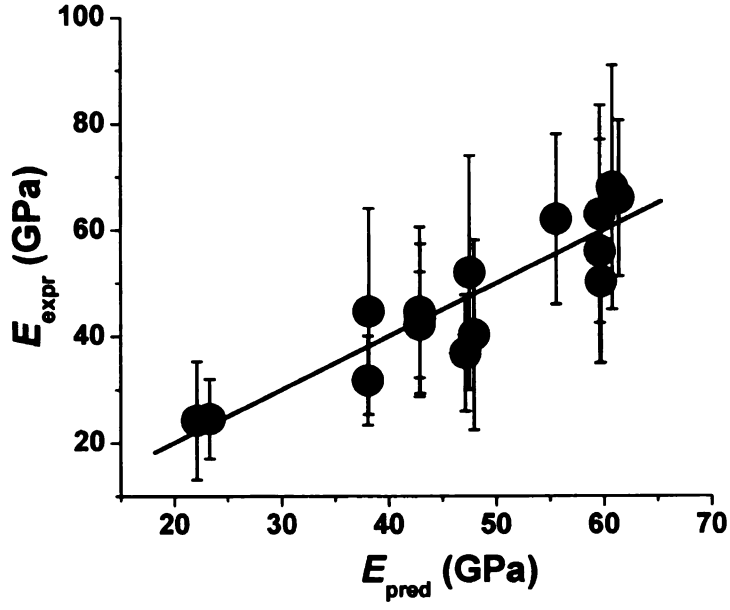

(c)

(as in subgroup C) results in significant differences in the Young's modulus-composition behavior.

Although the regression line of the E_{exper} versus E_{pred} data passes through all of the error bars and the slope and intercept of the regression line (solid line in Figure 3.2.5a), the least-squares fit of equation (5a) to the microindentation data yields an r^2 of less than 0.8 which is perhaps in part due to the sizeable variance in the microindentation data (Figure 3.2.2 and Appendix A). In addition, Table 3.2.2 shows that the value of the bowing parameter, b, found in the literature can be either positive or negative for a given material, however the magnitude of the literature values of b (Table 3.2.2) is as large as 289 GPa for the bulk modulus (BN_xAs_{1-x} [17]) and 220.9 GPa for Young's modulus ($Mn_{1-x}Cd_xFe_2O_4$ [13]). Thus, the bowing parameters obtained from the least-squares fit of the microindentation data to equation (5a) is from one to two orders of magnitude larger than those found in the literature.

As an alternative to equation (5a), equation (5b) was applied to the 10 nanoindentations data (Table 3.2.1b). During the non-linear regression, it was found that for this set of compositions, the norm of the residuals was insensitive to the presence or absence of c^2 and d^2 terms, as well as the constant p_0 so that an excellent fit to the nanoindentation data was obtained from

$$E_{pred}(a,b,c,d) = p_1 a + p_{Ag} a^2 + p_3 b + p_{Pb} b^2 + p_5 c + p_6 d \qquad (5b)$$

As was discussed in Section 3.2, the literature shows that Young's modulus versus composition (Table 3.2.2 and Figure 3.2.4) can be described either by a quadratic

function or a linear function of the single compositional variable, x. This is consistent with equation (5b) in that for the range of quaternary LAST compounds included in this study, since the least-squares analysis shows that a quadratic function in the silver and lead composition and linear in the antimony and tellurium composition (equation (5b) fits the Young's modulus versus composition data well.

Fitting the nanoindentation Young's modulus to equation (5b) yields an r^2 of 0.99, while the slope and intercept for the non-linear least-squares fit of E_{exper} and E_{pred} are 1.000 and 0.01 GPa, respectively. The corresponding fitting parameters are p_1 = 5513 GPa, p_{Ag} = -109204 GPa, p_3 = 5141 GPa, p_{Pb} = -4716 GPa, p_5 = 1232 GPa, and p_6 = -2751 GPa (Figure 3.2.5b). The least-squares fit of equation (5b) to the 16 microindentation-determined Young's modulus values (except for N58) resulted a slope of 1.000, an intercept of 0.015 GPa, and an r^2 of 0.83 (Figure 3.2.5c). As in Figure 3.2.5a, the error bars in figures 5b and 5c represent the standard deviation of the measured Young's moduli (16 nanoindentation measurements per specimen and 20 microindentation measurements per specimen). The much higher coefficient of determination for the nanoindentation data (Figure 3.2.5b) than that observed for the microindentation data (Figure 3.2.5c) is likely a function of the much lower scatter in the nanoindentation data compared to the microindentation data (Figure 3.2.2). The fit of the nanoindentation and microindentation data to equation (5b) does indicate that the Young's modulus-composition behavior for the quaternary system LAST can be described by a paraboloid function of the mole fractions of the four components.

In addition to fitting the modulus-composition data to functional forms such as equations (5a) or (5b), it is important to consider the range of compositions included in the study. To augment the list of compositions given in Table 3.2.1 for the microindentation (Table 3.2.1a) and the nanoindentation (Table 3.2.1b) data, two pseudo-ternary plots were constructed (Figure 3.2.6) as a visual aid in understanding the distribution of the quaternary compositions included in this study. In order to represent the aspects of the quaternary LAST system within a ternary diagram, the LAST compositions (Table 3.2.1) were normalized such that the mole fraction of Te was one for Figure 3.2.6a and the mole fraction of Pb was one in Figure 3.2.6b. In Figure 3.2.6a, the LAST compositions projected onto the Ag-Sb-Pb plane while in Figure 3.2.6b the LAST compositions projected onto the Ag-Sb-Te plane. In figures 6a and 6b, Te and Pb were selected as the elements over which to perform the normalization since Te and Pb are the majority elements in each composition included in this study (Table 3.2.1). As figures 6a and 6b illustrate, the compositions included in this study are reasonably uniformly distributed over the portion of the quaternary composition space included in this study.

In Figure 3.2.6, the magnitude of Young's modulus is indicated by a grey scale with the darker symbols corresponding to a higher Young's modulus. While E_{pred} is not indicated in Figure 3.2.6, a trend in Young's modulus versus composition is discernable in Figure 3.2.6. In both figures 6a and 6b, the locus of the higher Young's modulus values (darker plotting symbols) delineates the "ridge" oriented diagonally through both

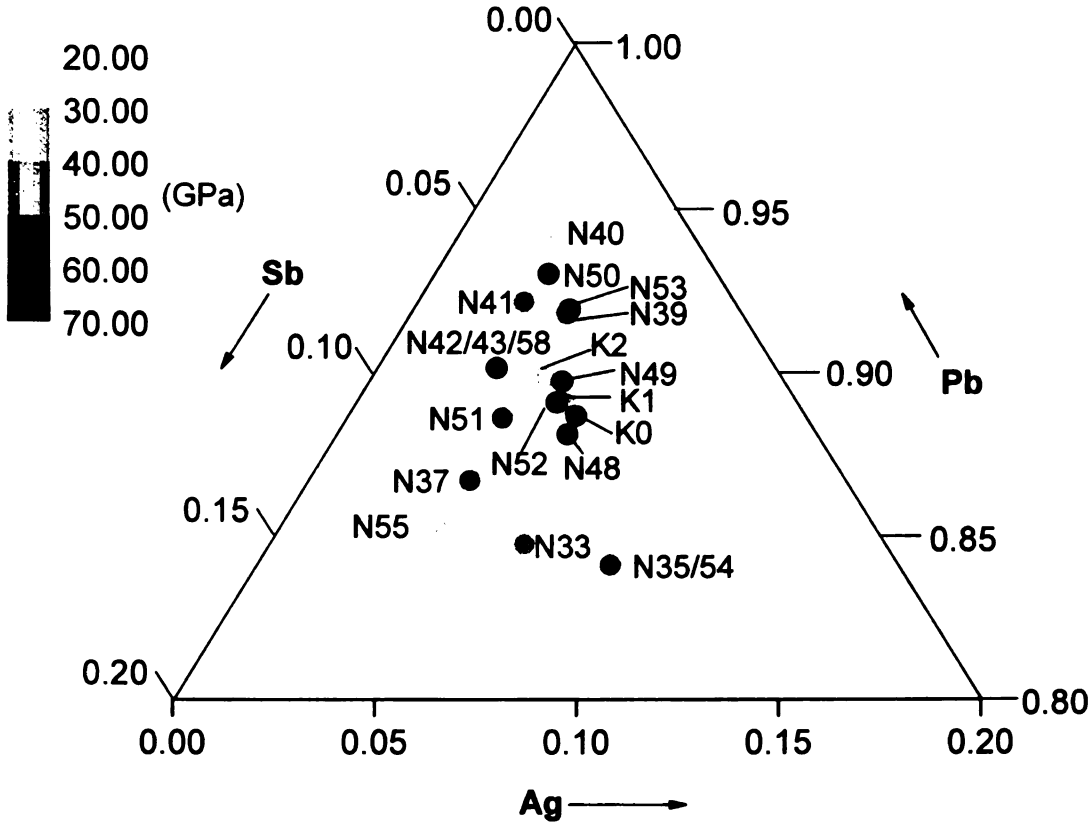

(a)

Figure 3.2.6. Pseudo-ternary diagrams depicting the compositions (a) the Ag-Sb-Pb plane, and (b) the Ag-Sb-Te plane for the 17 LAST cast ingot specimens included in this study along with three hot pressed LAST specimens studied by Kosuga *et al.* [5]. K_0, K_1, and K_2 indicate hot pressed specimens with compositions of $AgSbPb_{18}Te_{20}$, $Ag_{0.9}SbPb_{18}Te_{20}$, and $Ag_{0.7}SbPb_{18}Te_{20}$, respectively from Kosuga's study [5]. The grey scale for the plotting symbols corresponds to the Young's modulus values with the darker symbols indicating higher Young's modulus. Note that Kosuga's data [5] is clustered near the center of both diagrams.

Figure 3.2.6 continued.

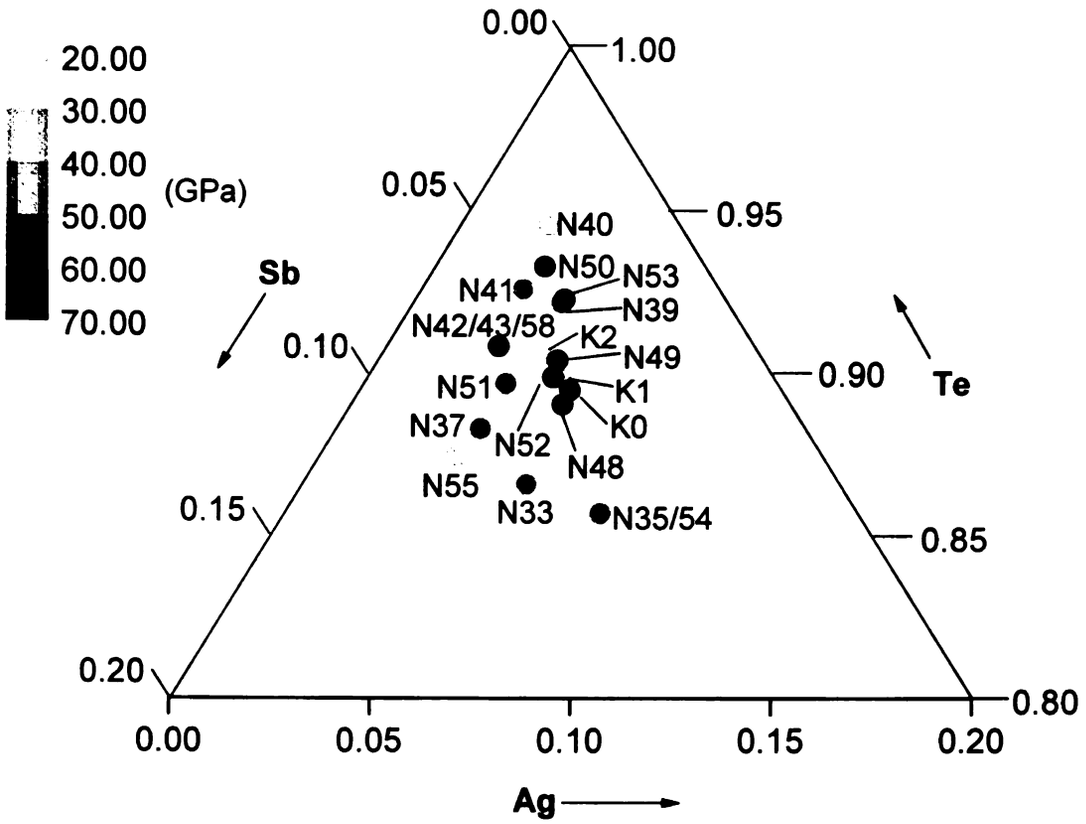

(b)

diagrams.

3.4 *A comparison of this study's modulus versus composition results with the literature*

The values for the elastic modulus of pure PbTe (58.05 GPa) [54, 65] and the limited elasticity data for LAST that is available in the literature from Kosuga *et al.* [5] (Table 3.2.3) fall within the range of composition-dependent Young's modulus values (24 GPa to 68 GPa) measured for the LAST specimens included in this study. However, the LAST specimens studied by Kosuga *et al.* [5] exhibit a different compositional dependence of Young's modulus than was observed in this study (Figure 3.2.6).

Ingots N48, N49, and N52 in this study possessed compositions similar to Kosuga's specimens (tables 1 and 3, Figure 3.2.6). While the Young's moduli are comparable among N48, N49, and N52 (Table 3.2.1, Figure 3.2.6), the Young's moduli among Kosuga's three specimens differ by up to a factor of two (Table 3.2.3).

Although both this study and Kosuga's [5] examined compositions in the LAST family of compounds, the specimen preparation and modulus measurement methods differed. Each of the 17 specimens included in this study was prepared by casting while each of the three specimens in Kosuga's study was hot pressed [5]. Furthermore, in this study the Young's modulus measurements were performed by microindentation and nanoindentation while Kosuga *et al.* used ultrasonic pulse-echo technique to measure moduli [5]. It is difficult to attribute the magnitude of the differences in the measured moduli between this study and Kosuga's study [5] to the difference in the measurement

techniques, especially since Kosuga *et al.* reported a modulus 54.2 GPa for their $AgSbPb_{18}Te_{20}$ specimen, which is roughly comparable to the average of the moduli (62.3 GPa) for our N48, N49 and N52 specimens of comparable composition. However, Young's modulus may be affected by defects, such as the macrocracks induced by external loading as discussed for specimen N58 in section 3.1 (Figure 3.2.2c). If Kosuga *et al's* processing introduced defects into some of their specimens, that could explain the drop in the moduli measured by Kosuga from 54.2 GPa to 29.2 and 27.6 GPa over a relatively small change in composition (Table 3.2.3). In pseudo-ternary diagrams given in Figure 3.2.6, the three Kosuga compositions (denoted as K_0, K_1 and K_2) are clustered in the center of each diagram, emphasizing that the range of LAST compositions included in the Kosuga specimens is small compared to the compositional range for the 17 LAST specimens included in this study.

Another mode of comparison between this study and the literature is to consider the range of modulus values measured as a function of the changing composition. The ratio of the maximum to minimum Young's modulus, $E_{max}/E_{min.}$ was approximately 2.83 for the 17 LAST compositions included in this study. Similar ranges of moduli variation with composition have been observed in several solid solution systems [13-18]. For example, E_{max}/E_{min} is approximately 3 as the compositional variable x ranges from 0.2 to 0.6 in $(20PbO)\cdot 80(Bi_2O_3)_{1-x}(B_2O_3)_x$ system [14] (figures 4a and 4b, Table 3.2.4). In addition, E_{max}/E_{min} ratios in $Mn_{1-x}Cd_xFe_2O_4$ [13] and $Ni_{0.7}Zn_{0.3}Gd_xFe_{2-x}O_4$ [15] are ~ 2.4 and 2.3, respectively, for $0 < x < 1$ (Figure 3.2.4, Table 3.2.4).

Table 3.2.3. Room temperature Young's modulus, E, for PbTe and for LAST compositions. The three LAST compositions from Kosuga [5] are compared to three similar compositions from this study.

Ref.	Chemical formula	Normalized composition				*E* (GPa)	Specimen Type	Technique
		Ag	Pb	Sb	Te			
[10,11]	PbTe	0	0.5	0	0.5	58.05	single crystal	ultrasound pulse-echo
[5]	$AgSbPb_{18}Te_{20}$	0.025	0.450	0.025	0.500	54.2	polycrystal	ultrasound pulse-echo
[5]	$Ag_{0.9}SbPb_{18}Te_{20}$	0.023	0.451	0.025	0.501	29.2	polycrystal	ultrasound pulse-echo
[5]	$Ag_{0.7}SbPb_{18}Te_{20}$	0.018	0.453	0.025	0.504	27.6	polycrystal	ultrasound pulse-echo
	This study							
N48	$Ag_{0.8}Pb_{14}Sb_{0.87}Te_{15.7}$	0.025	0.446	0.028	0.501	65.9	cast ingot	micro-indentation
N49	$Ag_{0.8}Pb_{18}Sb_{0.93}Te_{19.9}$	0.020	0.455	0.024	0.502	58.9	cast ingot	micro-indentation
N52	$Ag_{0.9}Pb_{19}Sb_{1.1}Te_{21.2}$	0.021	0.450	0.026	0.502	62.0	cast ingot	micro-indentation

Table 3.2.4. Ratio of maximum to minimum Young's modulus (E_{max}/E_{min}) or bulk modulus (B_{max}/B_{min}) for a number of solid solution systems from the literature.

Material System	Compositional variable range	E_{max}/E_{min} or B_{max}/B_{min}	Reference
$Mn_{1-x}Cd_xFe_2O_4$	$0 < x < 1$	~ 2.4 (E_{max}/E_{min})	[13]
$Mn_{1-x}Cd_xFe_2O_4$	$0 < x < 1$	~ 1.9 (B_{max}/B_{min})	[13]
$(20PbO)\cdot 80[(Bi_2O_3)_{1-x}(B_2O_3)_x]$	$0.2 < x < 0.6$	~ 3 (E_{max}/E_{min})	[14]
$Ni_{0.7}Zn_{0.3}Gd_xFe_{2-x}O_4$	$0.2 < x < 1$	~ 2.3 (E_{max}/E_{min})	[15]
$(Mg_{1-x}Be_x)_3N_2$	$0 < x < 1$	~ 2 (B_{max}/B_{min})	[16]
BN_xAs_{1-x}	$0 < x < 1$	~ 2.8 (B_{max}/B_{min})	[17]
BP_xAs_{1-x}	$0 < x < 1$	~ 1.2 (B_{max}/B_{min})	[17]
BN_xP_{1-x}	$0 < x < 1$	~ 2.3 (B_{max}/B_{min})	[17]
$Ga_xIn_{1-x}Sb$	$0 < x < 1$	~ 1.4 (B_{max}/B_{min})	[18]
$Zn_{1-x}Be_xS$	$0 < x < 1$	~ 1.3 (B_{max}/B_{min})	[43]
$Zn_{1-x}Be_xSe$	$0 < x < 1$	~ 1.3 (B_{max}/B_{min})	[43]
$Zn_{1-x}Be_xTe$	$0 < x < 1$	~ 1.3 (B_{max}/B_{min})	[44]
$Al_{1-x}Ga_xN$	$0 < x < 1$	~ 1.05 (B_{max}/B_{min})	[44]
$Al_{1-x}In_xN$	$0 < x < 1$	~ 1.5 (B_{max}/B_{min})	[44]

Bulk modulus also varies with composition [16-18]. The maximum to minimum bulk modulus ratios, B_{max}/B_{min}, are approximately 2.8 for BN_xAs_{1-x} [17], ~ 2 for $(Mg_{1-x}Be_x)_3N_2$ [16], ~ 1.4 for $Ga_xIn_{1-x}Sb$ [18], and ~ 1.2 for BP_xAs_{1-x} [17], for $0 \leq x \leq 1$ (Figure 3.2.4, Table 3.2.4). Thus, the ranges of E_{max}/E_{min} and B_{max}/B_{min} recorded in the literature are comparable to the E_{max}/E_{min} value measured in this study, indicating that the magnitude of composition-driven changes in elasticity observed for LAST specimens in the current study are broadly similar to that measured for other material systems.

3.5 *Microcracking as an additional source of variation in the elastic modulus*

In addition to composition-related changes, the elastic modulus can change as a function of the defect state and microstructure of the material.

For example, thermoelectric materials cast from the melt can have quite large grain sizes [7, 66-69]. For example, the grain size of the cast LAST specimens in this study was approximately 480 to 720 microns as determined by the linear intercept method. In contrast, the grain size of hot pressed TE specimens may be much smaller than the grain size for the ingot specimens included in this study, however Kosuga *et al.* does not give grain size or other microstructural information about their hot pressed specimens [5].

Although the elastic moduli of polycrystalline materials are independent of grain size [9, 70], Young's modulus can be affected by grain-size-dependent microcracking [9, 22-25, 70]. For non-cubic materials, grain sizes larger than a critical grain size can lead to

microcracking [22-25] that in turn lowers the elastic modulus [9, 22].

4. Summary and Conclusions

For the quaternary thermoelectric material LAST, the Young's modulus as a function of composition was measured via microindentation for 17 specimens (representing 14 different compositions) that were cut from cast ingots. A nanoindentation study provided independent determinations of the moduli for 10 of the 17 specimens. A statistical analysis of the mean and standard deviations for the microindentation and nanoindentation techniques is included in Appendix A. For both the microindentation and nanoindentation, the Young's modulus of LAST was found to be a function of composition, with the Young's modulus changing by a factor of up to 2.8 for the range of compositions included in this study.

In the literature, the characterization of compositional dependence of elastic modulus for solid solution systems has been limited to linear or quadratic functions of the single compositional variable x for pseudo binary compounds A_xB_{1-x} within a ternary system $A_xB_{1-x}C$ or a quaternary system $A_xB_{1-x}CD$ (Figure 3.2.4, Table 3.2.2). Using a paraboloid function in the four compositional variables (equations (5a and 5b)) rather than the quadratic form in a single compositional variable (equation (4)), we were able to characterize the compositional dependence of the Young's modulus change (Figure 3.2.5) for the quaternary compound LAST, in which each of the four compositional variables vary independently (Figure 3.2.6).

In addition to examining the functional form of the Young's modulus-composition relationship, we also compared the ratio of the maximum (E_{max}) and minimum (E_{min}) Young's moduli observed as a function of composition with similar data for pseudo-binary systems in the literature. In this study, E_{max} = 68 GPa and E_{min} = 24 GPa, giving an E_{max}/E_{min} of about 2.83 while in the literature E_{max}/E_{min} (and B_{max}/B_{min} for the bulk modulus) ranged from roughly 1.2 to 3 for the 14 pseudo-binary systems presented in Figure 3.2.4 and Table 3.2.4. Thus, the magnitude of the changes in Young's modulus (induced by composition changes) observed in this study is generally consistent with the magnitudes of Young's and bulk modulus changes reported for other material systems as a function of composition.

For the paraboloid functions of Young's modulus versus composition for LAST (equations (5a and 5b)), the magnitudes of the four bowing constants, p_{Ag}, p_{Pb}, p_{Sb} and p_{Te} are much larger than are the magnitudes of the bowing parameters for bulk or Young's moduli for pseudo-binary systems from the literature that are a function of a single compositional variable [13, 16 - 18, 43, 44, Table 3.2.2, Figure 3.2.4]. This may be in part due to the difficulty in selecting the appropriate end members to construct a four-component analogue of equation (4), however, the non-linear least-squares fit of the nanoindentation data to equation (5b) (with a coefficient of determination, r^2, of 0.99, Figure 3.2.5b) does show that a paraboloid function of the composition can describe the Young's modulus-composition behavior of the quaternary compound LAST.

The compositional dependence of Young's modulus of the LAST specimens has

important implications for the thermoelectric applications of the family of LAST compounds. Changes in the elastic modulus can be used as a diagnostic tool to assess the level of microcrack damage in a component since elastic modulus is a sensitive function of the microcrack damage state [9, 22-25]. If one compares LAST specimens of differing composition, the elastic moduli would be a function of both the composition and of possible defect states (such as microcracks or pores) as well as possible microstructural differences, thus it is important to attempt to distinguish between modulus changes induced by compositional changes and those modulus changes induced by defects. Furthermore, since the elastic response to a thermally or mechanically imposed strain is a function of the Young's modulus, the mechanical response of the LAST leg elements in a thermoelectric module could differ substantially according to the particular composition of the legs.

Appendix A. Statistical inferences concerning the data

In this study, two experimental techniques were used to determine the Young's modulus, namely microindentation and nanoindentation. For a given specimen, it was of interest to determine whether or not the two test techniques gave the same result, thus the t-test was used to test for an equivalence of the means of the microindentation and the nanoindentation measurements. In addition, the F-test was used to compare the variances of the microindentation and nanoindentation data for a given specimen. Also, the t-test and F-test were used to examine the equivalence of the means and variances among

replicates (specimens with identical compositions and/or processing history).

A. 1 *Test for normality of the data*

Since both t-test and F-test assume that the data is normally distributed, a test for normality of the data was performed on the indentation data [71], including the nanoindentation determined Young's modulus (nano-*E*) (Figure 3.2.A1a), microindentation determined hardness (micro-*H*) and hardness to modulus ratio (micro-*H/E*) (Figure 3.2.A1b).

Recall that the Young's modulus was determined via the model of Marshall *et al.* [7] in which *H/E* is determined from the elastic recovery of Knoop indentations (equation (2)). The reciprocal of the *H/E* value, multiplied by the value of H determined by Vickers indentation (equation (3)), yields the microindentation value of E via the protocol developed by Marshall *et al.* [7].

Plots of *E*, *H* and *H/E* versus the normal order statistic medians yielded coefficients of determination, r^2, which ranged between 0.86 and 0.98, although in the majority of instances, $r^2 \geq 0.95$ (Table 3.2.A1). This indicates that the nano-*E* data, micro-*H* data, and micro-*H/E* data in this study were approximately normally distributed. Since both micro-*H* and micro-*H/E* are normally distributed, we assume the microindentation Young's modulus (micro-*E*), which was calculated from micro-*H* and micro-*H/E* [7], also obeys normal distribution. Hence, the requirement is satisfied that the data for the t-test and F-test be approximately normally distributed.

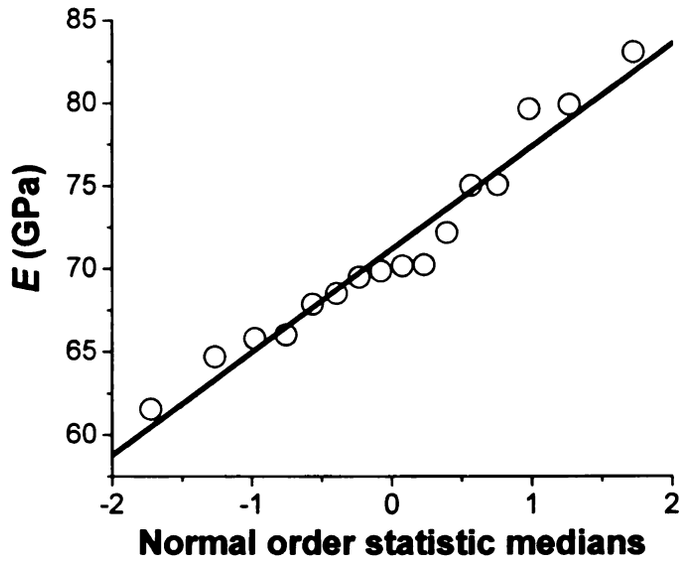

(a)

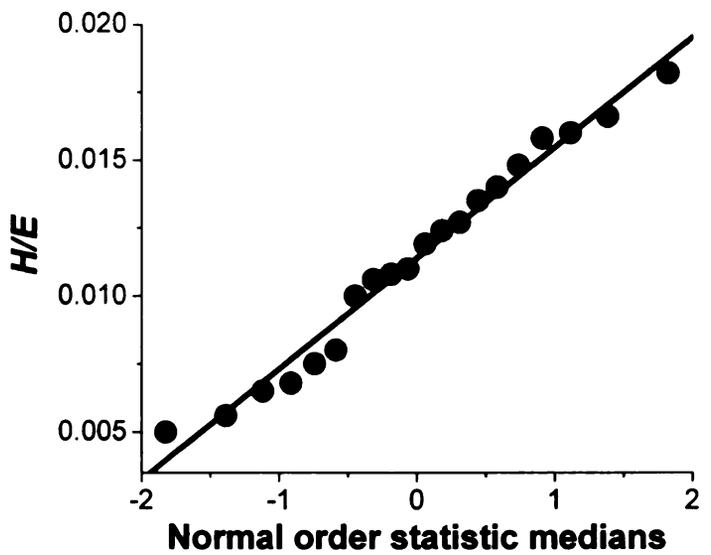

(b)

Figure 3.2.A1. Normal probability plots of (a) Young's modulus, E, obtained via nanoindentation for specimen N53, and (b) hardness to modulus ratio, H/E, obtained via microindentation for specimen N50. Linear regression yields coefficients of determination, r^2, of 0.94 for (a) and 0.98 for (b), indicating that the indentation data are approximately normally distributed which in turn implies that it is acceptable to use the t-test and F-test on these data sets.

A. 2 *Test for equivalence of sample means*

The standard t-test is appropriate to be applied to test for equivalence of sample means in cases for which (i) there is a small sample size, (ii) the data follows a normal distribution at least approximately and (iii) the sample variances are similar [72, 73]. In this study, the sample variances are very different between the nanoindentation and microindentation data (Figure 3.2.2), but a modified t-test may be used for the case of unequal variances, where the degrees of freedom is determined both by the number of specimens in the sample set and the relative size of the sample variances [72].

For a given specimen in subgroup A (Section 3.1 and Figure 3.2.2a), the t-test indicates that there is no statistically significant difference (at the 95% significance level) between the means determined by nanoindentation and by microindentation. Also, for subgroup B (Figure 3.2.2b) which includes two replicates (in both composition and processing history), the t-test shows there no statistically significant difference between the means of an individual specimen measured by nanoindentation and microindentation. Furthermore, the t-test indicates no statistically significant differences between the means of microindentation and nanoindentation between the two specimens. Thus, for subgroups A and B, there are no statistically significant differences between data measured by nanoindentation and by microindentation on a given specimen. In addition, the Young's modulus values for the two replicates in subgroup B show no statistically significant difference. For subgroup A, where the composition does change, there is a large difference in the measured Young's modulus across the range of specimen compositions.

For the replicates in subgroup B, where there is no difference in either composition or processing history, there is (as expected) no statistically significant difference among the values of Young's modulus measured by either microindentation or nanoindentation (specimens N35 and N53).

For subgroup C, which includes three composition replicates (N42, N43 and N58) for which the processing differed slightly (Figure 3.2.1 and Section 3.1), the results of the t-test is somewhat more complicated. A one-way ANOVA test at the 95% significance level showed that there is a statistically significant difference between the means of the three specimens measured by nanoindentation although the means of the moduli were not dramatically different (for specimens N42, N43 and N58, the mean values of the moduli were 59.1 ± 1.8 GPa, 56.3 ± 1.2 GPa and 58.2 ± 1.0 GPa, respectively). The reason the lack of statistically equivalence among the means is likely due to the very small standard deviation values for the nanoindentation data. Also, it should be noted that a t-test at the 95% significance level shows that there is no statistically significant difference between specimen N42 and N58, where N58 was the specimen that contained a set of macrocracks (Figure 3.2.3) and (for microindentation measurements) had a Young's modulus that was only about half of the moduli measured for N42 and N43. Differences among the specimens in group C may be due to the slight differences in processing (Figure 3.2.1), but there is not enough data for specimens with differing processing techniques (and hence possibly differing microstructures) to draw a conclusion on the importance of small changes in the processing.

Table 3.2.A1. The coefficient of determination, r^2, for the linear least-square fit of the Nano-*E*, Micro-*H*, and Micro-*H/E* data in the normal probability plots (Figure 3.2.A1).

	r^2		
	Nano-*E*	Micro-*H*	Micro-*H/E*
N35	0.97	0.98	0.98
N41	0.90	0.89	0.97
N42	0.95	0.97	0.91
N43	0.92	0.97	0.97
N50	0.94	0.96	0.98
N51	0.91	0.97	0.86
N53	0.94	0.92	0.88
N54	0.89	0.97	0.91
N55	0.97	0.95	0.97
N58	0.96	0.98	0.95

A. 3 *Test for equivalence of sample variances*

For each of the 10 specimens tested by both microindentation and nanoindentation (which includes subgroups A, B and C), the variance (square of the standard deviation) of Young's moduli obtained by microindentation (micro-E_{std}) is statistically larger than those obtained by nanoindentation (nano-E_{std}). This confirms the intuitive conclusion, that upon comparing the error bars for the microindentation and nanoindentation measurements in Figure 3.2.2, the scatter in the microindentation data far exceeds that of the nanoindentation data. However, the F-test shows no statistically significant differences among the variances determined for the set of 10 nanoindentation measurements for groups A, B and C and likewise there were no statistically significant differences among the microindentation data for the same set of specimens.

Acknowledgements

The authors acknowledge the financial assistance of the U. S. Department of Energy Grant DE-FC26-04NT42281 and Office of Naval Research MURI Grant number N000140310789. The authors also thank the Advanced Microscopy Center at Michigan State University for the use of the SEM facility, and Ms. Mingfei Li (Center for Statistical Training and Consulting, MSU) for her assistance in statistical analysis. The authors also acknowledge helpful conversations with Professors S. D. Mahanti and D. T. Morelli of Michigan State University and Professor M. G. Kanatzidis of Northwestern University.

References

[1] K.F. Hsu, S. Loo, F. Guo, *et al.*, Science **303** 818 (2004).

[2] E. Quarez, K. F. Hsu, R. Pcionek, *et al.*, J. Am. Chem. Soc. **127** 9177 (2005).

[3] T. C. Harman, P. J. Taylor, M. P. Walsh, *et al.*, Science **297** 2229 (2002).

[4] R. Venkatasubramanian, E. Siivola, T. Colpitts, *et al.*, Nature **413** 597 (2001).

[5] A. Kosuga, M. Uno, K. Kurosaki, *et al.*, J. Alloy. Compd. **387** 52 (2005).

[6] H. Wang, J. F. Li, C. W. Nan, *et al.*, App. Phys. Lett. **88** article No. 092104 (2006).

[7] F. Ren, E. D. Case, E. J. Timm, *et al.*, Phil. Mag. Lett. **86** 673 (2006).

[8] F. Ren, E. D. Case, E. J. Timm, *et al.*, J. Alloy. Compd. in press, doi:10.1016/j.jallcom.2007.01.086 (2007).

[9] E. D. Case, *Thermo-Mechanical Fatigue and Fracture* (WIT Press, Southampton, UK, 2002), pp. 137 – 208.

[10]N. E. Dowling, *Mechanical Behavior of Materials, Second Edition* (Prentice Hall, Upper Saddle River, New Jersey, 1999), pp 185 – 188.

[11]H. C. Martin and G. F. Carey, *Introduction to Finite Element Analysis* (McGraw-Hill, New York, 1973), Chapter 9.

[12]V. N. Kaliakin, *Introduction to Approximate Solution Techniques, Numerical Modeling, and Finite Element Methods* (Marcel Dekker, Inc., New York, 2002), Chapter 12.

[13]D. Ravinder and T. Alivelumanga, Mater. Lett. **49** 1 (2001).

[14]T. Watanabe, K. Muratsubaki, Y. Benino, *et al.*, J. Mater. Sci. **36** 2427 (2001).

[15]S. S. Rao and D. Ravinder, Mater. Lett. **57** 3802 (2003).

[16]A. Mokhtari and H. Akbarzadeh, J. Phys.: Condens. Matter **16** 6063 (2004).

[17]F. El Haj Hassan and H. Akbarzadeh, Mater. Sci. Eng. B **121** 170 (2005).

[18]N. Bouarissa, Mater. Sci. Eng. B **100** 280 (2003).

[19]D. B. Marshall, T. Noma, and A. G. Evans, Am. Ceram. Soc. Bull. **65** C175 (1982).

[20]J. B. Wachtman, *Mechanical Properties of Ceramics* (Wiley and Sons, New York, 1996).

[21]W. C. Oliver and G. M. Pharr, J. Mater. Res. **7** 1564 (1992).

[22] E. D. Case, J. R. Smyth, and O. Hunter, J. Mater. Sci. **15** 1491 (1980).

[23]J. J. Cleveland, and R. C. Bradt, J. Amer. Ceram. Soc. **61** 478 (1978).

[24]T. P. Hoepfner and E. D. Case, Mater. Lett. **58** 489 (2004).

[25]K. Matsushida, S. Kuratani, T. Okamoto, *et al.*, J. Mater. Sci. Lett., **3** 345 (1984).

[26]A. Sinha, K. Kokini, and K. J. Bowman, Mater. Sci. Eng. A **188** 317 (1994).

[27]P. L. Larsson, A. E. Giannakopoulos, E. Soderlund, *et al.*, Int. J. Solids. Struct. **33** 221 (1995).

[28]A. E. Giannakopoulos, P. L. Larsson, and R. Vestergaard, Int. J. Solids. Struct. **31** 2679 (1994).

[29]S. S. Chiang, D. B. Marshall, and A. G. Evans, J. Appl. Phys. **53** 298 (1982).

[30]R. Saha and W. D. Nix, Acta. Mater. **50** 23 (2002).

[31]T. Chudoba, M. Griepentrog, A. Duck, *et al.*, J. Mater. Res. **19** 301 (2004).

[32]L. Chouanine, M. Takano, O. Kamiya, *et al.*, Compos. Sci. Technol. **65** 1414 (2005).

[33]Y. J. Liu, A. Rosidian, and R. O. Claus, J. Clust. Sci. **10** 421 (1999).

[34]X. F. Li, Surf. Coat. Technol. **200** 5003 (2006).

[35]B. Guelorget, M. Francois, and H. Lu, Mater. Lett. **61** 34 (2007).

[36]K. Lambrinou, T. Lauwagie, F. Chalvet, *et al.*, J. Eur. Ceram. Soc. **27** 1307 (2007).

[37]E. Maeva, I. Severina, S. Bondarenko, *et al.*, Can. J. Phys. **82** 981 (2004).

[38]M. Radovic, E. Lara-Curzio, and L. Riester, Mater. Sci. Eng. A **368** 56 (2004).

[39]L. Bellaiche, S. H. Wei, and A. Zunger, Phys. Rev B **54** 17568 (1999).

[40]J. E. Bernard and A. Zunger, Phys. Rev. B **34** 5992 (1986).

[41]I. Vurgaftman and J. R. Meyer, J. Appl. Phys. **94** 3675 (2003).

[42]M. Reason, X. Weng, W. Ye, *et al.*, J. Appl. Phys. **97** 103523 (2005).

[43]H. Baaziz, Z. Charifi, F. E. Hassan, *et al.*, J. Magn. Magn. Mater. **302** 536 (2006).

[44]M. B. Kanoun, S. Goumri-Said, A. E. Merad, *et al.*, J. Appl. Phys. **98** Article number 063710 (2005).

[45]S. H. Wei, L. G. Ferreira, J. E. Bernard, *et al.*, Phys. Rev. B **42** 9622 (1990).

[46]S. H. Wei and A. Zunger, Phys. Rev. Lett. **76** 664 (1996).

[47]Y.K. Kuo, B.T. Liou, S. H. Yen, *et al.*, Opt. Commun. **237** 363 (2004).

[48]S. Gehrsitz, H. Sigg, N. Herres, *et al.*, Phys. Rev. B **60** 11601 (1999).

[49]M. Schenk and T. H. D. Le, Semicond. Sci. Technol. 13(1998) 335.

[50]M. Schenk and C. Silber, J. Mater. Sci.-Mater. Electron. **9** 295 (1998).

[51]V. V. Shchennikov, S. V. Ovsyannikov, and N. Y. Frolova, J. Phys. D **36** 2021 (2003).

[52]F. E. Hassan, Phys. Status. Solidi. B **242** 3129 (2005).

[53]F. D. Murnaghan, Proc. National Acad. Sci. **30** 244 (1944).

[54]G. Simmons and H. Wang, *Single Crystal Elastic Constants and Calculated Aggregate Properties: a Handbook* (The MIT Press, Cambridge, Massachusetts, 1971).

[55]E. Hashin and S. Shtrikman, J. Mech. Phys. Solids **10** 335 (1962).

[56]E. Hashin and S. Shtrikman, J. Mech. Phys. Solids **10** 343 (1962).

[57]R. Hill, Proc. Phys. Soc. London A **65** 349 (1952).

[58]R. A. Miller and D. E. Schuele, J. Phys. Chem. Solids **30** 589 (1969).

[59]J. R. Neighbors and G. A. Alers, Phys. Rev. **111** 707 (1958).

[60]S. G. Epstein and A. P. DeBretteville, Jr., Phys. Rev. **138** A771 (1965).

[61]C. K. N. Patel, Phys. Rev. Lett. **15** 1027 (1965).

[62]J. F. Nye, *Physical Properties of Crystals* (Oxford University Press, London, 1967).

[63]D. Royer and E. Dieulesaint, J. Appl. Phys. **50** 4042 (1979).

[64]P. W. Bridgman, Proc. Natl. Acad. Sci. U. S. **10** 411 (1924).

[65]B. Houston, R. E. Strakna, and H. S. Belson, J. Appl. Phys. **39** 3913 (1968).

[66] P. J. Taylor, J. R. Maddux, W. A. Jesser, *et al.*, J. Appl. Phys. **85** 7807 (1999).

[67] S. S. Kim, S. Yamamoto, and T. Aizawa, J. Alloys and Compd. **375** 107 (2004).

[68]J. Jiang, L. Chen, S. Bai, *et al.*, Mater. Sci. Eng. B **117** 334 (2005).

[69]J. Jiang, L. D. Chen, S. Q. Bai, *et al.*, Scripta Mater. **52** 347 (2005).

[70]R. W. Rice, *Mechanical Properties of Ceramics and Composites* (Marcel Dekker, New York, 2000), pp. 7 - 10.

[71]J. Mandel, *Statistical Analysis of Experimental Data* (Interscience publishers, New York, 1964).

[72]D. S. Moore, *The Basic Practice of Statistics* (W. H. Freeman, Inc, New York, 1995), pp. 442 - 4423

[73]J. E. Freund, R. E. Walpole, Mathematical Statistics (Prentice Hall, Englewood Cliffs, N. J., 1987), pp. 289 - 295.

Chapter 3

F. Ren, E. D. Case, E. J. Timm, M. D. Jacobs and H. J. Schock, "Weibull analysis of the biaxial fracture strength of a cast p-type LAST-T thermoelectric material", *Philosophical Magazine Letters*, **86**: 673-682 (2006).

Weibull analysis of the biaxial fracture strength of a cast p-type LAST-T thermoelectric material

F. REN†, E. D. CASE*†, E. J. TIMM‡, M. D. JACOBS†, and H. J. SCHOCK‡

†Chemical Engineering and Materials Science Department
Michigan State University, East Lansing, MI 48824, USA
‡Mechanical Engineering Department
Michigan State University, East Lansing, MI 48824, USA

This study is both (i) the first study to apply Weibull statistics to the strength distribution of any thermoelectric (TE) material and (ii) the first fracture strength study of a member of the LAST-T (Lead-Antimony-Silver-Tellurium- Tin) family of high-temperature TE materials. The p-type TE material $Ag_{0.9}Pb_9Sn_9Sb_{0.6}Te_{20}$ was cast from the melt. Specimens cut from the resulting ingot were fractured in a ball-on-ring biaxial fracture test. The Weibull parameters (characteristic strength and Weibull modulus) are obtained from the fracture data. Implications of the Weibull analysis on the fabrication of TE devices are discussed.

Keywords: Thermoelectric; Weibull analysis; Fracture strength

1. Introduction

The direct conversion of heat to electricity by thermoelectric (TE) materials has broad application in a number of heating, cooling and energy conversion devices. A family of high-temperature TE materials with the composition $Ag_nPb_mM_nQ_{m+2n}$ has recently received considerable attention in the literature[1-3], where the Q ions are chalcogenides such as S, Se, Te and the M metal ions may include Bi or Sb.

The performance of TE materials is typically characterized in terms of a nondimensional figure of merit, ZT, where T is the ambient temperature and the parameter Z is given by $(\alpha^2\sigma)/k$. The parameter α is the Seebeck coefficient, σ is the electrical conductivity and k is the thermal conductivity. Useful thermoelectric materials typically have ZT values of approximately 1 or greater [4]. For selected LAST (Lead – Antimony – Silver - Tellurium) and LAST-T (Lead – Antimony – Silver – Tellurium - Tin) compounds, a ZT as high as 2.2 at 800 K has been reported [1, 2].

There have been only a limited number of mechanical property studies for both high and low temperature TE materials. For example, although the bending strength has been measured for Bi_2Te_3-based TE materials [5-7] and Zn_4Sb_3 [8], the mechanical characterization of the $Ag_nPb_mM_nQ_{m+2n}$ family of TE materials is currently limited to a recent study of Young's and shear modulus as a function of the Ag composition [3].

This study provides the first fracture strength data on a member of the LAST-T family of p-type TE materials. Furthermore, this is the first study to characterize the strength distribution for any TE material.

2. Background

Mechanical integrity is critical for waste heat recovery applications. In addition to the thermal gradient imposed under steady-state conditions, the TE materials used in waste heat recovery must survive hundreds or thousands of heating and cooling cycles if they are to extract useful heat energy from an internal combustion engine. Mechanical loads and vibration also may be superimposed on the thermal stresses. For example, TE generator sub-assemblies may consist of 50 or more individual TE couples, where each couple consists of an n-type and a p-type TE "leg" joined electrically in series by a metal strap. Successful TE generator operation requires that not only the survival of legs having average strength, but also there must be a high probability that the weakest legs of the sub-assemblies also survive. Thus, rather than using the mean strength as a design criterion, information on the distribution of fracture strength is critical for the design of a variety of high-temperature TE devices.

TE materials are generally brittle semiconducting materials. Weibull analysis is well suited to characterize their strength distribution [9]. Weibull analysis is based on extreme distribution theory, a special case of order statistics [10]. In terms of fracture of brittle

materials, the Weibull distribution is based on a "weakest link" model in which fracture occurs at the largest flaw [9, 10]. Weibull statistics allows one to make inferences about the flaw population, which in turn provide information about the scatter in strength expected from a set of specimens. The Weibull relationship for fracture strength distributions may be written as

$$\ln\ln(1/(1-P_f)) = m\ln(\sigma/\sigma_0) = m\ln\sigma - m\ln\sigma_0 \qquad (1)$$

The exponent m (the Weibull modulus) is a shape parameter for the distribution and the characteristic strength, σ_0, is a scale parameter. From order statistics concepts, we can relate the failure probability, P_f, to the ranked (ordered) fracture data for a given set of specimens [9, 10]. For sample sizes > 30, P_f can be written as [11]

$$P_f = (i-0.5)/N \qquad (2)$$

for the i^{th} measured fracture strength in an experiment that includes a total of N fractured specimens.

A small m value (say between five and seven) indicates a broad flaw size distribution and significant scatter in otherwise nominally identical specimens. A large m value (say 20 - 30) indicates a narrow flaw size distribution and limited scatter in strength values [9].

3. Experimental Procedure

3.1 Materials and Specimen Preparation

For this study, the p-type TE material $Ag_{0.9}Pb_9Sn_9Sb_{0.6}Te_{20}$ was cast from the melt using high- purity materials (99.99% to 99.999%) from each element. Each element was weighed (±0.0004 g) and then sealed under high vacuum in a fused silica ampoule (25 mm diameter, 1.5 mm wall thickness, 300 mm length). The composition was then heated, melted and then cooled in a three-zone split tube-rocking furnace. The following time-temperature profile was used: (1) 50°C/hr from room temperature to 1020°C, (2) rock at 1020°C for 4 hr, (3) stop rocking and start cooling from 1020°C to 950°C at 70°C/hr, (4) cool from 950°C to 850°C at 50°C/hr, (5) cool from 850°C to 750°C at 5°C/hr, and (6) cool from 750°C to 50°C at 30°C/hr. After the furnace rocking was stopped, the furnace was rotated to a vertical position to obtain a cylindrical, flat ended, 200-gram ingot.

3.2 Biaxial Flexure Testing

The fracture strength was determined using the ball-on-ring biaxial flexure technique [9, 12] (Figure 3.3.1). Using biaxial flexure, one can (1) test either thin disk or plate specimen geometries, (2) avoid extensive machining, and (3) minimize the impact of edge flaws on the strength data. For many other fracture test techniques, extensive and precise machining is needed, which can be very expensive for brittle materials. However, in this study the most important feature of the biaxial flexure technique is that it is quite insensitive to edge flaws [9, 12].

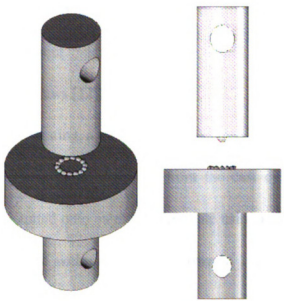

Figure 3.3.1. Schematic of the ball-on-ring load fixture used for biaxial flexure testing of cast ingots in this study.

For brittle materials, edge flaws are difficult to effectively remove and the sharp geometry of a specimen edge leads to stress concentrations that can lead to fracture. Thus, edge flaws generated by machining can significantly affect the measured fracture strength for many test methods. In contrast, biaxial flexure testing allows one to compare the fracture strength of TE materials of different chemical composition or different processing history without accounting for the complicating effects of machining-generated edge flaws [12].

For the biaxial flexure testing, a total of 20 disk-shaped specimens (approximately 22 mm in diameter and 3 mm thick) were cut from the cast cylindrical ingot. The cut specimens then were mounted onto an aluminum plate using a thermoplastic compound. Each specimen was polished with diamond grit down to 1 micron. After polishing, the specimens were first cleaned using ethanol to remove the residue of the thermoplastic mounting compound. Then the specimens were ultrasonically cleaned for about 20 minutes in a detergent solution.

For the ball-on-ring fixture, the diameter of the ring was 15.8 mm and the diameter of the ball was 6.35 mm (Figure 3.3.1). The biaxial flexure tests were conducted in air with a load and a loading rate that were controlled by a commercial test machine (Instron Corporation). For each test, the loading rate was 0.5 mm min^{-1}.

3.3 Microstructural characterization

Following the fracture of the specimens by biaxial flexure, the polished surfaces of selected specimens were chemically etched at room temperature using a solution of 1.0 M KOH + 0.7 M $K_3(Fe(CN)_6$ in deionized water [13]. The microstructure of both (i) polished and unetched specimens along with (ii) polished and etched specimens was characterized using a Scanning Electron Microscope (JEOL 6400, JEOL Corp. Japan). In addition, the fracture surfaces of selected specimens were examined. All specimens examined in the SEM were mounted on an aluminum stub using carbon tape. The unetched, polished specimens were used for porosity observations while the chemically etched specimens were used in grain size determinations. The specimens have sufficient electrical conductivity so as not to require a conductive coating to be applied for SEM examination.

4. Results and Discussion

4.1 Microstructure of the cast specimens

The grains comprising the LAST-T specimens examined in this study were approximately equiaxed and quite large. A mean grain size of roughly 706 microns was determined via the linear intercept technique on low magnification SEM micrographs of the polished and etched surfaces of selected specimens (Figure 3.3.2a). In order to assure suitable statistics, approximately 80 intercepts from each of three micrographs, thus a total number of about

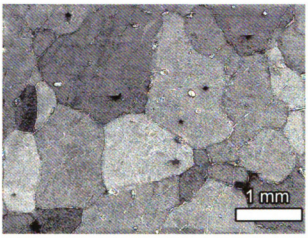

(a)

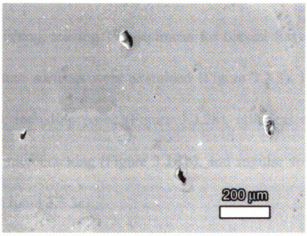

(b)

Figure 3.3.2. For the cast LAST-T specimens included in this study, (a) a chemically etched specimen surface showing approximately equiaxed grains and (b) an as-polished surface showing isolated surface pores.

240 intercepts, were used in the grain size determination.

Examination of the unetched, polished specimens (Figure 3.3.2b) revealed a few isolated quasi-spherical pores. The pores, which ranged from roughly 20 microns to 50 microns in diameter, were thus a factor of 15 to 35 smaller than the mean grain size.

4.2 Biaxial fracture tests

Of the 20 specimens initially cut from the ingot, five specimens failed either during cutting or during polishing, leaving 15 specimens for biaxial flexure testing. Following testing, selected fracture surfaces were examined (Figure 3.3.3). Four types of surface flaws were observed, including pores (Figure 3.3.2b), elliptical surface flaws (Figure 3.3.3a), near-surface microcracking (Figure 3.3.3b), and angular voids that were roughly tetrahedral in shape (Figure 3.3.3c).

The elliptical surface flaws where likely caused by the cutting and polishing of the cast ingot into disk-shaped specimens are likely the primarily cause of failure (Figure 3.3.3a). In Figure 3.3.3a, the major axis of the critical flaw is roughly 270 μm long and the semi-minor axis is approximately 100 μm long. Subsurface microcracking was observed in about half of the fracture surfaces examined by SEM. However, for the near-surface microcracking (Figure 3.3.3b), it is difficult to determine from the post-test examination of the fracture surfaces whether these microcracks were present before fracture or whether they were generated during flexure testing.

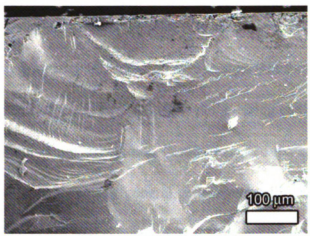

(a)

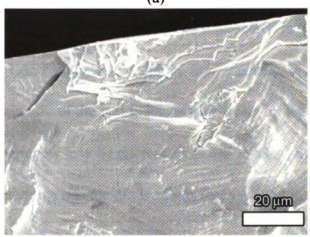

(b)

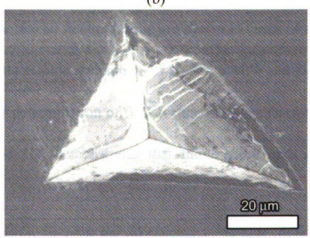

(c)

Figure 3.3.3. Flaws associated with the LAST-T specimens included in this study, including (a) an elliptical surface flaw, (b) subsurface microcracking and (c) a tetrahedrally-shaped surface flaw that may be associated with microcracking and fractional grain pullout during cutting and polishing.

The tetrahedrally-shaped voids were relatively infrequent and had side lengths as large as ~ 80 μm. The geometry of these defects suggests that they may result from the pullout of small segments of grains near the triple point during cutting or polishing of the specimens. Grain pullout is not uncommon in microcracked materials and the LAST-T specimens may be microcracked. In general, brittle crystalline materials with lower atomic symmetry than cubic are subject to a microcracking via thermal expansion anisotropy (TEA) [14-17], where the tendency to microcrack increases with increasing grain size. Since the LAST materials crystallize in a noncubic, distorted NaCl structure [18] and since the grain size of the cast ingots is very large (on the order of 700 microns in this study), then the ingots may be microcracked due to TEA, but further work would need to be done to determine if some of the microcracks present in then LAST ingots are generated by TEA.

The results of the biaxial flexure testing are shown in terms of a Weibull plot (Figure 3.3.4), where the characteristic strength is 15.3 +/- 5.6 MPa and the Weibull modulus is 3.19. A coefficient of determination of 0.93 for the fit of the fracture data to the Weibull relationship (equation (1)) demonstrates that the fracture data is described well by Weibull statistics.

The 15 MPa fracture strength for the specimens in this study is relatively low for brittle, dense materials. However, cast ingots of other TE materials also exhibit low fracture strength values. For example, for cast ingots of $Bi_{0.4}Sb_{1.6}Te_3$ and $Bi_{0.5}Sb_{1.5}Te_3$,

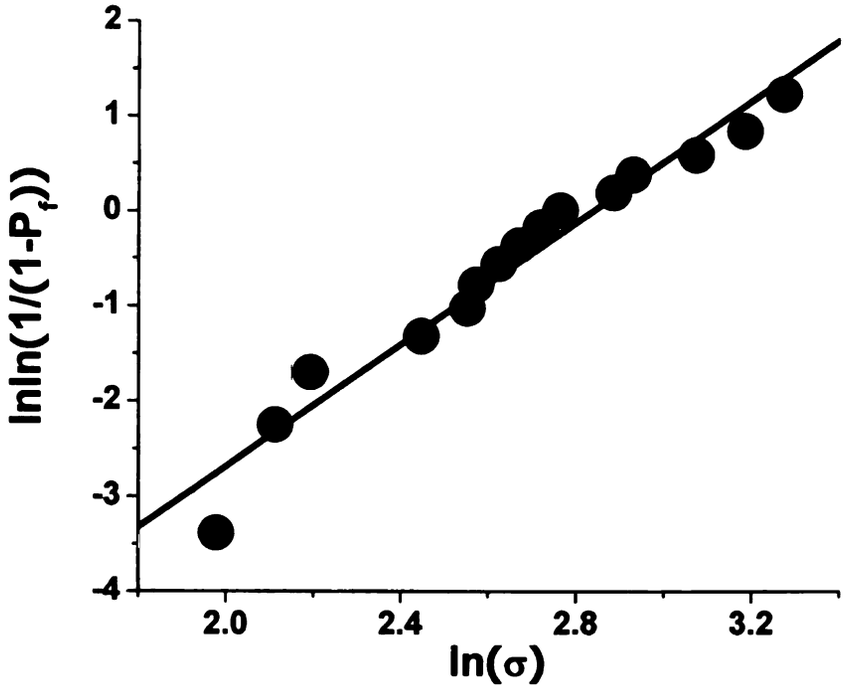

Figure 3.3.4. Weibull plot of biaxial strength data obtained from ball-on-ring biaxial flexure testing for disk-shaped specimens cut from cast p-type ingot of LAST-T material

Kim et al. [5] measured a three-point bend strength, σ_f, approximately 20 MPa. Also, for n-type $Bi_2(Te,Se)_3$ materials, Jiang et al. [6] found fracture strength of 12 ± 5 MPa as measured in three-point bend for cast ingots. In addition, for p-type $(Bi,Sb)_2Te_3$, Jiang et al. [7] measured a three-point bend strength of only about 10 MPa.

Thus, cast ingots of various TE materials including $Bi_{0.4}Sb_{1.6}Te_3$, $Bi_{0.5}Sb_{1.5}Te_3$ [5], n-type $Bi_2(Te,Se)_3$ [6], and p-type $(Bi,Sb)_2Te_3$ [7] all show three-point bend fracture strengths ranging from roughly 10 to 20 MPa, which is comparable in magnitude to the 15 MPa biaxial flexural strength found for the cast ingots of LAST-T material included in this study. However, the measured fracture strength, σ_f, can vary somewhat as a function of the test technique [9, 12, 19]. For example, Chao and Shetty [19] performed a study in which the goal of the research was to compare the strength values obtained from uniaxial testing (three-point bend and four-point bend) with those values obtained from biaxial flexure testing. For the polycrystalline alumina specimens included in their study, Chao and Shetty [19] found fracture strengths of 353.4 MPa, 385.9 MPa, and 338.7 MPa for the three-point bend, four-point bend, and biaxial flexure strength, respectively. In addition, for their polycrystalline silicon nitride specimens, Chao and Shetty [19] found fracture strengths of 768.5, 908.1, and 717.1 MPa for the three-point bend, four-point bend, and biaxial flexure strength, respectively.

Thus, while the fracture strength values obtained by three-point bend and biaxial flexure testing can differ, one can state that the 10 MPa - 20 MPa strength values observed for cast ingots of other TE materials are at least roughly similar to the 15 MPa

measured by biaxial flexure of LAST-T cast ingot materials. Unfortunately, no biaxial flexure or uniaxial flexure strength data is available in the literature for PbTe or for a doped PbTe material such as LAST-T.

In this study, biaxial flexure was selected as the test technique in order to avoid the complications of specimen failure from edge flaws which is often a problem in uniaxial testing of brittle materials [9]. In addition, most in-service loading conditions are multiaxial rather than uniaxial thus biaxial strength data may be more useful in terms of design considerations [20].

Although a Weibull modulus for other TE materials is not available in the literature, an m value of 3.19 indicates an extensive scatter in fracture strength that would be very problematic in constructing TE modulus consisting of hundreds of legs.

In this study and in the TE literature [4-6, 21], casting specimens from ingots produces specimens with large grain sizes (≈ 400 microns and larger). The Weibull analysis of the specimens fractured in this study and the strength measured for other TE materials [5-7] agrees with the general trend that brittle materials with large grain sizes tend to exhibit low strength and a high scatter in the strength values [9]. However, Jiang et al. [6, 7] and Kim et al. [5] have ground cast ingots into a powder and sintered them by hot pressing [5, 8] or plasma spark sintering [6, 7], yielding specimens with a much smaller grain size and a fivefold or more increase in the fracture strength.

5. Summary and Conclusions

The fracture strength of the as-cast $Ag_{0.9}Pb_9Sn_9Sb_{0.6}Te_{20}$ material is only approximately 15 MPa. The value of fracture strength is comparable to the strength of other cast TE materials [5-7]. Furthermore the low fracture strength is expected for brittle specimens with very large grain sizes [22, 23]. LAST-T specimens with smaller grain sizes (fabricated by hot pressing, for example) would likely be far stronger, since as the grain size of brittle materials decreases, the fracture strength typically increases dramatically [22, 23].

Although specimens with smaller grain sizes would likely be much stronger than the cast LAST-T material, one must also consider the scatter in strength values, especially for applications such as waste heat recovery that require the simultaneous survival of a large number of individual TE components (legs) that are subjected to cyclic thermal and mechanical loads. A Weibull analysis of the fracture data, conducted in this study for the first time for TE materials, can provide crucial design information on the scatter in fracture strength.

Acknowledgements

The authors acknowledge the financial assistance of the U. S. Department of Energy Grant DE-FC26-04NT42281 and Office of Naval Research MURI Grant number N000140310789. The authors also thank the Advanced Microscopy Center at Michigan State University for the use of the SEM facility.

References

[1] K. F. Hsu, S. Loo, F. Guo, *et al.*, Science **303** 818 (2004).

[2] D. Bilc, S. D. Mahanti, K. F. Hsu, *et al.*, Phys. Rev. Lett. **93** Art. No. 146403 (2004).

[3] A. Kosuga, M. Uno, K. Kurosaki, *et al.*, J. Alloy. Compd. **387** 52 (2005).

[4] Y. Xia, S. Bhattacharya, V. Ponnambalam, *et al.*, J. Appl. Physics, **88** 1952 (2000).

[5] S. S. Kim, S. Yamamoto, T. Aizawa, J. Alloys and Compd. **375** 107 (2004).

[6] J. Jiang, L. D. Chen, S. Q. Bai, *et al.*, Mater. Sci. Eng. B-Solid State Mater. Adv. Technol. **117** 334 (2005).

[7] J. Jiang, L. D. Chen, S. Q. Bai, *et al.*, Scripta Mater. **52** 347 (2005).

[8] K. Uneo, A. Yamamoto, T. Noguchi, *et al.*, J. Alloy. Compd. **388** 118 (2005).

[9] J. B. Wachtman, *Mechanical Properties of Ceramics* (Wiley and Sons, New York, 1996), pp 92 - 100.

[10] N. R. Mann, R. E. Schafer, and N. D. Singpurwall, *Methods for Statistical Analysis of Reliability and Life Data* (Wiley and Sons, New York, 1974), pp 103 – 111, 184 – 188.

[11] D.F. Wu and H. Jiang, J. Mat. Sci. Lett. **22** 1745 (2003).

[12] M. K. Ferber and H. T. Lin, Key Eng. Mat. **287** 367 (2005).

[13] V. V. Robozerov, V. A. Zykov, and T. A. Gavrikova, Inorg. Mater. **36** 127 (2000).

[14] S. G. Yousef, J Rodel, E. R. Fuller, *et al.*, J. Am. Ceram. Soc. **88** 2809 (2005).

[15] E. D. Case, I. O. Smith, and M. J. Baumann, Mater. Sci. Eng. A, **390** 246 (2005).

[16] T. P. Hoepfner and E. D. Case, Mater. Lett., **58** 489 (2004).

[17] T. Weiss, S. Siegesmund, and E. R. Fuller, Build. Environ. **38** 1251 (2003).

[18] E. Quarez, K. F. Hsu, R. Pcionek, *et al.*, J. Am. Chem. Soc. **127** 9177 (2005).

[19] L. Y. Chao and D. K. Shetty, J. Am. Ceram. Soc. **74** 333 (1991).

[20] C. H. Hsuesh, M. J. Lance, and M. K. Ferber, J. Am. Ceram. Soc. **88** 1687 (2005).

[21] P. J. Taylor, J. R. Maddux, W. A. Jesser, *et al.*, J. Appl. Phys. **85** 7807 (1999).

[22] M. W. Barsoum, *Fundamentals of Ceramics* (McGraw Hill, New York, 1997), pp 415 – 416.

[23] R. W. Rice, *Mechanical Properties of Ceramics and Composites* (Marcel Dekker, New York, 2000) pp. 176 – 180.

MICHIGAN STATE UNIVERSITY LIBRARIES
3 1293 02956 3602

THESIS

5
2502
V.2

170
657
THS

LIBRARY
Michigan State
University

PLACE IN RETURN BOX to remove this checkout from your record.
TO AVOID FINES return on or before date due.
MAY BE RECALLED with earlier due date if requested.

DATE DUE	DATE DUE	DATE DUE
012809 MAR 04 2009		
MAY 24 2013 OCT 05 2013		

6/07 p:/CIRC/DateDue.indd-p.1

MECHANICAL CHARACTERIZATION AND POWDER PROCESSING OF LEAD TELLURIDE BASED THERMOELECTRIC MATERIALS

VOLUME II

By

Fei Ren

A DISSERTATION

Submitted to
Michigan State University
in partial fulfillment of the requirements
for the degree of

DOCTOR OF PHILOSOPHY.

Materials Science and Engineering

2007

Chapter 4

F. Ren, E. D. Case, E. J. Timm, E. Lara-Curzio, R. M. Trejo, C. –H. Lin, and Mercouri G. Kanatzidis, "The Young's modulus and Poisson's ratio of Lead-Telluride based Thermoelectric Materials as a Function of Temperature", manuscript to be submitted to *Philosophical Magazine.*

The Young's modulus and Poisson's ratio of Lead-Telluride based Thermoelectric Materials as a Function of Temperature

Fei. Ren[1], Eldon. D. Case[1,*], Jennifer E. Ni[1], Edward. J. Timm[2], Edgar. Lara-Curzio[3], Rosa. M. Trejo[3], Chia-Her Lin[4], Mercouri G. Kanatzidis[5]

[1] Chemical Engineering and Materials Science Department, Michigan State University, East Lansing, MI 48824 USA

[2] Mechanical Engineering Department, Michigan State University, East Lansing, MI 48824 USA

[3] High Temperature Materials Laboratory, Oak Ridge National Laboratories, Oak Ridge, TN 37831, USA

[4] Department of Chemistry, Michigan State University, East Lansing, MI 48824

[5] Department of Chemistry, Northwestern University, Evanston, IL 60208

Abstract

This study provided the first measurements of the temperature dependence of Young's modulus and Poisson's ratio for Ag-, Sb-, Sn-, and S- doped PbTe thermoelectric materials between room temperature and 723 K. Specimens cut from both cast ingots and hot pressed billets were included in the study. A critical potential application of these materials is as thermoelectric generators, producing electrical energy from waste heat. Knowledge of the elastic moduli as a function of temperature is essential for the design of thermoelectric generators since both analytical and finite element stress calculations require knowledge of the temperature-dependence of these properties.

Keywords: semiconductors, elastic constants, ultrasonics

Please direct correspondence to: Eldon D. Case, Chemical Engineering and Materials Science Department, Room 2527 Engineering Building, Michigan State University, East Lansing, Michigan, 48824-1226, USA, e-mail casee@egr.msu.edu, FAX (517)-432-1105.

1. Introduction

Thermoelectric materials are of considerable interest for applications such as electric power generation from waste heat [Chen 2003, Riffat 2003, Tritt 2006, Yang 2006] and cooling of electronic substrates [Riffat 2003, Sharp 2006]. A family of n-type lead-antimony-silver-tellurium (LAST) [Hsu 2004, Quarez 2005] and p-type lead-antimony-silver-tellurium-tin (LASTT) [Androulakis 2006] thermoelectric compounds are promising for power generation applications, with a unitless figure of merit, ZT, of about 1.7 at 700 K for LAST and a ZT of about 1.45 at 600 K for LASTT.

There is a very limited literature on the mechanical properties of thermoelectric materials in general and for LAST compounds in particular, although recently the room temperature biaxial flexure strength was studied for LASTT [Ren 2006] and the room temperature hardness as a function of composition was measured for LAST [Ren 2007a]. To date, only two studies have been published on the elastic moduli of LAST: (1) Kosuga *et al.* used the pulse echo technique to determine the room temperature elastic moduli for three hot pressed LAST specimens that spanned a narrow composition range [Kosuga 2005] while (2) Ren *et al.* used micro- and nanoindentation to measure the room temperature elastic moduli for 17 polycrystalline cast LAST ingot specimens over a much wider composition range [Ren 2007b].

This study is the first to present elastic moduli (Young's modulus and Poisson's ratio) versus temperature for LAST and other doped PbTe specimens and is one of the few studies to report on the temperature dependence of the elastic moduli for any

thermoelectric material.

2. Background

2.1 Requirement for temperature-dependent elastic moduli

In power generation applications, the thermoelectric materials will be subjected to both mechanical and thermal stresses. For example, in an automotive application, in which waste heat is recovered from automobile exhaust to generate electrical energy, the thermoelectric elements will be subjected to temperature gradients and thermal transients.

For the fully constrained case, the maximum thermal stress, $\sigma_{TH\text{-}MAX}$, due to a temperature change ΔT can be approximated by [Case 2002; Cheng 1951; Lu 1998]:

$$\sigma_{TH\text{-}MAX} = \frac{E}{1-\nu}\alpha\Delta T \cdot f(Bi) \qquad (1)$$

where E is the elastic modulus, ν is Poisson's ratio, α is the thermal expansion coefficient and f(Bi) is a function of the Biot modulus, Bi. The normalized thermal stress, $\sigma_{TH\text{-}MAX}/(E\alpha\Delta T/(1-\nu))$, as function of Bi is illustrated in Figure 3.4.1.

The Biot modulus is defined by Bi = *ah/k* [Case 2002, Manson 1966], where *a* is a characteristic specimen dimension, *h* is the surface heat transfer coefficient, and *k* is the thermal conductivity of the solid [Cheng 1951, Lu 1998, Zhao 2000]. For a plate, *a* is the half thickness of the plate. The heat transfer coefficient, *h*, is a function of the quench medium itself and conditions at the interface between the solid and the surrounding medium, including: (i) the temperature of the quench medium, (ii) the rate of flow of the quench medium past the interface and (iii) the temperature of the specimen

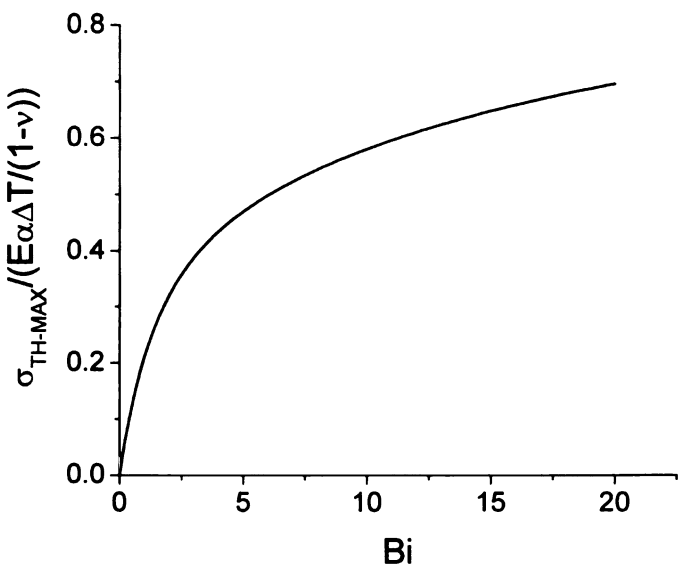

Figure 3.4.1. The maximum normalized thermal stress, $\sigma_{TH-MAX}/(E\alpha\Delta T/(1-\nu))$, as a function of Biot modulus, Bi.

when it enters the quench medium [Incropera 1985, Kim 1991, Kingery 1976, Lee 1993, Ozisik 1985]. Thus, the heat transfer coefficient and the particular value of f(Bi) is a function of the details of the thermal cycling environment.

For complex specimen geometries such as thermoelectric modules in which an array of thermoelectric elements are attached to metallic interconnects that are in turn mounted on dielectric plates, both mechanically imposed and thermally-induced stresses can no longer be estimated analytically. Instead, finite element analysis (FEA) must be employed to calculate the stress and strain response of the complex system (such as a TE module) to thermal and/or mechanical loading which in turn requires Young's modulus and Poisson's ratio data in order to construct the stiffness matrix the FEA [Kaliakin 2002]. Thus for both the numerical (FEA) and the analytical (Eq.(1), for example) stress calculations, the knowledge of Young's modulus and Poisson's ratio is essential.

In addition to their importance in stress calculations, E and ν also can be used to characterize the microcrack damage state [Case 2002, Budiansky 1976, Case 1993, Case 1981, 1983, Laws 1987, Lee 1989, 1990]. The decrease in Young's modulus with microcrack damage can be approximated as $E = E_0[1 - f(\nu)\varepsilon]$, where E_0 is the Young's modulus of the non-microcracked material, $f(\nu)$ is a function of Poisson's ratio and ε is a crack damage parameter that is proportional to the volumetric number density of microcracks and the third moment of the microcrack diameter [Budiansky 1976, Laws 1987]. Thermoelectric modules used for power conversion will be subjected to both mechanical vibration and thermal cycling, thus monitoring microcrack-induced changes

in Young's modulus will be important in characterizing microcrack damage that might be induced by in-service conditions.

Thus, the Young's modulus and Poisson's ratio data are needed for (i) stress calculations, including FEA for mechanically complex systems such as thermoelectric modules and (ii) characterize the evolution of microcrack damage in a body. In this study, we measure the temperature-dependent elastic moduli of PbTe-based compounds without intentionally introducing microcrack damage.

2.2 Resonant Ultrasound Spectroscopy

The elastic constants of solids can be determined by static or dynamic methods. Dynamic methods are preferred because they have higher accuracy than static methods and because the stresses/strains involved in these tests are far below the elastic limit of the material. This is important for measurements at elevated temperatures because the possibility of time-dependent deformation or rate dependency in the measurements is minimized. Furthermore, because the stresses are infinitesimal the test specimen is not permanently deformed and therefore the same test specimen can be used for repeated measurements as a function of temperature. Resonant Ultrasound Spectroscopy (RUS) is one of the more accurate and popular test methods to determine the elastic properties of solids [Migliori 1997, Radovic 2004, Ulrich 2002].

This test technique is based on the principle that the vibrational spectrum induced in a mechanically driven specimen is a function of the geometry, dimensions, and mass

density of the specimen. The details of the modulus calculation technique are linked to the concepts of "direct" and "inverse" problems in mathematical physics. For example, given the elastic moduli, as well as the mass and dimensions of the specimen, the "direct problem" consists of calculating the resonant frequencies of the specimen. However for the RUS analysis, the inverse problem must be solved; that is, the specimen resonant frequencies, mass and dimensions are known and one seeks to calculate the elastic moduli [Migliori 1997, Dulikravich 1999, Kac 1966]. One method for solving inverse problems is by an iterative, non-linear least-squares fitting procedure such as the Levenberg-Marquardt (LM) algorithm [Migliori 1997, Ulrich 2002, Press 1992]. For the LM algorithm and for non-linear least-squares techniques in general, an "initial guess" of the fitted parameter is required prior to iteration. These physical/mathematical considerations thus lead to a RUS software package supplied by the vendor (Quasar, Inc., Albuquerque NM) that requires initial guesses for the elastic moduli and proceeds to the solution via an interactive (LM) technique [Migliori 1997, Ulrich 2002]. An elastically isotropic polycrystalline solid has two independent elastic constants [Schreiber 1973], in which case two initial guesses (say, Young's modulus and Poisson's ratio) would be needed in order to compute the elastic moduli from the acoustic resonance (RUS) data.

For the RUS technique, cylinders, disks, and rectangular parallelepipeds are typically used as test specimens. The test specimen is typically placed on a tripod arrangement of supports, with one support attached to a "driver" transducer that generates the mechanical vibration and the other two supports are attached to "pickup" transducers that sense the

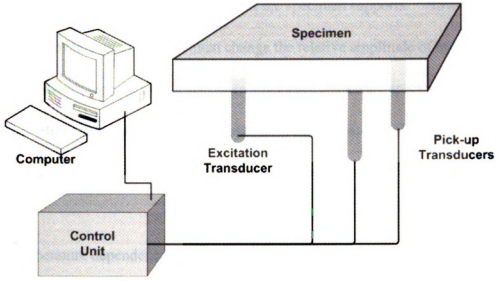

Figure 3.4.2. Schematic of equipment configuration during a typical RUS experiment.

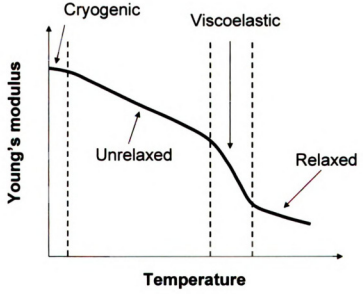

Figure 3.4.3. Schematic of temperature dependent Young's modulus including four regions: (1) the cryogenic region, (2) unrelaxed modulus region, (3) viscoelastic region due to grain boundary sliding, and (4) relaxed modulus region.

mechanical vibrations in the specimen (Figure 3.4.2). During the measurement with the tripod configuration, the specimen can shift on the specimen supports. However while small lateral movements of the specimen change the relative amplitude of the resonant peaks in the acoustic spectrum; the specimen's resonant frequency spectrum is unchanged. Since the moduli are calculated from the resonant frequencies, the calculated moduli are unaffected by small shifts in the specimen position [Migliori 1997].

2.3 The temperature dependence of Young's modulus

Young's modulus of polycrystalline materials is a function of temperature. A typical modulus vs. temperature relationship includes four regions (Figure 3.4.3), namely (i) a cryogenic regime in which the modulus is a relatively weak function of temperature [Wachtman 1996, Varshni 1970], (ii) the unrelaxed modulus at lower temperature [Kingery 1976, Wachtman 1996], (iii) the viscoelastic region due to grain boundary sliding at elevated temperatures [Wachtman 1996, Wachtman 1959] and (iv) the relaxed modulus region.

For many materials, an empirical exponential function, known as the Wachtman equation [Wachtman 1996], can be used to describe the relationship between Young's modulus and temperature, such that

$$E(T) = E_0 - b_1 T \exp\left(\frac{-T_0}{T}\right) \qquad (2a)$$

where E is the Young's modulus at temperature T, E_0 is the modulus at 0 K, b_1 is a

constant related to the Gruneisen's parameters and T is the absolute temperature. T_0 is a constant that approaches half of the Debye temperature, θ_D, at elevated temperatures [Schreiber 1973, Anderson 1966]. In order to examine the behavior of the Wachtman relationship (Eq. (2a)) for a variety of materials, we plotted E(T) versus T for polycrystalline aggregate elasticity data for the ionically bonded solid LiF [Briscoe 1957, Suess 1961], the metal Cu and the semiconducting material PbTe [Houston 1968] (Table 3.4.1, Figure 3.4.4a). LiF, Cu, and PbTe all show a linear temperature versus modulus relationship with increasing temperature (Figure 3.4.4a).

If we first express Eq. (2a) in terms of the "reduced temperature" T_R (where $T_R = T/\theta_D$) and then we normalize both sides of the equation Eq. (2a) by E_0, then we obtain the unitless relationship

$$\frac{E(T_R)}{E_0} = 1 - \left\{\frac{b_1}{E_0}\right\} T_R \exp\left(\frac{-T_0}{T_R}\right) \qquad (2b)$$

If we plot Eq. (2b) as a function of reduced temperature T_R (Figure4b), we see that in the normalized coordinates, the Young's modulus curve becomes linear for temperatures greater than above about roughly $\theta_D/2$ to $\theta_D/3$, such that temperature dependence of E can often be approximated as [Case 1983]:

$$E(T) = E_0(1 - bT) \qquad (2c)$$

for temperatures greater than about $\theta_D/2$ to $\theta_D/3$, where the coefficient b is a constant. (Also, Eq. (2c) can be obtained directly from Eq. (2a) using a power series expansion for $\theta_D/2 \geq T_0 \geq \theta_D/3$). In particular, for PbTe, θ_D is about 175 K [Houston 1968] while

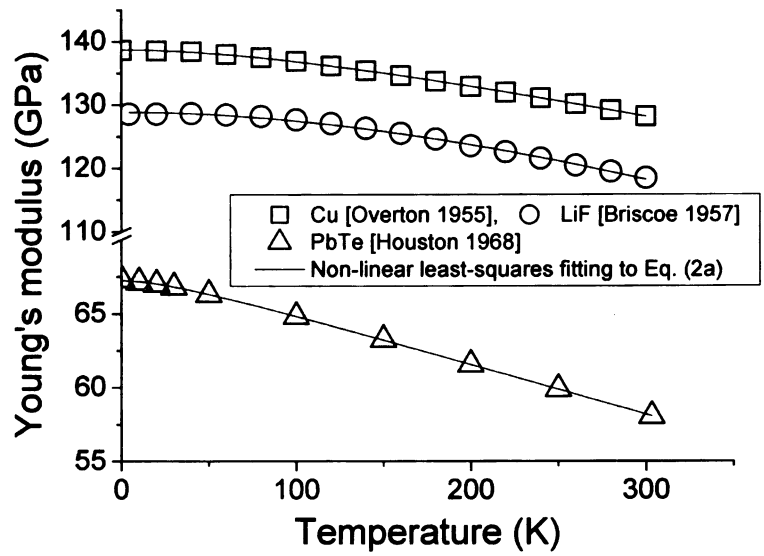

(a)

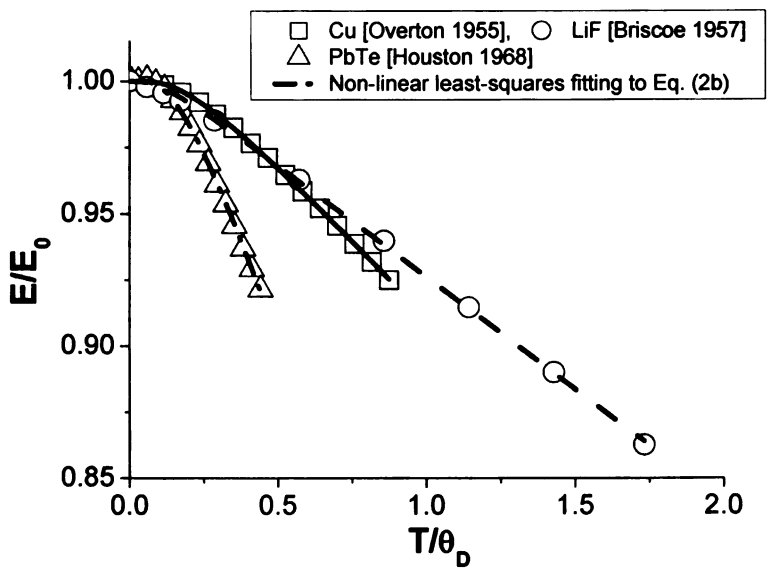

(b)

Figure 3.4.4. (a) The aggregate Young's modulus as a function of temperature for Cu [Overton 1955], LiF [Briscoe 1957], and PbTe [Houston 1968], with non-linear least squares fitting to the Wachtman's equation (Eq. (2a)). (b) The aggregate Young's modulus normalized to the Young's modulus at 0 K, E_0, as a function of temperature normalized to the Debye temperature, θ_D, for Cu [Overton 1955], LiF [Briscoe 1957], and PbTe [Houston 1968], with non-linear least squares fitting to Eq. (2b).

Table 3.4.1. Non-linear least-squares fit parameters b_1/E_0 and T_0/θ_D in the normalized Wachtman equation (Eq. (2b)), and number of data points, N, used in least squares fit over a given temperature range. The non-linear least-squares fit to Eq. (2b) yielded a coefficient of determination, r^2, of at least 0.999 for each material. In addition, Debye temperature, θ_D, from literature for each material is also included.

Material	θ_D (K)	b_1/E_0 (1/K)	T_0/θ_D	N	Temp. Range	Reference
LiF	680 [Omar 1975]	0.453±0.004	0.361±0.009	25	4.2 K—300 K	[Briscoe 1957]
Cu	343 [Omar 1975]	0.121±0.001	0.304±0.004	31	0 K – 300 K	[Overton 1955]
PbTe	175 [Houston 1968]	0.086±0.001	0.147±0.017	10	0 K- 303.2 K	[Houston 1968]

Table 3.4.2a. Processing method, composition, dimensions, and mass for the specimens tested in high temperature RUS experiments. All specimens were rectangular parallelepipeds.

Specimen	Processing Technique	Composition	Dimensions (mm)	Mass (g)	Density (g/cm^3)	Relative density
L145	Cast	$Pb_{0.95}Sn_{0.05}Te_{0.92}S_{0.08}$	6.585 x 5.074 x 4.404	1.179	8.012	0.991
N138	Cast	$Ag_{0.43}Pb_{18}Sb_{1.2}Te_{20}$	6.323 x 4.806 x 3.831	0.921	7.911	0.984
UMHP6	HPed	$Ag_{0.43}Pb_{18}Sb_{1.2}Te_{20}$	4.987 x 4.929 x 4.908	0.822	6.813	0.848
MSUHP6	HPed	$Ag_{0.43}Pb_{18}Sb_{1.2}Te_{20}$	10.543x7.576 x 2.255	1.360	7.576	0.942

Table 3.4.2b. Additional specimens included in the room temperature RUS measurements of modulus versus porosity. Specimens UMHP6 and MSUHP6 (Table 3.4.2a) were also included in the room temperature modulus measurements.

Specimen	Processing Technique	Composition	Dimensions (mm)	Mass (g)	Density (g/cm^3)	Relative density
MSUHP5	HPed	$Ag_{0.43}Pb_{18}Sb_{1.2}Te_{20}$	12.27 x 6.498 x 2.216	1.452	7.916	0.985
MSUHP7	HPed	$Ag_{0.43}Pb_{18}Sb_{1.2}Te_{20}$	13.98 x 9.565 x 3.292	3.239	7.355	0.914

for LAST materials, θ_D is a function of composition. Kosuga found θ_D values that varied from 132 K and 170 K as a function of composition [Kosuga 2005]. Thus, for PbTe and LAST, one would predict E(T) versus T to be linear for temperatures above roughly 65 to 85 K.

3. Experimental procedure

3.1 Specimen preparation

Four specimens were examined by RUS to determine the temperature dependent elastic moduli, including an n-type Sn- and S- doped PbTe ingot specimen L145, an n-type ingot LAST specimen N138, and two n-type hot pressed LAST specimens UMHP6 and MSUHP6 (Table 3.4.2a).

Samples of $(Pb_{0.94}Sn_{0.06}Te)_{1-x}$-$(PbS)_x$ (x=0.16) (L145) were prepared after mixing appropriate ratios of high purity elemental starting materials and 0.055 mol % of PbI_2 as an n-type dopant. The initial load was sealed in an aqua regia-cleaned fused silica tube under vacuum and heated at 1273 K for 6 h. The samples were then rapidly cooled to 773 K and held there for 72 h. The existence of a biphasic PbTe-PbS system was readily confirmed by powder x-ray diffraction [Androulakis 2007]. The phases in the PbTe-PbS system were nano or nano/micro phases depending on the composition [Androulakis 2007].

The ingot LAST specimen N138 which has the composition $Ag_{0.43}Pb_{18}Sb_{1.2}Te_{20}$ (Table 3.4.2a) was cast from high purity elements in a three zone split tube furnace. The

pure elements were sealed in a fused silica ampoule, which was heated to 1293 K at 50 K/hr and then rocked at 1293 K for 8 hrs. After the rocking stopped, the ampoule was first cooled to 1148 K in 1.5 hr, then to 948 K at 5 K/hr, and finally to 323 K at 30 K/hr.

Powder used for hot pressing specimen UMHP6 was milled from an n-type ingot with the composition of $Ag_{0.43}Pb_{18}Sb_{1.2}Te_{20}$, which was fabricated as follows: 1) heated to 1293 K at 50 K/hr in a sealed fused silica ampoule, (2) rocked at 1293 K for 8 hrs and then stopped rocking, (3) cooled to 1193 K in 1hr, (4) cooled to 1093 K at 5 K/hr, and (5) cooled to 323 K at 30 K/hr. For hot pressed specimen MSUHP6, the ingot fabrication procedure was similar to that of UMHP6 with differences in cooling steps 3 and 4, such that MSUHP6 was cooled to 1163 K in 1.5 hr in step 3 and then cooled to 963 K at 5 K/hr in step 4.

The cast ingots were crushed, ground with a mortar and pestle, sieved and reground until all particles passed through a 53-micron sieve. The sieved powders were then milled in a planetary ball mill (Retsch PM100, Haan, Germany) for 3 hrs at 100 rpm, resulting in a mean powder particle size of 6.4 ± 3.3 microns.

Specimen UMHP6 was hot pressed using facilities at University of Michigan (Astro HP4560-20, Astro Industries Inc. Santa Barbara, CA) at 603 K for 90 min with a pressure of ~ 100 MPa under a N_2 atmosphere. Specimen MSUHP6 was processed at Michigan State University were the powder was first annealed for 2 hours in a reducing environment (95% Ar + 5% H_2, 623 K) and then hot pressed in a graphite die using a 890 kN capacity (100 ton) hot press (Thermal Technology Inc., Concord New Hampshire) at

623 K for 1.5 hr with a pressure of about 60 MPa in an Ar atmosphere.

Using a slow speed diamond saw, the cast ingots and hot pressed billets were cut into rectangular parallelepipeds. Table 3.4.2a summarizes the dimensions, mass, composition, and processing method of each specimen included in this study.

3.2 Energy Dispersive X-Ray Spectroscopy measurements of specimen composition

During ingot fabrication, small amounts of Pb or Te can deposit on the inner walls of the sealed silica ampoule in which the ingots are cast, which potentially shifts the composition of the cast ingot from that of the starting materials. In order to semi-quantitatively estimate the extent of possible processing-induced shifts in composition of the ingots (and hot pressed materials) the composition of specimens was evaluated via SEM/EDS measurements. For specimens L145, N138, and MSUHP6, EDS the experiments were performed on a Hitachi S-3400N SEM (Hitachi Ltd., Japan) with working distance of 10 mm and an accelerating voltage of 15 kV, while for specimen UMHP6 the EDS measurements were performed on a JOEL 6400 SEM (JOEL Ltd., Japan) using a working distance of 15 mm and an accelerating voltage of 20 kV.

For specimens L145A, N138, and MSUHP6, the composition was averaged from six different locations with magnifications ranging between 200X and 6000X. For specimen UMHP6, the composition was calculated from four different locations with magnifications of 200X.

3.3 Nanoindentation

Prior to RUS measurements, nanoindentation (Nano Indenter XP, MTS Systems Corporation, Oak Ridge, TN) was performed on specimens L145, N138, and MSUHP6 to obtain an initial guess of the Young's modulus that was subsequently used as input to the RUS calculations (Section 2.2), a 4 X 4 array of indents was made on each of the three specimens, with a loading rate of 10 nm/s and a constant tip penetration depth of 2000 nm. After nanoindentation, Young's modulus of each specimen was calculated from the unloading curve according to Oliver and Pharr [Oliver 1992]. The nanoindentation determined Young's modulus values were used as the initial guesses in the RUS fitting program (RPModel, Quasar International, Inc. Albuquerque, NM).

In addition to providing the initial guesses to serve as input to the RUS elasticity calculations, the nanoindentation (TriboIndenter Hysitron Inc., Minneapolis, MN) studies were done to determine the extent of elastic anisotropy of the specimens. For specimens L145, N138, and UMHP6, six different locations (A –F) on three different specimen faces were selected for indentation (Figure 3.4.5a); while four locations (A – D) on the 10 x 12 mm^2 face of specimen MSUHP6 were indented (Figure 3.4.5b). At each location, nine nanoindents (a 3 x 3 array) were measured, yielding a total number of 54 indents on each of the specimens L145, N138, and UMHP6, and 36 indents on specimen MSUHP6. During nanoindentation, the specimen was loaded to 2000 μN with a loading rate of 200 μN/sec, followed by a 10-second hold at 2000 μN. The specimen was then unloaded to 10% of the peak load with an unloading rate of 200 μN/sec.

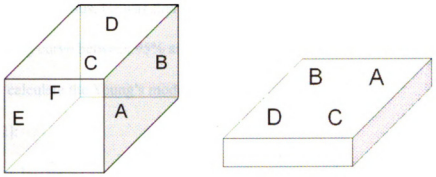

(a) (b)

Figure 3.4.5. Nanoindent locations selected to examine the anisotropy of Young's modulus for (a) specimen L145, N138, and UMHP6, and (b) MSUHP6.

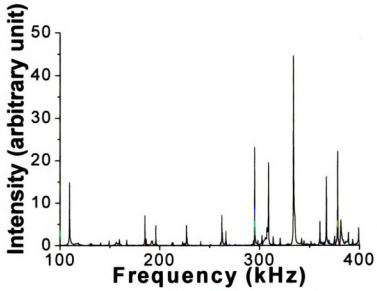

Figure 3.4.6. A typical spectrum obtained from the RUS measurement, where peaks correspond to mechanical vibrational modes.

The reduced modulus, E_r, was first calculated from the load versus displacement data on the unloading curve between 95% and 20% of the peak load (2000 μN), which was then used to calculate the Young's modulus of the examined specimens according to [Oliver 1992]:

$$\frac{1}{E_r} = \frac{1-\upsilon^2}{E} + \frac{1-\upsilon_i^2}{E_i}$$

where E and ν are the Young's modulus and Poisson's ratio of the specimen, while E_i and ν_i are the Young's modulus and Poisson's ratio of the indenter.

3.4 Resonant Ultrasound Spectroscopy (RUS) measurements

For each of the four specimens included in this study, RUS measurements were performed in a sealed chamber with flowing Ar. After the furnace chamber was sealed and before heating, the specimen chamber was evacuated to an absolute pressure of about 21 kPa and then purged with Ar (100 mL/min) for about 3 minutes. The evacuation and Ar filling procedure was repeated three to four times. During the entire heating/cooling cycle a steady flow of Ar was maintained. The oxygen partial pressure in the chamber was monitored by an oxygen analyzer (Model 6000, Illinois Instruments, Inc. Johnsburg, IL) and it ranged between 0.10% and 0.21%.

In this study, a sine wave excitation was used as the input signal. RUS spectra were taken between ~ 50 kHz and 500 kHz depending on the specimen dimensions. The scan step was set at 13 to 15 Hz for each of the RUS spectra.

The temperature in the furnace chamber was monitored using a K-type thermocouple, where the thermocouple bead was placed within 3 to 4 mm of the specimen. The nominal heating and cooling rates were 5 K/min. For temperatures below approximately 473 K, lack of active cooling of the furnace resulted in an actual cooling rate of that approximately 2 K/min rather than the programmed cooling rate of 5 K/min.

When the temperature reached one of the hold points (listed below), a 5-minute isothermal hold allowed the specimen to achieve thermal equilibrium. The acoustic spectra were then taken during another 5-minute isothermal hold. A spectrum scan was typically completed within 2 minutes.

Two individual sets of RUS measurements were conducted on specimens L145 and N138 seven months apart to check the repeatability of the RUS measurements. During the first of elasticity measurements of ingot specimens L145 and N138, the RUS spectra were taken between room temperature and 723 K with a 50 K interval up heating and at 523 K during cooling. For the second measurements of L145 and N138, RUS scans were performed between room temperature and 773 K with a 50 K interval during both heating and cooling.

For the hot pressed specimen UMHP6, the RUS spectra were scanned between room temperature and 573 K with a 50 K interval during both heating and cooling, while measurements of MSUHP6 were taken between room temperature and 603 K with a 30 K interval upon heating and cooling.

The heating and cooling rates during all the RUS measurements were 5 K/min with

two 5-minute isothermal holds at each temperature. The first isothermal hold allowed the specimen temperature to come to thermal equilibrium. The RUS scans were completed during the second isothermal hold.

4. Data analysis

4.1 Elasticity calculations

Based on specimen dimensions, mass and an initial estimate of the Young's modulus and Poisson's ratio, a "theoretical" or predicted spectrum was calculated for the specimen [Migliori 1997, Ulrich 2002]. An initial estimate for the Young's modulus was obtained via nanoindentation technique for the dense specimens L145, N138, and MSUHP6 (Table 3.4.2a) (Section 3.2), while the initial estimate of UMHP6 was obtained by extrapolating the Young's modulus versus porosity relationship to the relative density of about 85% (Section 5.2.1).

The initial estimate of 0.27 for the Poisson's ratio was obtained from the literature for pure PbTe [Houston 1968, Einspruch 1963, Simmons 1971]. Since the compositions of all the specimens included in this study are based on doped PbTe, PbTe is then reasonable to use as a comparison material to LAST and Sn- and S- doped PbTe, although the elastic properties of a solid solution system such as LAST can change appreciably with composition [Ren 2007b, Bouarissa 2003, Hassan 2005, Mokhtari 2004, Rao 2003, Ravinder 2001, Watanabe 2001].

Using a nonlinear least-squares fitting program (RPModel, Quasar International, Inc.

Albuquerque, NM), the predicted spectrum was then used as the initial guess in fitting the acoustic spectrum to the calculated vibrational modes of the specimen (Figure 3.4.6).

Successive iterations then gave the least-squares best-fit values for the elastic moduli and Poisson's ratio (Section 2.2). The fitting software calculated an rms error as a measure of the "goodness-of-fit" for the overall fit of the experimentally determined RUS spectrum to the calculated vibrational modes of the specimen. Only those fitting attempts with an rms error of less than one-percent were used to calculate the elastic moduli and Poisson's ratio. (Each of the measured RUS spectra in the first set of measurements was successfully fit with an rms error of less than one percent, while data analysis of the second set of measurements yielded rms values less than 0.33 %.)

4.2 Error calculation for Young's modulus, E, and Poisson's ratio, ν

The errors dE and dν in the calculated Young's modulus and Poisson's ratio were calculated from the elastic constants c_{11} and c_{44}. Based on nanoindentation results that will be presented in Section 5, it was assumed that the four polycrystalline specimens included in this study are elastically isotropic. For elastically isotropic polycrystalline materials, the two independent elastic constants, c_{11} and c_{44}, are related to the Young's modulus, E, and Poisson's ratio ν by [Nye 1967]:

$$E = \frac{c_{44}(3c_{11} - 4c_{44})}{c_{11} - c_{44}} \quad \text{and} \quad \nu = \frac{c_{11} - 2c_{44}}{2(c_{11} - c_{44})} \tag{3}$$

Computing the total differential dE gives

$$dE = \frac{d\left[\frac{c_{44}(3c_{11}-4c_{44})}{c_{11}-c_{44}}\right]}{dc_{11}}dc_{11} + \frac{d\left[\frac{c_{44}(3c_{11}-4c_{44})}{c_{11}-c_{44}}\right]}{dc_{44}}dc_{44}$$

$$= \frac{c_{44}^2 dc_{11} + (3c_{11}^2 - 8c_{11}c_{44} + 4c_{44}^2)dc_{44}}{(c_{11}-c_{44})^2} \quad (4)$$

The total differential dv is

$$dv = \frac{d\left[\frac{c_{11}-2c_{44}}{2(c_{11}-c_{44})}\right]}{2dc_{11}}dc_{11} + \frac{d\left[\frac{c_{11}-2c_{44}}{2(c_{11}-c_{44})}\right]}{2dc_{44}}dc_{44} = \frac{c_{44}dc_{11} - c_{11}dc_{44}}{2(c_{11}-c_{44})^2} \quad (5)$$

The uncertainties dc_{11} and dc_{44} in the RUS measurements of c_{11} and c_{44}, respectively, were provided by the RUS software (RPModel, Quasar International, Inc. Albuquerque, NM). In this study, dc_{11} ranged between 0.1% and 1.7% while dc_{44} was between 0.01% and 0.22%.

5. Results and discussion

5.1 EDS results

Giving the semi-quantitative nature of the EDS technique, the observed composition of hot pressed specimens MSUHP6 and UMHP6 was consistent with the nominal composition (Table 3.4.3). For the ingot specimen L145, the observed concentration of Pb, Sn, and Te compared fairly well with the nominal composition (Table 3.4.3). However the observed S concentration was considerably higher than the nominal concentration. For ingot specimen N138, the observed Pb and Te compared well with the nominal compositions, while the concentrations of Ag and Sb elements were lower by

Table 3.4.3. Comparison between nominal composition and measured composition obtained from EDS. The values are atomic percentage.

Specimen	Composition	Ag	Pb	Sb	Te
$Ag_{0.43}Pb_{18}Sb_{1.2}Te_{20}$	Nominal	1.1	45.4	3.0	50.5
MSUHP6	Measurement	0.8	45.1	3.9	50.1
UMHP6	Measurement	0.9	45.6	2.9	50.5
N138	Measurement	0.6	45.6	1.8	52.0
	Composition	Pb	Sn	Te	S
$Pb_{0.95}Sn_{0.05}Te_{0.92}S_{0.08}$	Nominal	50.8	2.7	49.2	4.3
L145A	Measurement	49.1	2.7	50.9	18.1

about 40% to 45% than the nominal (Table 3.4.3).

The difference between observed compositions and the nominal compositions for ingot specimens (L145 and N138) may result from the compositional inhomogeneity in cast ingots due to composition segregation during cooling [Nolas 2001]. In contrast, materials fabricated from powder processing such as hot pressing likely have uniform composition distributions.

The results shown in Table 3.4.3 are in general agreement with the results of a recent study in which the present authors showed that the composition of the powders derived from cast LAST ingots is essentially the same as the nominal composition of the ingots [Pilchak 2007]. Thus, the EDS results from this study and the earlier study by Pilchak *et al.* [Pilchak 2007] indicate that there are no significant shifts in composition from that of the raw materials (the nominal composition) to the composition of the cast ingots, ground powders, or hot pressed materials.

5.2 Nanoindentation results

5.2.1. Nanoindentation measurements to provide initial guesses for RUS modulus calculations

In order to provide initial guesses for RUS fitting program (Section 2.2), nanoindentation was performed on the polished surfaces of the four specimens. Young's modulus measured by nanoindentation (Table 3.4.4) along with a Poisson's ratio of 0.27 for pure PbTe [Houston 1968] were used as the initial guesses for specimens L145, N138,

Table 3.4.4. Values of Young's modulus obtained from the nanoindentation measurements that were used to generate the "initial guesses" for the RUS calculations.

Specimen	L145	N138	MSUHP6
Young's modulus (GPa)	58.51 ± 1.29	57.35 ± 2.32	52.04 ± 2.47

Table 3.4.5. Young's modulus measured by nanoindentation as a function of indent locations (Figure 3.4.5).

	Young's modulus (GPa)					
Specimen	A	B	C	D	E	F
L145	50.6 ± 2.4	51.4 ± 2.6	50.2 ± 2.2	53.3 ± 1.5	57.7 ± 2.7	55.8 ± 1.4
N138	59.6 ± 1.6	58.8 ± 2.4	56.8 ± 1.3	55.1 ± 2.6	65.2 ± 3.8	66.3 ± 2.8
UMHP6	41.6 ± 2.5	39.7 ± 1.6	44.1 ± 2.0	43.9 ± 2.9	44.5 ± 2.2	44.2 ± 2.3
MSUHP6	53.5 ± 3.8	53.5 ± 4.6	51.0 ± 3.8	53.3 ±4.2		

and MSUHP6.

5.2.2. Nanoindentation measurements to assess the elastic isotropy of the specimens included in this study

In order to determine whether or not the four polycrystalline specimens measured in this study by the RUS technique can be approximated as being elastically isotropic (Section 2.2), an independent elastic modulus measurement technique was needed to assess the elastic moduli as a function of specimen orientation. In this study, the nanoindentation technique was selected as the technique to independently determine the specimen's elastic isotropy or anisotropy. The four specimens were nanoindented at differing locations (Fig 5a and Fig 5b), with the result that the elastic modulus was relatively independent of specimen orientation (Table 3.4.5 and Figure 3.4.7).

5.3 Elastic moduli measured via RUS

5.3.1 Room temperature Young's modulus as a function of porosity

The initial estimate of Young's modulus for specimens L145, N138, and MSUHP6 (Table 3.4.2a) were determined from nanoindentation (Section 5.2.1). However, since UMHP6 has a relative density of approximately 85% (Table 3.4.2a), and Surface-limited nanoindentation technique may overestimate the Young's modulus of bulk materials by up to ~ 50% due to its insensitivity to defects such as cracks and pores [Ren 2007b, Radovic 2004], Young's modulus measured from nanoindentation was not used as the initial guess in RUS for UMHP6.

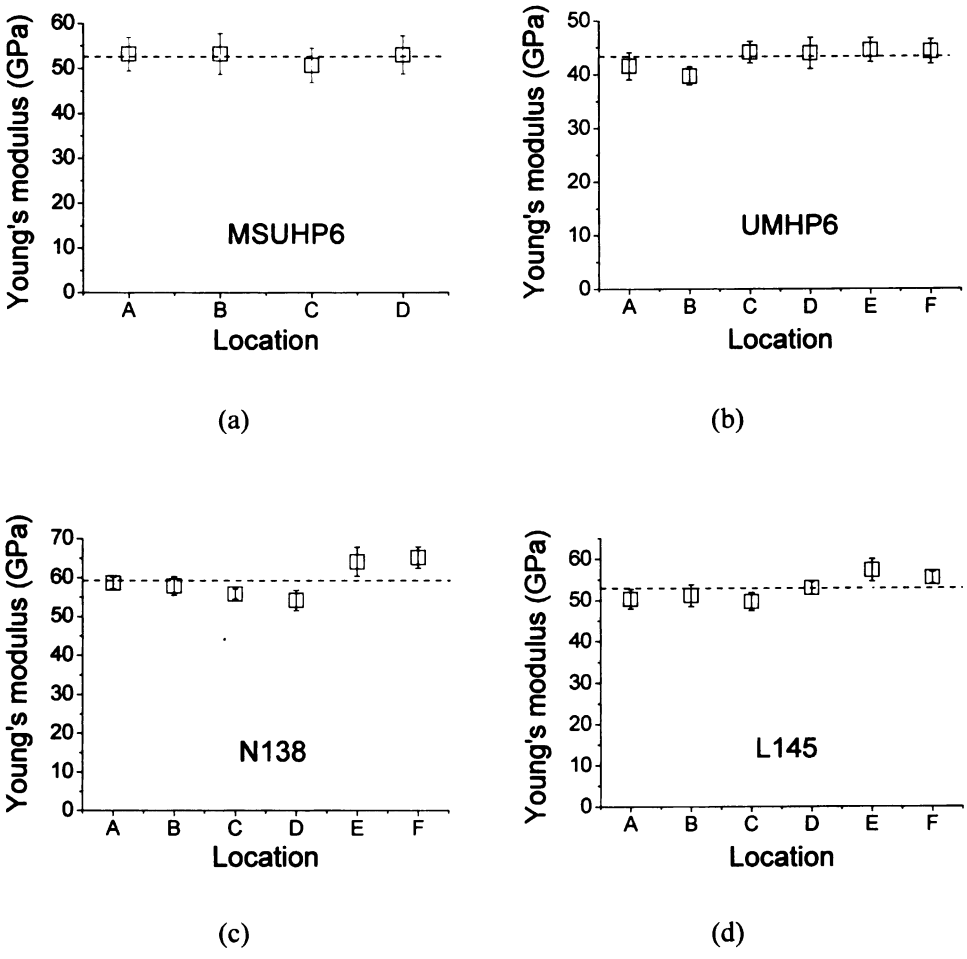

Figure 3.4.7. Young's modulus measured by nanoindentation as a function of indent location (Figure 3.4.5) on specimens (a) MSUHP6, (b) UMHP6, (c) N138, and (d) L145. No significant anisotropy was observed for all four specimens. The dash lines indicate the mean values of the Young's modulus for each specimen.

In order to obtain an appropriate initial guess for UMHP6, two additional hot pressed specimens, MSUHP5 and MSUHP7 that have the identical composition but different porosity (Table 3.4.6), were included to obtain the relationship between room temperature Young's modulus and volumetric porosity. The room temperature Young's modulus values of MSUHP5, MSUHP6, and MSUHP7 (Table 3.4.2b and Table 3.4.6) were then fit to [Rice 1998]:

$$E(P) = E_d \exp(-b' P) \qquad (6)$$

where E(P) is a function of porosity, P, E_d is the Young's modulus of dense material, and b' is a constant. The non-linear least-squares fitting to Eq. (6) yield an E_d of 61 ± 2 GPa and a b' of 4.9 ± 0.5 with an r^2 of 0.98 (Figure 3.4.8), from which a Young's modulus of 27GPa for P = 0.15 was calculated as the initial guess for specimen UMHP6.

5.3.2 Young's modulus and Poisson's ratio as a function of temperature

For polycrystalline materials, typically E decreases linearly with increasing temperature until viscoelastic grain boundary sliding occurs at elevated temperatures [Wachtman 1996] (Figure 3.4.2). For the four specimens examined in this study, Young's modulus of the Sn- and S- doped ingot specimen L145 decreased linearly from room temperature up to about 800 K (Figure 3.4.9a). Linear least-squares fitting of L145 data to Eq. (2c) yields an intercept (E0) of 51.54 ± 0.03 GPa and a slope (b) of 3.40 ± 0.02 K-1 with coefficient of determination r2 of 0.998 (Table 3.4.7). The LAST ingot specimen N138 exhibited a linear E-T relationship between room temperature and 723 K (Figure 3.4.9b) with

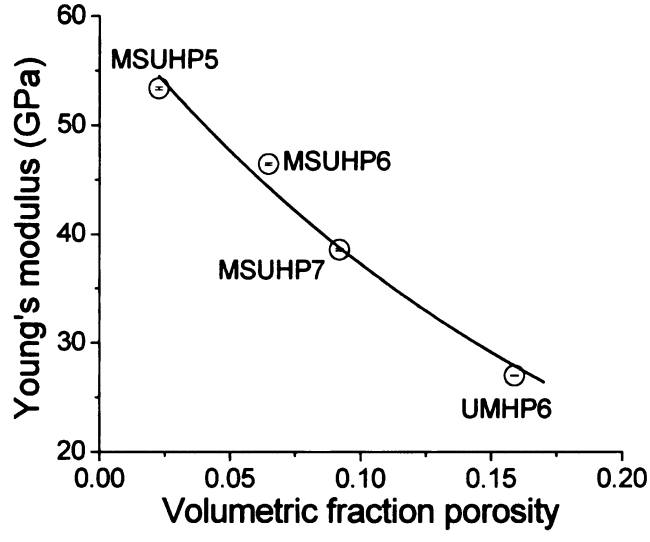

Figure 3.4.8. Room temperature RUS measurement of Young's modulus as a function of porosity for hot pressed LAST ($Ag_{0.43}Pb_{18}Sb_{1.2}Te_{20}$) specimens MSUHP5, MSUHP6, and MSUHP7 as determined from non-linear least-squares fitting to Eq. (6). A Young's modulus of about 27 GPa was extrapolated to the volumetric fraction porosity of about 0.16, which was used as the initial guess in RUS fitting program for specimen UMHP6.

Table 3.4.6. For three hot pressed n-type LAST specimens, room temperature Young's modulus measurement via RUS as a function of volume fraction porosity. All three specimens have the identical composition ($Ag_{0.43}Pb_{18}Sb_{1.2}Te_{20}$) and processing technique as UMHP6 (Table 3.4.2).

Specimen	Relative density	Volume fraction porosity	Young's modulus (GPa)
MSUHP5	0.978	0.022	53.36 ± 0.24
MSUHP6	0.942	0.058	46.44 ± 0.12
MSUHP7	0.908	0.092	38.74 ± 0.22

Table 3.4.7. Linear temperature dependence of Young's modulus for specimens L145, N138, UMHP6, and MSUHP6 as determined by linear least-squares fitting to Eq. (2c) over the given temperature range.

Specimen	$E(T) = E_0(1 - bT)$ (Eq. (2c))			Temp. Range
	E_0 (GPa)	b (x 10^{-4} K^{-1})	r^2	
L145	51.54±0.03	3.40±0.02	0.998	RT to 773 K
N138	50.99±0.07	3.90±0.05	0.994	RT to 773 K
MSUHP6	46.06±0.05	4.90±0.08	0.996	RT to 503 K
UMHP6	26.97±0.01	1.30±0.04	0.994	RT to 473 K
	26.59±0.03	0.50±0.05	0.96	473K to 573 K

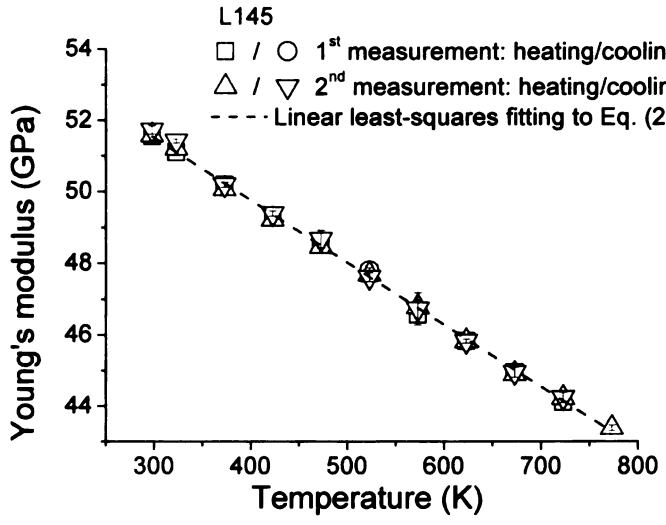

(a)

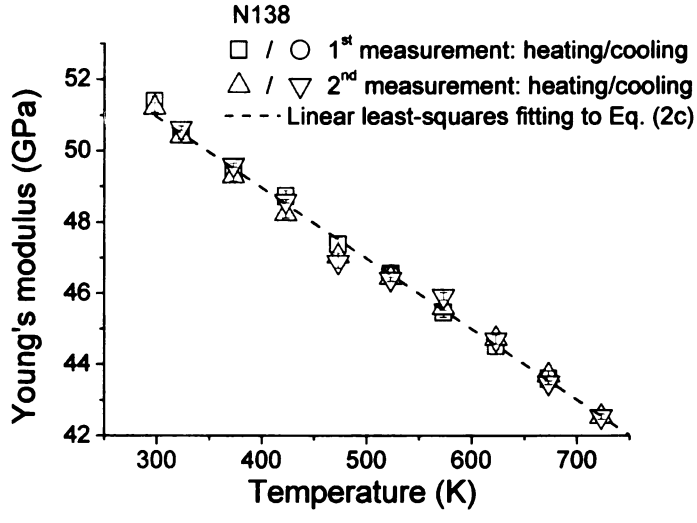

(b)

Figure 3.4.9. Young's modulus as a function of temperature with linear least-squares fitting to Eq. (2c) for specimens (a) L145, (b) N138, (c) MSUHP6, and (d) UMHP6 included in this study.

Figure 3.4.9 continued.

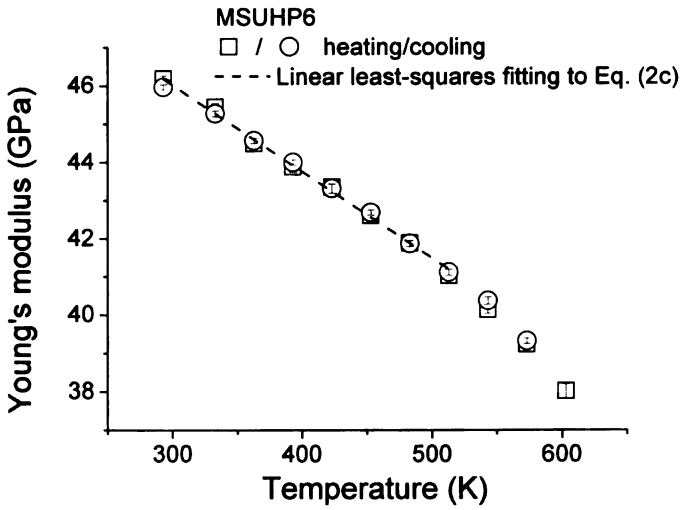

(c)

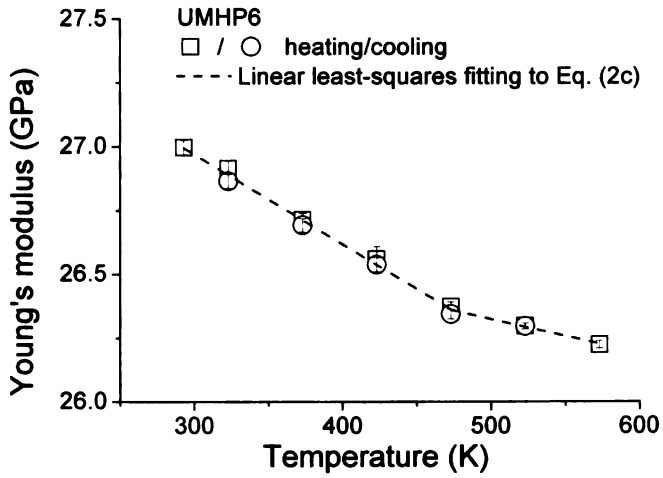

(d)

$E_0 = 50.99 \pm 0.07$ GPa, $b = 3.90 \pm 0.05$ K^{-1}, and $r^2 = 0.994$ (Table 3.4.7) as determined from linear least-squares fitting to Eq. (2c).

For the dense hot pressed specimen MSUHP6, Young's modulus decreased linearly between room temperature and about 500 K (Figure 3.4.9c), with $E_0 = 46.06 \pm 0.0$ GPa, b $= 4.90 \pm 0.08$ K^{-1}, and $r^2 = 0.996$ (Table 3.4.7). However, above 500 K the Young's modulus of MSUHP6 deviated from the linear relationship and showed a rapid decrease with increasing temperature (Figure 3.4.9c), which is likely due to grain boundary softening and sliding [Wachtman 1996].

The Young's modulus of hot pressed specimen UMHP6 showed a linear temperature dependence between room temperature and approximately 470 K (Figure 3.4.9d), where $E_0 = 26.97 \pm 0.01$ GPa, $b = 1.30 \pm 0.04$ K^{-1}, and $r^2 = 0.994$ (Table 3.4.7), as determined from linear least-squares fitting to Eq. (2c). A "kink" (slope change) around 470 K was observed in the E-T relationship, where the slope between about 470 K and 570 K is 0.50 ± 0.05 K^{-1} (Table 3.4.7). Dole and coworkers [Dole 1983] observed similar slope changes in the temperature dependent Young's modulus for $Tb_2Hf_2O_7$ and $Tb_2Zr_2O_7$, which was believed to originate from point defect relaxation [Wachtman 1963a, 1963b].

In general, Poisson's ratio, ν, may either increase or decrease as a function of temperature [Simmons 1971]. For example, Poisson's ratio of dense $LaNi_5$ fabricated by hot isostatic pressing increases monotonically from about 0.307 at 0 K to 0.313 at 400 K [Atteberry 2004], while Poisson's ratio of polycrystalline ZrCo first decreases from 0.3385 at 0 K to 0.338 at 40 K, and then increased to 0.3435 near 400 K [Agosta 2002].

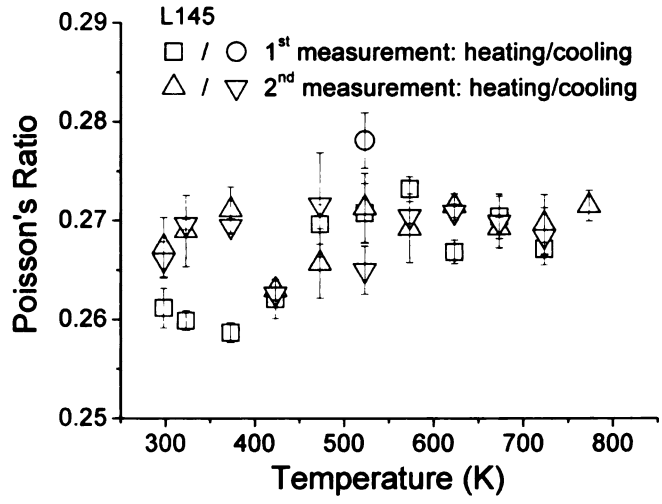

(a)

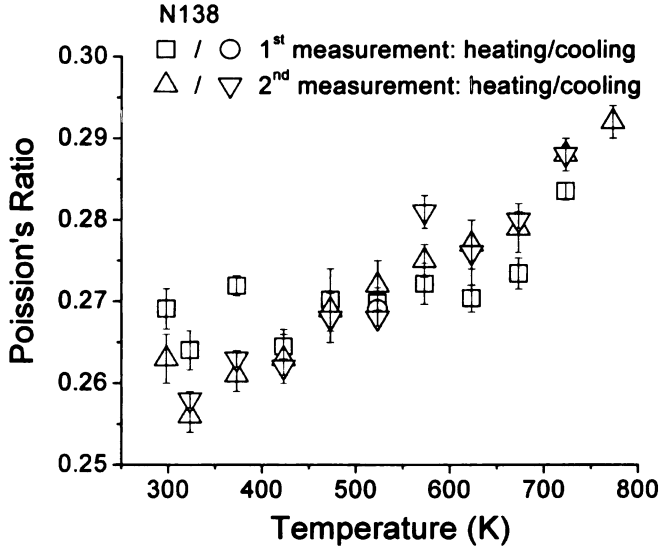

(b)

Figure 3.4.10. Temperature dependent Poisson's ratio for specimens (a) L145, (b) N138, (c) MSUHP6, and (d) UMHP6 included in this study.

Figure 3.4.10 continued.

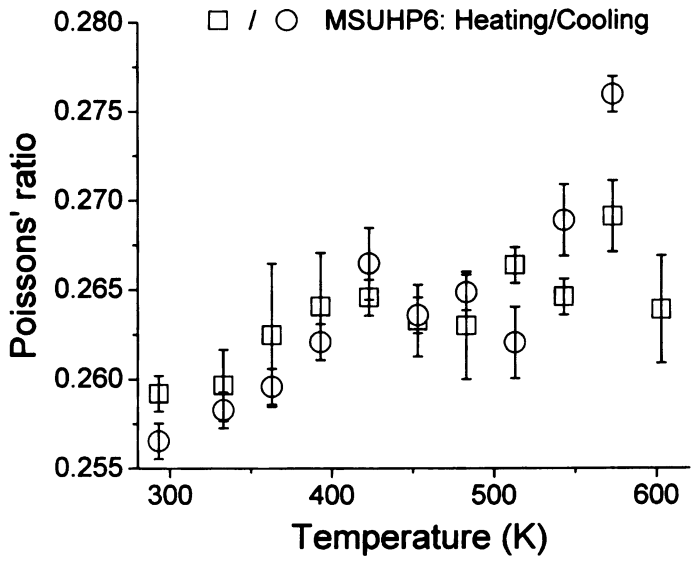

(c)

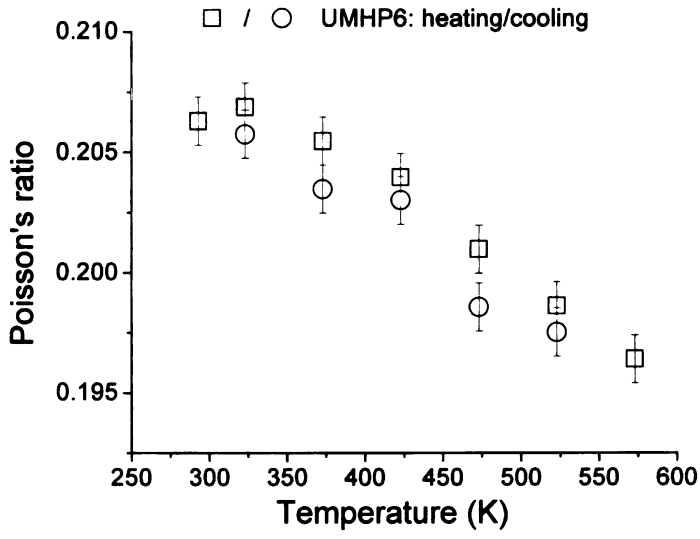

(d)

For CMSX-4 superalloy, the Poisson's ratio of the system remains relatively constant around 0.395 between 300 K and 1000 K then jumps to 0.42 at about 1250 K, while in contrast the Poisson's ratio of the matrix phase and the inclusion phase both exhibit nearly linear temperature dependence [Sieborger 2001].

In this study, the Poisson's ratio of the Sn- and S- doped ranged between approximately 0.26 and 0.28 (Figure 3.4.10a), while for the ingot LAST specimen N138, ν monotonically increased from about 0.26 at room temperature to 0.29 at approximately 800 K (Figure 3.4.10b).

For the dense hot pressed specimen MSUHP6, Poisson's ratio increased from about 0.255 to 0.275 when temperature increased from room temperature to 600 K (Figure 3.4.10c), while a monotonic decrease in Poisson's ratio from about 0.205 at room temperature to 0.195 at 550 K was observed for UMHP6 (Figure 3.4.10d).

The Young's modulus-temperature slope for the specimens obtained in this study over the range between room temperature and about 800 K (Table 3.4.7) is smaller than the Young's modulus-temperature slope for pure PbTe data in literature over the range from 0 K to room temperature [Houston 1968] (Figure 3.4.11a). For Poisson's ratio, ν versus T relationship for the TE materials included in this study seems to follow the ν-T curve of the pure PbTe between 0 K and 300 K [Houston 1968], except for specimen UMHP6 that has a decreasing Poisson's ratio with increasing temperature (Figure 3.4.11b).

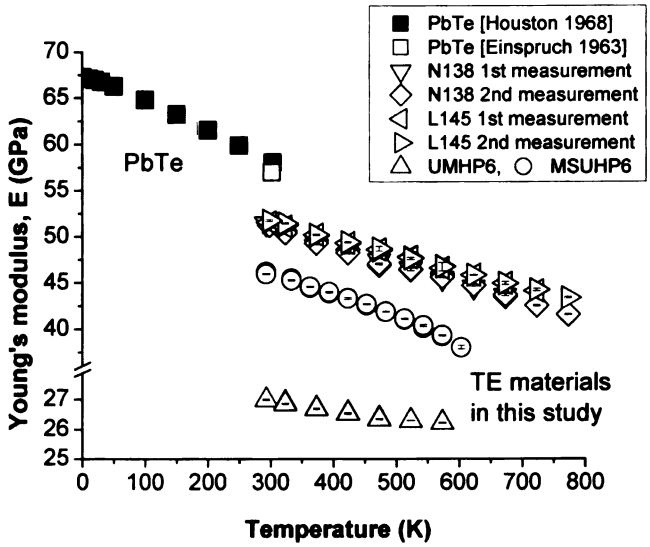

(a)

Figure 3.4.11. Comparison between literature data of pure PbTe [Houston 1968, Einspruch 1963] with TE materials included in the current study in terms of (a) Young's modulus as a function of temperature, (b) temperature dependent Poisson's ratio, and (c) the effective modulus, $E/(1-\nu)$, as a function of temperature.

Figure 3.4.11 continued.

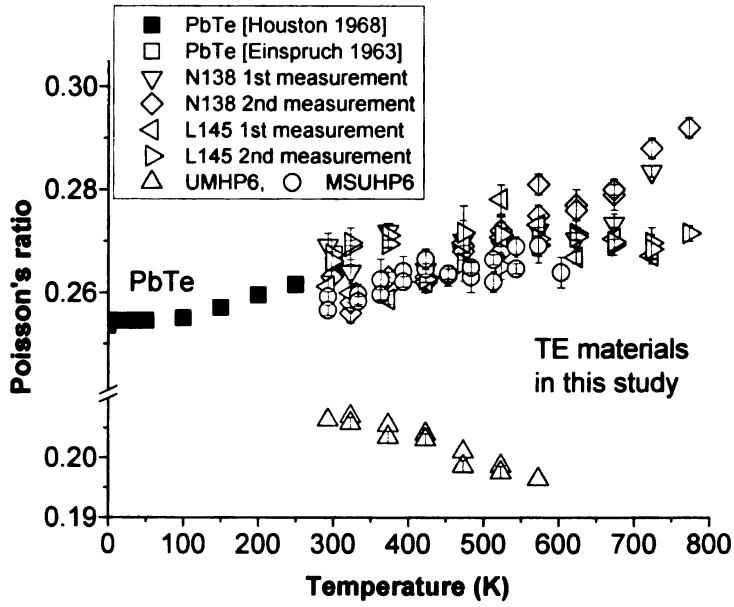

(b)

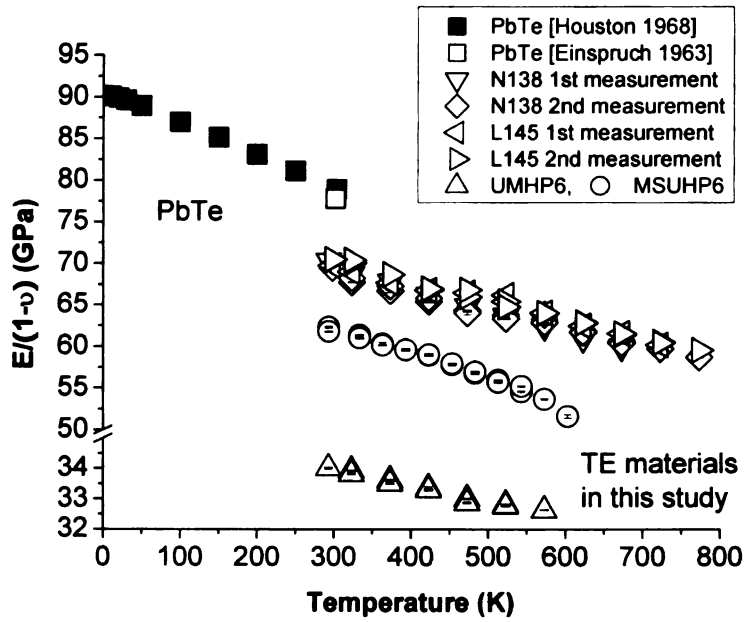

(c)

It should be noted that there are no temperature-dependent data for the Young's modulus and Poisson's ratio of pure PbTe available above room temperature in the literature and there are no temperature-dependent data available for any LAST compounds. Thus, we can not directly compare the elastic modulus-temperature behavior of our materials over the range between room temperature and about 800 K for LAST or for pure PbTe. Again, while LAST may be viewed as a doped PbTe compound, the elastic moduli can change considerably with doping [Ren 2007b, Bouarissa 2003, Hassan 2005, Mokhtari 2004, Rao 2003, Ravinder 2001, Watanabe 2001].

Eq. (1) shows that the quantity $E/(1-\nu)$, or the effective modulus, is central to the calculation of stress. The plots of the effective modulus $E/(1-\nu)$ versus temperature are very similar for the Sn- and S- doped PbTe ingot specimen and the LAST ingot specimen, thus the elevated temperature stress-strain response of the two ingot materials should be very similar over the temperature range of the data (room temperature to about 800 K) (Figure 3.4.11c). Hot pressed specimen MSUHP6 exhibits a lower effective modulus than the ingot specimens between room temperature and about 600 K (Figure 3.4.11c), which implies the magnitude of thermal stress due to the same temperature difference (Eq. (1)) will be less for MSUHP6 than the two ingot specimens. For hot pressed specimen UMHP6, the effective modulus is much lower than the pure PbTe [Houston 1968] and other TE materials included in this study (Figure 3.4.11c), likely due to the porosity induced reduction in Young's modulus.

It should be noted that the maximum ZT of the PbTe-based thermoelectric materials

included in this study occurs at roughly 700 K [Hsu 2004], so the temperature range for the modulus measurements included in this study (room temperature to 773 K) includes the much of the useful temperature range for these materials.

In addition, the shallow slope of the E/(1-ν) versus temperature curves (Figure 3.4.11c) indicates that the stress-strain response of the four PbTe-based specimens is relatively insensitive to temperature over the range from room temperature to about 800 K. The E/(1-ν) – temperature slope values for the Sn-S doped ingot specimen, the ingot LAST specimen, and the dense hot pressed LAST specimen are approximately -0.023 GPa/K, -0.021 GPa/K and -0.028 GPa/K, while porous hot pressed LAST specimen has a slope of only -0.005 GPa/K (Figure 3.4.11c). In contrast the E/(1-ν) -temperature slope for pure PbTe is approximately -0.04 GPa/K, between 100 and 300 K (Figure 3.4.11c).

6. Summary and Conclusions

Using RUS, we have examined the elastic properties (Young's modulus and Poisson's ratio) for four PbTe-based thermoelectric compounds as functions of temperature between room temperature and 773 K, which includes much of the temperature range these materials would be subjected to in applications such as thermoelectric power generation from waste heat. This study also represents one of the few studies of the temperature-dependent Young's modulus and Poisson's ratio for thermoelectric materials that includes temperatures well above room temperature. Such studies are critical for the development of viable thermoelectric devices since a detailed finite element

calculation of stresses within a thermoelectric module must include the stresses generated within the thermoelectric materials themselves as well as those that arise from temperature gradients and from interconnections with the other components of the module.

For the PbTe-based materials included in this study, the effective modulus $E/(1-\nu)$ is relatively insensitive to temperature over the range of 300 K to 773 K, which indicates that thermally induced stresses within the material should vary relatively slowly with temperature. Although the relatively small slope of $E/(1-\nu)$ versus temperature should be beneficial to designers, a complete stress analysis (such as by FEA) should include the detailed influence of the other components of the module.

Acknowledgements

The authors acknowledge the financial assistance of the U. S. Department of Energy Grant DE-FC26-04NT42281 and Office of Naval Research MURI Grant number N000140310789. The research work at the High Temperature Materials Laboratory was sponsored by the Assistant Secretary for Energy Efficiency and Renewable Energy, Office of Freedom CAR and Vehicle Technologies, as part of the High Temperature Materials Laboratory User Program, Oak Ridge National Laboratory, managed by UT-Battelle, LLC, for the U.S. Department of Energy under contract number DE-AC05-00OR22725. The authors would like to thank Mr. M. Kim Johnson at Quasar International, Inc. for his helpful discussion on error estimation for the RUS technique.

Also, the authors thank Dr. Michael Atzmon of the University of Michigan, Ann Arbor, for the use of the Materials Science Department's hot pressing in fabricating the LAST specimen UMHP6.

References

[Agosta 2002] D. S. Agosta, J. E. Hightower, K. Foster, R. G. Leisure and Z. Gavra, "Elastic moduli of polycrystalline ZrCo as a function of temperature", *Journal of Alloys and Compounds*, **346**: 1-5 (2002).

[Ali Omar 1975] M. Ali Omar, *Elementary Solid State Physics*, (Addison-Wesley Publishing Company, Inc., Reading, Massachusetts, 1975), pp. 84.

[Anderson 1966] O. L. Anderson, "Derivation of Wachtmans Equation for Temperature Dependence of Elastic Moduli of Oxide Compounds", *Physical Review*, **144**: 553-557 (1966).

[Androulakis 2006] J. Androulakis, K. F. Hsu, R. Pcionek, H. Kong, C. Uher, J. J. DAngelo, A. Downey, T. Hogan and M. G. Kanatzidis, "Nanostructuring and high thermoelectric efficiency in p-type Ag(Pb1-ySny)(m)SbTe2+m", *Advanced Materials*, **18**: 1170-1173 (2006).

[Androulakis 2007] J. Androulakis, C. H. Lin, H. Kong, C. Uher, C. I. Wu, T. Hogan, B. A. Cook, T. Caillat and M. G. Kanatzidis, "Spinodal Decomposition and Nucleation and Growth as a Means to Bulk Nanostructured Thermoelectrics: Enhanced Performance in Pb1-xSnxTe-PbS", *Journal of the American Chemical Society*, **129**: 9780-9788 (2007).

[Atteberry 2004] J. E. Atteberry, D. S. Agosta, C. E. Nattrass, R. G. Leisure, I. Jacob, R. C. Bowman and O. Yeheskel, "Temperature dependence of the elastic moduli of polycrystalline LaAlxNi5-(x) and LaSnxNi5-x", *Journal of Alloys and Compounds*, **376**: 139-144 (2004).

[Bouarissa 2003] N. Bouarissa, "Compositional dependence of the elastic constants and the Poisson ratio of GaxI1-xSb", *Materials Science and Engineering B-Solid State*

Materials for Advanced Technology, **100**: 280-285 (2003).

[Briscoe 1957] C. V. Briscoe and C. F. Squire, "Elastic Constants of Lif from 4.2-Degrees-K to 300-Degrees-K by Ultrasonic Methods", *Physical Review*, **106**: 1175-1177 (1957).

[Budiansky 1976] B. Budiansky and R. J. Oconnell, "Elastic-Moduli of a Cracked Solid", *International Journal of Solids and Structures*, **12**: 81-97 (1976).

[Case 1981] E. D. Case, J. R. Smyth and O. Hunter, "Microcracking in large grain Al2O3", *Mater. Sci. and Eng.*, **51**: 175-179 (1981).

[Case 1983] E. D. Case, J. R. Smyth and O. Hunter, "Microcrack healing during temperature cycling of single phase ceramics", in *Fracture Mechanics of Ceramics, Vol.5*, edited by R. C. Bradt, A. G. Evans, D. P. H. Hasselman and F. F. Lange (Plenum Press, New York, 1983), pp. 507-530.

[Case 1993] E. D. Case, Y. Kim and W. J. Lee, "Cyclic thermal shock in SiC whisker reinforced alumina and in other ceramic systems", in *Proceedings of the Thermal Shock Behavior and Thermal Fatigue of Advanced Ceramics*, edited by G. A. Schneider and G. Petzow (Kluwer Academic Publishers, the Nederlands, 1993), pp. 393-406.

[Case 2002] E. D. Case, "The Saturation of Thermomechanical Fatigue in Brittle Materials", in *Thermo-Mechanical Fatigue and Fracture*, edited by M. H. Alibadi (WIT Press, Southampton, UK, 2002), pp. 137-208.

[Chen 2003] G. Chen, M. S. Dresselhaus, G. Dresselhaus, J. P. Fleurial and T. Caillat, "Recent developments in thermoelectric materials", *International Materials Reviews*, **48**: 45-66 (2003).

[Cheng 1951] C. M. Cheng, "Resistance to thermal shock", *J. Am. Rocket Soc.*, **21**: 147-153 (1951).

[Dole 1983] S. L. Dole and O. Hunter, "Elastic Properties of Hafnium and Zirconium-Oxides Stabilized with Praseodymium or Terbium Oxide", *Journal of the American Ceramic Society*, **66**: C47-C49 (1983).

[Dulikravich 1999] G. S. Dulikravich, T. J. Martin and B. H. Dennis, "Multidisciplinary inverse problems", in *Inverse problems in engineering: theory and practice*, edited by K. A. Woodbury (The American society of mechanical engineers, New York, 1999), 1-8.

[Einspruch 1963] N. G. Einspruch and R. J. Manning, "Elastic Constants of Compound Semiconductors Zns, Pbte, Gasb", *Journal of the Acoustical Society of America*, **35**: 215-216 (1963).

[Gates 1977] R. S. Gates and C. A. P. Horton, "Grain-Boundary Sliding in Type-316 Austenitic Steels .1. Grain-Size Dependence", *Materials Science and Engineering*, **27**: 105-114 (1977).

[Gifkins 1977] R. C. Gifkins, "Effect of Grain-Size and Stress Upon Grain-Boundary Sliding", *Metallurgical Transactions a-Physical Metallurgy and Materials Science*, **8**: 1507-1516 (1977).

[Grant 1953] N. J. Grant, I. S. Servi and A. Chaudhuri, "Slip and Grain Boundary Sliding as Affected by Grain Size", *Transactions of the American Institute of Mining and Metallurgical Engineers*, **197**: 217-218 (1953).

[Hassan 2005] F. E. Hassan and H. Akbarzadeh, "First-principles investigation of BNxP1-x, BNxAs1-x and BPxAs1-x ternary alloys", *Materials Science and Engineering B-Solid State Materials for Advanced Technology*, **121**: 170-177 (2005).

[Houston 1968] B. Houston, R. E. Strakna and H. S. Belson, "Elastic Constants Thermal Expansion and Debye Temperature of Lead Telluride", *Journal of Applied Physics*, **39**: 3913-3916 (1968).

[Hsu 2004] K. F. Hsu, S. Loo, F. Guo, W. Chen, J. S. Dyck, C. Uher, T. Hogan, E. K. Polychroniadis and M. G. Kanatzidis, "Cubic AgPbmSbTe2+m: Bulk thermoelectric materials with high figure of merit", *Science*, **303**: 818-821 (2004).

[Incropera 1985] F. P. Incropera and D. P. Dewitt, *Introduction to Heat Transfer*, (John Wiley and Sons, New York, 1985), pp. 431.

[Kac 1966] M. Kac, "Can One Hear the Shape of a Drum?" *American Mathematical*

Monthly, **73**: 1-23 (1966).

[Kaliakin 2002] V. N. Kaliakin, *Introduction to Approximate Solution Techniques, Numerical Modeling, and Finite Element Methods*, (Marcel Dekker, Inc., New York, 2002),

[Kim 1991] Y. Kim, W. J. Lee and E. D. Case, "The measurement of the surface heat transfer coefficient of ceramics quenched into a water bath", *Mater. Sci. and Eng. A*, **145**: L7-L11 (1991).

[Kingery 1976] W. D. Kingery, H. K. Bowen and D. R. Uhlmann, *Introduction to ceramics (2nd edition)*, (Wiley-Interscience, New York, 1976), pp. 816-823.

[Kosuga 2005] A. Kosuga, M. Uno, K. Kurosaki and S. Yamanaka, "Thermoelectric properties of Ag1-xPb18SbTe20 (x = 0, 0.1, 0.3)", *Journal of Alloys and Compounds*, **387**: 52-55 (2005).

[Laws 1987] N. Laws and J. R. Brockenbrough, "The Effect of Micro-Crack Systems on the Loss of Stiffness of Brittle Solids", *International Journal of Solids and Structures*, **23**: 1247-1268 (1987).

[Lee 1989] W. J. Lee and E. D. Case, "Cyclic Thermal-Shock in Sic-Whisker-Reinforced Alumina Composite", *Materials Science and Engineering a-Structural Materials Properties Microstructure and Processing*, **119**: 113-126 (1989).

[Lee 1990] W. J. Lee and E. D. Case, "Thermal Fatigue in Polycrystalline Alumina", *Journal of Materials Science*, **25**: 5043-5054 (1990).

[Lee 1993] W. J. Lee, Y. Kim and E. D. Case, "The effect of quenching media on the heat transfer coefficient of polycrystalline alumina", *J. Mater. Sci.*, **31**: 2079-2083 (1993).

[Lu 1998] T. J. Lu and N. A. Fleck, "The thermal shock resistance of solids", *Acta Mater.*, **46**: 4755-4768 (1998).

[Manson 1966] S. S. Manson, *Thermal Stress and Low Cycle Fatigue*, (McGraw-Hill, New York, 1966), Chapter 7.

[Migliori 1997] A. Migliori and J. L. Sarrao, *Resonant Ultrasound Spectroscopy: Applications to Physics, Materials Measurements, and Nondestructive Evaluation*, (Academic Press, New York, 1997),

[Mokhtari 2004] A. Mokhtari and H. Akbarzadeh, "First principles investigation of the electronic and structural properties of Mg3xBe3-3xN2 ternary alloy", *Journal of Physics-Condensed Matter*, **16**: 6063-6074 (2004).

[Nolas 2001] G. S. Nolas, J. Sharp and H. J. Goldsmid, *Thermoelectrics: basic principles and new materials developments*, (Springer, Berlin; New York, 2001), pp. 151-159.

[Nye 1967] J. F. Nye, *Physical Properties of Crystals* (Oxford University Press, London, 1967),

[Oliver 1992] W. C. Oliver and G. M. Pharr, "An Improved Technique for Determining Hardness and Elastic-Modulus Using Load and Displacement Sensing Indentation Experiments", *Journal of Materials Research*, **7**: 1564-1583 (1992).

[Overton 1955] W. C. Overton and J. Gaffney, "Temperature Variation of the Elastic Constants of Cubic Elements .1. Copper", *Physical Review*, **98**: 969-977 (1955).

[Ozisik 1985] M. N. Ozisik, *Heat Transfer*, (McGraw-Hill, New York, 1985), Chapter 10.

[Pilchak 2007] A. L. Pilchak, F. Ren, E. D. Case, E. J. Timm, H. J. Schock, C. I. Wu and T. Hogan, "Particle size reduction by planetary ball milling and powder characterization of LAST (Lead-Antimony-Silver-Tellurium) thermoelectric material", *Philosophical Magazine*, **87**: 4567-4591 (2007).

[Press 1992] W. H. Press, *Numerical recipes in FORTRAN 77: the art of scientific computing*, (Cambridge University Press, Cambridge, England, 1992), pp. 53, 111.

[Quarez 2005] E. Quarez, K. F. Hsu, R. Pcionek, N. Frangis, E. K. Polychroniadis and M. G. Kanatzidis, "Nanostructuring, compositional fluctuations, and atomic ordering in the thermoelectric materials AgPbmSbTe2+m. The myth of solid solutions", *Journal of the American Chemical Society*, **127**: 9177-9190 (2005).

[Radovic 2004] M. Radovic, E. Lara-Curzio and L. Riester, "Comparison of different experimental techniques for determination of elastic properties of solids", *Materials Science and Engineering a-Structural Materials Properties Microstructure and Processing*, **368**: 56-70 (2004).

[Rao 2003] S. S. Rao and D. Ravinder, "Composition dependence of elastic moduli of gadolinium-substituted nickel-zinc ferrites", *Materials Letters*, **57**: 3802-3804 (2003).

[Ravinder 2001] D. Ravinder and T. Alivelumanga, "Room temperature elastic behaviour of cadmium substituted manganese ferrites", *Materials Letters*, **49**: 1-6 (2001).

[Ren 2006] F. Ren, E. D. Case, E. J. Timm, M. D. Jacobs and H. J. Schock, "Weibull analysis of the biaxial fracture strength of a cast p-type LAST-T thermoelectric material", *Philosophical Magazine Letters*, **86**: 673-682 (2006).

[Ren 2007a] F. Ren, E. D. Case, E. J. Timm and H. Schock, "Hardness as a function of composition for n-type LAST thermoelectric material", *Journal of Alloys and Compounds*, available online at doi:10.1016/j.jallcom.2007.01.086 (2007a).

[Ren 2007b] F. Ren, E. D. Case, E. J. Timm and H. Schock, "Young's modulus as a function of composition for an n-type lead-antimony-silver-telluride (LAST) thermoelectric material", *Philosophical Magazine*, **87**: 4907-4934 (2007b).

[Rice 1998] R. W. Rice, *Porosity of Ceramics*, (Marcel Dekker, Inc., New York, 1998), pp. 100-131.

[Riffat 2003] S. B. Riffat and X. L. Ma, "Thermoelectrics: a review of present and potential applications", *Applied Thermal Engineering*, **23**: 913-935 (2003).

[Schreiber 1973] E. Schreiber, O. L. Anderson and N. Soga, *Elastic constants and their measurement*, (McGraw-Hill Book Company, New York, 1973),

[Sharma 2003] P. Sharma and S. Ganti, "On the grain-size-dependent elastic modulus of nanocrystalline materials with and without grain-boundary sliding", *Journal of Materials Research*, **18**: 1823-1826 (2003).

[Sharp 2006] J. Sharp, J. Bierschenk and H. B. Lyon, "Overview of solid-state thermoelectric refrigerators and possible applications to on-chip thermal management", *Proceedings of the Ieee*, **94**: 1602-1612 (2006).

[Sieborger 2001] D. Sieborger, H. Knake and U. Glatzel, "Temperature dependence of the elastic moduli of the nickel-base superalloy CMSX-4 and its isolated phases", *Materials Science and Engineering a-Structural Materials Properties Microstructure and Processing*, **298**: 26-33 (2001).

[Simmons 1971] G. Simmons and H. Wang, *Single Crystal Elastic Constants and Calculated Aggregate Properties: a Handbook* (the MIT Press, Cambridge, MA, 1971), pp. ix-x, 200.

[Suess 1961] C. Suess, "Measurement of the elastic constants of LiF and MgO as a function of temperature and pressure", *J. des Recherches du C.N.R.S.*, **54**: 23-59 (1961).

[Tritt 2006] T. M. Tritt and M. A. Subramanian, "Thermoelectric materials, phenomena, and applications: A bird's eye view", *MRS Bulletin*, **31**: 188-194 (2006).

[Ulrich 2002] T. J. Ulrich, K. R. McCall and R. A. Guyer, "Determination of elastic moduli of rock samples using resonant ultrasound spectroscopy", *Journal of the Acoustical Society of America*, **111**: 1667-1674 (2002).

[Varshni 1970] Y. P. Varshni, "Temperature dependence of the elastic constants", *Physical Review B-Solid State*, **2**: 3952-3958 (1970).

[Wachtman 1959] J. B. Wachtman and D. G. Lam, "Young Modulus of Various Refractory Materials as a Function of Temperature", *Journal of the American Ceramic Society*, **42**: 254-260 (1959).

[Wachtman 1963a] J. B. Wachtman, "Mechanical and Electrical Relaxation in Tho2 Containing CaO", *Physical Review*, **131**: 517-527 (1963a).

[Wachtman 1963b] J. B. Wachtman, E. P. Levine and H. S. Peiser, "Symmetry Splitting of Equivalent Sites in Oxide Crystals and Related Mechanical Effects", *Journal of Research of the National Bureau of Standards Section a-Physics and Chemistry*, **A 67**:

281-289 (1963b).

[Wachtman 1996] J. B. Wachtman, *Mechanical Properties of Ceramics*, (Wiley Interscience, New York, 1996), pp. 33-35.

[Watanabe 2001] T. Watanabe, K. Muratsubaki, Y. Benino, H. Saitoh and T. Komatsu, "Hardness and elastic properties of Bi2O3-based glasses", *Journal of Materials Science*, **36**: 2427-2433 (2001).

[Yang 2006] J. H. Yang and T. Caillat, "Thermoelectric materials for space and automotive power generation", *MRS Bulletin*, **31**: 224-229 (2006).

[Zhao 2000] L. T. Zhao, T. J. Lu and N. A. Fleck, "Crack channeling and spalling in a plate due to thermal shock loading", *J. Mech. Phys. Solids*, **48**: 867-897 (2000).

Chapter 5

The high temperature elastic moduli of polycrystalline PbTe measured by resonant ultrasound spectroscopy

1. Introduction

1.1. Temperature dependent Young's modulus and shear modulus for polycrystalline brittle materials

Young's modulus of brittle polycrystalline materials can be described by the empirical Wachtman equation [Wachtman 1996]:

$$E(T) = E_0 - b_E T \exp\left(\frac{-T_0}{T}\right) \quad (1)$$

where E_0 is the Young's modulus at T = 0 K, b_E and T_0 are fitting parameters. Anderson showed b_E is related to Grüneisen parameters, while T_0 approaches 1/2 of the Debye temperature, θ_D, when $T >> \theta_D$ [Anderson 1966].

At temperatures higher than half of the melting temperature, Wachtman equation simplifies to a linear relationship, such that [Wachtman 1996]:

$$E(T) = E_0(1 - b_{E1}T) \quad (2)$$

where E_0 is the extrapolation of the linear Young's modulus versus temperature relationship to 0 K, and b_{E1} is a fitting parameter. In this study, elastic moduli were measured at and above room temperature, or about 298 K. Thus it is convenient to rewrite Eq. (2) as:

$$E(T) = E_{RT}\left[1 - b_{E-RT}(T - 298)\right] \quad (3)$$

where E_{RT} is the room temperature Young's modulus, and $b_{E\text{-}RT}$ is a fitting parameter.

The empirical relationships for Young's modulus (Eqs. (1) and (2)) also apply to the temperature dependent shear modulus for polycrystalline materials [Wachtman 1996], thus for shear modulus as a function of temperature:

$$G(T) = G_0 - b_G T \exp\left(\frac{-T_0}{T}\right) \quad (4)$$

and for $T >> \theta_D$:

$$G(T) = G_{RT}\left[1 - b_{G-RT}(T - 298)\right] \quad (5)$$

where G_0 and G_{RT} are the shear modulus at 0 K and room temperature, while b_G and $b_{G\text{-}RT}$ are fitting parameters.

1.2. Studies of temperature dependent elasticity of PbTe in literature

LAST (Pb-Sb-Ag-Te) [Hsu 2004] and LASTT (Pb-Sb-Ag-Te-Sn) [Androulakis 2006] thermoelectric (TE) materials are essentially doped PbTe. PbTe is itself a TE material that has a wide application in thermoelectric power generation [Rowe 1995, Nolas 2001, Rowe 2006, Yang 2006]. Thus it is important to understand the mechanical behavior of PbTe in order to study the mechanical properties of LAST and LASTT materials.

Nevertheless, there are few studies of the temperature dependent elasticity of PbTe in the open literature [Houston 1968, Salamov 2006]. For example, Houston *et al.* measured the elastic stiffness constants of single crystal PbTe using ultrasonic pulse echo technique

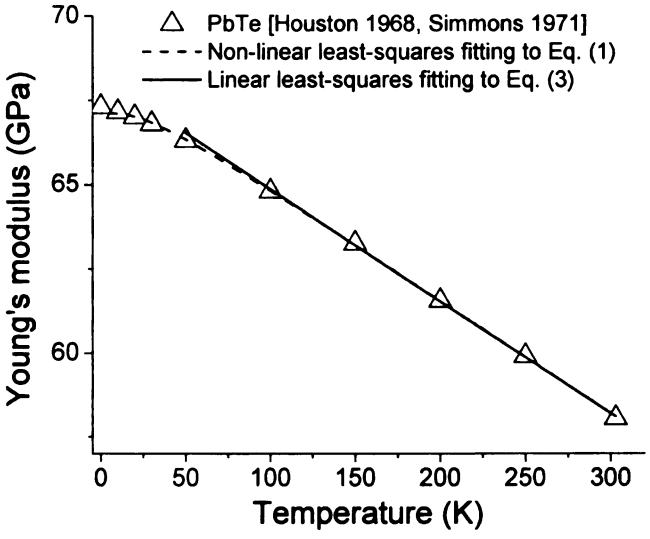

(a)

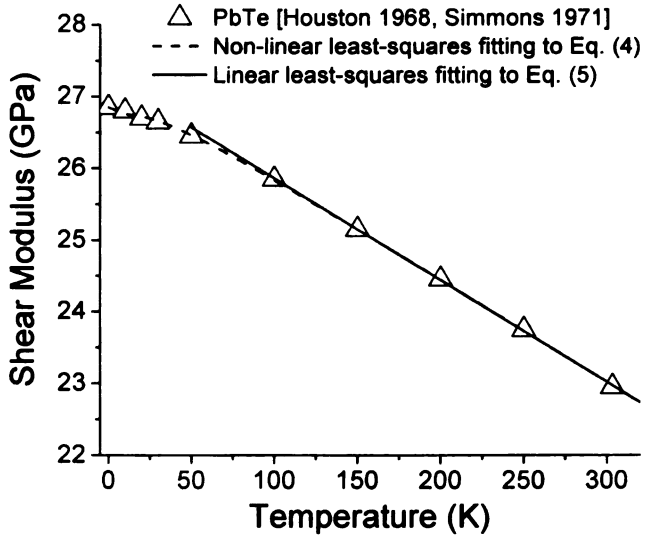

(b)

Figure 3.5.1. Temperature dependent elastic moduli of pure and doped PbTe in literature: (a) the aggregate Young's modulus, (b) the aggregate shear modulus, (c) the aggregate Poisson's ratio for pure PbTe [Houston 1968, Simmons 1971], and (d) the relative shear modulus of pure and Cr-doped PbTe [Salamov 2006].

Figure 3.5.1 continued.

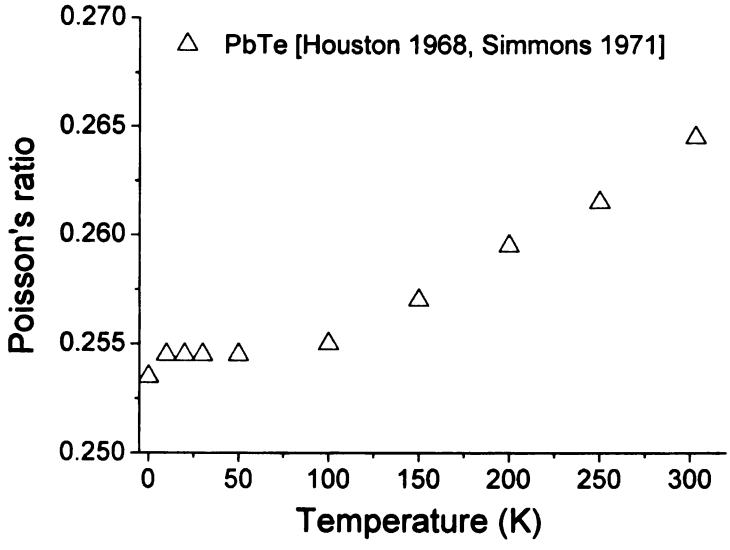

(c)

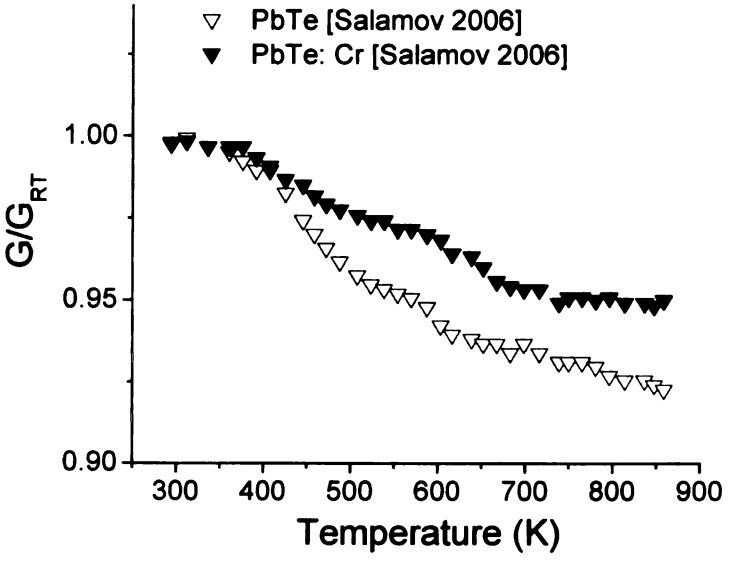

(d)

between 0 K and about 300 K [Houston 1968]. Based on Houston's work, Simmons and Wang calculated the aggregated elastic moduli, i.e. Young's modulus, shear modulus, and Poisson's ratio for polycrystalline PbTe [Simmons 1971]. Simmons and Wang's calculated aggregate properties [Simmons 1971] indicates that the Young's modulus and the shear modulus decrease linearly with increasing temperature, while Poisson's ratio increases monotonically with increasing temperature (Figs. 1a-1c) [Simmons 1971].

Salamov and coworkers utilized the torsional pendulum method to determine the relative change in shear modulus of pure PbTe and Cr-doped PbTe single crystals as a function of temperature between 20°C and 600°C (Figure 3.5.1d) [Salamov 2006]. Salamov *et al.* found Cr doping increased the shear modulus of PbTe by a factor of approximately 2.4 at room temperature, while the shear modulus decreased with increasing temperature for both doped and undoped PbTe (Figure 3.5.1d) [Salamov 2006].

2. Materials and methods

In the current study, elastic constants of polycrystalline PbTe specimens were obtained from resonant ultrasound spectroscopy (RUS) measurements between room temperature and approximately 770 K. Two polycrystalline specimens, i.e. a pure PbTe and a doped PbTe with 0.031 at. % PbI_2, were prepared using Bridgman method. The ingots were then cut to parallelepipeds that were approximately 10 mm x 7 mm x 2 mm for RUS measurements.

RUS experiments were performed on a commercial unit (RUSpec, Quasar International, Albuquerque, NM) located at the High Temperature Material Laboratory of Oak Ridge National Laboratory (Oak Ridge, TN). The specimen stage and transducers were placed in a vacuum chamber. A continuous 100 mL/min Ar flow was supplied to the chamber during the measurements to minimize oxidation of the specimens. RUS scans were taken at 50 K intervals with a heating and cooling rate of 5 K/min. Two five-minute isothermal holds were applied at each measurement temperature such that the first hold allowed the specimen to equilibrate while the RUS scans were taken during the second hold. The RUS measurement was typically completed within 2 minutes. RUS scan frequency ranged between 30 kHz to 500 kHz.

From RUS spectra, the Young's modulus, shear modulus, and Poisson's ratio were calculated using commercial software (RP Model, Quasar International, Albuquerque, NM) by non-linear least-squares fitting [Migliori 1993]. The overall goodness of fitting was characterized by the root mean squares (rms) errors, which was less than 0.5% in this study. The errors in Young's modulus, shear modulus, and Poisson's ratio, were estimated from the uncertainties of elastic stiffness constants dc_{11} and dc_{44}, which were calculated using the commercial software RP Model (Quasar International, Albuquerque, NM).

Table 3.5.1a. Fitting results of linear least-squares fitting of Young's modulus as a function temperature to Eq. (3).

Specimen	Temp. Range (K)	E_{RT} (GPa)	$b_{E\text{-}RT}$ (1/K)	r^2
PbTe	298 to 773	57.5	4.5×10^{-4}	0.998
PbTe-0.031%PbI_2	298 to 673	57.7	6.2×10^{-4}	0.996
PbTe [Houston 1968]	100 to 303	58.2	5.7×10^{-4}	0.999

Table 3.5.1b. Fitting results of linear least-squares fitting of shear modulus as a function temperature to Eq. (5).

Specimen	Temp. Range (K)	G_{RT} (GPa)	$b_{G\text{-}RT}$ (1/K)	r^2
PbTe	298 to 773	21.9	3.7×10^{-4}	0.991
PbTe-0.031%PbI_2	298 to 673	22.9	6.9×10^{-4}	0.996
PbTe [Houston 1968]	100 to 303	23.0	5.7×10^{-4}	0.999

Table 3.5.1c. Fitting results of non-linear least-squares fitting of Poisson's ratio as a function temperature to Eq. (6).

Specimen	Temp. Range (K)	ν_{RT}	ν_1 (1/K)	ν_2 ($1/K^2$)	r^2
PbTe	298 to 773	0.298	6.0×10^{-5}	-4.3×10^{-7}	0.86
PbTe-0.031%PbI_2	298 to 673	0.258	8.0×10^{-5}	1.2×10^{-7}	0.96
PbTe [Houston 1968] and PbTe-0.031%PbI_2	100 to 673	0.261	6.0×10^{-5}	1.5×10^{-7}	0.97

3. Results and discussion

3.1. Pure polycrystalline PbTe

The Young's modulus of the polycrystalline pure PbTe specimen was determined between room temperature (~ 298 K) and 773 K on both heating and cooling. The data taken upon heating and during cooling agree very well (Figure 3.5.2a). The linear least-squares fitting of the Young's modulus to Eq. (3) yields an E_{RT} of 57.5 GPa, a $b_{E\text{-}RT}$ of 4.5 x 10^{-4} K^{-1}, and an r^2 of 0.998 (Table 3.5.1a, Figure 3.5.2a). For shear modulus data, the linear least-squares fitting to Eq. (5) gives G_{RT} = 21.9 GPa, $b_{G\text{-}RT}$ = 3.7 x 10^{-4} K^{-1}, and r^2 = 0.991 (Table 3.5.1b, Figure 3.5.2b).

Poisson's ratio exhibits a monotonic decrease with increasing temperature. The room temperature Poisson's ratio of pure PbTe is around 0.3, but as the temperature increases to about 770 K, Poisson's ratio decreases to approximately 0.25 (Figure 3.5.2c). The Poisson's ratio for the pure PbTe specimen can be expressed as a parabolic function of temperature, such that

$$\upsilon(T) = \upsilon_{RT} + \upsilon_1(T - T_{RT}) + \upsilon_2(T - T_{RT})^2 \qquad (6)$$

where ν_{RT} is the Poisson's ratio at room temperature, ν_1 and ν_2 are fitting parameters, while T_{RT} is the room temperature which was assumed to be 298 K (25°C) in this study. Non-linear squares fitting of the pure PbTe data to Eq. (6) yields ν_{RT} = 0.298, ν_1 = 6.0 x 10^{-5} K^{-1}, and ν_2 = -4.3 x 10^{-7} K^{-2} with an r^2 of 0.86 (Table 3.5.1c, Figure 3.5.2c).

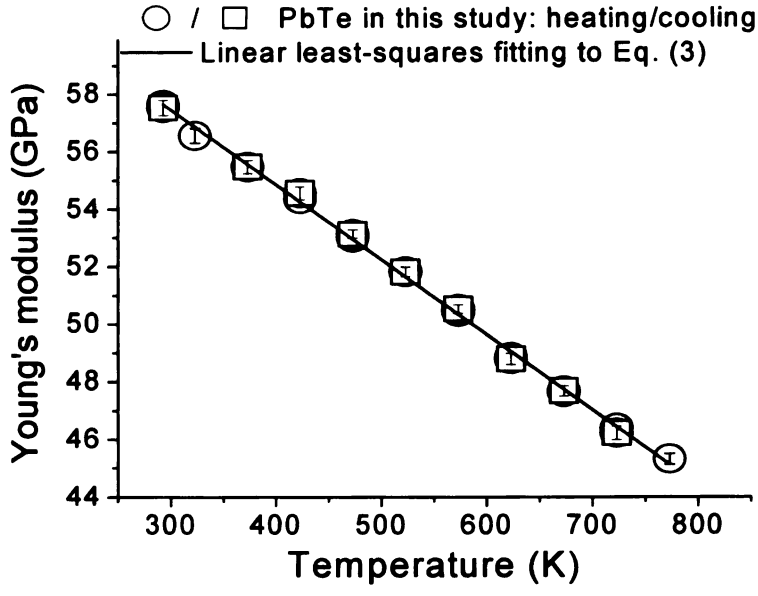

(a)

Figure 3.5.2. Temperature dependent (a) Young's modulus, (b) shear modulus, and (c) Poisson's ratio for the pure PbTe specimen in this study.

Figure 3.5.2 continued.

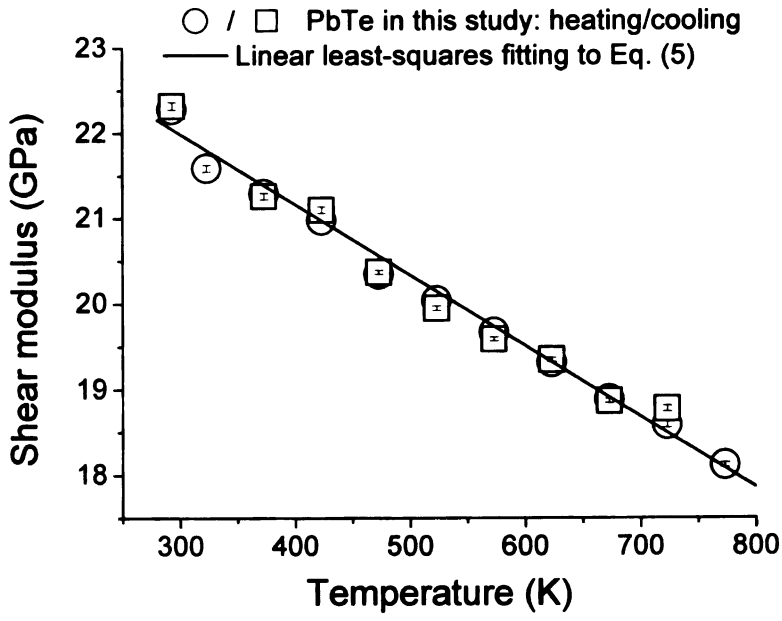

(b)

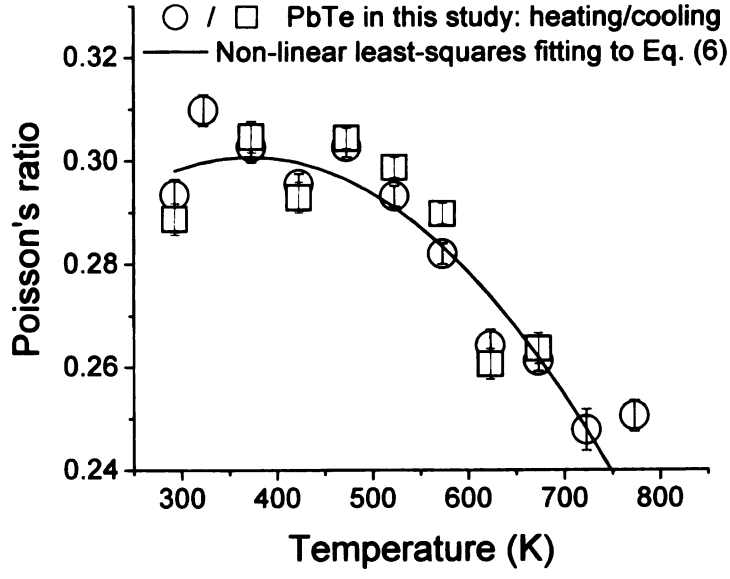

(c)

3.2. PbI_2-doped PbTe

For the 0.031% PbI_2 doped PbTe, both the Young's modulus and the shear modulus depend linearly on temperature and show good agreement between heating and cooling measurements (Figs. 3a and 3b). For the linear least-squares fitting of the Young's modulus to Eq. (3), E_{RT} = 57.7 GPa, $b_{E\text{-}RT} = 6.2 \times 10^{-4}\ K^{-1}$, and $r^2 = 0.996$ (Table 3.5.1a, Figure 3.5.3a). The temperature dependent shear modulus decreases from 22.9 GPa at room temperature to about 17 GPa at 673 K, with a $b_{G\text{-}RT}$ of $6.9 \times 10^{-4}\ K^{-1}$ and an r^2 of 0.996 (Table 3.5.1b, Figure 3.5.3b). Poisson's ratio increases monotonically with temperature, which can be described by the parabolic function Eq. (6). The non-linear least-squares fitting of Poisson's ratio data to Eq. (6) yields $\nu_{RT} = 0.258$, $\nu_1 = 8.0 \times 10^{-5}\ K^{-1}$, and $\nu_2 = 1.2 \times 10^{-7}\ K^{-2}$ with an r^2 of 0.96 (Table 3.5.1c, Figure 3.5.3c).

3.3. Comparison between the polycrystalline pure PbTe specimen and the PbI_2-doped PbTe specimen included in this study

The room temperature Young's modulus of 57.5 GPa for the pure polycrystalline PbTe specimen agrees well with the room temperature Young's modulus of 57.7 GPa for the PbI_2-doped PbTe specimen (Table 3.5.1a). The room temperature shear modulus of the pure PbTe specimen was 21.9 GPa, which was about 4.6 percent lower than that of the PbI_2-doped PbTe specimen (22.9 GPa) (Table 3.5.1b). The room temperature Poisson's ratio values of the pure PbTe specimen and the PbI_2-doped PbTe specimen were 0.298 and 0.258 (Table 3.5.1c), which differ by about 15 percent.

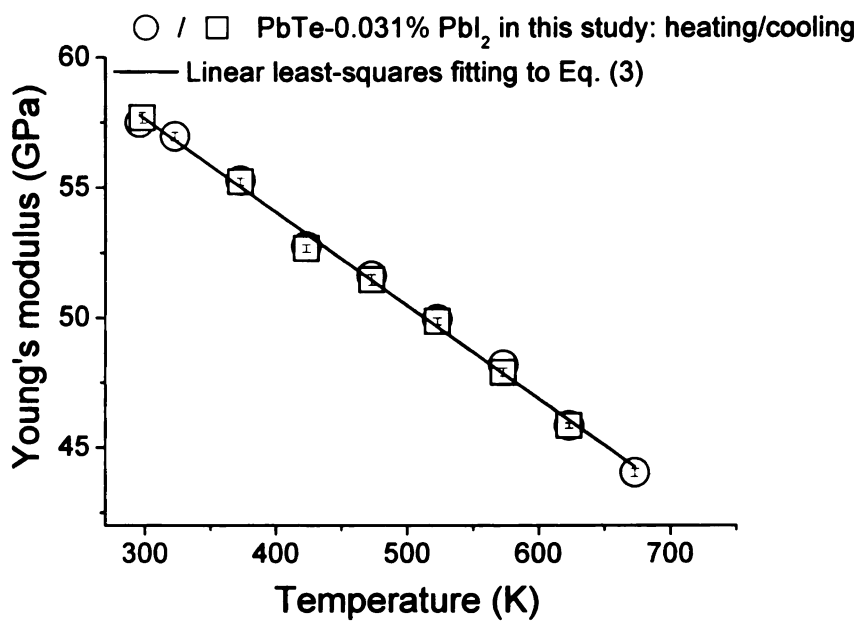

(a)

Figure 3.5.3. Temperature dependent (a) Young's modulus, (b) shear modulus, and (c) Poisson's ratio for the PbI_2-doped PbTe specimen in this study.

Figure 3.5.3 continued.

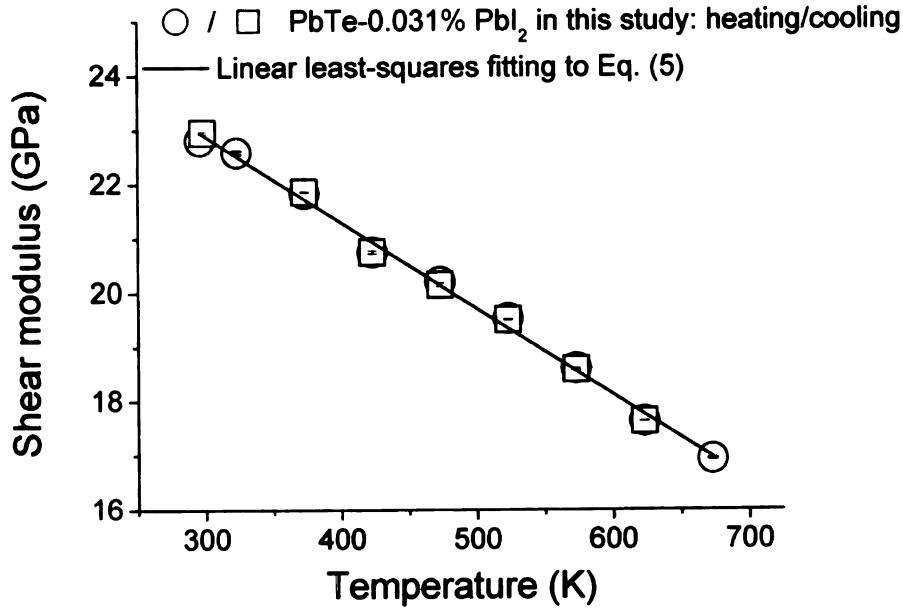

(b)

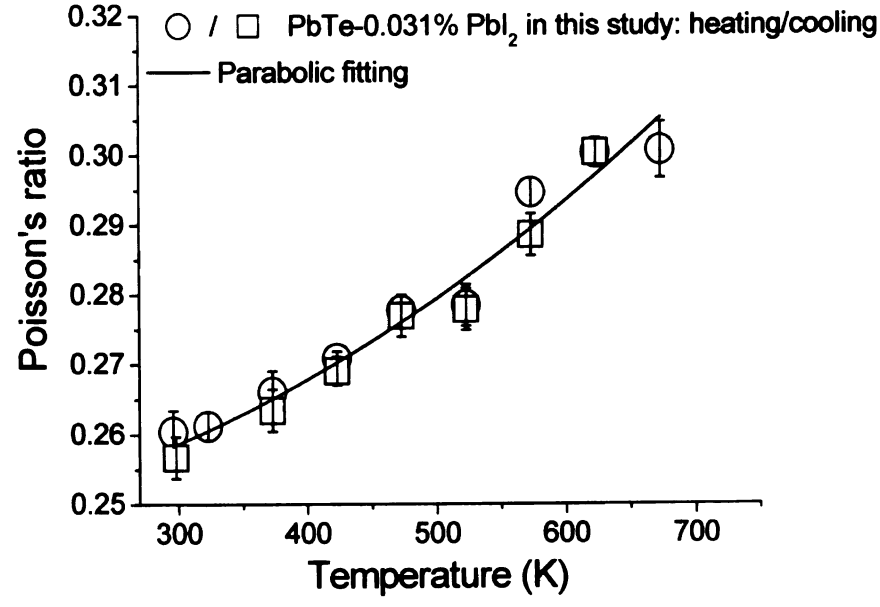

(c)

From linear least-squares fitting to Eq. (3), the slope of the Young's modulus versus temperature relationship was 4.5 x 10^{-4} K^{-1} for the pure PbTe specimen, which was about 27 percent lower than that for the PbI_2-doped PbTe specimen (Table 3.5.1a). The slope of the shear modulus versus temperature relationship as obtained from linear least-squares fitting to Eq. (5) was 3.7 x 10^{-4} K^{-1} for the pure PbTe specimen, which was about 54 percent of the value of 6.9 x 10^{-4} K^{-1} for the PbI_2-doped PbTe specimen (Table 3.5.1b).

The Poisson's ratio of the pure PbTe specimen decreases with temperature with a ν_1 of 6.0 x 10^{-5} K^{-1} and a negative curvature, ν_2, of -4.3 x 10^{-7} K^{-2}, while the values of ν_1 and ν_2 are 8.0 x 10^{-8} K^{-1} and 1.2 x 10^{-7} K^{-2} for the PbI_2-doped PbTe specimen, respectively (Table 3.5.1c).

3.4. Comparison between this study and literature data

Non-linear least-squares fitting of the aggregate Young's modulus data of pure PbTe [Simmons 1971] calculated from single crystal data [Houston 1968] between 0 K and 303 K to Eq. (1) yields E_0 = 67.1 GPa, b_E = 0.034 GPa/K, and T_0 = 38.6 K, with an r^2 > 0.999.

Linear least-squares fitting with Eq. (3) for the aggregate Young's modulus of pure PbTe [Simmons 1971, Houston 1968] between 100 K and 303 K reveals a good linear relationship with the following fitted parameters: E_{RT} = 58.2 GPa, $b_{E\text{-}RT}$ = 5.7 x 10^{-4} K^{-1}, and r^2 = 0.999 (Table 3.5.1a, Figure 3.5.1a).

The aggregate shear modulus [Simmons 1971, Houston 1968] also exhibits linear

temperature dependence at temperatures greater than 100 K (Table 3.5.1b, Figure 3.5.1b); while aggregate Poisson's ratio of pure PbTe [Simmons 1971, Houston 1968] increases monotonically from 0.255 at 0 K to 0.265 at about 300 K (Figure 3.5.1c).

The aggregate Young's modulus and Poisson's ratio obtained from the literature [Simmons 1971, Houston 1968] are plotted with the RUS measured data in this study if Figure 3.5.4a and Figure 3.5.4b, respectively. For Young's modulus, the room temperature values compare well among the two specimens in this study and the pure PbTe from [Houston 1968] (Table 3.5.1a, Figure 3.5.4a). The slopes of the linear least-squares fitting lines to Eq. (3) for the PbTe and the PbTe-0.031% PbI_2 in this study are approximately 21 percent lower and about 9 percent higher than that of Houston's PbTe data (Table 3.5.1a).

In addition, the general good agreement of Young's modulus between this study and the aggregate values obtained from Houston's work [Houston 1968] (Figure 3.5.4) indicates the pure PbTe and the lightly doped PbTe included in this study do not have significant texture.

For Poisson's ratio, PbTe-0.031% PbI_2 agrees well with literature data for pure PbTe [Simmons 1971, Houston 1968], in terms of the room temperature values as well as the monotonic trends with increasing temperature (Table 3.5.1c, Figure 3.5.4b, Table 3.5.1). However, Poisson's ratio of the pure PbTe specimen in this study exhibits

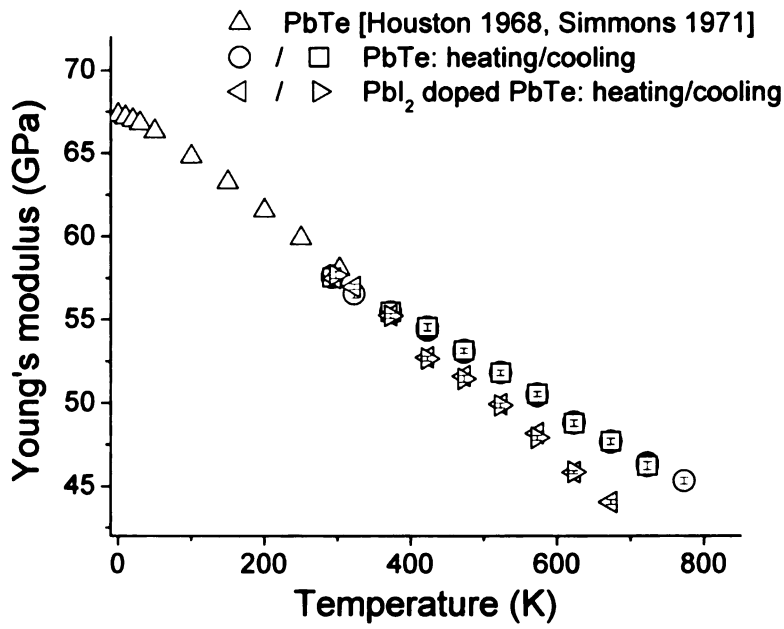

(a)

Figure 3.5.4. Comparison of temperature dependent elastic moduli between this study and literature [Houston 1968, Simmons 1971, Salamov 2006] for (a) the Young's modulus, (b) the Poisson's ratio, and (c) the relative shear modulus.

Figure 3.5.4 continued.

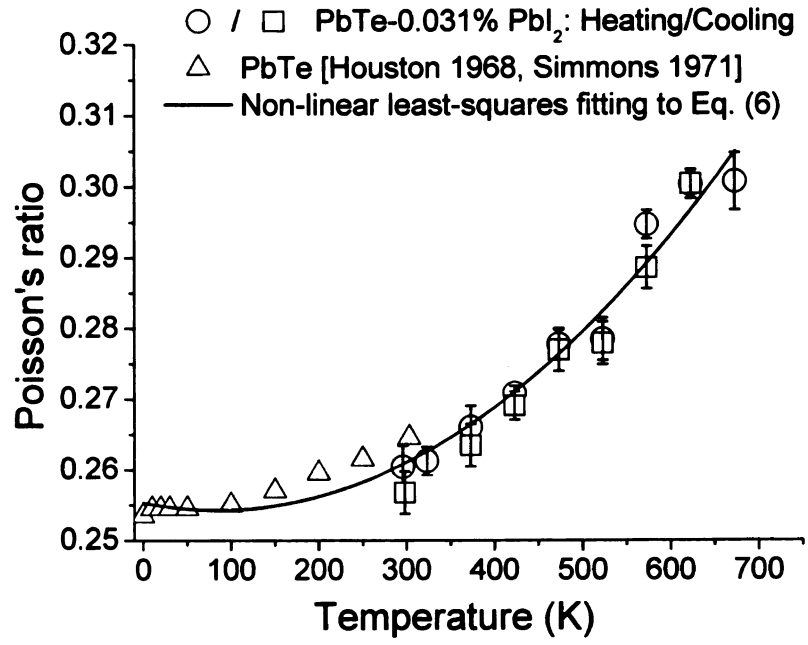

(b)

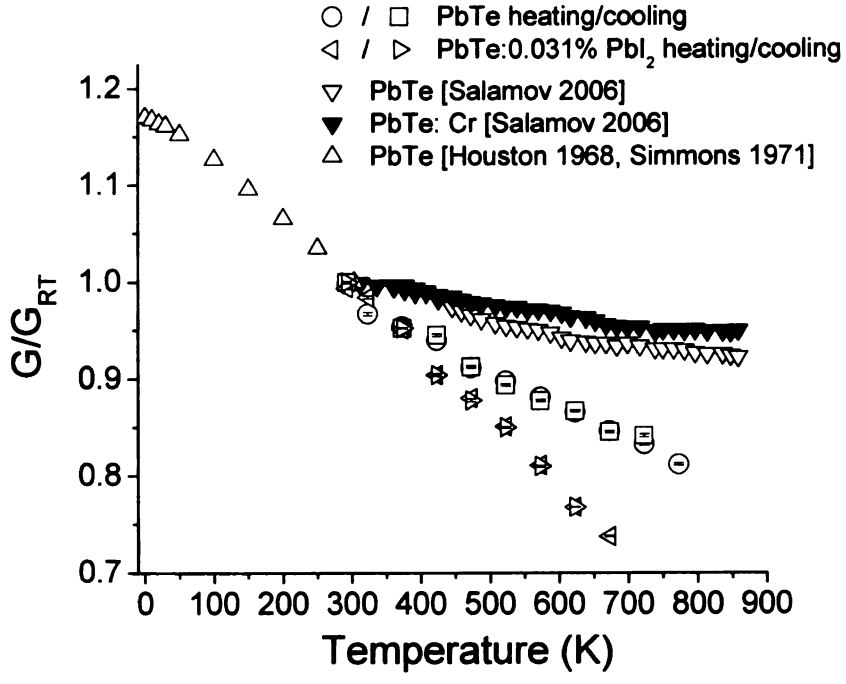

(c)

temperature dependence that is different than that observed by Houston *et al.* [Houston 1968], such that it deceases monotonically from room temperature to about 770 K (Figure 3.5.2c).

The relative shear modulus change studied by Salamov and coworkers [Salamov 2006] is also included. Shear modulus values obtained in this study, Houston's study [Houston 1968, Simmons 1971], and Salamov's study [Salamov 2006] are normalized with respect to their room temperature values (Figure 3.5.4c).

After normalization, the temperature dependence of shear modulus of the PbTe-0.031% PbI_2 specimen agrees well with the pure PbTe in Houston's study [Houston 1968, Simmons 1971] (Figure 3.5.4c). However, the pure PbTe in the current study has a smaller slope as determined by linear least-squares fitting to Eq. (5) (Table 3.5.1b). Salamov and coworkers [Salamov 2006] found a monotonic decrease in the relative shear modulus with increasing temperature for both the pure PbTe and the Cr-doped PbTe data obtained from torsional pendulum [Salamov 2006] (Figure 3.5.1d). However, the magnitude of decrement in the relative shear modulus for both the pure PbTe and the Cr-doped PbTe specimens studied by Salamov *et al.* [Salamov 2006] are much smaller than those observed for the pure PbTe specimen and the PbI_2-doped PbTe specimen included in this study (Figure 3.5.4c). The relative shear modulus values at 673 K were approximately 0.85 for the pure PbTe specimen and about 0.74 for the PbI_2-doped PbTe specimen in this study, while the relative shear modulus values at 673 K were approximately 0.95 and 0.98 for the pure and doped PbTe specimens reported in

Salamov's study [Salamov 2006] (Figure 3.5.4c).

It is worthwhile to note the different techniques used in the determination of the elastic moduli (Table 3.5.2). In the current study, the elastic moduli were measured by RUS in the frequency range between 30 kHz and 500 kHz. Houston *et al.* [Houston 1968] utilized a MHz ultrasonic pulse echo technique [Houston 1968]. However, the frequency used in Salamov's study was between 4.8 and 5 Hz [Salamov 2006]. Thus the elastic moduli determined in this study and those from [Houston 1968] are considered as dynamic moduli, while Salamov's modulus values [Salamov 2006] are quasi-static or static. Also it is important to point out that elastic moduli were measured directly from polycrystalline materials in the current study while the aggregate values of the pure PbTe was estimated from single crystal data [Houston 1968] by the Voight-Reuss-Hill method [Simmons 1971].

It has been shown that doping level affects the elastic properties of semiconducting materials [Keyes 1961, Sreedhar 1971]. For example, for n-type Ge, the shear modulus can vary up to 8 percent a function of doping level [Keyes 1961]. For p-type PbTe, the increase in c_{44} is greater than 10 percent when the carrier concentration increased from 10^{18} cm^{-3} to 10^{21} cm^{-3} [Sreedhar 1971]. In addition, the effect of dopant on c_{44} of the p-type PbTe varies with temperature, such that the contribution of carrier to c_{44} increases when temperature increases from 0 K to 300 K for a carrier concentration of 10^{21} cm^{-3}, while for a carrier concentration of 10^{18} cm^{-3}, the effect of dopant on c_{44} is nearly constant between 0 K and 300 K [Sreedhar 1971].

Table 3.5.2. Comparison of measurement techniques and frequency between this study and literature.

	Technique	Frequency
This study	RUS	30 to 500 kHz
[Houston 1968]	Ultrasonic pulse echo	~ MHz
[Salamov 2006]	Torsional pendulum	4.8 to 5 Hz

Table 3.5.3. Room temperature carrier concentration of the pure and doped PbTe specimens in this study and in literature.

Specimen	Carrier type	Carrier concentration (carrier/cm^3)
PbTe [Houston 1968]	hole	4.1×10^{18}
PbTe [Salamov 2006]	hole	1.2×10^{19}
PbTe:Cr [Salamov 2006]	electron	4.1×10^{18}
PbTe in this study	electron	4.8×10^{17}

The room temperature carrier concentration of the PbTe specimen studied by Houston *et al.* [Houston 1968] was 4.1 x 10^{18} hole/cm^{-3} (Table 3.5.3). For the PbTe specimen and the Cr-doped PbTe specimen included in Salamov's study [Salamov 2006], the room temperature carrier concentrations were 1.2 x 10^{18} hole/cm^{-3} and 4.1 x 10^{18} electron/cm^{-3} (Table 3.5.3).

In this study, the room temperature carrier concentration of the pure PbTe specimen is 4.8 x 10^{17} electron/cm^{-3} (Table 3.5.3). The PbTe-0.031% PbI_2 specimen in this study is being analyzed by Prof. Uher's group at University of Michigan. However, it is likely that the PbTe-0.031% PbI_2 specimen has a higher carrier concentration than the undoped PbTe. Thus, the different elastic constants room temperature between the two specimens in this study and the difference between measurements from this study and the literature data [Houston 1968, Simmons 1971, Salamov 2006] may, as least in part, due to the different carrier concentration, which also affects the temperature dependency of the elastic moduli.

References

[Wachtman 1996] J. B. Wachtman, *Mechanical Properties of Ceramics*, (Wiley Interscience, New York, 1996), pp. 33-35.

[Anderson 1966] O. L. Anderson, "Derivation of Wachtmans Equation for Temperature Dependence of Elastic Moduli of Oxide Compounds", *Physical Review*, **144**[2]:553-557 (1966).

[Hsu 2004] K. F. Hsu, S. Loo, F. Guo, *et al.*, "Cubic AgPbmSbTe2+m: Bulk thermoelectric materials with high figure of merit", *Science*, **303**[5659]:818-821 (2004).

[Androulakis 2006] J. Androulakis, K. F. Hsu, R. Pcionek, *et al.*, "Nanostructuring and high thermoelectric efficiency in p-type Ag(Pb1-ySny)(m)SbTe2+m", *Advanced Materials*, **18**[9]:1170-1173 (2006).

[Fano 1995] V. Fano, "Lead telluride and its alloys", in *CRC handbook of thermoelectrics*, edited by D. M. Rowe (CRC Press, Inc., New York, 1995), pp 257-266.

[Nolas 2001] G. S. Nolas, J. Sharp and H. J. Goldsmid, *Thermoelectrics: basic principles and new materials developments*, (Springer, Berlin; New York, 2001), pp. 146-149.

[Yang 2006] J. H. Yang and T. Caillat, "Thermoelectric materials for space and automotive power generation", *MRS Bulletin*, **31**[3]:224-229 (2006).

[Houston 1968] B. Houston, R. E. Strakna and H. S. Belson, "Elastic Constants Thermal Expansion and Debye Temperature of Lead Telluride", *Journal of Applied Physics*, **39**[8]:3913-3196 (1968).

[Salamov 2006] B. G. Salamov, O. I. Davarashvili, T. S. Mamedov, *et al.*, "Investigation of the temperature dependence of the internal friction in PbTe crystals", *Physica Status Solidi a-Applications and Materials Science*, **203**[15]:3679-3684 (2006).

[Simmons 1971] G. Simmons and H. Wang, *Single Crystal Elastic Constants and Calculated Aggregate Properties: a Handbook* (the MIT Press, Cambridge, MA, 1971).

[Migliori 1993] A. Migliori, J. L. Sarrao, W. M. Visscher, *et al.*, "Resonant Ultrasound Spectroscopic Techniques for Measurement of the Elastic-Moduli of Solids", *Physica B*, **183**[1-2]:1-24 (1993).

[Keyes 1961] R. W. Keyes, "The electron contribution to the elastic properties of germanium", *IBM Journal of Research*, **5**:266-278 (1961).

[Einspruch 1963] N. G. Einspruch and P. Csavinzky, "Electronic effect in the elastic constant c' of silicon", *Appl.Phys. Lett.*, **2**[1]:1-3 (1963).

[Sreedhar 1972] A. K. Sreedhar and S. C. Gupta, "Electronic effects in elastic constants of PbTe", *Phys. Rev. B*, **5**[5]:3160-3164 (1972).

Chapter 6

Microstructural and mechanical characterization of LAST (Pb-Ag-Sb-Te) thermoelectric materials fabricated via slow-cool casting

1. Microstructures of LAST materials

LAST (Pb-Sb-Ag-Te) materials are essentially Ag- and Sb- doped PbTe. The stoichiometric LAST materials with the composition of $AgPb_mSbTe_{m+2}$ can be expressed as m·PbTe + $AgSbTe_2$ [Quarez 2005]. Several studies have suggested that a solid solution exists between PbTe and $AgSbTe_2$ [Borisova 1984, Maier 1963, Ono 1962]. For example, a pseudo-binary phase diagram of $(2PbTe)_x(AgSbTe_2)_{1-x}$ proposed by Maier [Maier 1963] shows that a solid solution exists for the composition parameter, x, ranging between ~ 0.15 and 1 at room temperature, while in the region where $x < \sim 0.15$, the solid solution coexists with α-Ag_2Te and/or Sb_2Te_3 (Figure 3.6.1). The solid solution of PbTe-$AgSbTe_2$ was originally thought to posses a rock salt (NaCl) structure, with Ag and Sb occupying the Na sites [Geller 1959].

However, a recent study using single crystal XRD, high resolution TEM, and electron diffraction revealed nanoscopic inhomogeneity in LAST materials [Quarez 2005]. Based on single crystal X-ray diffraction data, Quarez *et al.* suggested that the crystal structure of LAST can be refined to tetragonal or rhombehedral, both of which have lower symmetry than cubic cells [Quarez 2005]. However, the distortion from cubic structure is very small [Quarez 2005].

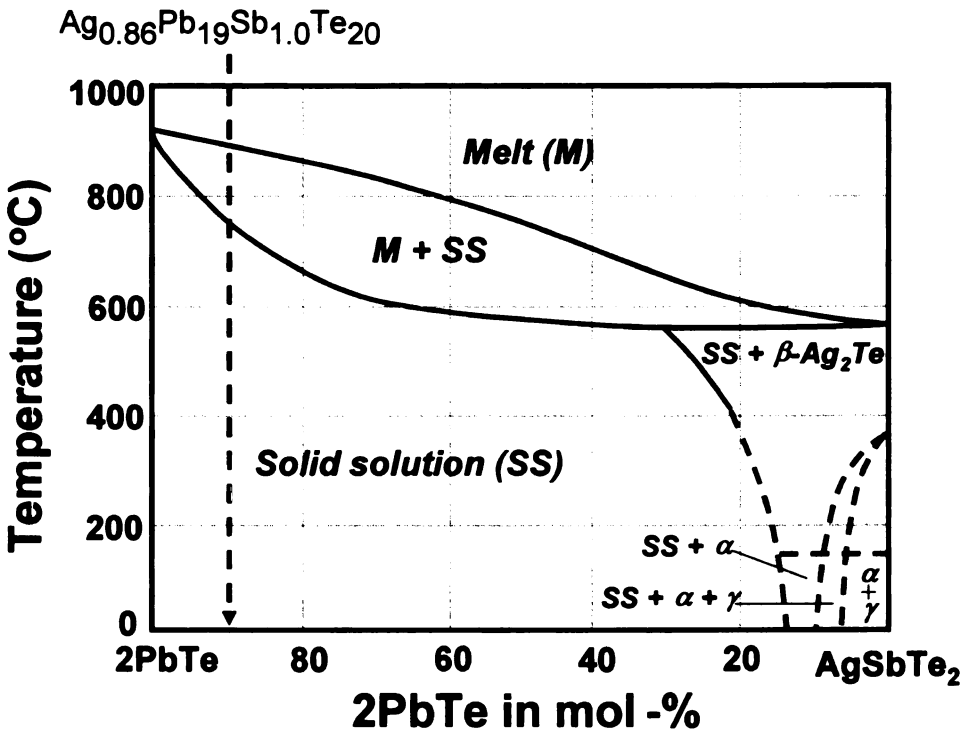

Figure 3.6.1. Pseudo-binary phase diagram of the PbTe-$AgSbTe_2$ where $\alpha = \alpha$-Ag_2Te, $\beta = \beta$-Ag_2Te, and $\gamma = Sb_2Te_3$ (after [Maier 1963]). For non-stoichiometric LAST compounds $Ag_{0.86}Pb_{18}Sb_{1.0}Te_{20}$, which can be approximated as $(AgSbTe_2)+9(2PbTe)$ for temperature below about 750°C, the nominal composition is located in the solid solution region near PbTe end as indicated by the dotted line.

In addition, high resolution TEM and electron diffraction results showed nanoinclusions that were rich in Ag and Sb, which coherently embedded within a Ag- and Sb- poor matrix [Quarez 2005]. Similar nano-regions were also found in the PbTe-PbS system [Androulakis 2007], where PbS-rich nanostructures existed in PbTe-rich matrix. This nano-scale compositional inhomogeneity has been attributed to spinodal decomposition [Androulakis 2007] and could be utilized to create nanostructures that may enhance the performance of thermoelectric materials [Androulakis 2007]. Thus, for stoichiometric LAST materials ($AgPb_mSbTe_{m+2}$), one would expect a homogeneous solid solution at microscopic scale [Maier 1963] with nano-sized inhomogeneity [Androulakis 2007, Hsu 2004, Quarez 2005].

However, the phases present in the pseudo-ternary system PbTe-$AgSbTe_2$-Sb_2Te_3 may be much more complicated that Ag and Sb nano-inclusions in an Ag and Sb poor matrix. In addition to the end members, i.e. PbTe, $AgSbTe_2$, and Sb_2Te_3 [Buyanov 1999, Maier 1963], the existence of other phases were reported in literature, including c-SbTe [Tani 2001], $AgTe_2$ [Maier 1963, Matsushita 2004], and $Pb_2Sb_6Te_{11}$ [Buyanov 1999, Ikeda 2007]. Also it is important to note that the phase diagrams of PbTe- $AgSbTe_2$ and $AgSbTe_2$- Sb_2Te_3 [Maier 1963] were proposed more than 40 years ago and may not reflect the actual situation in PbTe- $AgSbTe_2$- Sb_2Te_3 system.

Phase diagrams are constructed under equilibrium conditions [Porter 1990]. In practice, phases present in the final products depend on not only the initial stoichiometry but also the processing details, such as sublimation and cooling rates if the materials are

grown from melts [Nolas 2001]. Composition segregation will occur if the cooling conditions deviate from equilibrium [Nolas 2001]. Further more, compositional gradients may result from the limited mass diffusivity in the solid and/or liquid phases, which in turn may introduce second phases [Porter 1990].

For melt-grown non-stoichiometric LAST materials, such as $Ag_{0.86}Pb_{19}SbTe_{20}$, one may expect the major phase is the PbTe-$AgSbTe_2$ solid solution, while there is a possibility that other phases may exist as a result of non-stoichiometry as well as the detailed processing history during fabrication.

2. LAST materials grown from melt

The specimens included in this chapter (Table 3.6.1) were fabricated via casting using a three-zone split-tube rocking furnace using high purity (> 99.99%) elemental materials. The temperature-time profiles during ingot casting are illustrated in Figure 3.6.2.

The specimens can be categorized into two groups, i.e. a fast cooled (FC) group including ingots N29, N58, and N106, and a slow cooled (SC) group including ingots N152 to N167. The major difference between the two groups is the cooling rate between maximum temperature of the melt (1020°C for FC and 1050°C for SC) and ~ 600°C to 750°C, which approximates the solidus line in PbTe-$AgSbTe_2$ phase diagram (Figure 3.6.1). Therefore, it is convenient to characterize the processing conditions of each specimen with their average cooling rates between maximum temperature of the melt and

Table 3.6.1. Composition and cooling rate between the maximum temperature of the melt and solidus temperature for the LAST ingot specimens included in this study.

Specimen	Composition	Cooling rate* (°C/hr)	Temperature range (°C)
N106	$Ag_{0.85}Pb_{19}Sb_{1.0}Te_{20}$	7.80	1020 – 700
N29	$Ag_{0.80}Pb_{18}Sb_{1.0}Te_{20}$	6.36	1020 – 600
N58	$Ag_{0.43}Pb_{18}Sb_{1.2}Te_{20}$	10.0	1020 – 750
N152	$Ag_{0.86}Pb_{19}Sb_{1.0}Te_{20}$	2.08	1050 – 700
N155	$Ag_{0.86}Pb_{19}Sb_{1.0}Te_{20}$	2.08	1050 – 700
N156	$Ag_{0.86}Pb_{19}Sb_{1.0}Te_{20}$	2.92	1050 – 700
N157	$Ag_{0.86}Pb_{19}Sb_{1.0}Te_{20}$	2.43	1050 – 700
N159	$Ag_{0.86}Pb_{19}Sb_{1.0}Te_{20}$	1.82	1050 – 700
N160	$Ag_{0.86}Pb_{19}Sb_{1.0}Te_{20}$	2.08	1050 – 700
N165	$Ag_{0.86}Pb_{19}Sb_{1.0}Te_{20}$	2.08	1050 – 700
N167	$Ag_{0.86}Pb_{19}Sb_{1.0}Te_{20}$	2.92	1050 – 700

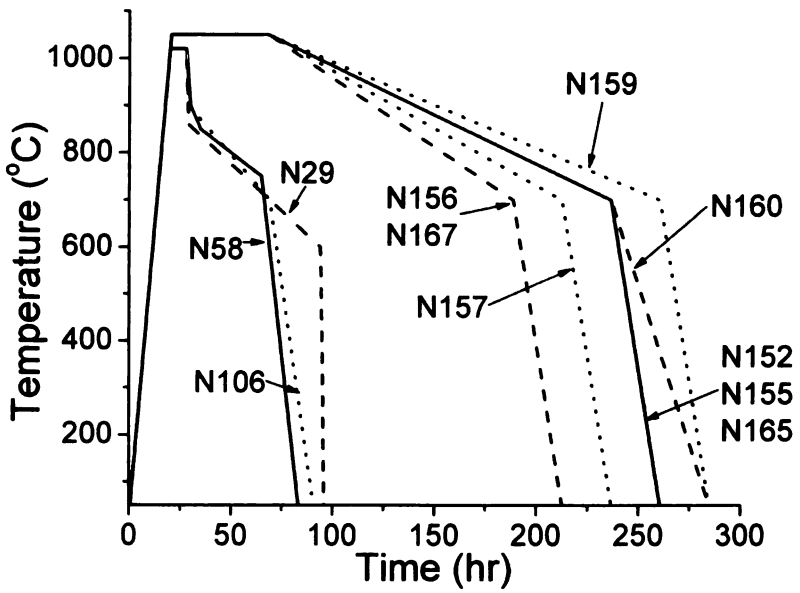

Figure 3.6.2. Temperature versus time profiles for the ingot specimens included in this study.

the solidus temperature. Table 3.6.1 lists the specimens included in this study, along with their nominal compositions and average cooling rates over the given temperature ranges.

3. Microstructure of slow cooled ingots

In this study, microstructures of the cast ingots were examined by SEM and EDS (see **Part II section 5.1**). The fracture surface of ingot N159 (Figure 3.6.3a) shows a typical brittle fracture behavior indicated by cleavage steps. In addition, several quasi-spherical inclusions (> 100 microns) were observed on the N159 fracture surface (Figure 3.6.3a). A higher magnification backscattered electron image of a quasi-spherical inclusion (Figure 3.6.3b) reveals the composition of the inclusion is different from bulk. The inclusion appears darker than the surrounding matrix, which implies the inclusion has a lower average atomic number than the matrix [Flegler 1995]. Similar quasi-spherical inclusions were found in other ingot specimens, for example specimen N157.

In addition to quasi-spherical inclusions, needle-shaped inclusions (Figure 3.6.3c) and plate-like inclusions (Figure 3.6.3d) were also observed. The longer axis of needle-shaped inclusions, which were up to 20 microns long in the axial direction, appear to be aligned in parallel (Figure 3.6.3c). The plate-like inclusions consist of layers that extend laterally for approximately 20 microns and were approximately 1 micron thick per layer (Figure 3.6.3d).

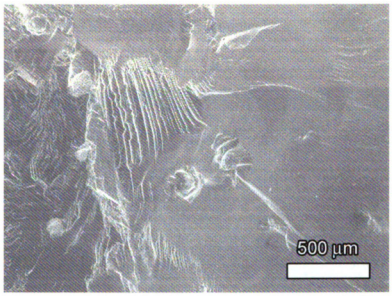

(a)

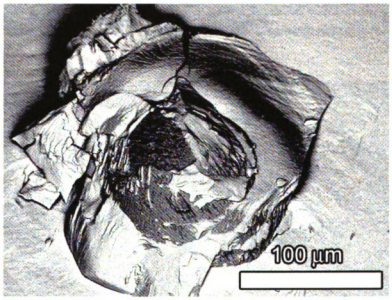

(b)

Figure 3.6.3. SEM micrographs of inclusions observed in the slow cooled LAST materials: (a) fracture surface of N159 (Table 3.6.1), (b) spherical inclusion observed in N159, (c) needle-shaped inclusions observed in N155, and (d) plate-like inclusions observed in N155 (Table 3.6.1).

Figure 3.6.3 continued.

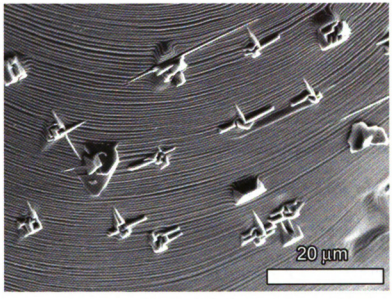

(c)

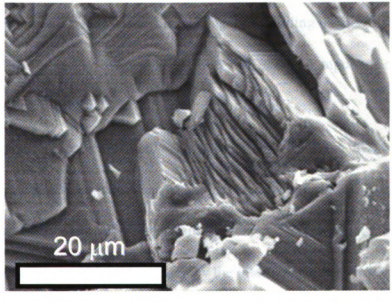

(d)

The EDS analysis was utilized to examine the composition of the inclusions semi-quantitatively. For all three types of inclusions, high concentrations of Sb and Te and low concentrations of Pb and Ag were observed. For example, the concentration of both Sb and Te concentrations in the plate-like inclusions (Figure 3.6.3d) were more than 40 atomic percent, while only a few percent of Pb and Ag was observed (Table 3.6.2).

EDS elemental mapping on a quasi-spherical inclusion in specimen N159 (Figure 3.6.4a) showed that the matrix was rich in Pb and Te (Figure 3.6.4b), which is expected since LAST materials are essentially doped PbTe compounds. The make-up of the inclusions were mostly Sb and Te, while Ag was sparsely distributed in the regions where Sb and Te were abundant (Figure 3.6.4b). Based on the SEM and EDS examinations, the inclusions observed in the slow-cooled LAST ingots, including the quasi-spherical, needle-shaped, and plate-like inclusions, are likely Sb and Te compounds or the combination of Sb-Te compounds with other minor phases.

The large spherical inclusions likely came out above the solidus line, while the needle-shaped and plate-like inclusions might form below the solidus. In addition, the nature of the inclusions may be inferred from the shape of the inclusions.

The shape of an inclusion is determined by the interfacial energy between the inclusion and the matrix, γ, and the elastic strain energy due to the lattice misfit between the inclusion phase and the matrix phase, ΔG_S, such that the equilibrium shape of an

Table 3.6.2. As determining using EDS, the composition in terms of atomic percentage for the plate-like inclusions observed specimen N155 (Figure 3.6.3d).

Element	Sb	Te	Pb	Ag
At. %	44.2	45.6	6.7	3.5

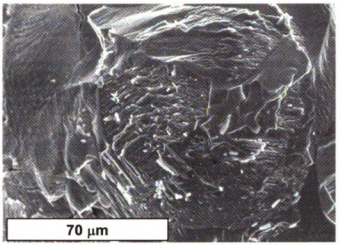

(a)

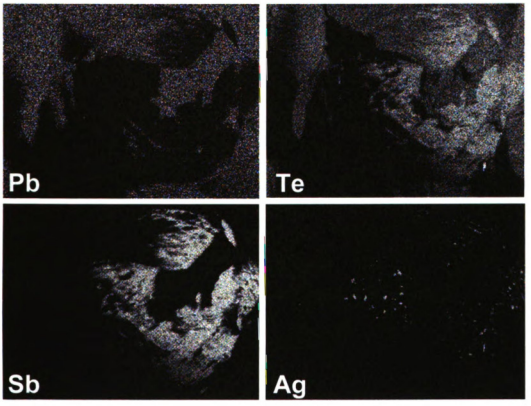

(b)

Figure 3.6.4. (a) SEM micrograph of a spherical inclusion observed in specimen N159 (Table 3.6.1) and (b) the corresponding elemental mapping for Pb, Te, Sb, and Ag for the inclusion.

inclusion corresponds to the minimum of $\gamma + \Delta G_S$ [Porter 1990].

The shape of the coherent inclusions in an isotropic matrix depends on the elastic strain energy due to volumetric misfit, which is proportional to the size of the inclusions. Thus, a small misfit usually results in spherical inclusions while large misfit results in disc-shaped inclusions [Porter 1990], which does not agree with the observation in this study where spherical inclusions had larger dimensions (> 100 microns) than the plate-like inclusions about 20 microns in the lateral dimension.

For a fully coherent inclusion with a small lattice misfit, the shape is usually spherical if the inclusion phase is harder than the matrix phase or disc-shaped if the inclusion phase is softer than the matrix phase [Porter 1990], while the shape of a partially coherent inclusions is either plate-like or needle-like depending on the orientation of the inclusion within the matrix [Porter 1990]. In this study, spherical inclusions, plate-like inclusions, and needle-shaped inclusions were observed in the slow-cooled LAST ingot specimens (Figure 3.6.3). Thus, the inclusions observed in this study are likely coherent or partially coherent with a small lattice misfit. Since the matrix phase of LAST materials, PbTe, has a NaCl structure, the inclusions likely have a cubic structure. For the composition of the inclusions in this study, the ratio of the Sb concentration to the Te concentration was approximately 1:1 (Table 3.6.1), which implies that these inclusions are likely crystalline c-SbTe that also has a NaCl structure [Tani 2001] (see Section 5.1).

However, these inclusions might be detrimental to the performance of LAST materials, especially the mechanical properties. Large inclusions may behave as the crack

initiation sites and consequently reduce the fracture strength compared to the inclusion-free materials [Barsoum 1997]. A possible approach to eliminate the large inclusions is by means of powder processing. For example, by milling the cast materials into micron-sized powders, the hundred-micron inclusions will be broken into millions of small particles, which will be uniformly distributed in the final materials.

4. Room temperature mechanical properties

In this study, fracture strength, hardness, and elastic moduli were measured at room temperature on both slow cooled and fast cooled ingot specimens (Table 3.6.3). The fracture strength was obtained from biaxial flexure testing (see **Part II section 3.3**) [Ren 2006], hardness and Young's modulus were measured by both microindentation and nanoindentation (see **Part II sections 3.1 and 3.2**) [Ren 2007a, b], while the dynamic moduli including Young's modulus, shear modulus, and Poisson's ratio were examined by resonant ultrasound spectroscopy (see **Part II section 3.4**).

4.1 Biaxial flexure strength

Three LAST ingots with different cooling rates (Table 3.6.3a, Figure 3.6.5a) were tested using the biaxial flexure testing. The mean strength values of the three specimens range from 13 MPa to 26 MPa (Table 3.6.3a, Figure 3.6.5a), which are comparable to the fracture strength of LASTT (Pb-Sb-Ag-Te-Sn) ingot specimens [Ren 2006].

Despite the relatively large scatter in the strength data, a general trend can be seen in

Table 3.6.3. For the ingot specimens included in this study (Table 3.6.1) the (a) Biaxial flexure strength and (b) hardness and Young's modulus as determined by indentation

(a)

Specimen	**σ_{mean} (MPa)**	**σ_{stdev} (MPa)**	**N**
N29	16.9	3.4	7
N58	12.9	2.6	8
N167	25.7	6.3	6

(b)

Specimen	**Microindentation (GPa)**		**Nanoindentation (GPa)**			
	H_{mean}	H_{stdev}	H_{mean}	H_{stdev}	E_{mean}	E_{stdev}
N106	0.67	0.10	0.790	0.024	54.3	0.8
N152	0.77	0.04	0.878	0.028	62.1	1.3
N155	0.63	0.02	0.782	0.014	59.4	1.0
N156	0.57	0.02	0.751	0.009	59.7	0.8
N157	0.60	0.04	0.874	0.013	61.1	1.2
N159	0.67	0.04	0.796	0.010	57.0	1.0
N160	0.56	0.03	0.646	0.005	61.3	1.7

the fracture strength as a function of cooling rate, such that fracture strength increases with decreasing cooling rate (Figure 3.6.5a). In addition, the increased fracture strength in slow-cooled specimens is in agreement with the improved machinability compared to fast-cooled ingots. Both the fast and slow cooled specimens were cut on a K. O. Lee surface grinder/cutter (Model S3618HS, the K. O. Lee Company, Aberdeen, SD).

However, upon cutting the specimens from the ingot, less cracking and chipping were observed during cutting of slow-cooled materials. The higher strength and better machinability imply a reduced crack density in slow-cooled materials.

However, it must be noted that the three ingot specimens tested in this study have different compositions (Table 3.6.1). For LAST materials, it is shown that hardness and Young's modulus can be affected by composition [Ren 2007a, b]. Thus composition may also affect the fracture strength.

4.2 Indentation hardness and Young's modulus

Six slow-cooled specimens and one fast-cooled specimen were selected to study the effect of cooling rate on the room temperature hardness and Young's modulus (Table 3.6.3b). For the comparison of hardness and Young's modulus, all the slow-cooled specimens had an identical composition of $Ag_{0.86}Pb_{19}Sb_{1.0}Te_{20}$, while the fast-cooled specimen N106 had a comparable composition of $Ag_{0.85}Pb_{19}Sb_{1.0}Te_{20}$. Thus the effect of composition on hardness [Ren 2007a] and Young's modulus [Ren 2007b] was minimized.

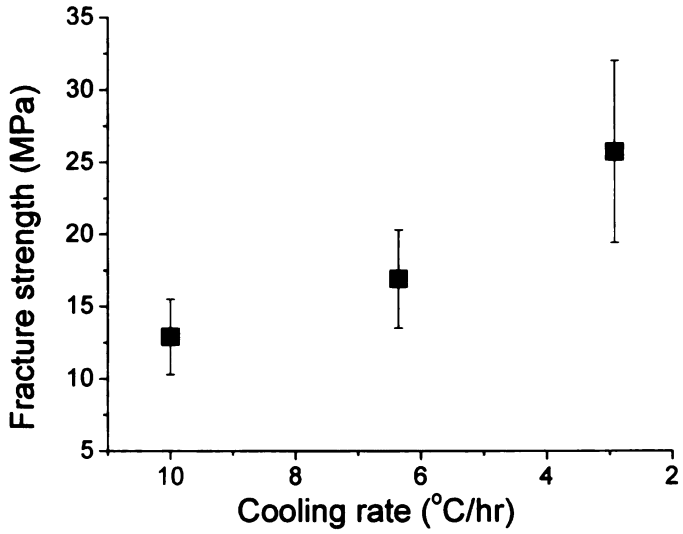

(a)

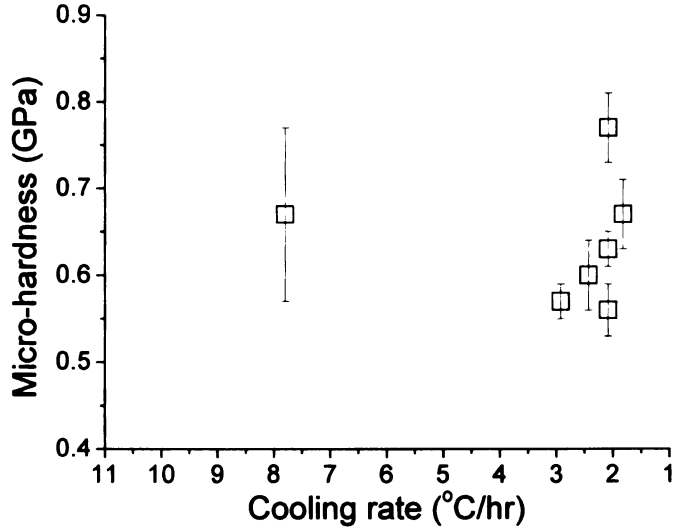

(b)

Figure 3.6.5. The effect of ingot cooling rate on (a) fracture strength, (b) microindentation hardness, (c) nanoindentation hardness, and (d) Young's modulus for ingot LAST specimens (Table 3.6.1).

Figure 3.6.5 continued.

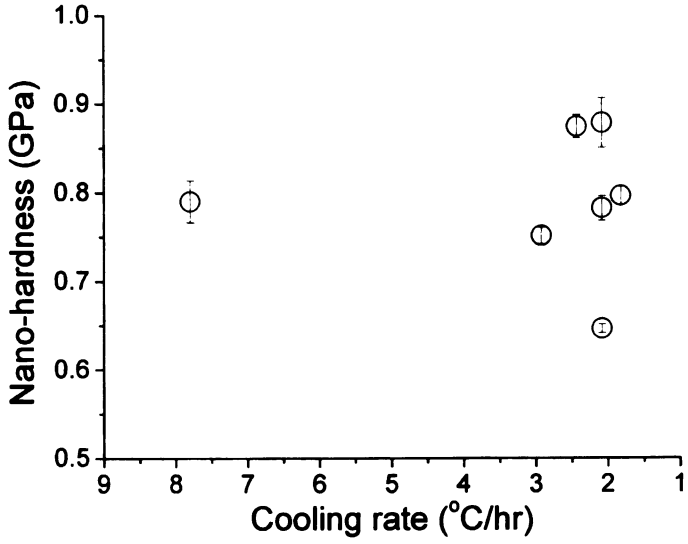

(c)

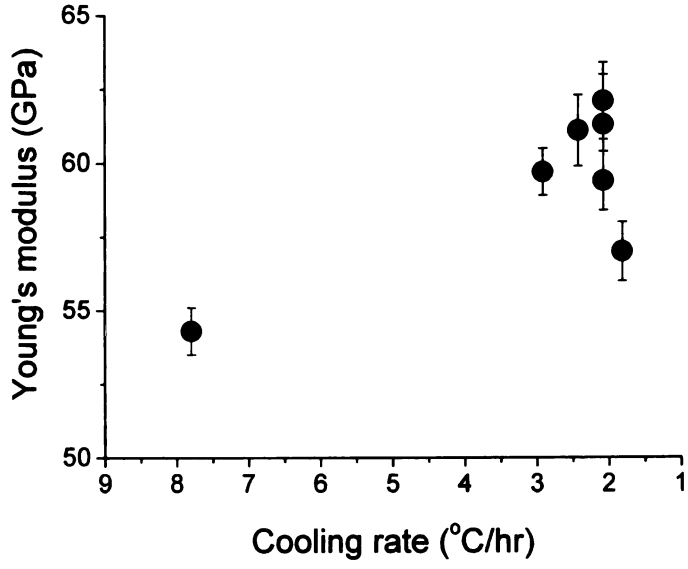

(d)

The hardness and Young's modulus data measured via nanoindentation as a function of cooling rate are similar to the aging behavior, where the hardness and Young's modulus for the fast-cooled specimen was under-aged, the 2.08 K/min data showed peak-aged properties, and the hardness and Young's modulus became over-aged for the 1.82 K/min specimen (Figures 5c and 5d).

Hardness as a function of cooling rate was illustrated in Figure 3.6.5b for microindentation results and in Figure 3.6.5c for nanoindentation results. For both the microindentation and nanoindentation data, hardness values of fast-cooled specimens fall within the hardness range of slow-cooled specimens (Figures. 5b and 5c), implying no significant difference in hardness between slow-cooled and fast-cooled materials.
In terms of Young's modulus obtained by nanoindentation, slow-cooled specimens have Young's modulus between 57 GPa and 63 GPa, while that of the fast-cooled specimen N106 is about 54 GPa. It is well documented that microcracking can significantly reduce the Young's modulus of polycrystalline brittle materials [Case 2002].

4.3 Dynamic elastic moduli

Room temperature dynamic elastic moduli were measured by resonant ultrasound spectroscopy (RUS) on six slow-cooled ingot specimens with identical compositions ($Ag_{0.86}Pb_{19}Sb_{1.0}Te_{20}$) and cooling rate (2.08°C/hr) (Table 3.6.1).

Among the six slow-cooled specimens, the elastic moduli exhibited some variability, such that Young's modulus varied from 49.5 GPa to 52.3 GPa (Figure 3.6.6a), while the

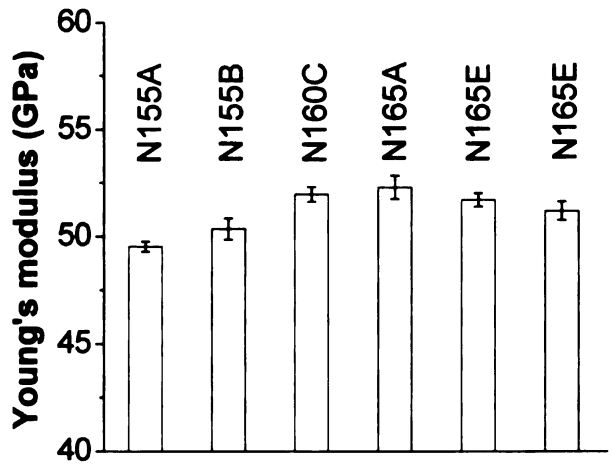

(a)

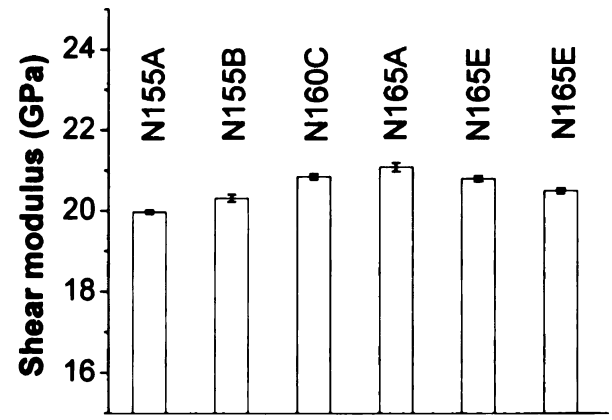

(b)

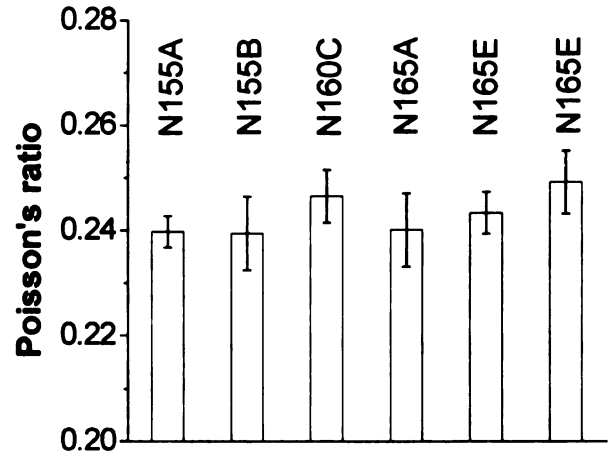

(c)

Figure 3.6.6. Room temperature dynamic elastic moduli including (a) Young's modulus, (b) shear modulus, and (c) Poisson's ratio, for six slow cooled ingot specimens with identical composition (Table 3.6.1) and processing history (Figure 3.6.1).

ranges of shear modulus and Poisson's ratio were about 20 to 21 GPa and 0.240 to 0.249, respectively (Figures 6b and 6c). Given the fact that these six slow-cooled specimens had an identical composition and cooling rate (Table 3.6.1), the variation in the dynamic elastic moduli was likely due to the composition inhomogeneity among the individual specimens.

5. Temperature dependent elastic moduli

In addition to room temperature RUS experiments, Young's modus as a function of temperature was also measured on two specimens cut from ingot N155, i.e. specimens N155-A and N155-B. Specimen N155B was measured twice using different heating/cooling rates during the modulus measurements. The first measurement was conducted under a heating/cooling rate of 5 K/min between room temperature and 773 K, while the heating/cooling rate during the second measurement was 2 K/min between 323 K and 573 K.

During the first measurement on specimen N155-B (Figure 3.6.7a) the Young's modulus first decreased linearly during heating with a slope of -0.039 ± 0.002 GPa/K between room temperature and about 500 K. Upon further heating, the slope of Young's modulus versus temperature curve changed. Although the modulus still decreased nearly linearly between about 500 K and 773 K, the slope decreased to -0.015 ± 0.001 GPa/K (Figure 3.6.7a). During cooling, Young's modulus measured between ~ 600 K and 400 K are higher than the corresponding heating measurements, resulting a hysterisis between

heating and cooling (Figure 3.6.7a).

The Young's modulus versus temperature behavior from the second measurement on specimen N155-B with a slower heating/cooling rate also exhibits a "kink" (slope change) near 500 K. However, in contrast to the 5 K/min heating and cooling rate data shown in Figure 3.6.7a, for the 2 K/min heating and cooling rate data shown in Figure 3.6.7b no hysterisis between cooling and heating was observed. The slopes in the lower temperature region (room temperature to 500 K) and higher temperature region (500 K to 773 K) are -0.042 ± 0.002 GPa/K and -0.018 ± 0.001 GPa/K, respectively, which agree well with the corresponding values obtained from the5 K/min heating and cooling rate data (Figure 3.6.7a).

A separate measurement on a different specimen N155-A (cut from the same ingot as N155-B) was conducted with a heating/cooling rate of 5 K/min. For the temperature dependent Young's modulus, a kink was observed around 500 K with a hysterisis between heating and cooling in the temperature range of ~ 450 K and 600 K (Figure 3.6.7c). The slopes are -0.035 ± 0.002 GPa/K and -0.014 ± 0.001 GPa/K for the lower and higher temperature regions, respectively. Thus for both specimens N155-A and -B measured under 5 K/min heating/cooling rate, the Young's modulus versus temperature behaviors were very similar with a slope change ~ 500 K and a hysterisis between heating and cooling (Figure 3.6.7c).

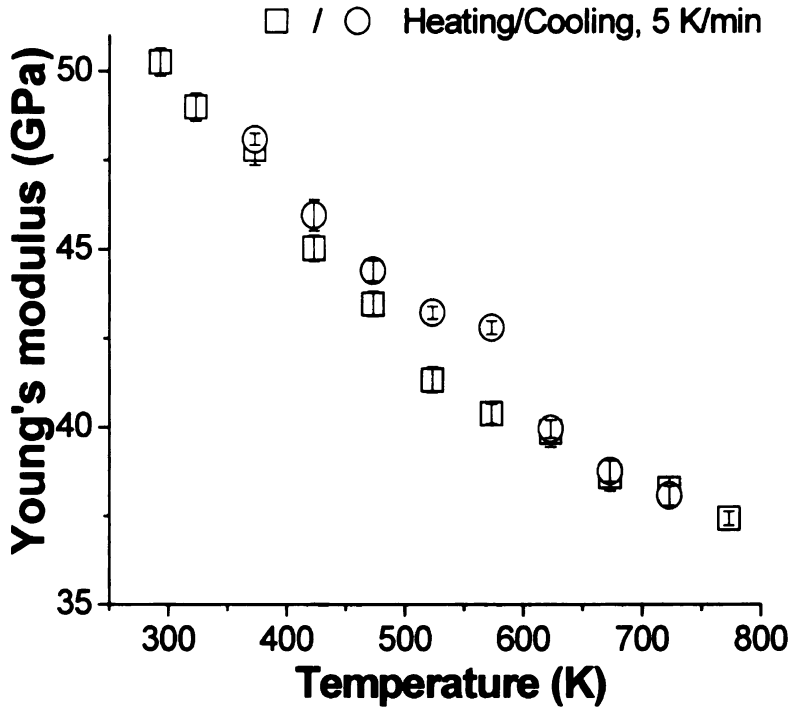

(a)

Figure 3.6.7. Young's modulus of slow cooled ingot specimens N155A and B as a function of temperature: (a) specimen N155B measured with a 5 K/min heating/cooling rate, (b) specimen N155B measured with a 2 K/min heating/cooling rate, and (c) comparison of N155A measured with 5 K/min heating/cooling rate to the two measurements on N155B ((a) and (b)). Specimens N155A and B were cut from a single cast ingot.

Figure 3.6.7 continued.

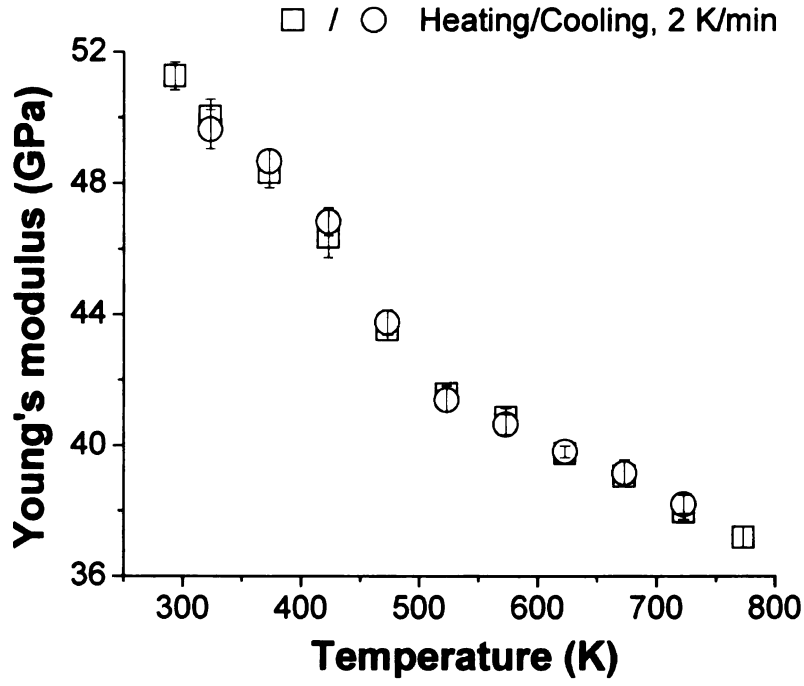

(b)

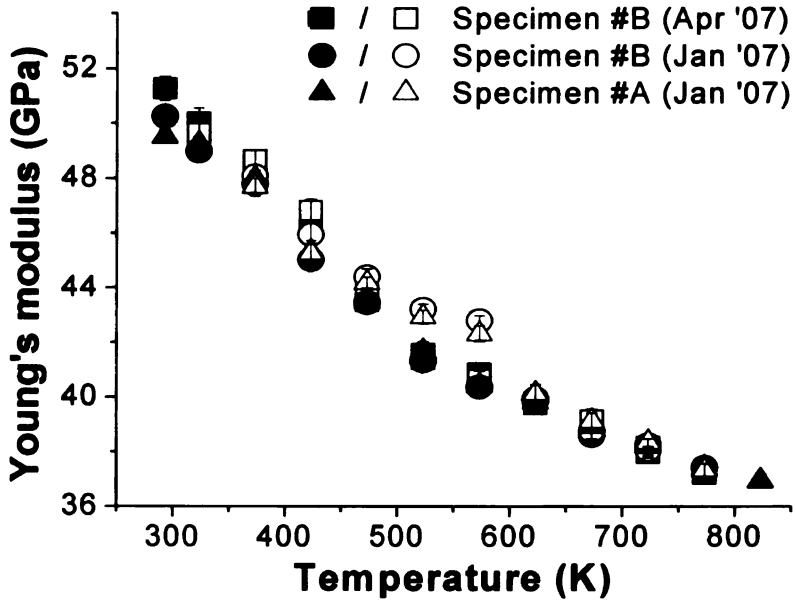

(c)

The Poisson's ratio data for both N155-A and -B increased from about 0.22 at room temperature to approximately 0.27 at around 500 K, and stayed relatively constant between 0.26 and 0.28 upon further heating above 500 K. Thus, the kink observed in the Young's modulus versus temperature relationship corresponds to an onset point of "plateau" in the Poisson's ratio – temperature curve.

There are several possible mechanisms that might be responsible for the observed kink and the heating heating/cooling rate dependent hysteresis in the Young's modulus data for specimens N155-A and N155-B, namely (1) phase change(s) (2) electron-elastic wave coupling, and (3) point defect relaxation, which are discussed below.

5.1 Phase change(s)

As discussed earlier in this chapter, phases other than PbTe and $AgSbTe_2$ may exist in the non-stoichiometric LAST materials, including Sb_2Te_3, Ag_2Te, and SbTe, which have phase transformations as a function of temperature and/or pressure.

For example, $AgTe_2$ changes between an orthorhombic phase and a cubic phase at approximately 410 K, although the phase transformation temperature is affected by the stoichiometry [Dhere 1970, Gnanadurai 2006, Sharma 1963, 1969]. For $AgTe_2$ thin films, a hysterisis was observed in the electrical resistance versus temperature relationship between heating and cooling data due to a phase transition between the orthorhombic phase and the cubic phase [Gnanadurai 2006]. In addition, the size of the hysteresis loop was affected by heating rate, such that with a 2 K/min heating and cooling rate the

orthorhombic phase changed to the cubic phase at about 396 K upon heating while the reverse transition took place at about 382 K during cooling, while the phase transition temperatures were 394 K upon heating and 378 K during cooling for a heating/cooling rate of 0.2 K/min [Gnanadurai 2006].

SbTe has two phases, i.e. the NaCl-type crystalline c-SbTe and the amorphous a-SbTe [Tani 2001]. The reversible phase change between a-SbTe and c-SbTe has been induced by laser heating. The phase transition between the a-SbTe and c-SbTe implies potential application is phase-change optical recording [Tani 2001], which is based on writing and erasing amorphous marks in a crystalline material [van Pieterson 2005]. In fact, many Sb-Te based compounds show phase change behaviors between amorphous and crystalline forms, including $Ge_2Sb_2Te_5$ which is used in DVD-random access memories and AgInSbTe used in CD-RW and DVD-RW technology [van Pieterson 2005]. The phase transformation temperature of these compounds varies as a function of stoichiometry, ranging from 376 K for Sb_2Te to 544 K for $Ge_{22}Sb_{78}$ [van Pieterson 2005].

In fact, inclusions that are rich in Sb and Te were observed in several slow-cooled LAST specimens, as seen from the SEM and EDS results included in this study. In literature, it is hypothesized that crystalline Sb_2Te_3 undergoes several phase changes under hydrostatic pressure at different temperatures, as inferred from abnormal changes in electrical conductivity and/or Seebeck coefficient [Khvostantsev 1980, 1985, Sakai

1981]. For example, phase I Sb_2Te_3 changed to phase IV Sb_2Te_3 at 6.8 GPa and at about 493 K while the reverse phase change occurred at 2.7 GPa around 433 K [Khvostantsev 1985].

5.2 Electron-elastic wave coupling

In addition to phase changes, the kink observed in the high temperature elasticity behavior of slow-cooled LAST materials may be a result of the effect of the electron band structure on the elasticity. Using RUS, Sarrao and coworkers observed a slope change (kink) in elastic constants near 240 K for single crystal FeSi, a narrow-gap semiconductor (band gap is about 0.05 eV) [Mandrus 1995, Sarrao 1994]. A later study of FeSi showed abnormal changes in heat capacity, bulk thermal expansion, and electrical resistivity in the same temperature range [Mandrus 1995].

Sarrao and Mandrus [Sarrao 1994, Mandrus 1995] attributed the abnormal elasticity behavior of FeSi to the coupling between electron and elastic waves, i.e. deformation-potential coupling, such that

$$E_k = E_{k0} + d_{k\Gamma}\varepsilon_\Gamma \qquad (1)$$

where E_k and E_{k0} are the electron energy with and without the deformation-potential coupling, $d_{k\Gamma}$ and ε_Γ are the coupling constant and strain tensor, respectively [Mandrus 1995]. It can be shown [Mandrus 1995] that the elastic constant, c(T), as a function of temperature can be expressed in terms of

$$c(T) = c^0(T) - (d_c - d_v)^2 \frac{1}{k_B T} \frac{Ng}{W} \left(\frac{I_v I_c}{I_v + I_c} \right) \quad (2)$$

where k_B is the Boltzmann constant, Ng is the total number of the electron states, W is the band width, $c^0(T)$ is the elastic constant without deformation-potential coupling, d_C and d_V are coupling constants for the conduction band and the valence band respectively, and I_V and I_C are defined as

$$I = \int f(1-f)dE \quad (3)$$

where f is the Fermi function [Mandrus 1995].

For polycrystalline brittle materials, Young's modulus decrease linearly with temperature at elevated temperatures [Wachtman 1996], such that:

$$E(T) = E_{RT}[1 - b_E(T - T_{RT})] \quad (4)$$

where E_{RT} is the Young's modulus at room temperature, T_{RT}, while b_E is a fitting parameter (see Part I, **section 2.3.1**). In Eq. (2), the effect of deformation-potential coupling on elastic constants is proportional to 1/T. Thus, in order to relate the deformation-potential coupling to the Young's modulus for polycrystalline materials, Eq. (4) can be modified as:

$$E(T) = E'\left(1 - b'T\right) - \frac{C}{T} \quad (5)$$

where C is the deformation-potential coupling parameter, while E' and b' are fitting parameters.

Linear least-squares fitting of the Young's modulus data for specimen N155-B with 2 K/min heating/cooling rate (Figure 3.6.7b) between room temperature and about 500 K to

Eq. (4) yields E_{RT} = 51.3±0.3 GPa, b_E = 8.3 x 10^{-4} ±0.3 x 10^{-4} K^{-1}, and r^2 = 0.98 (Table 3.6.4, Figure 3.6.8). Nonlinear least-squares fitting of the Young's modulus data for the expanded temperature range from room temperature to 773 K to Eq. (5) gives E' = 39±5 GPa, b' = 2.7 x 10^{-4} ±0.9 x 10^{-4} K^{-1}, and C = -4540±1119 GPa·K, with an r^2 of 0.99 (Table 3.6.4, Figure 3.6.8).

Although non-linear least-squares fitting to Eq. (5) can well describe the data for N155-B between room temperature and 773 K with an r^2 of 0.99 (Table 3.6.4, Figure 3.6.8), it is difficult to interpret the fitting parameters due to the lack of details of the deformation-potential coupling for LAST materials.

5.3 Point defect relaxation

The third possible mechanism for the kink in the elasticity plots for slow-cooled LAST specimens (Figure 3.6.7) may be related to point defect relaxation. In a study of $Tb_2Hf_2O_7$ and $Tb_2Zr_2O_7$, Dole and coworkers [Dole 1983] observed kinks in Young's modulus versus temperature curve around 670 K, where the slope, b_E (Eq. (4)), between 298 K and 670 K was about 2.8 x 10^{-4} K^{-1} while the slope changed to approximately 1.2 x 10^{-4} K^{-1} above 670 K. In addition, Dole noted that this abnormal behavior was reproducible [Dole 1983].

Dole [Dole 1983] proposed that the kinks in $Tb_2Hf_2O_7$ and $Tb_2Zr_2O_7$ were due to mechanical relaxation. Upon mechanical excitation, point defects can jump from high-energy sites to low energy sites, which were equivalent sites in the unstrained

Table 3.6.4. Regression results for Young's modulus values of specimen N155-B measured with a heating/cooling rate of 2 K/min fit to the linear temperature-modulus relation given by Eq. (4) and the non-linear least-squares fit to Eq. (5).

Fitting function:	$E = E_{RT}[1 - b_E(T-T_{RT})]$			(Eq. (4))
Temperature range:	293 to 523 K			
Parameters	E_{RT} (GPa)	b_E (x 10^{-4} K^{-1})	r^2	
	51.3±0.3	8.3±0.3	0.98	
Fitting function:	$E = E'(1 - b'T) - C/T$			(Eq. (5))
Temperature range:	293 to 773 K			
Parameters	E' (GPa)	b' (K^{-1})	C (GPa·K)	r^2
	39 ± 5	2.7±0.9	-4540±1119	0.99

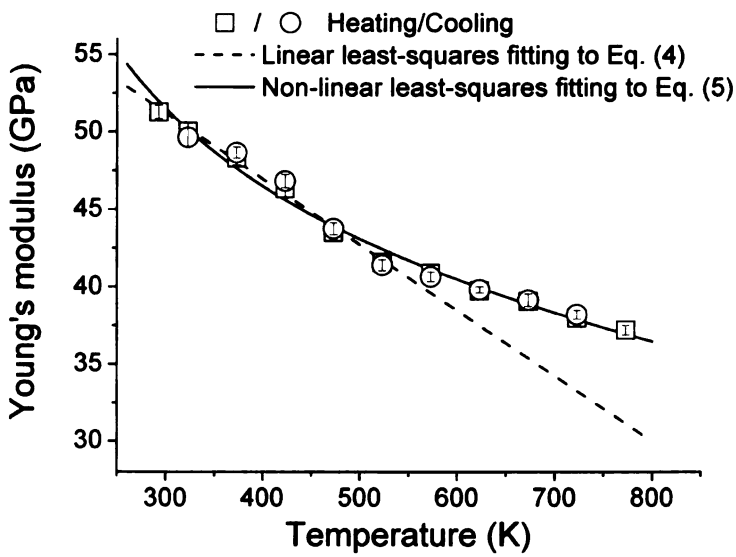

Figure 3.6.8. Young's modulus versus temperature data from specimen N155-B with the 2 K/min heating/cooling rate fit to Eq. (4) with linear least-squares regression between room temperature and about 500 K and a non-linear least-squares regression to Eq. (5) between room temperature and about 800 K.

materials. These equivalent point defect sites became un-equivalent after the strain due to elastic modulus measurement was imposed [Dole 1983, Nowick 1972, Wachtman 1963a, Wachtman 1963b].

Two theoretical treatments have been applied to point defect relaxation, i.e. an "elastic dipole" approach by Nowick and Berry [Nowick 1972] and a crystallographic approach by Wachtman [Wachtman 1963a, Wachtman 1963b].

Nowick and Berry [Nowick 1972] adopted the "elastic dipole" concept from Kröner [Kroner 1958] to characterize the interaction between an applied stress field and point defects. The elastic dipole is actually a second rank tensor, which Nowick defined as [Nowick 1972]:

$$\varepsilon_{ij}^{d} - \varepsilon_{ij}^{0} = \sum_{p=1}^{n_d} \lambda_{ij}^{(p)} C_p \tag{6}$$

where ε^{d} and ε^{0} are strain in the crystal with and without defects, $\lambda^{(p)}$ is the so-called elastic dipole in an orientation p, C_p is the dipole concentration in an orientation p, n_d is the number of possible defect orientations.

It can be shown that the change in elastic compliance, δS, can be expressed as [Nowick 1972]:

$$\delta S = \beta \left(\frac{C_0 V_0}{k_B T} \right) (\delta\lambda)^2 \tag{7}$$

where β is a numerical factor, C_0 is the total molar concentration of point defects, V_0 is the molar volume, k_B is the Boltzmann constant, T is temperature, and $\delta\lambda$ is the appropriate difference in principle values of the λ tensor, which depends on the crystal

symmetry, defect symmetry, and applied stress field. The quantity $\delta\lambda$ can be visualized as a "shape factor" for the ellipsoid that represents the magnitude of the λ tensor as a function of crystallographic direction [Nowick 1972]. Thus the tensor λ ellipsoid characterizes the anisotropy imposed on the defect by the stress field.

Eq. (7) is valid under two assumptions: (1) only one species of defect is present, and (2) the defect concentration is dilute enough so that there are no interactions among defects [Nowick 1972]. Thus Eq. (7) may not be appropriate in describing LAST materials, which are heavily doped with Ag and Sb. However, the general criterion to determine the possibility of point defect relaxation can be applied to this study: point defect relaxation can only occur when the defect symmetry is lower than the crystal symmetry [Nowick 1972]. The matrix material for LAST can be visualized as PbTe, which has a NaCl-type structure. The fact that the electron diffraction patterns for LAST materials can be refined to tetragonal or rhombehedral structures [Quarez 2005] implies that the symmetry of the defective crystal is lower than that of PbTe. Thus it is possible that the elastic abnormality (the kink) observed in LAST materials is, as least in part, due to point defect relaxation.

Wachtman and coworkers [Wachtman 1963a, Wachtman 1963b] considered strain effects on imperfect crystals with point defects (vacancies, substitutes, and interstitials) and developed the symmetry conditions for when equivalent defect sites will become un-equivalent under stress fields. Two general rules were proposed, such that: 1) mechanical relaxation will not occur if there is only one point defect site per primitive

cell or if there are only two defect sites that are centrosymmetric, and 2) the splitting factor of equivalent sites into un-equivalent sites depends on the point group symmetries of the unstrained crystal and the strained crystal, such that:

$$f = \frac{N_{un}}{N_{st}} \tag{6}$$

where f is the splitting factor, N_{un} is the total number of the equivalent sites in the unstained crystal while N_{st} is the number of equivalent sites in a subset in the strained crystals, respectively [Wachtman 1963b]. For example, if there is a set of six equivalent sites in the unstrained crystal, which divides into two subsets with three sites in each subset upon mechanical relaxation, then the splitting factor for this relaxation process is two (six divided by three). In the strained crystal, sites within a given subset are equivalent, but are different than the sites in other subsets.

Watchman *et al.* then discussed splitting possibilities in several common crystal structures, including Al_2O_3, MgO, TiO_2, diamond, perovskites, and spinels, *etc.* [Wachtman 1963b]. For the rock salt type crystals, mechanical relaxation is unlikely due to isolated point defects, but mechanical relaxation can occur when defect pairs (vacancy-substitute) without centrosymmetry are present [Wachtman 1963b]. In addition, mechanical relaxation can also occur if the symmetry of the crystal with defects is lower than the symmetry of the defect-free crystal [Wachtman 1963b]. LAST materials are essentially doped PbTe, and pure PbTe has a rock salt structure. Quarez *et al.* suggested that substituting Ag and Sb atoms may lower the crystal symmetry to tetragonal or

rhombehedral [Quarez 2005], which implies point defect relaxation may occur in LAST materials. The lowering of the symmetry of LAST may thus be a function of the concentration of dopants.

For the LAST specimen N155-B included in this study, and $Tb_2Hf_2O_7$ and $Tb_2Zr_2O_7$ studied by Dole *et al.* [Dole 1983], normalized Young's modulus with respect to the Young's modulus at the "kinks" are plotted as a function of the normalized temperature with respect to the "kink" temperature (Figure 3.6.9). In addition, the normalized elastic constant of c_{11} of FeSi [Mandrus 1995, Sarrao 1994] is included in Figure 3.6.9.

In the normalized elastic modulus versus temperature relationship (Figure 3.6.9), N155-B has the largest slope values both below and above the "kink" temperature, while the $Tb_2Hf_2O_7$ specimen shows the smallest slope values (Figure 3.6.9). However, the four different modulus-temperature curves can be overlapped with each other by an in-plane rotation about an axis that passes through the kink and is perpendicular to the paper plane (Figure 3.6.9), which implies the differences between the slope value in the low temperature region and that in the high temperature region are comparable among the four materials. Thus the behavior of the elastic modulus observed in the LAST specimen N155 (Figure 3.6.7) is consistent with point defect relaxation.

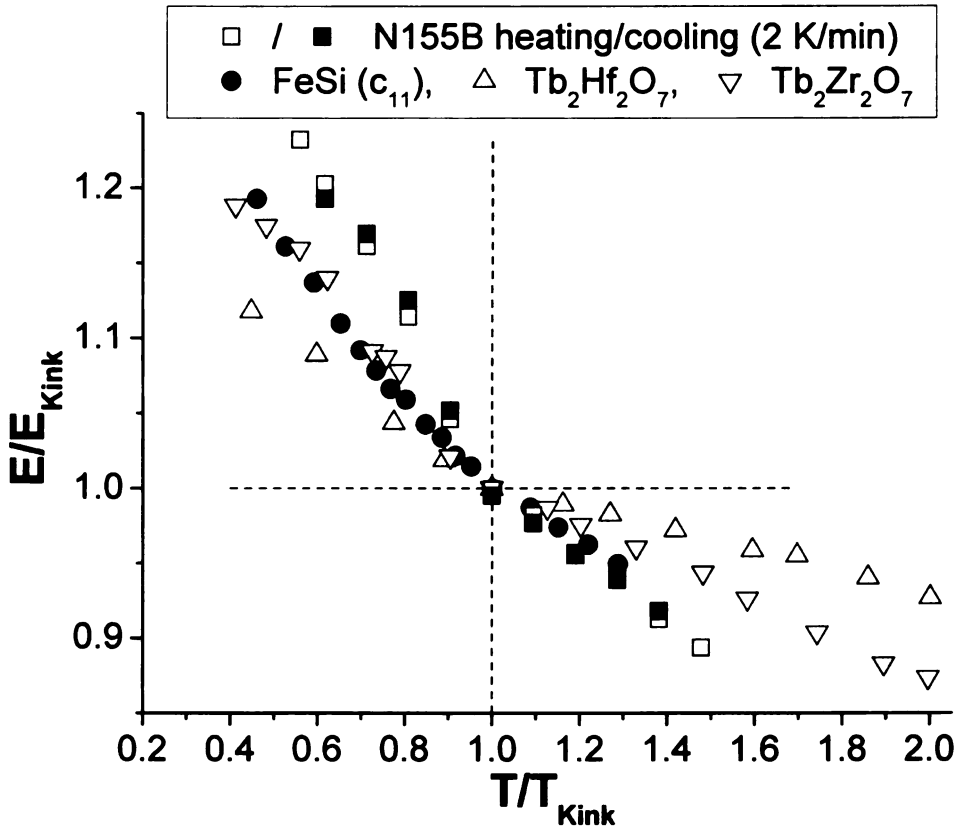

Figure 3.6.9. Young's modulus or elastic constant c_{11} as a function of temperature, where the moduli and temperature are normalized with respect to E_{kink} and T_{kink}, the modulus and temperature at the kink, respectively, for the LAST specimen N155-B in this study, $Tb_2Hf_2O_7$ and $Tb_2Zr_2O_7$ [Dole 1983], and FeSi [Mandrus 1995, Sarrao 1994].

6. Conclusions

For LAST ingot fabricated by slow-cool casting, the microstructures, room temperature mechanical properties, and high temperature elasticity were studied. Three types of inclusions were observed, i.e. quasi-spherical (> 100 microns in diameter), needle-shaped (up to 20 microns in axial dimension), and plate-like (~ 1 micron/layer) inclusions. EDS analysis indicated that each of the three inclusion types (morphologies) was rich in Sb and Te in contrast to the Pb and Te rich matrix.

Room temperature hardness measured from microindentation showed no significant difference between slow-cooled materials and fast-cooled ingots. However, a higher fracture strength and Young's modulus were obtained in slow-cooled specimens, which imply slow cooling process might reduce cracking in cast ingots. The hardness and Young's modulus data versus cooling rate exhibited a similar behavior as seen in aging. Variation in the room temperature dynamic elasticity for specimens with identical (nominal) composition and cooling rate perhaps may be attributed to composition inhomogeneity in the cast materials, but further research is needed to determine the magnitude of the compositional variation among these specimens.

RUS measurements revealed a kink in the Young's modulus – temperature relationship for a slow-cooled ingot. The kink (slope change) was observed at about 500 K. The kink was repeatable. The hysterisis between heating and cooling depended on the heating/cooling rate during measurements. Three possible mechanisms were proposed to explain the modulus kink, including phase change(s), an electronic structure effect, and a

point defect relaxation process. A more complete understanding of the

modulus-temperature kink behavior will require additional research.

References

[Androulakis 2007] J. Androulakis, C. H. Lin, H. Kong, C. Uher, C. I. Wu, T. Hogan, B. A. Cook, T. Caillat and M. G. Kanatzidis, "Spinodal Decomposition and Nucleation and Growth as a Means to Bulk Nanostructured Thermoelectrics: Enhanced Performance in Pb1-xSnxTe-PbS", *Journal of the American Chemical Society*, **129**: 9780-9788 (2007).

[Barsoum 1997] M. W. Barsoum, *Fundamentals of ceramics*, (McGraw-Hill Co., Inc., New York, 1997), pp. 410-415.

[Borisova 1984] L. Borisova, "Density-of-States Effective Mass in Solid-Solutions of the (Agx/2Pb1-xSbx/2)Te Type", *Physica Status Solidi B-Basic Research*, **126**: K155-K158 (1984).

[Buyanov 1999] Y. I. Buyanov, L. V. Goncharuk and V. R. Sidorko, "Phase composition and thermodynamic properties of alloys of the Te-PbTe-Sb2Te3 system", *Powder Metallurgy and Metal Ceramics*, **38**: 270-273 (1999).

[Case 2002] E. D. Case, "The Saturation of Thermomechanical Fatigue in Brittle Materials", in *Thermo-Mechanical Fatigue and Fracture*, edited by M. H. Alibadi (WIT Press, Southampton, UK, 2002), pp. 137-208.

[Dhere 1970] N. G. Dhere and A. Goswami, "Growth of Vapour Phase Deposits of Ag2Se and Ag2Te on Single Crystals", *Thin Solid Films*, **5**: 137-144 (1970).

[Dole 1983] S. L. Dole and O. Hunter, "Elastic Properties of Hafnium and Zirconium-Oxides Stabilized with Praseodymium or Terbium Oxide", *Journal of the American Ceramic Society*, **66**: C47-C49 (1983).

[Flegler 1995] S. L. Flegler, J. W. Heckman and K. L. Klomparens, *Scanning and Transmission Electron Microscopy: An Introduction* (Oxford University Press, New York,

1995), pp. 74-75.

[Geller 1959] S. Geller and J. H. Wernick, "Ternary Semiconducting Compounds with Sodium Chloride-Like Structure - AgSbSe2, AgSbTe2, AgBiS2, AgBiSe2", *Acta Crystallographica*, **12**: 46-54 (1959).

[Gnanadurai 2006] P. Gnanadurai, N. Soundararajan and C. E. Sooriamoorthy, "Effect of heating rate on the hysteresis in the phase transition in silver telluride thin films", *Vacuum*, **81**: 1-7 (2006).

[Hsu 2004] K. F. Hsu, S. Loo, F. Guo, W. Chen, J. S. Dyck, C. Uher, T. Hogan, E. K. Polychroniadis and M. G. Kanatzidis, "Cubic AgPbmSbTe2+m: Bulk thermoelectric materials with high figure of merit", *Science*, **303**: 818-821 (2004).

[Ikeda 2007] T. Ikeda, S. M. Haile, V. A. Ravi, H. Azizgolshani, F. Gascoin and G. J. Snyder, "Solidification processing of alloys in the pseudo-binary PbTe-Sb2Te3 system", *Acta Materialia*, **55**: 1227-1239 (2007).

[Khvostantsev 1980] L. G. Khvostantsev, A. I. Orlov, N. K. Abrikosov and L. D. Ivanova, "Thermoelectric Properties and Phase-Transition in Sb2te3 under Hydrostatic-Pressure up to 9 Gpa", *Physica Status Solidi a-Applied Research*, **58**: 37-40 (1980).

[Khvostantsev 1985] L. G. Khvostantsev, A. I. Orlov, N. K. Abrikosov and L. D. Ivanova, "Kinetic-Properties and Phase-Transitions in Sb2te3 under Hydrostatic-Pressure up to 9-Gpa", *Physica Status Solidi a-Applied Research*, **89**: 301-309 (1985).

[Kroner 1958] E. Kroner, "Berechnung Der Elastischen Konstanten Des Vielkristalls Aus Den Konstanten Des Einkristalls", *Zeitschrift Fur Physik*, **151**: 504-518 (1958).

[Maier 1963] R. G. Maier, "Zur Kenntnis Des Systems Pbte-Agsbte2", *Zeitschrift Fur Metallkunde*, **54**: 311-312 (1963).

[Mandrus 1995] D. Mandrus, J. L. Sarrao, A. Migliori, J. D. Thompson and Z. Fisk, "Thermodynamics of Fesi", *Physical Review B*, **51**: 4763-4767 (1995).

[Matsushita 2004] H. Matsushita, E. Hagiwara and A. Katsui, "Phase diagram and

thermoelectric properties of Ag3-xSb1+xTe4 system", *Journal of Materials Science*, **39**: 6299-6301 (2004).

[Nolas 2001] G. S. Nolas, J. Sharp and H. J. Goldsmid, *Thermoelectrics: basic principles and new materials developments*, (Springer, Berlin; New York, 2001), pp. 151-159.

[Nowick 1972] S. Nowick and B. S. Berry, *Anelastic Relaxation in Crystalline Solids* (Academic Press, New York, 1972), pp. 176-221.

[Ono 1962] T. Ono, T. Irie and T. Taahama, "Thermoelectric Properties of AgSbTe2-AgBiTe2, -PbTe and -SnTe Systems", *Journal of the Physical Society of Japan*, **17**: 1070-1071 (1962).

[Porter 1990] W. D. Porter and K. E. Easterlin, *Phase transformation in metals and alloys*, (Campman and Hill, New York, 1990), pp. 1-4, 150-161, 208-222.

[Quarez 2005] E. Quarez, K. F. Hsu, R. Pcionek, N. Frangis, E. K. Polychroniadis and M. G. Kanatzidis, "Nanostructuring, compositional fluctuations, and atomic ordering in the thermoelectric materials AgPbmSbTe2+m. The myth of solid solutions", *Journal of the American Chemical Society*, **127**: 9177-9190 (2005).

[Ren 2006] F. Ren, E. D. Case, E. J. Timm, M. D. Jacobs and H. J. Schock, "Weibull analysis of the biaxial fracture strength of a cast p-type LAST-T thermoelectric material", *Philosophical Magazine Letters*, **86**: 673-682 (2006).

[Ren 2007a] F. Ren, E. D. Case, E. J. Timm and H. Schock, "Hardness as a function of composition for n-type LAST thermoelectric material", *Journal of Alloys and Compounds*, available online at doi:10.1016/j.jallcom.2007.01.086 (2007a).

[Ren 2007b] F. Ren, E. D. Case, E. J. Timm and H. Schock, "Young's modulus as a function of composition for an n-type lead-antimony-silver-telluride (LAST) thermoelectric material", *Philosophical Magazine*, **87**: 4907-4934 (2007b).

[Sakai 1981] N. Sakai, T. Kajiwara, K. Takemura, S. Minomura and Y. Fujii, "Pressure-Induced Phase-Transition in Sb2Te3", *Solid State Communications*, **40**: 1045-1047 (1981).

[Sarrao 1994] J. L. Sarrao, D. Mandrus, A. Migliori, Z. Fisk and E. Bucher, "Elastic Properties of Fesi", *Physica B*, **199**: 478-479 (1994).

[Sharma 1963] S. K. Sharma, "Transformation of Structure in Silver - Tellurium Alloy Films", *Nature*, **198**: 280-281 (1963).

[Sharma 1969] S. K. Sharma, "Structural Transformation in Thin Films of Binary Alloys", *Journal of Materials Science*, **4**: 189-194 (1969).

[Tani 2001] K. Tani, N. Yiwata, M. Harigaya, S. Emura and Y. Nakata, "EXAFS study of Sb-Te alloy films", *Journal of Synchrotron Radiation*, **8**: 749-751 (2001).

[van Pieterson 2005] L. van Pieterson, M. H. R. Lankhorst, M. van Schijndel, A. E. T. Kuiper and J. H. J. Roosen, "Phase-change recording materials with a growth-dominated crystallization mechanism: A materials overview", *Journal of Applied Physics*, **97**: Art. No. 083520 (2005).

[Wachtman 1963a] J. B. Wachtman, "Mechanical and Electrical Relaxation in Tho2 Containing Cao", *Physical Review*, **131**: 517-527 (1963a).

[Wachtman 1963b] J. B. Wachtman, E. P. Levine and H. S. Peiser, "Symmetry Splitting of Equivalent Sites in Oxide Crystals and Related Mechanical Effects", *Journal of Research of the National Bureau of Standards Section a-Physics and Chemistry*, **A 67**: 281-289 (1963b).

[Wachtman 1996] J. B. Wachtman, *Mechanical Properties of Ceramics*, (Wiley Interscience, New York, 1996), pp. 33-35.

Chapter 7

A. L. Pilchak, F. Ren, E. D. Case, E. J. Timm, H. J. Schock, C. I. Wu and T. Hogan, "Particle size reduction by planetary ball milling and powder characterization of LAST (Lead-Antimony-Silver-Tellurium) thermoelectric material", *Philosophical Magazine*, **87**: 4567-4591 (2007).

Characterization of dry milled powders of LAST

(Lead – Antimony – Silver – Tellurium) thermoelectric material

A. L. PILCHAK†§, F. REN†, E. D. CASE*†, E. J. TIMM‡, H. J. SCHOCK‡, C-I WU¶, and T. P. HOGAN¶

†Chemical Engineering and Materials Science Department,
Michigan State University, East Lansing, MI 48824 USA
‡Mechanical Engineering Department, Michigan State University,
East Lansing, MI 48824 USA
¶Electrical and Computer Engineering Department, Michigan State University,
East Lansing, MI 48824 USA
§Current address: Materials Science and Engineering Department,
Ohio State University, Columbus, OH 43210 USA

Although thermoelectric (TE) materials are often fabricated as cast ingots, there has been recent interest in the powder processing of these materials. Cast TE materials typically have grain sizes as large as several hundred microns, but powder processing (grinding, milling and then sintering) can produce dense specimens with a reduced grain size, an improved mechanical integrity, and enhanced thermoelectric properties. In the TE literature when powder processing is employed, little or no description is provided for the powder processing techniques and the powder processing parameters are either not characterized or only a mean particle size is given. In this study, powders milled from solid cast ingots of the thermoelectric compound LAST (Lead-Antimony-Silver-Tellurium) were characterized via Coulter Counter to measure the mean powder particle size and the size distribution, scanning electron microscopy (SEM) to examine the powder

particle morphology, and X-ray diffraction (XRD) to detect possible phase changes or amorphization. The impurity levels in the milled powders were examined by wear rate measurements on the milling media as well as by energy dispersive x-ray analysis and inductively coupled plasma measurements.

Keywords: Energy materials; Thermoelectric materials; Compound semiconductors; Powder metallurgy; Ball-milling; Materials characterization; Electron microscopy; X-ray diffraction; Particle size

1. Introduction

Although thermoelectric (TE) materials have frequently been fabricated by solidification from a melt, there has been considerable recent interest in milling and powder processing of TE materials [1-7]. For example, planetary ball milling has been used for particle size reduction of TE materials [6, 7] as well as for synthesis by mechanical alloying [8-11].

TE materials solidified from a melt typically exhibit a grain size of several hundred microns [1, 12-15]. Since the strength of brittle materials is proportional to the inverse square root of grain size [16, 17], these large grain sizes produced by casting lead to low strength and hence poor mechanical integrity [15]. However, powder processing can produce small powder particle sizes which in turn can produce dense TE specimens with micron-scale grains when the powders are densified by techniques such as hot-pressing [2-5, 18] and spark plasma sintering [1, 7].

Planetary milling can serve a number of roles in powder processing, such as particle size reduction, mixing powders with binders or lubricants [19-21], mixing composite powders [22-24], and particle deagglomeration [25]. In this study, dry planetary milling of cast ingots of LAST (Lead-Antimony-Silver-Tellurium) [26] thermoelectric material produced a fine equiaxed powder that is free of agglomeration. The milled powders were characterized by several analytical techniques. Scanning Electron Microscope (SEM) and X-ray diffraction were used to characterize changes in particle shape and size as a function of milling time. Scanning Electron Microscope (SEM) was used to determine

the particle morphology and Coulter Counter measurements provided the mean particle size and the particle size distribution. X-ray diffraction was used to determine whether or not phase changes occurred during milling. These powder processing parameters (particle morphology, mean particle size, particle size distribution) are critical to the powder flow [21, 27], powder particle packing [21, 27], sintering rate [21, 27] and the final density [21, 27] of the sintered compacts. The phases present can influence the mechanical [28] and thermoelectric properties [26] of the sintered material. The microstructure (grain size and porosity) that evolves during sintering is in turn important for the mechanical, thermal and electrical properties of the thermoelectric material. However, the powder processing parameters are seldom reported in the thermoelectrics literature. In contrast, this study characterizes the powder particle size distribution and particle morphology, phases present in LAST TE materials, and is the first comprehensive study of powder processing and powder characterization on any TE material system in literature.

In addition to characterizing the particle morphology, mean particle size, particle size distribution of the milled powders, and the impurity concentration in the milled powders were examined by three independent techniques. The mass of the alumina milling media was measured as a function of time in order to determine the alumina contamination due to the wear of the milling media. In addition, the concentration of impurities in the as-milled powders was determined from energy dispersive x-ray analysis and from inductively coupled plasma measurements.

2. Background

The heat to electricity conversion efficiency of thermoelectric materials is characterized by the dimensionless figure of merit (*ZT*), such that

$$ZT = \frac{\sigma S^2}{\kappa} T$$

where σ is the electrical conductivity, S is the thermopower or Seebeck coefficient, κ is the thermal conductivity, and T is the temperature [29]. A high *ZT* value is desired for the applications such as thermoelectric power generator. Hsu *et al.* [29] reported a *ZT* of ~ 1.7 at 700 K for LAST ($AgPb_mSbTe_{m+2}$, with $m = 18$) semiconductor materials. Further study by Quarez and coworkers [26] suggested that LAST materials are inhomogeneous at nano-scale with Ag and Sb rich nanophases embedded in the matrix that is poorer in Ag and Sb. The superior *ZT* of LAST material is believed to originate from the enhancement of the thermoelectric properties due to these nano-domains [26].

However, cast thermoelectric materials including cast LAST specimens have low mechanical strength. For example, Ren *et al.* reported a biaxial fracture strength of ~ 15 MPa for a cast Ag-Sb-Sn-doped PbTe with a mean grain size of 706 μm [15]. A study by Jiang and coworkers [1] compared p-type $(Bi_2Te_3)_x(Sb_2Te_3)_{1-x}$ (for $x = 0.16$, 0.20 and 0.24) thermoelectric materials prepared by zone-melting and by spark plasma sintering (SPS). The spark plasma sintering reduced the grain size (relative to the zone melted material) that resulted in a three-point bend strength of SPS specimens of about 65 MPa,

while the bending strength of zone-melted specimens was around 10 MPa.

A primary motivation for powder processing of the LAST or other TE materials is to decrease the grain size of the densified material and hence increase the fracture strength, a fine grained microstructure also can increase the thermoelectric figure of merit, *ZT* [1, 6, 7, 30]. As an example, the grain size refinement achieved by SPS (compared to zone melting) lead to an increased *ZT* by a factor of from 1.08 to 1.15 for the p-type $(Bi_2Te_3)_x(Sb_2Te_3)_{1-x}$ materials studied by Jiang et al. [1]. In addition, a fine particle size enhances sinterability of the powders [17, 21].

Although various particle size reduction techniques have been applied to TE materials, including crushing and grinding [31], crushing, grinding and sieving [1-3], and planetary ball milling [7, 32], the powder processing parameters such as particle size, particle morphology, particle size distribution, and phases present after milling or grinding have not been characterized in detail for TE materials. Nevertheless, since these powder processing parameters have a fundamental impact on the microstructure (and hence the mechanical and other physical properties of a sintered body), powders have been characterized in detail for many brittle material systems, including powders fabricated by planetary milling and other milling techniques [33-39].

For example, in a study of Bi/MgO, Bi/Al_2O_3, Bi/SiO_2, Cu/FeS nanocomposites and PbS nanoparticles prepared by high-energy milling, Balaz *et al.* [33] used SEM to examine the powder particle morphology, XRD to study the phase present in the milled powders, and gas absorption to measure the powders' specific surface area. Furthermore,

the SEM has been utilized to study the powder particle morphology of B-C powders fabricated via planetary ball milling [34], g-C_3N_4 powders from high-energy ball milling [35], Bi2333 powders from planetary ball milling/attrition milling [36], and Z-phase $Ba_3Co_2Fe_{24}O_{41}$ powders from dry/wet milling [37], while XRD was used to examine the phases present [34-37]. Wongmaneerung et al. [38] used laser diffraction to determine the particle size of niobate powders while Filio *et al.* [39] used BET to study the specific surface area of talc powders.

Thus, given the critical importance of powder processing parameters to the densification and subsequent physical properties of materials, many researchers have focused their work on the characterization of the fundamental powder processing parameters [33-39] in ways that are the same as or similar to the methods employed in this study of powders milled from LAST thermoelectric ingots.

3. Experimental Procedure

3.1 *Materials*

The raw materials used in this study were high purity lead (99.99% purity, Surepure Chemetals, Florham Park, NJ, USA), antimony (99.999% purity, Cerac, Milwaukee, WI, USA), silver (99.99% purity, Royal Canadian Mint, Ottawa, Ontario, Canada) and tellurium (99.999% purity, Cerac, Milwaukee, WI, USA). The impurities reported by the vendors for each of the four raw materials are listed in Table 3.7.1 [40 – 42].

Table 3.7.1 Concentration of impurity elements in the raw materials used to cast LAST ingots in this study.

Element	Impurity element (concentration in ppm)	Ref.
Lead (Pb)	Ag (2), As (2), Bi (2), Cd (1), Cu (2), Ni (1), Sb (4), Sn (7), Zn (2)	[40]
Antimony (Sb)	Cu (2)	[41]
Silver (Ag)	Bi (5), Cu (100), Pb (10)	[42]
Tellurium (Te)	Pb (1), Se (1), Si (1)	[41]

3.2 *Ingot Preparation*

The lead, antimony, silver and tellurium were cast to form either 100 gram or 200 gram n-type LAST thermoelectric ingots with the composition $Ag_{0.43}Pb_{18}Sb_{1.2}Te_{20}$ The mass of each element was determined to an accuracy of ± 0.0004 g. The casting procedure began by placing the four raw materials into a 25 mm diameter fused silica ampoule. The ampoule was then evacuated and sealed, leaving a residual pressure of approximately 0.01 Pa. The raw materials were melted and then cooled in a 3-zone split-tube rocking furnace (Applied Test Systems, Inc. Butler, PA, USA) using the heating profile shown in Figure 3.7.1.

3.3 *Pre-milling treatment*

Planetary milling can only be done effectively if the mean size of the powder particles are initially (at the onset of the milling process) ≈100 microns or less [21, 43]. Thus, prior to planetary milling the cast ingots were crushed and ground to convert the solid ingots into a powder that could then be milled. Two pre-milling treatments were used, namely (i) crushing and grinding without sieving and (ii) crushing, grinding, sieving and re-grinding (Table 3.7.2).

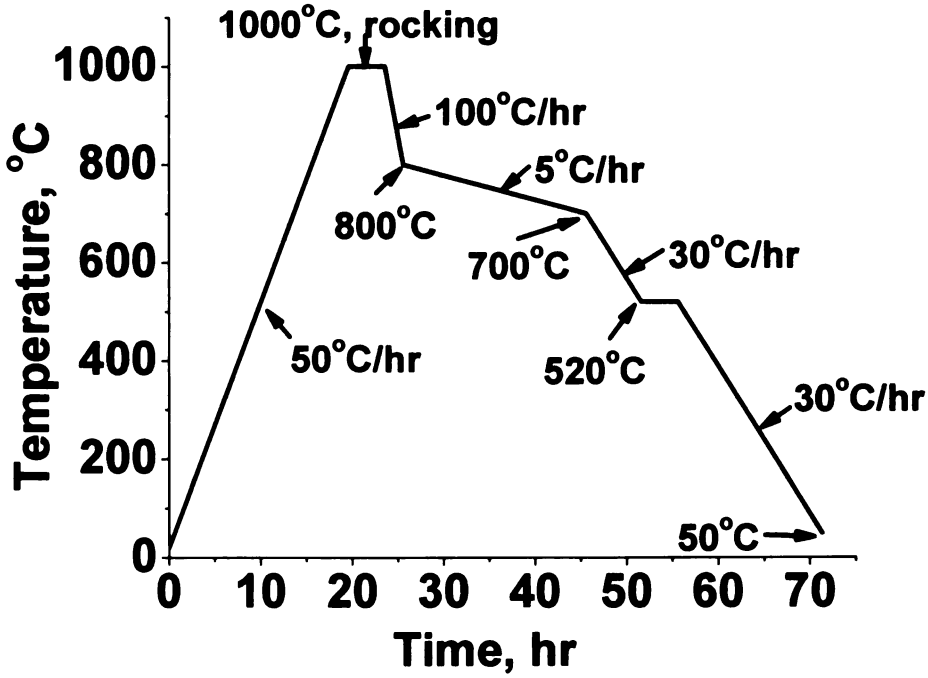

Figure 3.7.1. The time-temperature profile for the cast ingots used in this study.

Table 3.7.2 Powder size reduction methods used in this study.

Treatment	Method
C	Crushed from the ingot with slowly applied pressure
CG	Crushed powders ground in a mortar and pestle
CGM-t	CG powders milled for time t in minutes
CGSR	Crushed powders ground in a mortar and pestle and reground until all powders passed through a 53 μm sieve
CGSRM-t	CGSR powders milled for time *t* in minutes

3.3.1. Crushing and grinding without sieving (CG)

The as cast ingots were crushed into very coarse particles, ranging from roughly 0.5 to 1 cm in diameter, using pressure slowly applied by a steel block. Prior to crushing, all ingots were wrapped in two 100 mm x 100 mm x 0.03 mm weighing papers (VWR Scientific Products, #12578-165, West Chester, PA, USA) so that the ingot did not contact the steel block directly. The crushed ingot was then ground using a mortar (CoorsTek #60316, Golden, CO, USA) and pestle (CoorsTek #60317, Golden, CO, USA) for approximately five minutes.

3.3.2 Crushing, Grinding, Sieving and Re-grinding (CGSR)

The crushing, sieving, re-grinding procedure employed the same initial crushing and grinding technique described in Section 3.3.1. However, after grinding the powders were sieved using a vibratory sieve unit (Retsch AS 200, Haan, Germany) operated at 70 Hz. A four-sieve stack with openings of descending size (250 μm, 125 μm, 75 μm and 53 μm) was used, with the crushed and ground powders placed on the 250 μm sieve. All powders retained on the sieves were reground and re-sieved until all powders passed through the 53 μm sieve.

3.4 *Milling (CGM-t and CGSRM-t)*

A planetary ball mill (Retsch PM100, Haan, Germany) with 4 kg counterweight was used

to mill the CG and CGSR powders. The milling jar that was used was cylindrical with an inner diameter of 76.2 mm and a total volume of 250 mL. The milling jar was lined with 99.7% pure alumina (Retsch 01.462.0221, Haan, Germany). The milling media consisted of 99.64% pure alumina spheres, approximately 20 mm in diameter (Glen Mills 7250-020000-5, Clifton, NJ, USA). The detailed compositions of both the alumina milling jar and the alumina milling media are given in Table 3.7.3. The milling jar lid was secured with rubber o-rings and a screw clamp with a locking mechanism that provided an airtight seal. All powders were milled at 100 rpm with milling times ranging from 3 minutes to 420 minutes.

Between each batch, the mill and milling media were cleaned using an acetone rinse. After every fourth batch of powders, the milling jar was cleaned using about 50 mL of spherical glass beads with diameters ranging from 600 to 850 microns (Potter's Industries, Ballotini Glass Impact Media, Valley Forge, PA, USA). After running the glass beads in the mill at 130 rpm for 8 minutes, the beads were removed from the mill and discarded. The milling jar and the milling media were then cleaned with acetone.

3.5 *X-ray diffraction analysis*

A powder X-ray diffraction study was conducted on the milled LAST powders using a rotating anode diffractometer (Rigaku 20B, Rigaku Corp., Japan). Filtered Cu K-α radiation was used, with a step size of 0.02 degrees, a scan rate of 2 to 3 degrees/min, a

Table 3.7.3 Composition (in percentage) of Retsch Milling jar and Glen Mills milling media used in this study.

	Al_2O_3	SiO_2	Fe_2O_3	CaO	MgO	Na_2O	K_2O
Milling jar liner	99.700	0.075	0.010	0.070	0.075	0.010	0.000
Milling media	99.640	0.100	0.020	0.040	0.150	0.040	0.010

tube current of 100 mA, and a tube voltage of 45 kV. The specimens were scanned over a 2θ range from 20° to 80°, which includes all of the major XRD peaks observed for the LAST material [26].

3.6 *SEM Analysis*

Samples of powders from each milling procedure (Table 3.7.2) were examined by SEM (JEOL 6400V, JEOL Corp. Japan). Conductive carbon tape was placed on aluminum stubs and the LAST powders were placed directly onto the carbon tape. Prior to loading the specimens into the SEM chamber, a stream of compressed air was used to remove loose powder particles from the surface of the carbon tape in order to minimize contamination of the SEM chamber. All of the SEM images were taken at a working distance of 15 mm with a 20 kV accelerating voltage.

3.7 *Particle Size Analysis*

The particle size distribution analyses were performed at CCE Technologies (Cottage Grove, MN, USA) using a Multisizer™ 3 Coulter Counter® (Beckman Coulter, Fullerton, CA, USA). The particles were suspended in a weak electrolyte (Beckman Coulter ISOTON® II) 0.9% NaCl by volume, with a density and viscosity of 1.01 g cm^{-3} and

0.01 g $cm^{-1} s^{-1}$, respectively [45]. In order to determine the particle size distribution, the powder suspension is drawn through a small aperture in the Coulter Counter. The volume of electrolyte displaced by each particle corresponds to a change in electrical impedance. The Coulter Counter® software then calculates particle diameter based on the impedance changes.

3.8 *Analysis of Impurities in the as-ground powder*

The concentration of impurities in the milled LAST powders was examined by three independent techniques, namely (i) wear rate measurements on the alumina milling media, (ii) inductively coupled plasma – mass spectroscopy measurements and (iii) energy dispersive x-ray analysis (EDS).

The wear rate measurements on the alumina milling media were taken after the media had been cleaned using glass beads and acetone, as described in Section 3.4. Following the cleaning with the glass beads, the media was heated in air to remove water or other volatiles that may have been absorbed by the milling media. The milling media was first loaded into an alumina boat and then the alumina media and the boat were heated in air at 200°C for four hours in an electric furnace. The mass of the milling media was then measured using an electronic balance in order to determine the mass loss as a function of milling time for the alumina media. The mass loss of the milling media corresponds to a contamination by alumina that occurs during milling.

In addition to measuring the mass loss of the alumina media, two LAST powder specimens (each with a mass of approximately 2 grams) was submitted to Shiva Technologies, Inc., Syracuse NY [45] for an analysis of impurity concentration via inductively coupled plasma – mass spectroscopy (ICP-MS). The ICP-MS is capable of resolving impurity concentrations down to the level of 1 ppm and below [45].

The EDS analysis of impurities in the LAST powders was performed using a JEOL (Tokyo, Japan) JSM-6400 scanning electron microscope equipped with a lanthanum hexaboride emitter and an Oxford Instruments (High Wycombe, Bucks, England) INCA energy dispersive X-ray spectroscopy (EDS) analysis system. Prior to examining the LAST powders, a background measurement was done on a conductive carbon tape (Ted Pella, Inc. Redding, California) attached to an aluminum stub. Then LAST powder was sprinkled onto the carbon tape for an EDS measurement on the powders. For both the background runs and the measurements on the LAST powders, the EDS data was collected using an accelerating voltage of 20 kV, a 15 mm working distance, a 300 second live time, and a 30-40% dead time.

4. Results and Discussion

4.1 *X-ray diffraction characterization of the milled powders*

Milling of brittle powders can induce phase changes [36] or partial or complete

amorphization [36, 37, 39, 46]. For example, Yavuz et al. [36] found that dry planetary milling for 3 hours with yttria-stabilized zirconia media in a polypropylene jar at 150 rpm led to the decomposition of the superconducting Bi2212 phase in Bi2223 materials into non-superconducting phases including Ca_2PbO_4, $(Sr, Ca)_2CuO_3$ and CuO. In addition to the phase decomposition, Yavuz et al. [36] observed that planetary milling led to the formation of an "extensive amorphous phase". The material included in this study, LAST, comprises a family of brittle, semiconducting quaternary compounds, thus based on the literature on other brittle compounds [36, 37, 39, 46, 47], milling-induced phase changes and/or amorphization is possible. Since the LAST materials are quaternary compounds, there are many binary or ternary compounds (some of which may not be good thermoelectric materials) that could possibly be formed upon milling. Thus, it is important to determine whether or not such crystallographic transformations took place during the milling process. In this study, we used X-ray diffraction to investigate phase changes and amorphization in the milled LAST powders.

The XRD peak positions and relative intensities of the powders milled in this study, agreed well with the XRD patterns for both (i) pure PbTe [48] and (ii) a similar LAST composition studied by Quarez et al. [26] (Table 3.7.4). In addition, the powders included in this study, the XRD peak position and intensity showed no significant differences among the powder specimens dry milled for 30 minutes, 3 hours and 7 hours (Figure 3.7.2). The observations that (i) the XRD pattern did not change during milling

Table 3.7.4 Comparison of the Miller indices, 2θ, and relative peak intensities among LAST powders in this study and pure PbTe in literature.

	111		200		220		311	
	2θ (deg)	Int.	2θ (deg)	Int.	2θ (deg)	Int.	2θ (deg)	Int.
PbTe [43]	23.42	10	27.19	100	38.90	80	46.28	10
LAST [26]	23.85	5	27.54	100	39.42	37	46.60	2
CGM-75	23.72	4	27.44	100	39.34	29	46.52	2
CGM-180	23.82	5	27.64	100	39.52	42	46.70	2
CGM-420	23.70	5	27.52	100	39.44	40	46.50	3
CGRSM-30	23.82	7	27.56	100	39.40	53	46.62	3
CGRSM-180	23.84	6	27.58	100	39.48	45	46.72	3
CGSRM-420	23.80	7	27.58	100	39.48	45	46.64	3

	222		400		420		422	
	2θ (deg)	Int.	2θ (deg)	Int.	2θ (deg)	Int.	2θ (deg)	Int.
PbTe [43]	48.23	30	56.31	20	63.54	50	70.59	40
LAST [26]	48.80	10	57.00	13	64.54	13	†	†
CGM-75	48.76	11	56.98	11	64.52	14	71.52	7
CGM-180	48.90	13	57.16	8	64.62	12	71.68	7
CGM-420	48.86	11	56.96	9	64.50	13	71.56	8
CGRSM-30	48.80	17	57.04	11	64.60	17	71.74	14
CGRSM-180	48.88	13	57.08	9	64.64	14	71.62	8
CGSRM-420	48.88	13	57.08	8	64.60	14	71.74	8

† The 2θ range in [26] did not include the (422) peak.

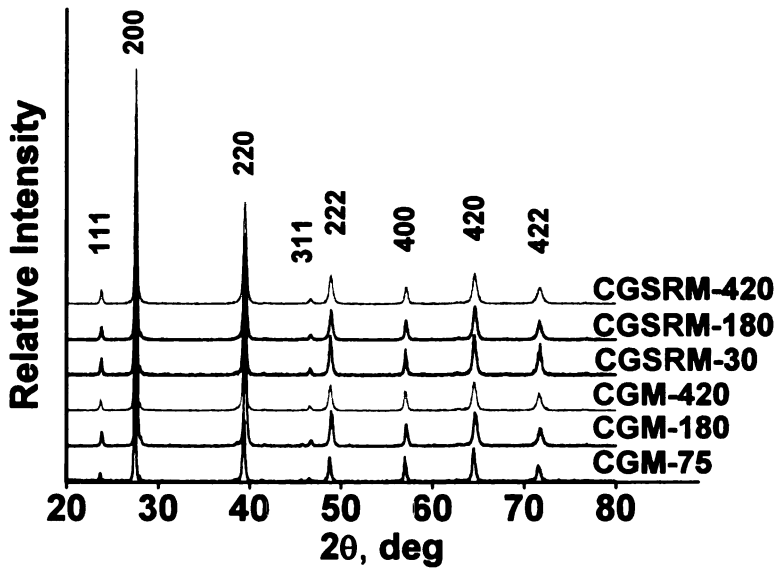

Figure 3.7.2. X-ray diffraction patterns of powders milled in this study. Table 3.7.2 lists the acronyms for the various powder processing techniques used in this study.

and (ii) the agreement among the XRD patterns for the milled powders, the pure PbTe [48] and the LAST specimens in the Quarez study [26] indicates that no significant quantities of new crystallographic phases were induced by the grinding or milling operations in this study.

In addition, none of the XRD patterns (Figure 3.7.2) displayed the low 2θ "amorphous hump" that is characteristic of amorphous materials [49]. Therefore, there is no evidence of significant amorphization due to the planetary dry milling in this study.

4.2 *SEM characterization of particle shape of the ground and the milled powders*

Scanning electron microscopy (SEM) was used to examine the particle morphology and details of powder surfaces. The particle morphology and state of agglomeration are crucial to the efficiency of powder packing [27]. Also, powder surface details indicate the mechanism of powder size reduction [47].

The powder particle shape evolves during the communition process (Table 3.7.2). The as crushed and ground (CG) powder and the CGSR (crushed, ground, sieved and re-ground, but not milled) powders are angular with cleavage steps visible, indicating brittle fractures during crushing and grinding (Figure 3.7.3a). For milling times of 3 to 30 minutes, the CGM powder and CGSRM powders still show sharp, angular edges and cleavage steps (Figure 3.7.3b), with particle aspect ratios that range from about 2:1 for 3

minutes (Figure 3.7.3c) milling time to 1.5 for 30 minutes milling time. For milling times of 180 minutes and 420 minutes (Figures III.7.3d-f, the particles are roughly equiaxed with relatively smooth surfaces (little evidence of cleavage steps) likely indicating a smoothing effect due to interparticle friction.

Both the (i) particle aspect ratio and (ii) the particle surface roughness that result from communition milling can affect the subsequent powder processing. For example, equiaxed powder particles pack to higher green densities than elongated particles and thus the initial packing density can have significant effects on the densification of the powder compact [21]. Particle agglomeration also can lead to poor powder packing and to differential shrinkage during sintering, which can in turn generate pores and cracks in the sintered component [27]. In addition, powder particle roughness affects the flow of particles where freely flowing powders are crucial to shape forming processes such as rapid dry pressing [21, 27]. However, regardless of the speed of the process, achieving near-equiaxed particle shape in an agglomerate-free powder is critical to effective densification of powder compacts [21]. For CGM powders, the particles become equiaxed for milling times of 180 minutes and longer although for CGSRM powders it only takes 30 minutes to reach a similar state.

As we demonstrated in this study, at short milling times, the milling process fractures the ground particles into angular fragments with rough surfaces (Figures III.7. 3b-c). With increasing milling time, powder particles become more equiaxed with smoother surfaces, likely due to the inter-particle friction (Figures III.7.3d-f).

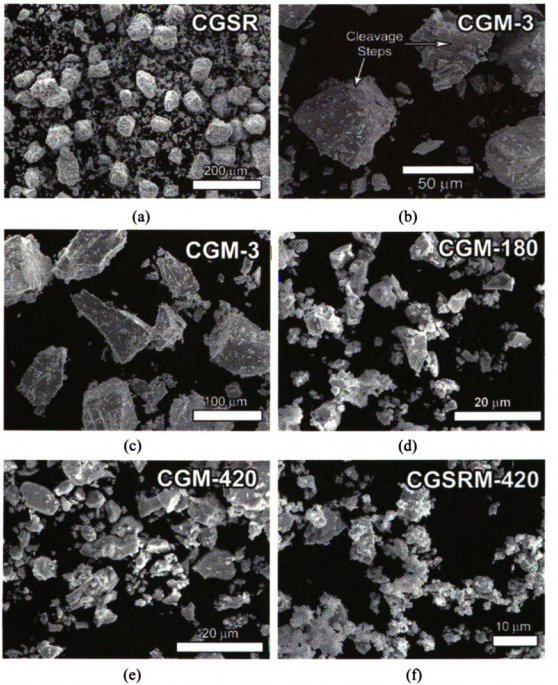

Figure 3.7.3. SEM micrographs showing particle morphology of powders received various milling treatments, (a) particle morphology of CGSR (crushing, grinding, sieving, and re-grinding) powder, (b) cleavage steps indicated by arrows for CGM-3 (milled) powder, (c)-(f) particle morphology for CGM-3, CGM-180, CGM-420, and CGSRM-420 milled powders.

It is important to note that under all of the milling conditions and for all milling times used in this study, the powders examined in the SEM were free of agglomeration. Thus, dry milling by the procedures described in this study does not require additional processing steps to remove or break up agglomerates. (In situations where agglomerates are present, procedures to eliminate them can be time consuming and costly [27]).

4.3 *Particle size analysis*

Particle size distribution can affect the sintering behavior of the powder compacts [50-53]. A theoretical model by Chappell *et al.* [50] showed that the sintering rate during the initial and intermediate stages was a strong function of the particle size distribution such that the sintering rate decreased for a broader particle size distribution. An experimental study by Ting and Lin [51] showed that alumina powders with a narrower size distribution exhibited a lower sintering rate during the intermediate sintering stage but a higher densification rate after the onset of grain growth. In addition, Shiau *et al.* [52] demonstrated a finer particle size with a uniform particle size distribution leads to pore channel pinch off at densities > 83%, prolonging the intermediate sintering stage and prohibiting grain growth. (Grain growth and densification are competing processes, so inhibiting grain growth generally enhances densification [17]). For quasi-equiaxed alumina powders (AKP20, AKP30, and AKP53, Sumitomo Chemical Co., Japan), Ma

and Lim [53] found that although a broad powder particle size distribution can have the potentially beneficial effect of allowing a higher initial packing density, the broad distribution ultimately has the negative effect of enhancing grain growth in the intermediate sintering stage resulting in inhomogeneous densification.

Large particles can also lead to abnormal grain growth, which in turn results in large grain sizes that can deteriorate the mechanical properties [17]. A narrow grain size distribution is usually preferred, since it "will decrease the propensity for abnormal grain growth" [17].

In this study, the powder particle size distribution was determined by the Coulter Counter technique. The Coulter Counter® analysis provides the particle size distribution, the mean particle size, and the standard deviation about the mean. First we will discuss the changes in particle size distribution as a function of the milling time (Figures III.7.4 and 5). Then we present a relationship for the change in mean particle size as a function of the milling time (Figure 3.7.6).

4.3.1 Particle size distribution as a function of the milling time

The pre-milling treatment leads to considerable differences in the evolution of the particle size distribution for the CGM and the CGSRM powders (Figures III.7.4 and 5, respectively). After 3 minutes of milling, the CGM powders exhibited a broad bimodal particle size distribution with a mean particle size of 120 μm ± 86 μm including particles as large as ~ 250 μm (Figure 3.7.4a). In contrast, CGSRM-3 powder was essentially

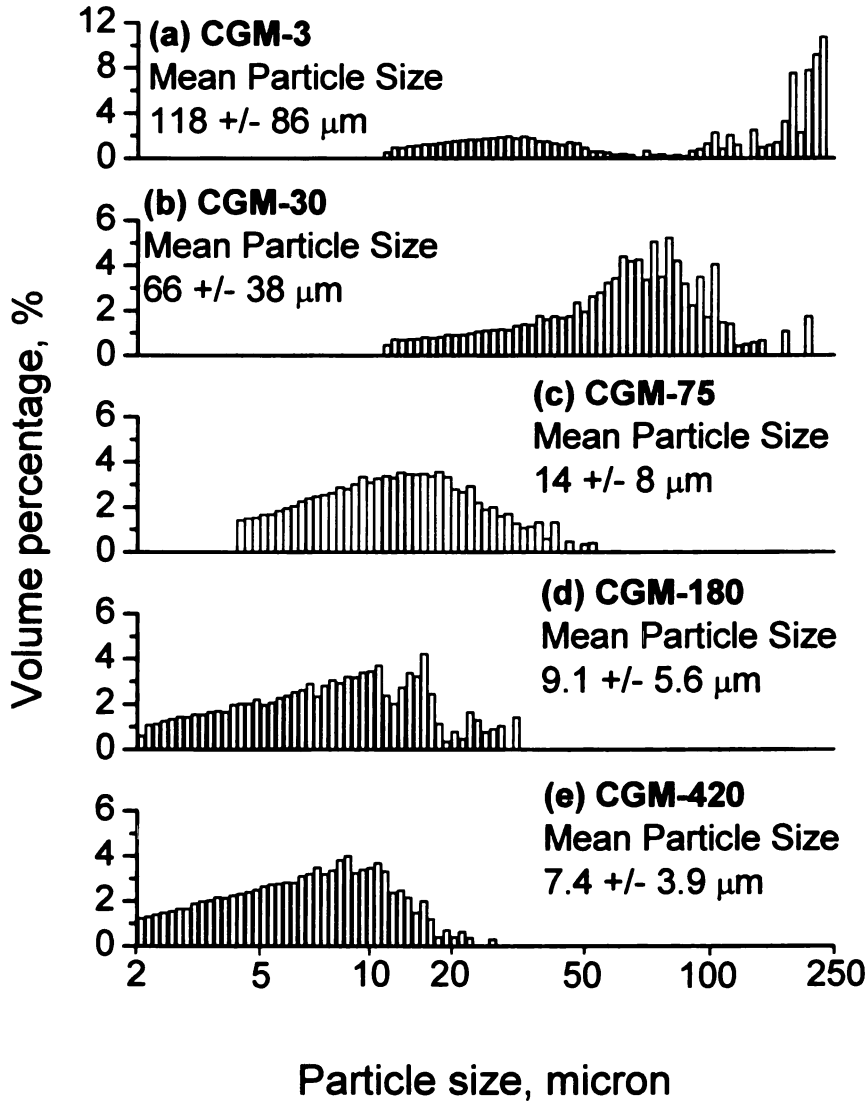

Figure 3.7.4. For CGM (crushed, ground and milled powders) the particle size distribution as a function of milling time. Figure 3.7.6a gives the mean particle size as a function of milling time.

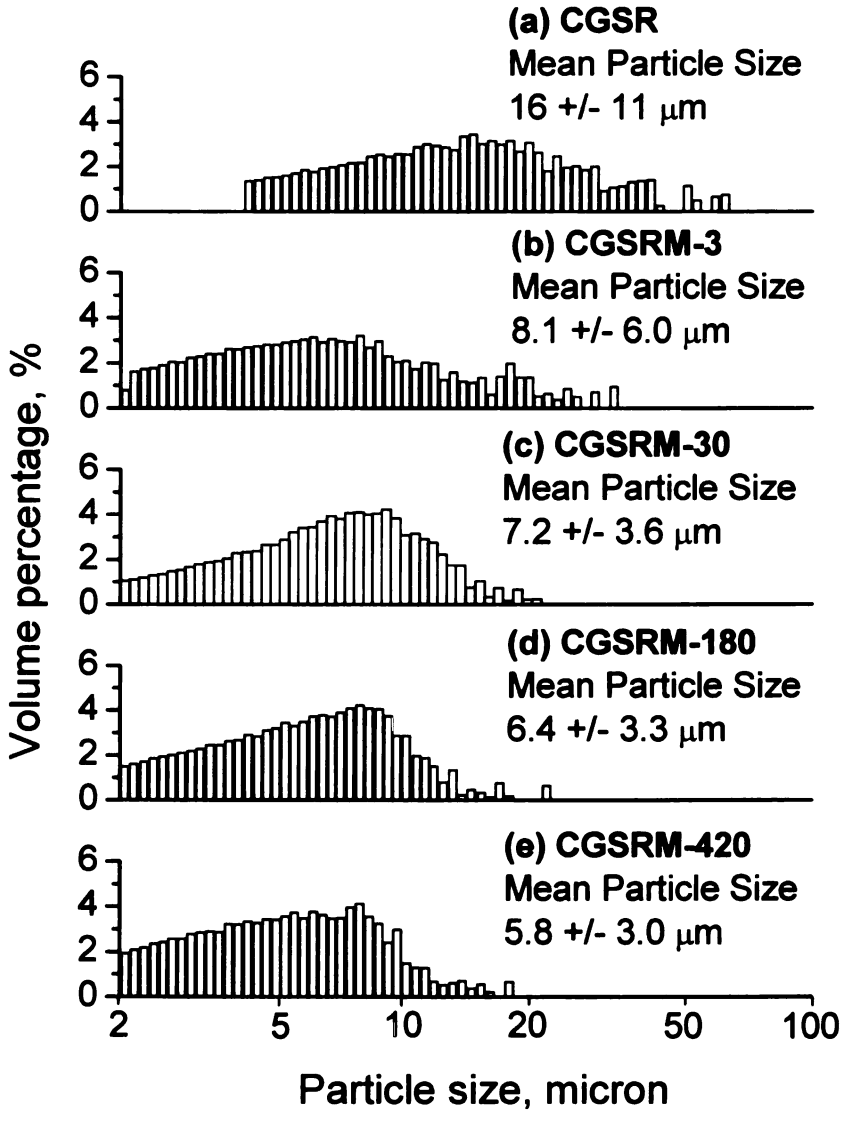

Figure 3.7.5. The particle size distribution for (a) the CGSR (crushed, ground, sieved and reground to pass through a 53-micron sieve) (b) - (e) the particle size distribution as a function of milling time for the CGSR powders. Figure 3.7.6b gives the mean particle size as a function of milling time.

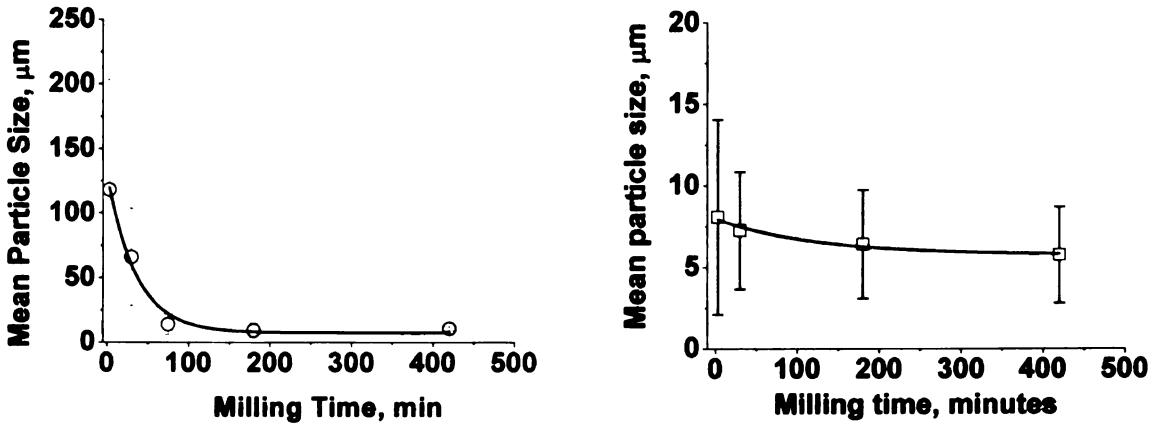

(a) (b)

Figure 3.7.6. a) Mean particle size versus milling time for CGM (crushed, ground and milled) LAST powders. The particle size reaches a steady state (grindability limit) at approximately 7 microns. b) Mean particle size versus milling time for CGSRM (crushed, ground, sieved, reground and milled) LAST powders. Although the sieving and regrind (via mortar and pestle) steps reduced the mean size of the powders that were subsequently milled, the grindability limit was about 5 microns.

unimodal with of a mean particle size of 8.1 μm ± 5.9 μm (Figure 3.7.5b). After planetary milling for 30 minutes, the mean particle size of CGM powder was reduced to 66 ± 38 μm, although some large particles up to 200 μm were observed (Figure 3.7.3c).

For the CGM (Figure 3.7.3) and the CGSRM powders (Figure 3.7.4), as the milling time increased, there is a decrease in both (i) the width of the particle size distribution (as measured by the standard deviation) and (ii) the mean particle size. Also, each of the particle size distributions is skewed towards the smaller particle size (Figures III.7.4 and 5), which is typical of particle size reduction by communition [21, 27]. After longer milling time (180 minutes and 420 minutes), the largest particles were ~ 20 to 30 μm (Figures III.7.4d-e, 5d-e) as compared to 250 μm present in CGM-3 powder (Figure 3.7.4a). The elimination of the population of large particles is important in reducing the tendency for exaggerated or discontinuous grain growth during sintering [17].

As expected, the premilling treatment (sieving and regrinding the powders) truncated the particle size distribution at about 50 microns (Figure 3.7.5). With pre-milling treatment, the particle size of CGSRM-30 powder (Figure 3.7.5c) is comparable to CGM powder milled for 420 minutes (Figure 3.7.4e). For both CGSRM-30 and CGM-420, the mean particle sizes are approaching the steady state mean particle size (Section 4.3.2). Thus the pre-milling treatment (sieving and regrinding the powders) is very effective in reducing the milling time required to reach the steady-state particle size.

It is important to note that the crushing and grinding coupled with short milling

times resulted in a population of large residual powder particle sizes. As discussed above, the literature shows that such population of large particle sizes can lead to discontinuous grain growth, which can be very detrimental to the mechanical properties of the sintered material.

4.3.2 Evolution of the mean particle size

During the milling of brittle powders, the mean particle size typically decreases monotonically in time, with a rapid initial decrease in particle size being followed by an asymptotic approach to a "steady-state" particle size or "grindability limit" [27, 47]. For this study, the mean powder particle size of the milled powders decreased with increasing milling time, t, can be described by the relationship

$$d(t) = (d_0 - d_L)\exp(-t/\tau) + d_L \qquad (1)$$

where d_0 is the initial powder particle size (at an elapsed milling time of zero) and τ is a time constant and d_L is the grindability limit. Thus d_0-d_L represents the total change from the initial particle size (milling time $t = 0$) to the grindability limit d_L for which particle size no longer changes as the milling time increases.

For the CGM powders, a least squares best fit of the data to equation (1) yielded a coefficient of determination, r^2, of 0.989 with the fitted constant values of $(d_0 - d_L)$ = 123 ± 9 microns, d_L = 6.0 ± 5.2 microns and τ = 36.4 ± 6.9 minutes. In comparison, the fit of the CGRSM powder data to equation (1) gives r^2 = 0.965, $(d_0 - d_L)$ = 2.2 ± 0.5

microns, $d_L = 5.7 \pm 0.5$ microns and $\tau = 121 \pm 86$ minutes.

Comparing Figure 3.7.6a (CGM powders) and Figure 3.7.6b (CGSRM powders), we observe that although the mean particle size at the beginning of the milling process was considerably smaller for the CGSRM powders than the CGM powders, the grindability limits were comparable for the two processes. This result is consistent with that described by Suryanarayana [47] for the planetary milling of TiB_2 powders.

4.4 *Analysis of impurities in the as-milled powders*

First, we shall consider the analysis of alumina impurities introduced from the wear of the alumina milling media. For the alumina media, the measured mass loss was linear as a function of time (Figure 3.7.7). The mass of the milling media, $m(t)$, as a function of time, t was fit to the linear relationship

$$m(t) = m_0 + at \qquad (2)$$

where m_0 is the mass of the media prior to milling and a is the slope of the mass versus time plot (Figure 3.7.7). A least-squares fit of equation (2) to the data yields a coefficient of determination, r^2 of 0.996 and the values $m_0 = 198.901 \pm 0.006$ g and $a = -1.76 \times 10^{-5} \pm 8.13 \times 10^{-7}$ g/min.

For a 180 minute milling time at the loss rate given by equation (2), approximately 3.2×10^{-3} grams of alumina would have been lost into the milled powders. Assuming a 20 gram powder batch, this represents a 0.016 wt% contamination of the LAST powders

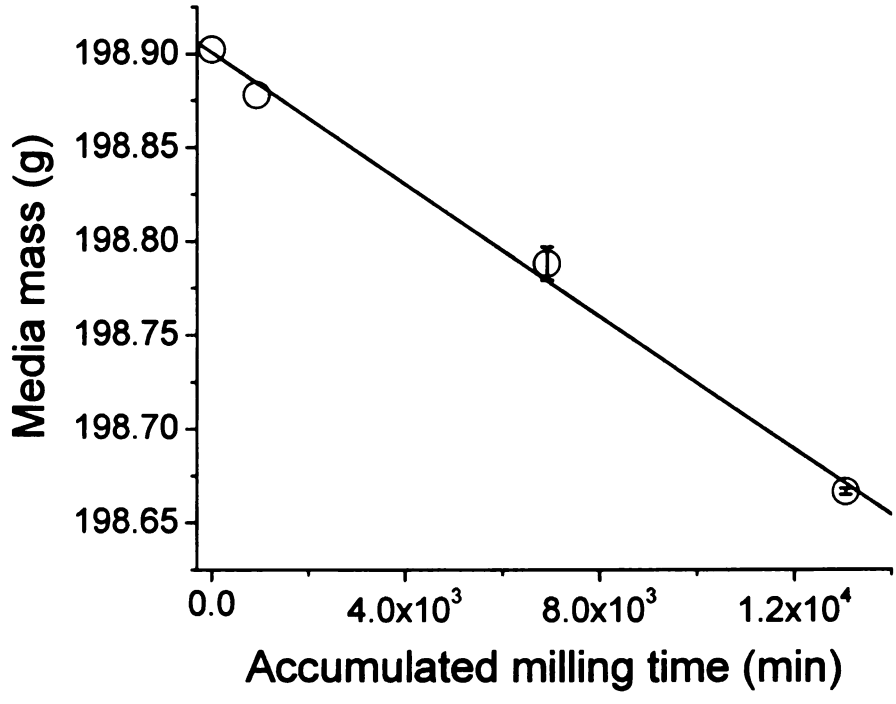

Figure 3.7.7. The mass of the alumina milling media (Table 3.7.3) as a function of milling time, depicting the wear rate of the milling media. The mass lost from the media represents a milling-induced alumina contamination of the milled powder batch.

by the alumina (Al_2O_3) milling media, or equivalently an 8.5×10^{-3} wt% Al ion contamination due to the wear of the milling media.

Since the mill jar will also experience wear during milling and because both the milling jar and the milling media are composed of high-purity alumina (Table 3.7.3), then the alumina milling jar may experience roughly the same mass loss as the milling media. Thus, for a 20 gram powder batch, milled for 3 hours using the alumina media and alumina mill jar, it is estimated that an Al ion contamination of roughly 1.7×10^{-2} wt% (170 wt ppm) may be expected from the milling process alone, not including the pre-milling steps.

For the ICP-MS and EDS evaluation of processing-induced impurities, samples were taken from four powder batches, labeled here as batches 1 – 4. Powder batches 1 – 4 were each obtained from ingots of identical composition ($Ag_{0.43}Pb_{18}Sb_{1.2}Te_{20}$) which were then crushed, ground, reground, sieved and then dry milled for 3 hours at 100 rpm (Sections 3.3.3 and 3.3.4). The two powder batches submitted for ICP-MS analysis gave dramatically different results (tables 5a and 5b). For powder batch 1, a Si ion impurity level of about 1.1 wt% (1.1×10^4 ppm), along with 92 ppm of B and several other metallic ion contaminates that exceeded a 2 ppm concentration level (Table 3.7.5a). A second ICP-MS analysis was performed on a second powder batch, milled in the same manner as batch 1, but milled from another ingot of the same nominal composition as the ingot used for batch 1. The elements selected for ICP-MS analysis on the batch 2 powders included all of the contaminants at a level of 10 ppm or greater, but the analysis

on powder batch 2 showed dramatically lower levels of contamination (Table 3.7.5b). For example, for powder batch 2, the Si ion concentration reported was < 25 ppm and the B concentration was < 0.1 ppm (Table 3.7.5b).

Before discussing the EDS measurement of the powder contamination, we shall first briefly discuss the several potential Si contamination sources that the powders may be exposed to during the pre-milling steps in powder preparation, namely (1) the mortar and pestle used in the initial grinding of the ingot, (2) the glass beads used to clean the milling jar, and (3) the silica ampoule used in casting the ingots. The initial grinding of ingots was done in a porcelain mortar and pestle, where porcelain is a multi-phase aluminosilicate with a range of compositions that typically includes K and/or Na as well as Al and Si. During grinding, small amounts of the porcelain could have been introduced into the powder. Also, the milling media and the milling jar were cleaned periodically (every fourth powder batch, see Section 3.4) by milling with glass beads. These glass beads may have left a silicate glass powder residue in the mill. If a substantial amount of silica originated from the glass beads, then the silica content likely depends on the number of batches milled since the last cleaning. While the silica ampoule used during casting is a possible source of Si contamination, there is no evidence of chemical reaction between the ampoule and the LAST ingot. It should be pointed out that while the quantity of impurities introduced by planetary milling with the high purity alumina milling media and mill jar and crushing and grinding in the porcelain mortar and pestle should be relatively repeatable from powder batch to powder batch, however the periodic process of

Table 3.7.5a As determined by ICP-MS analysis, the impurity levels in batch 1 of a dry milled LAST powder (ground and then planetary milled for three hours at 100 rpm). Note the high concentrations of Si compared to a similarly processed powder shown in Table 3.7.5b.

Element	Concentration (ppm by weight)	Element	Concentration (ppm by weight)
Si	1.1×10^4	P	16
B	92	Fe	15
Na	55	Nb	8.6
K	55	W	7.8
Sn	44	Ca	5.6
Al	35	Ni	2.4

Table 3.7.5b As determined by ICP-MS analysis, the impurity levels in batch 2 of dry milled LAST powders (ground and then planetary milled for three hours at 100 rpm). The analysis was done for the elements exceeding 10 ppm in Table 3.7.5a. Compared to the results shown in Table 3.7.5a, the impurity concentrations shown here are in much better agreement with the EDS results discussed in Section 4.4.

Element	Concentration (ppm by weight)
Si	< 25
B	< 0.1
Na	<0.1
Sn	2.2
Al	7.3
P	<10
Ca	35
Fe	<10

cleaning process with glass beads might occasionally induce relatively large amounts of Si (and lesser amount of impurities such as Na, K and B) from either a glass powder residue on the milling media and jar, or perhaps from a portion of a glass bead being retained with the milling and being subsequently crushed in the next batch of powder processed.

In order to measure the impurity concentration independently of the ICP-MS, EDS measurements were performed on the LAST powders (Figures III.7.8a-c). In contrast to the high Si contamination measured by ICP-MS on powder batch 1 (Table 3.7.5a), the EDS measurements on powder batches 3 and 4 were in much better agreement with the ICP-MS results from powder batch 2 (Table 3.7.5b).

The Al and Si ion concentrations were measured by EDS. Prior to the EDS measurement of the LAST powders, a background spectrum was taken for the carbon tape mounted on the aluminum stub (Figure 3.7.8a), which revealed carbon, oxygen and as well as low levels of Si and Al contamination. For the background spectrum (Figure 3.7.8a), the Al ion concentration ranged from (0.03 ± 0.01) wt% to (0.13 ± 0.03) wt% while the Si ion concentration ranged from (0.01 ± 0.01) wt% to (0.09 ± 0.04) wt%. The source of the apparent Si and Al ion impurities in the background (carbon tape) EDS data could be the SEM chamber or stub and in the case of Si ions, silicone-based compounds in the carbon tape or adhesive.

The Al and Si ion contamination measured by EDS in the LAST powders in some cases did not greatly exceed the background levels (Figures III.7.8b and 8c). For example,

at an SEM magnification of 1000X for powders from batch 4, two different locations gave a Si ion impurity level of (0.13 ± 0.07) wt% and Al ion impurity levels of (0.08 ± 0.07) wt% and (0.12 ± 0.07) wt% for the same two locations. The EDS analysis of powder batch 3 gave similar results for the Al and Si ion impurity level. Note that the nominal Al ion impurity level in the powders as determined by EDS is about 4 to 6 times higher than the Al impurity concentration inferred from the milling media wear rate measurements and that there are additional sources of possible Al contamination, such as the porcelain (aluminosilicate) mortar and pestle. However, given that the background EDS spectra (Figure 3.7.8a) show similar contamination levels in Al and Si to that of the LAST powders, the EDS measurements allow us only to say that the Al and Si ion concentration in the milled powders is relatively low, likely in the range of roughly 0.05 to 0.13 wt%.

In order to perform a check on the EDS concentration measurements for higher concentration levels, the EDS was used to experimentally determine the composition of the $Ag_xPb_mSb_yTe_z$ matrix for two different locations on each of two powder-covered SEM stubs for powder batches 1 and 3. Upon examining the matrix composition in terms of atomic percent concentrations and after normalizing m to 18, the mean of the four EDS measurements on the LAST powders corresponds to x = 0.44, y = 1.35 and z = 20, which agrees relatively well with the nominal composition of m = 18, x = 0.43, y = 1.2 and z = 20. (The nominal composition corresponds to the initial raw materials used in the casting, without accounting for possible losses in Pb and Te that may occur during casting as

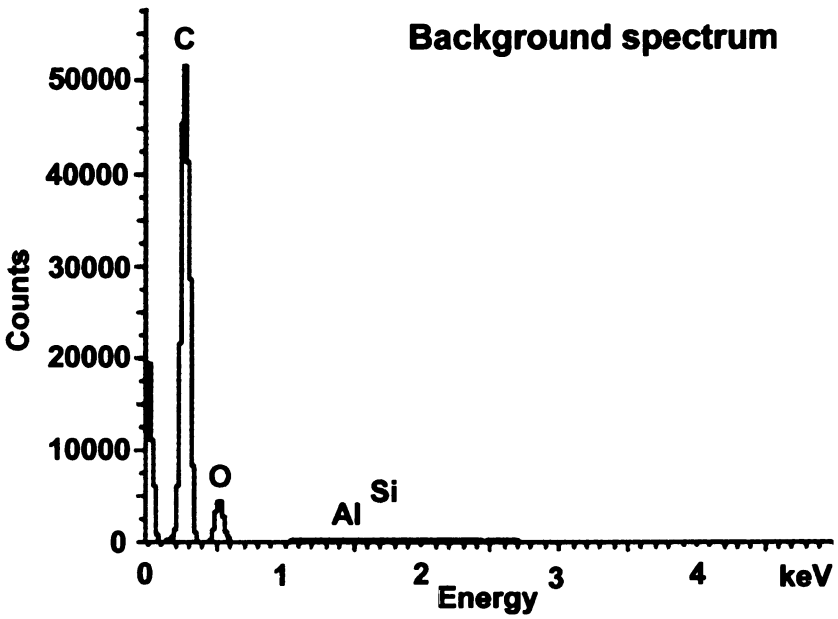

(a)

Figure 3.7.8. For the EDS measurements of the LAST powders (a) a "background" spectrum for the carbon tape itself mounted on an aluminum stub, (b) results for powder batch 3 and (c) results for powder batch 4.

Figure 3.7.8 continued.

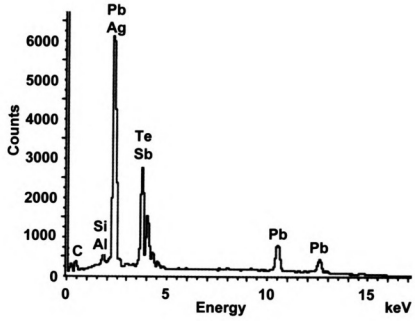

(b)

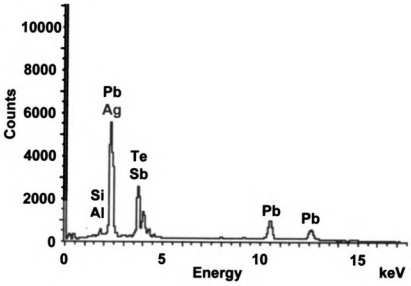

(c)

small amounts of Pb or Te are coated onto the interior of the silica ampoule during casting). Thus, the agreement between the measured matrix composition and the nominal composition in the EDS measurements for the LAST powders implies that the EDS apparatus used in this study functions well at least for concentration levels on the order of 0.60 wt% (in the case of Ag) and higher.

5. Summary and Conclusions

In the thermoelectrics literature, powder processing has been identified as being important to enhance mechanical integrity of TE components. However in the TE literature when powder processing is done, few details of the powder processing procedures are included and often there is either little or no characterization of the powders. (At most, a mean powder size is given without details of the measurement method).

This study is the first to provide a comprehensive characterization of powder processing of a TE material. Cast ingots of LAST thermoelectric material were processed into a fine, equiaxed powder with a narrow size distribution, The XRD results were consistent with the literature values for pure PbTe and for LAST powders of similar composition [26], confirming that no amorphous phase or new phases were formed as a result of the planetary milling.

Also, a detailed SEM examination revealed that the particle shape evolved during

the crushing, grinding and milling process (Figure 3.7.3). Initially, the particles were angular and sharp-edged with some elongated flake-shaped particles, but as the milling time increased to 180 minutes or more, the particle shapes became equiaxed and the particle surfaces became smoother. Particle morphology is important in powder processing since equiaxed particles pack better than elongated flake-shaped particles and the higher green densities in the initial powder particle compacts leads to a lower residual porosity in the sintered components. Thus, as milling time increased, the powders became more equiaxed, which enhances both the initial particle packing and the densification process. In addition, SEM analysis showed that no significant agglomeration of powders was observed during any stage of the grinding and milling process. Since agglomeration of powders can lead to porosity and cracking in the final sintered body, avoiding agglomeration is beneficial.

In addition to the changes in particle size, a Coulter Counter analysis showed that the mean particle size and the breadth of the particle size distribution evolved during milling (Figures III.7.4 and 5), with both the particle size and the width of the particle size distribution decreasing with increasing milling time. The mean particle size of the LAST powders milled decreased exponentially (equation (1) as a function of increasing milling time until a steady state particle size (grindability limit) of roughly 5 microns was achieved (Figure 3.7.6).

As is the case with many thermoelectric materials, a fine particle size is important to enhancing mechanical properties and the literature shows that a fine particle size is also

beneficial to the sintering rate and the final density of a sintered component. Furthermore, increases in ZT with powder processing have been reported.

In this study, a grindability limit was reached at a mean particle size of about 5 microns for dry milling. Wet milling can be employed in the future if a smaller mean particle size is desired [54-58]. In wet ball milling, a liquid milling medium such as hexane [54, 55], acetone [54], toluene [56] or distilled water [57] is introduced into the milling jar along with the powder in order to aid in decreasing the powder size. In addition, the particle size distribution can be even narrower for wet milled powders than for dry milled powders [47].

The analysis of contamination in the milled powders by the alumina wear rate measurements, EDS and ICP-MS reveals that except for one of the ICP-MS measurements (powder batch 1, Table 3.7.5a), the contamination of the milled powders is on the order of a few tenths of weight percent or lower (Table 3.7.5b, Figure 3.7.8, Section 4.4). In regard to the Si and B contamination observed in the ICP-MS measurements on powder batch 1 (Table 3.7.5a), the glass beads used to periodically clean the milling jar and the milling media was likely the source of the contamination. In the future the milling media and jar will no longer be cleaned using the glass beads. Also, to avoid possible contamination from the porcelain mortar and pestle, a high-purity alumina mortar and pestle will be used in future studies.

Acknowledgements

This study is supported by the U. S. Department of Energy Grant DE-FC26-04NT42281 and Office of Naval Research MURI Grant number N000140310789. The authors acknowledge the use of scanning electron microscope facility at the Advanced Microscopy Center, Michigan State University. The authors also acknowledge helpful conversations with Prof. M. G. Kanatzidis of Northwestern University. In addition, the authors acknowledge the assistance of Mr. Bradley Hall, Michigan State University, with the ICP measurements.

References

[1] J. Jiang, L. Chen, S. Bai, *et al.*, Mater. Sci. Eng. B **117** 334 (2005).

[2] Y. Horio, H. Yamashita, T. Hayashi, Mat. Trans. **45** 3309 (2004).

[3] K. Ueno, A. Yamamoto, T. Noguchi, *et al.*, J. Alloys Compd. **392** 295 (2005).

[4] T. Caillat, J-P Fleurial, A. Borshchevsky, J. Phys. Chem Solids **58** 1119 (1997).

[5] I. Yashima, R. Tsukuda, T. Sato, *et al.*, J. Ceram. Soc. Jpn. **105** 1018 (1997).

[6] T. Tokiai, T. Uesugi, and K. Koumoto, J. Ceram. Soc. Jpn. **103** 1182 (1995).

[7] K. Kishimoto and T. Koyanagi, J. Appl. Phys. **92** 2544 (2002).

[8] J. Y. Peng, J. Y Yang, T. J. Zhang, *et al.*, J. Alloys Compd. **381** 313 (2004).

[9] B. L. Yu, X. F. Tang, Q. Qi, *et al.*, Acta Phys. Sin. Ch. Ed. **53** 3130 (2004).

[10] J. Y. Yang, Y. H. Chen, J. Y. Peng, *et al.*, J. Alloys Compd. **375** 229 (2004).

[11] N. Bouad, R. M. Marin-Ayral, G. Nabias, *et al.*, J. Alloys Compd. **353** 184 (2003).

[12] P. J. Taylor, J. R. Maddux, W. A. Jesser *et al.*, J. Appl. Phys. **85** 7807 (1999).

[13] S. S. Kim, S. Yamamoto, and T. Aizawa, J. Alloys Compd. **375** 107 (2004).

[14] J. Jiang, L. D. Chen, S. Q. Bai, *et al.*, Scripta Mater. **52** 347 (2005).

[15] F. Ren, E. D. Case, E. J. Timm, *et al.*, Phil. Mag. Lett. **86** 673 (2006).

[16] R. W. Rice, *Mechanical Properties of Ceramics and Composites* (Marcel Dekker, New York, 2000), pp. 201 - 217.

[17] M. W. Barsoum, *Fundamentals of Ceramics* (McGraw-Hill, New York, 1997), pp. 415 - 418.

[18] H. Chen, X. Zhao, E. Mueller, *et al.*, J. Univ. Sci. Tech. Beijing **11** 67 (2004).

[19] K.Y. Lee, E. D. Case, J. Asmussen, *et al.*, Scripta Mater. **35** 107 (1996).

[20] K. Y. Lee, E. D. Case, J. Asmussen, in *Microwaves: Theory and Applications in Materials Processing IV*, edited by D. E. Clark, W. H. Sutton, and D. A. Lewis (American Ceramics Society, Inc., Westerville, OH, 1997), pp. 539-546.

[21] R. M. German, *Powder Metallurgy Science*, second ed. (Metal Powder Industries Federation, New Jersey, 1994).

[22] K. Y. Lee, E. D. Case, J. Mat. Sci. Lett. **18** 201 (1999).

[23] E. D. Case, in *Joining 2002, 6th International Conference On Joining Ceramics, Glass and Metal* (Deutsche Kermaische Gesellschaft, Cologne, Germany, 2002), pp. 9-16.

[24] J. Kano, S. Saeki, M. Tanjo, *et al.*, J. Chem. Eng. Jpn. **34** 595 (2001).

[25] M. L. L. Oliveira, K. Chen, and M. F. Ferreira, J. Eur. Ceram. Soc. **22** 1601 (2002).

[26] E. Quarez, K. Hsu, R. Pcionek, *et al.*, J. Am. Chem. Soc. **127** 9177 (2005).

[27] M. N. Rahaman, *Ceramic Processing and Sintering*, second ed. (Marcel Dekker, Inc., New York, 2003), pp. 50-56, 136-137, 343-344, 693-696.

[28] J. B. Wachtman, *Mechanical Properties of Ceramics* (Wiley and Sons, New York, 1996).

[29] K. F. Hsu, S. Loo, F. Guo, *et al.*, Science **303** 818 (2004).

[30] M. S. Toprak, C. Stiewe, S. Williams, *et al.*, Adv. Funct. Mater. **14** 1189 (2004).

[31] T. Caillat, J. Kulleck, A. Borshchevsky, *et al.*, J. Appl. Phys. **79** 8419 (1996).

[32] J. L. Cui, X. Qian, X. B. Zhao, J. Alloys Compd. **358** 228 (2003).

[33] P. Balaz, E. Godocikova, L. Krilova, *et al.*, Mater. Sci. Eng. A **386** 441 (2004).

[34] A. S. Ramos, S. P. Taguchi, E.C.T. Ramos, *et al.*, Mater. Sci. Eng. A **422** 184 (2006).

[35] H. Zhao, X. L. Chen, C. Jia, *et al.*, Mater. Sci. Eng. B **122** 226 (2005).

[36] M. Yavuz, H. Maeda, L. Vance, *et al.*, Supercond. Sci. Technol. **11** 1153 (1998).

[37] J. Temuujin, M. Aoyama, M. Senna, *et al.*, J. Mater. Res. **20** 1939 (2005).

[38] R. Wongmaneerung, T. Sarakonsri, R. Yimnirun, *et al.*, Mater. Sci. Eng. B **130** 246 (2006).

[39] J. M. Filio, K. Sugiyama, F. Saito, *et al.*, Powder Technol. **78** 121 (1994).

[40] Surepure Chemetals. Available on line at: http://www.surepure.com.

[41] Cerac, Inc. Available on line at: http://www.cerac.com.

[42] Royal Canadian Mint. Available on line at: http://www.mint.ca.

[43] D. W. Richerson, *Modern Ceramic Engineering: Properties, Processing and Use in Design* (Taylor and Francis, New York, 2006), pp. 379-383.

[44] Beckman Coulter, Inc., Fullerton, CA, Available on line at: http://www.beckman.com.

[45] Shiva Technologies, Inc., Syracuse NY, Available on line at: http://www.shivatec.com/

[46] Y. Cao, D. Q. Yi, L. Yin, *et al.*, Rare Metal Mat. Eng. **11** 946 (2003).

[47] C. Suryanarayana, Prog. Mater. Sci, **46** 1 (2001).

[48] Joint Committee on Powder Diffraction Standards (JCPDS) card no. 11-768

[49] B. D. Cullity and S. R. Stock, *Elements of X-Ray Diffraction*, third ed. (Prentice Hall, Upper Saddle River, NJ, 2001), pp. 182 - 183.

[50] J. S. Chappell, T. A. Ring, and J. D. Birchall, J. Appl. Phys. **60** 383 (1986).

[51] J. M. Ting and R. Y. Lin, J. Mater. Sci. **30** 2382 (1995).

[52] F. S. Shiau, T. T. Fang, and T. H. Leh, Mater. Chem. Phys. **57** 33 (1998).

[53] J. Ma and L. C. Lim, J. Eur. Ceram. Soc. **22** 2197 (2002).

[54] Y. H. Choa, N. Bamba, H. Hayashi, *et al.*, J. Mater. Sci. **34** 3789 (1999).

[55] Y. Doi, H. Akimoto, K. Matsuki, *et al.*, J. Jpn. Inst. Met. **64** 518 (2000). (in Japanese)

[56] T. Venogopal, K. Prasad, B. S. Murty, Mater. Sci. Eng. A **393** 382 (2005).

[57] S. Ozcan, B. Kaynar, M. M. Can, *et al.*, Mater. Sci. Eng. B **121** 278 (2005).

[58] S. K. Pabi, J. Joardar, and B. S. Murty, J. Mater. Sci, **31** 3207 (1996).

Chapter 8

Bloating of hot pressed specimens during annealing

Under in-service conditions, the hot side temperature of TE elements may be as high as 773 K. In addition, during TE module fabrication, for example bonding between TE legs and metal contacts, the processing temperature may approach 973 K. Thus it is critical to evaluate the thermal stability of LAST and LASTT materials that are targeted as TE materials in the application of exhaust waste heat recovery applications.

1. Bloating phenomena in hot pressed specimens upon annealing

Hot pressed specimens fabricated using facilities at University of Michigan (UMHP), Oak Ridge National Laboratory (ORNLHP), Jet Propulsion Laboratory (JPLHP), and Michigan State University (MSUHP) (see **section 2.1.3**) exhibited porosity after annealing between 673 K and 973 K under reducing atmosphere (95% Ar + 5% H_2), while the as-hot pressed specimens were very dense (typically greater than 95 percent of theoretical density).

1.1. Hot pressed specimens at University of Michigan (UMHP)

The as-hot pressed specimen UMHP1 (Table 3.8.1) fractured upon removing from the die, giving several millimeter-sized broken pieces for microstructure analysis. The specimen likely had a density greater than 95 percent as estimated from the SEM micrograph of the fracture surface (Figure 3.8.1a) while a few micropores were observed. Table 3.8.1a. Processing conditions of the hot pressed specimens included in this chapter.

Specimen	Composition	Hot pressing condition				
		T_{max} (°C)	Duration (min)	Pressure (MPa)	Rate (°C/min)	Atmosphere
UMHP1	$Ag_{0.43}Pb_{18}Sb_{1.2}Te_{20}$	400	60	62	10	N_2
UMHP3	$Ag_{0.43}Pb_{18}Sb_{1.2}Te_{20}$	330	90	62	10	N_2
UMHP5	$Ag_{0.43}Pb_{18}Sb_{1.2}Te_{20}$	330	90	62	2.5	N_2
UMHP6	$Ag_{0.43}Pb_{18}Sb_{1.2}Te_{20}$	330	90	100	2.5	N_2
ETP20-HP1	$Ag_{0.5}Pb_6Sn_2Sb_{0.2}Te_{10}$	420	~ 30	41.3	~ 4	N_2
ORHP2	$Ag_{0.43}Pb_{18}Sb_{1.2}Te_{20}$	506	~ 20	33.8	~ 20	Vacuum
ORHP4	$Ag_{0.43}Pb_{18}Sb_{1.2}Te_{20}$	527	~ 20	33.8	~ 17	Vacuum
JPL-HP	$Ag_{0.43}Pb_{18}Sb_{1.2}Te_{20}$	550	Not provided by JPL			
MSUHP3	$Ag_{0.43}Pb_{18}Sb_{1.2}Te_{20}$	400	90	75	5	Ar
MSUHP4	$Ag_{0.9}Pb_9Sn_9Sb_{0.6}Te_{20}$	350	90	60	3.3	Ar

Table 3.8.1b. Thermal annealing conditions of the specimens involved in this chapter.

Specimen	Annealing Temp (K)	Annealing Time (hr)	Annealing atmosphere
UMHP1	898	2	95% Ar + 5% H_2, 300 torr
UMHP3	773	1	*ibid*
UMHP5	773	1	*ibid*
	873	1	*ibid*
UMHP6	673	1	*ibid*
	773	1	*ibid*
	873	1	*ibid*
ETP20-HP1	773	1	*ibid*
	823	1	*ibid*
ORHP2	823	1	*ibid*
ORHP4	823	1	*ibid*
JPL-HP	773	1	*ibid*
MSUHP3	973	6	*ibid*
MSUHP4	973	6	*ibid*

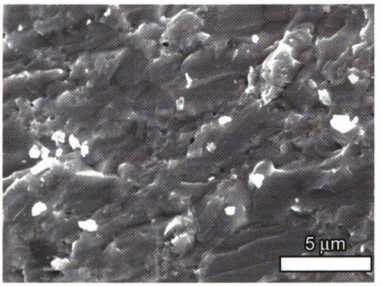

(a)

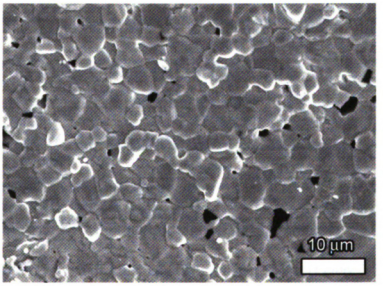

(b)

Figure 3.8.1. SEM micrographs of UMHP1 showing (a) fracture surface of the as hot pressed specimen, and (b) fracture surface after annealing at 898 K for 2hr. The mean grain size is ~ 4 microns as determined by linear intercept method.

After thermal annealing at 898 K for 2 hr, micropores appeared across the entire specimen surface (Figure 3.8.1b). Most of the pores were spherical or semi-spherical and had a diameter smaller than 5 microns (Figure 3.8.1b).

The as-hot pressed UMHP3 specimen (Table 3.8.1) possessed a high mass density and few pores were observed on the cut surface (Figure 3.8.2a) and the fracture surface (Figure 3.8.2b). After annealing at 773 K for 1 hr, UMHP3 specimen showed serious bloating. Macroscopic pores were observed on the fracture surfaces with dimensions of about 500 microns long and 100 microns wide (Figure 3.8.3a). On the microscopic scale, pores up to 20 microns were seen on the fracture surface (Figure 3.8.3b).

The hot pressed specimen UMHP5 (Table 3.8.1) was annealed for 1hr at 773 K and 873 K, consecutively. After annealing at 773 K, interconnected cracks were formed on the polished surface. The cracks were several microns wide and as long as 50 microns. Isolated pores that are several microns in diameters are also observed across the polished surface (Figure 3.8.4a). A large number of etch pits were visible on the etched surface. The polished surface of the 873 K annealed UMHP5 also exhibited interconnected pores that were as extended as several hundred microns and etch pits (Figure 3.8.4b).

After hot pressing, specimen UMHP6 received heat treatment at 673 K (Figure 3.8.5), 773 K (Figure 3.8.6), and 873 K (Figure 3.8.7) for 1hr, respectively (Table 3.8.1). UMHP6 annealed at 673 K for 1 hr showed isolated pores on the polished surface which were approximately 5 microns or smaller (Figure 3.8.5a). Higher magnification SEM image revealed the isolated pores were quasi-spherical.

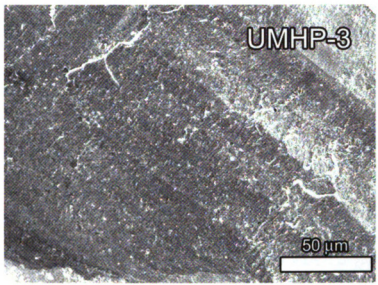

(a)

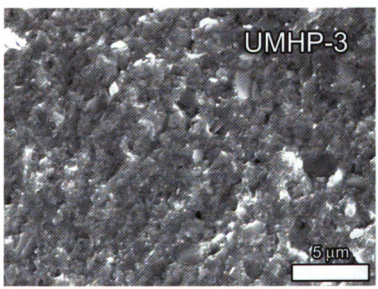

(b)

Figure 3.8.2. SEM micrographs of as hot pressed UMHP3 specimen showing (a) the cut surface and (b) the fracture surface.

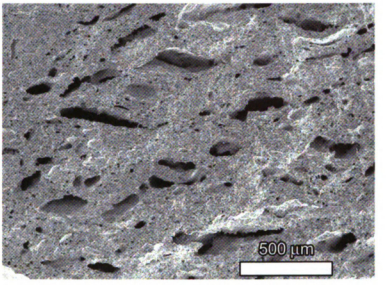

(a)

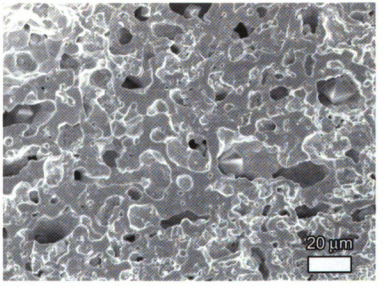

(b)

Figure 3.8.3. SEM micrographs of UMHP3 after annealing at 773 K for 1hr showing (a) the macroscopic porosity and (b) the micro-porosity on the fracture surface.

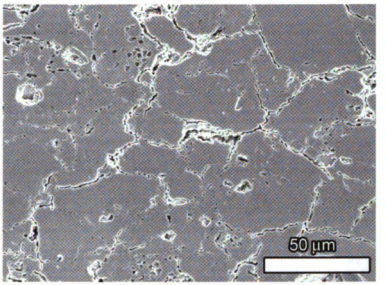

(a)

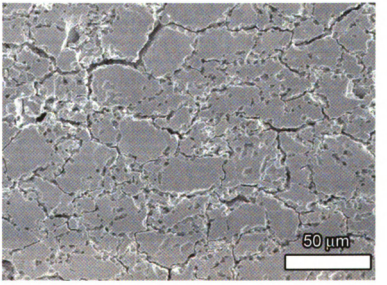

(b)

Figure 3.8.4. SEM micrographs of the polished surfaces of UMHP5 after thermal annealing (a) at 773 K for 1hr, and (b) at 873 K for 1hr.

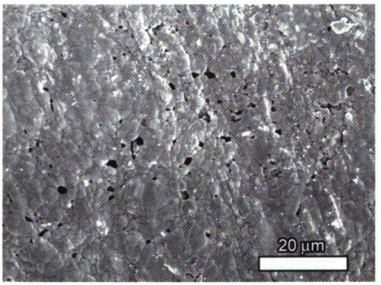

(a)

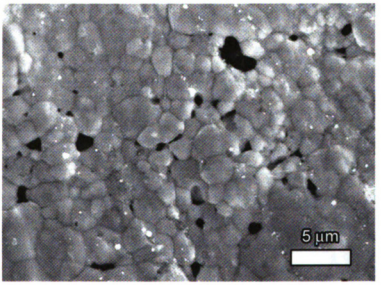

(b)

Figure 3.8.5. (a) Low magnification and (b) high magnification SEM images showing polished surfaces of UMHP6 after thermal annealing at 673 K for 1hr.

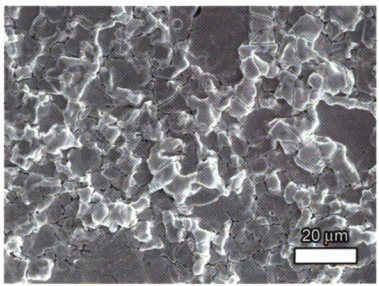

(a)

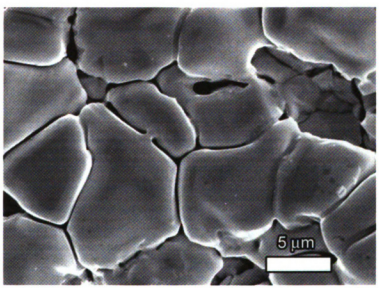

(b)

Figure 3.8.6. (a) Low magnification and (b) high magnification SEM images showing polished surfaces of UMHP6 after thermal annealing at 773 K for 1hr.

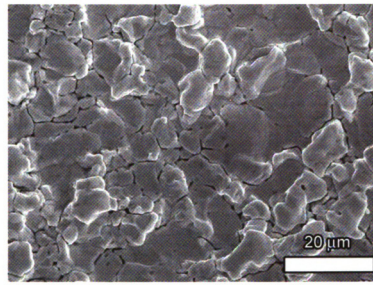

(a)

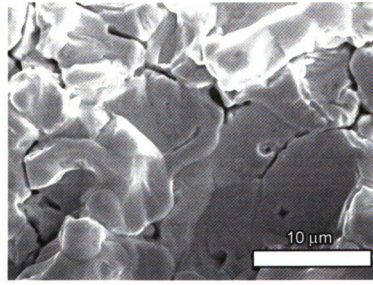

(b)

Figure 3.8.7. (a) Low magnification and (b) high magnification SEM images showing polished surfaces of UMHP6 after thermal annealing at 873 K for 1hr.

The average grain size of this specimen is about 3.8 microns as determined from the linear intercept method with about 290 intercepts on each micrograph.

Heat treatment at 773 K for 1hr on a different specimen of UMHP6 showed some extruding grains (bright area) on the polished surface (Figure 3.8.6a), which might result from bloating. From a higher magnification SEM image, it can be seen that grains were well defined with some grain boundaries deeply etched (Figure 3.8.6b). The average grain size is approximately 6.75 microns as determined from the linear intercept method with about 270 intercepts on each micrograph. The UMHP6 specimen annealed at 873 K exhibited similar extruding grains (Figure 3.8.7a). The average grain size of this specimen is 7.09 microns as determined from the linear intercept method with about 280 intercepts on each micrograph. A high magnification SEM image showed that grain boundaries were etched inhomogeneously. Etch pits were also visible within some grains (Figure 3.8.7b).

1.2. Hot pressed specimens at ORNL

Two p-type hot pressed specimens ETP20-HP1 fabricated using ORNL facility were thermally etched at 773 K (Figure 3.8.8) and 823 K (Figure 3.8.9) for 1 hr, respectively (Table 3.8.1). Large lenticular pores up to 1 mm long were observed on the polished surfaces of ETP20-HP1 annealed at 773 K for 1 hr (Figure 3.8.8a). In addition, isolated quasi-spherical pores also exist. These isolated pores were approximately 20 microns in diameter (Figure 3.8.8b). The surface seemed "melted" and covered with a "glassy" phase (Figure 3.8.8b).

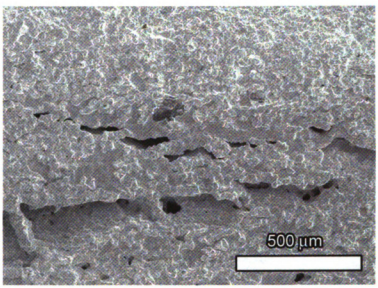

(a)

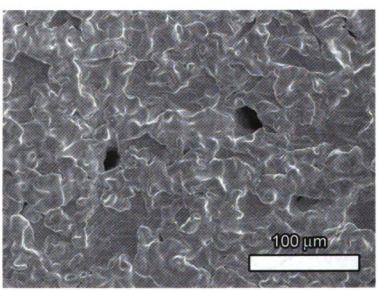

(b)

Figure 3.8.8. (a) lenticular pores and (b) quasi-spherical pores observed in ETP20-HP1 annealed at 773 K for 1hr.

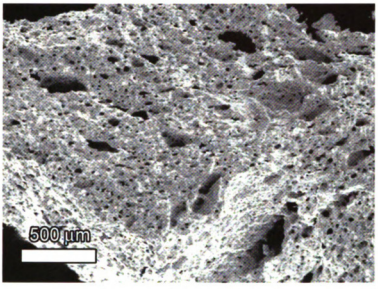

(a)

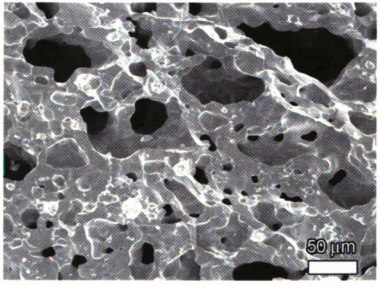

(b)

Figure 3.8.9. (a) macropores and (b) micropores observed in ETP20-HP1 annealed at 823 **K for** 1hr.

ETP20-HP1 annealed at 823 K for 1 hr severely bloated with both macro- and micro-pores across the entire specimen surface (Figure 3.8.9a). The macropores were about 100 to 400 microns in their longer dimension (Figure 3.8.9a) and the micropores were either elliptical or semi-spherical with diameters ranging from 5 to 50 microns (Figure 3.8.9b).

The as-hot pressed ORHP2 (Table 3.8.1) was dense as few pores were visible on the fracture surface. Cleavage steps were observed, indicating brittle fractures across the grains. From the dimensions of the cleavage steps, the grain size can be approximated to be between 30 and 50 microns for this specimen (Figure 3.8.10a). After annealing at 823 K for 2hr, pores developed on the polished surface. The macropores were approximately 200 to 1000 microns in length and about 50 to 200 microns across (Figure 3.8.10b). Also micropores were observed across the specimen surface, which were approximately 3 to 10 microns in diameter (Figure 3.8.10c).

The as-cut surface of ORHP4 (Table 3.8.1) showed little porosity while chipping and pulling-out were observed (Figure 3.8.11a). After heat treatment at 823 K for 1hr, lenticular-shaped pores as long as 50 microns developed. Many micropores were also visible across the surface (Figure 3.8.11b).

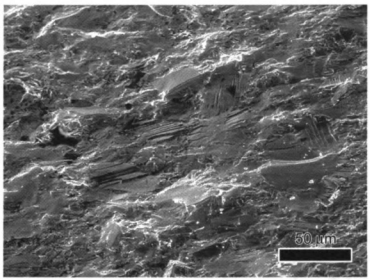

(a)

Figure 3.8.10. SEM micrographs of (a) the fracture surface of as ORHP2, and free surfaces after annealing at 823 K for 2hr depicting (b) macropores and (c) micropores.

Figure 3.8.10 continued.

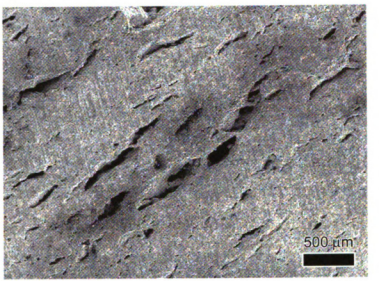

(b)

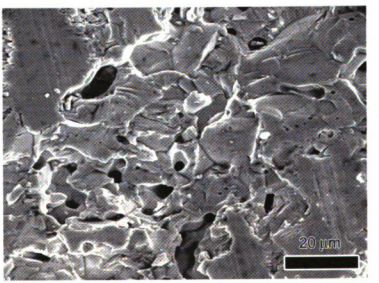

(c)

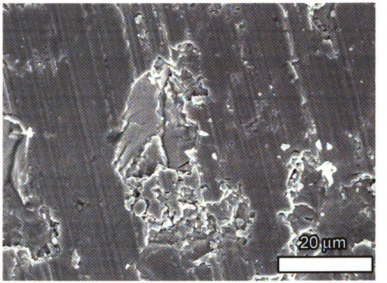

(a)

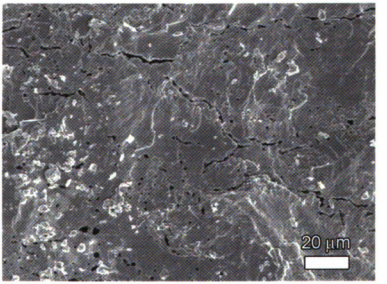

(b)

Figure 3.8.11. SEM micrographs showing free surfaces of (a) the as-cut ORHP4, and (b) the specimen thermally annealed at 823 K for 1hr.

1.3. Hot pressed specimen at JPL (JPLHP)

The as-hot pressed JPLHP specimen (Table 3.8.1) showed a high density, as seen from the SEM image of the fracture surface, while a few micropores were visible (Figure 3.8.12a). With annealing at 773 K for 1hr, both lenticular-shaped macropores as long as 50 microns (Figure 3.8.12b) and spherical micropores were observed (Figure 3.8.12c), indicating the bloating problem existed in the JPL-HP specimen.

1.4. Hot pressed specimen at Michigan State University

Hot pressed specimens fabricated using the facility at Michigan State University (Table 3.8.1) developed both lenticular and spherical pores after annealing at 973 K for 1 hr (Figure 3.8.13). The lenticular pores were as long as 100 microns (Figure 3.8.13a) while the diameter of spherical pores ranged from approximately 2 microns to 20 microns (Figure 3.8.13b).

2. Thermogravity – Mass spectroscopy (TG-MS) analysis

Bloating problem during annealing of hot pressed LAST and LASTT was likely due to gas evolution and sublimation. The composition specie(s) that was evolved during heating may be from either the starting materials or contaminates introduced during the powder processing. In order to determine the evaporation species, two hot pressed samples along with two ingot samples (Table 3.8.2) were submitted to the Application Laboratories at Netzsch Co. The specimens were analyzed by Dr. A. Schindler using

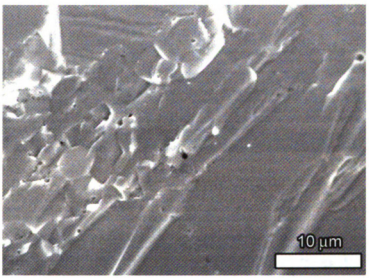

(a)

Figure 3.8.12. SEM micrographs of (a) the fracture surface of the hot pressed JPL-HP specimen, and (b) macro- and (c) micropores observed on the polished surface after annealing at 773 K for 1hr.

Figure 3.8.12 continued.

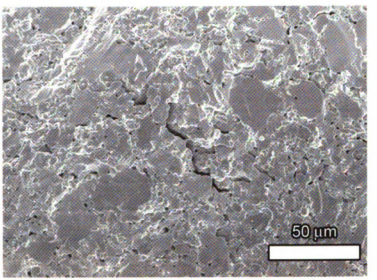

(b)

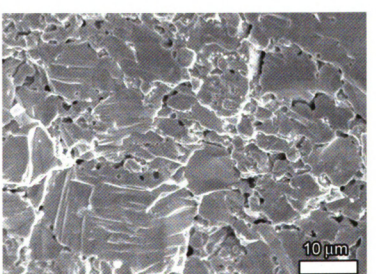

(c)

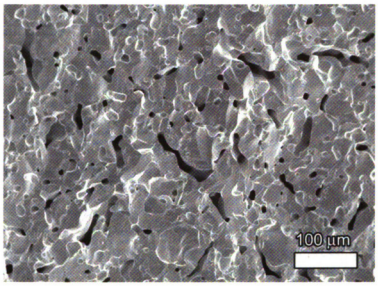

(a)

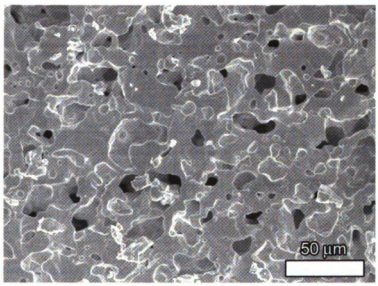

(b)

Figure 3.8.13. SEM micrographs of fracture surfaces of specimens (a) MSUHP3 and (b) MSUHP4 hot pressed at Michigan State University specimens after annealing at 973 K for 1 hr.

Table 3.8.2. Nominal composition, processing technique, and mass loss due to heating for the specimens analyzed by TG-MS at Netzsch Inc.

Specimen	Composition	Semiconductor type	Processing	Mass loss at 973 K
ETN174	$Ag_{0.86}Pb_{19}Sb_{1.0}Te_{20}$	n-type	casting	0.17%
ETP40	$Ag_{0.9}Pb_9Sn_9Sb_{0.6}Te_{20}$	p-type	casting	0.36%
MSUHP10	$Ag_{0.86}Pb_{19}Sb_{1.0}Te_{20}$	n-type	hot pressing	0.28%
MSUHP4	$Ag_{0.9}Pb_9Sn_9Sb_{0.6}Te_{20}$	p-type	hot pressing	0.63%

Table 3.8.3. Elemental concentration as indicated by atomic percentage measured by AES at five different point locations on the fracture surface of MSUHP6 (Figure 3.8.17).

Point	**C**	**O**	**Te**	**Pb**	**Sb**
1	59.1	1.5	12.7	25.7	1.0
2	29.4	1.9	49.2	0.0	19.6
3	41.0	1.3	18.8	37.8	1.1
4	37.9	2.3	44.2	0.0	15.6
5	30.7	2.5	50.3	0.0	16.5
6	52.2	1.7	10.4	34.9	0.8
7	45.4	1.2	15.4	33.8	4.1
8	53.0	0.4	11.0	34.5	1.1

Table 3.8.4. Elemental concentration as indicated by atomic percentage measured by AES at two different point locations on the fracture surface of MSUHP6 (Figure 3.8.18).

Point	C	O	Te	Pb	Sb
1	16.7	2.3	51.4	10.2	19.4
2	21.7	1.3	28.5	47.9	0.5

thermogravity-mass spectroscopy (TG-MS) (Skimmer®, Netzsch Co., Germany). The TG-MS experiments were conducted between room temperature and 973 K with a continuous Ar flow of 70 mL/min.

TG-MS study on all of the four specimens (Table 3.8.2) showed mass loss above 773 K (Figure 3.8.14, Table 3.8.2). Compared to the ingot specimens, hot pressed specimens exhibited bigger mass losses such that the mass loss of the p-type hot pressed specimen MSUHP4 was 0.63 percent at 973K in contrast to 0.36 percent for p-type ingot specimen ETP40 at the same temperature, while the mass losses at 973K of n-type hot pressed specimen MSUHP10 and n-type ingot specimen ETN174 were 0.28 percent and 0.17 percent, respectively (Figure 3.8.14, Table 3.8.2). In addition, n-type specimens lost more mass than p-type specimens having the same processing technique (casting or hot pressing) at the same temperature (Figure 3.8.14, Table 3.8.2).

Above 773 K, the gas was evolved from the n-type hot pressed specimen MSUHP10. The majority of the gas from the p-type hot pressed MSUHP4 showed a molecular weight (amu) of 44, which was likely CO_2 (Figure 3.8.15). In addition, some of the gas evaporated from the p-type hot pressed specimen MSUHP4 had molecular weights of about 128 or 256, which was either Te or Te_2 (Figure 3.8.16). For the p-type ingot specimen ETP40, a trace amount of Te or Te_2 was observed above 773 K (Figure 3.8.16).

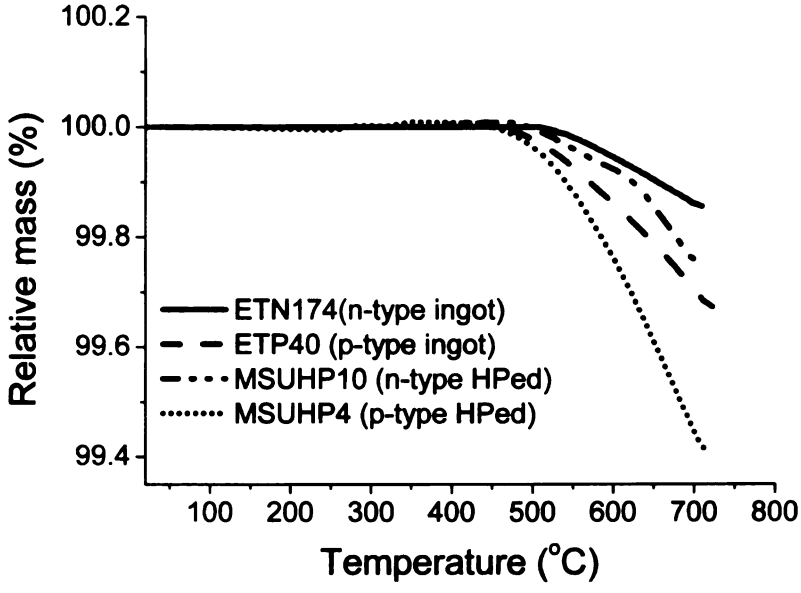

Figure 3.8.14. Relative mass changes as a function of temperature for the n-type ingot specimen ETN174 (straight line), the p-type ingot specimen ETP40 (dashed line), the n-type hot pressed specimen MSUHP10 (dash-dot line), and the p-type hot pressed specimen MSUHP4 (dotted line), as determined from TG-MS analysis.

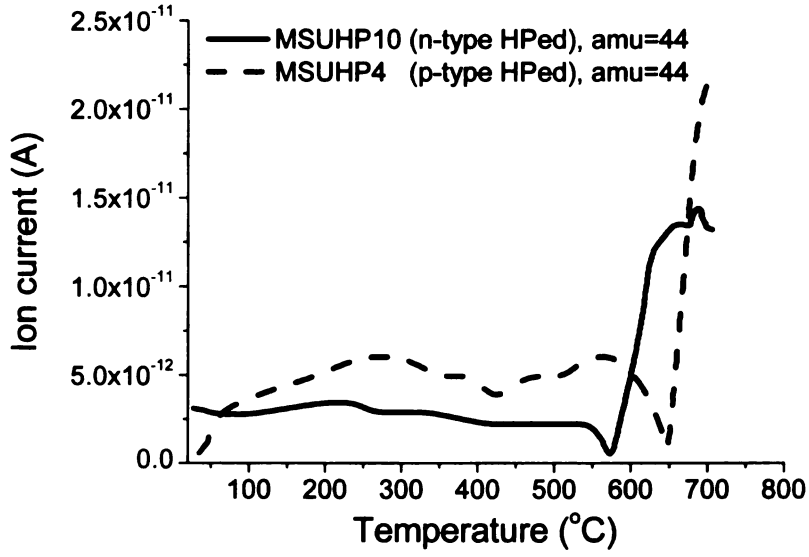

Figure 3.8.15. Ion current intensity of CO_2 (amu = 44) as a function of temperature for the n-type hot pressed specimen MSUHP10 (straight line), and the p-type hot pressed specimen MSUHP4 (dashed line), as determined from TG-MS analysis.

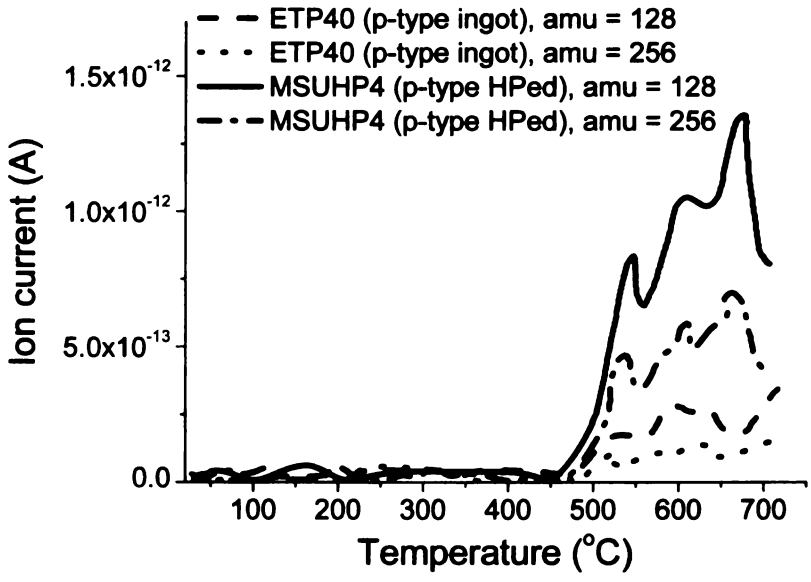

Figure 3.8.16. Ion current intensity of Te (amu = 128) and Te_2 (amu = 256) as a function of temperature for the n-type hot pressed specimen MSUHP10 and the p-type hot pressed specimen MSUHP4, as determined from TG-MS analysis.

Thus both n-type and p-type hot pressed specimens out-gassed CO_2 above 773 K (Figure 3.8.15). Both hot pressed and ingot p-type specimens out-gassed Te and Te2 at elevated temperatures (Figure 3.8.16). The sublimation of Te and Te_2 was due to the low vapor pressure of Te. The CO_2 may originate from decomposition of carbon compounds in the hot pressed specimens.

3. Auger electron spectroscopy (AES)

The existence of carbon in the hot pressed specimens was also confirmed from Auger electron spectroscopy (AES) observation on an n-type hot pressed specimen MSUHP6. THE AES analysis was performed by Dr. Harry Meyer at High Temperature Materials Laboratory of Oak Ridge National Laboratory (Oak Ridge, TN). The rectangular prismatic specimen about 3 mm x 3 mm x 30 mm in dimension was fractured inside the AES chamber in order to minimize the environmental contamination on the fracture surface.

From Auger electron microscopy, several needle-shaped inclusions were observed on the fracture surface of the hot pressed specimen MSUHP6 (Figs. 17 and 18). The inclusions were approximately 20 to 50 microns long (Figs. 17 and 18).

The composition of both the matrix and the inclusions were examined by AES. Since LAST materials are essentially doped PbTe, Pb and Te were included in the initial study. In addition, carbon, oxygen, aluminum, and silicon were included as possible contaminations. Carbon might be introduced during the hot pressing step where graphite

dies were used. Also, carbon may be present in the ingots due to possible back-streaming of vacuum pump oil into the fused silica ampoules. Oxygen might originate from atmosphere contamination during powder processing. Powder processing may also introduce aluminum since the mortars, pestles, milling jars, and milling media used in this study were made of alumina. Silicon contamination might be introduced by the ingot casting process where fused silica ampoules were used. Thus six elements, i.e. Pb, Te, O, C, Al, and Si, were initially included in the initial composition study (Table 3.8.3).

For specimen MSUHP6 the matrix (points o3, o4, o5 in Figure 3.8.17) had high concentrations of Pb and Te (Tables 3), which was expected since LAST materials are essentially doped PbTe. While Al and Si were not detected, up to 45.3 atomic percent of carbon and up to 5.3 atomic percent of oxygen were found on the fracture surface (Tables 3). In contrast, Pb was not found from the inclusion while a high concentration of Te up to about 80 atomic percent was observed (points o1 and o2 in Figure 3.8.17, Table 3.8.3). Up to 46.8 atomic percent of carbon and less than 5 atomic percent of oxygen were also found in the inclusion (points o1 and o2 in Figure 3.8.17, Table 3.8.3).

For a subsequent AES compositional analysis, Sb and Ag were included in addition to Pb, Te, C, and O. However, no Ag was detected on the fracture surface. The composition of the matrix, for example point o1 in Figure 3.8.18, contained less than one percent of Sb, while about 20 atomic percent of Sb was observed in the inclusion (point o2 in Figure 3.8.18, Table 3.8.4).

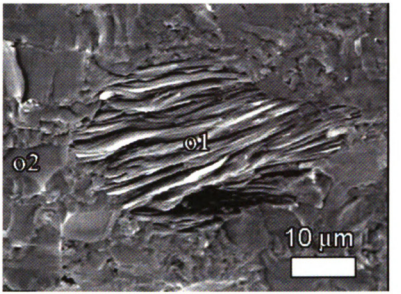

Figure 3.8.17. SEM micrograph depicting needle-shaped inclusions observed on the fracture surface of MSUHP6 during AES analysis.

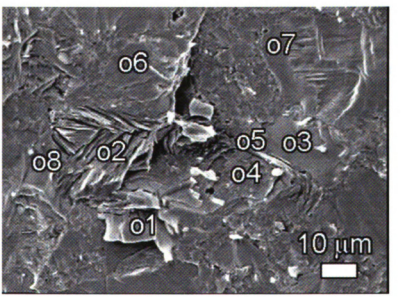

Figure 3.8.18. SEM micrographs showing need-shaped inclusions and the surrounding matrix observed on the fracture surface of specimen MSUHP6.

For both hot pressed specimen MSUHP6 analyzed by AES and the slow cooled specimens studied via SEM/EDS (see **Part III, Chapter 6**), the matrix mostly consisted of Pb and Te while inclusions were rich in Te and Sb.

The carbon concentration observed from both matrix and inclusions on the fracture surface of MSUHP6 ranged from about 16 percent to 47 percent (Tables 2 and 3). AES is a surface-sensitive technique [Childs 1995]. Although the specimen was fractured inside the Auger microscopy chamber, it was ineviTable 3.8.that gas molecules such as CO_2 and or CO that may have existed in the chamber prior to fracturing the specimen then deposited on the fracture surface, which in turn contributed to the observed C concentration. Thus it is likely that the Auger study overestimated the C content within the specimen.

Nevertheless, it can be concluded that a significant amount of C existed in the hot pressed specimens. The residual carbon evolved into CO_2 during annealing in the presence of oxygen (as suggested by the above discussed TG-MS study). The generation of gas at high temperature can yield porosity after annealing.

References

[Childs 1995] K. D. Childs, B. A. Carlson, L. A. La Vanier, *et al.*, *Handbook of Auger electron spectroscopy*, (Physical Electronics, Inc., Eden Priarie, MN, 1995).

Chapter 9

Thermal expansion, thermal diffusivity, and thermal fatigue properties of LAST and LASTT materials

1. Coefficient of thermal expansion (CTE)

In this study, the linear coefficient of thermal expansion (CTE) as a function of temperature for LAST and LASTT materials were obtained from thermomechanical analysis (TMA) (see **Part II, section 6.1.1**), as well as from the temperature dependent lattice parameter determined from by high temperature X-ray diffraction (HT-XRD) experiments.

1.1. Thermomechanical analysis (TMA) of LAST and LASTT materials

In this study, the average CTE, α_{avg}, between room temperatures T_{RT} and temperature T is calculated from:

$$\alpha_{avg} = \frac{1}{L_{RT}} \frac{L(T) - L_{RT}}{T - T_{RT}} = \frac{1}{L_{RT}} \frac{\Delta L(T)}{T - T_{RT}} \quad (1)$$

where L_{RT} and L(T) are the lengths of the specimen at room temperature temperature and at temperature T, respectively. $\Delta L(T)$ is the dimensional change at temperature T with respect to room temperature.

Table 3.9.1. Composition, processing technique, and the TMA measurement conditions including the temperature range, heating/cooling rate and gas environment for the LAST and LASTT specimens included in this study.

Specimen	Composition	Processing	Temp. Range	Rate	Environment
N155	$Ag_{0.86}Pb_{19}Sb_{1.0}Te_{20}$	Casting	RT to 673 K	3 K/min	Ar
MSUHP6	$Ag_{0.43}Pb_{18}Sb_{1.2}Te_{20}$	Hot pressing	RT to 623 K	3 K/min	Ar
P45	$Ag_{0.9}Pb_{9}Sn_{9}Sb_{0.6}Te_{20}$	Casting	133 to 673 K	3 K/min	He
MSUHP18	$Ag_{0.9}Pb_{9}Sn_{9}Sb_{0.6}Te_{20}$	Hot pressing	RT to 623 K	3 K/min	Ar

In the TMA experiments, four specimens were included: (1) an n-type ingot specimen N155, (2) an n-type hot pressed specimen MSUHP6, (3) a p-type ingot specimen P45, and (4) a p-type hot pressed specimen MSUHP18. The compositions and the processing techniques for each of the four specimens are summarized in Table 3.9.1, along with the TMA experimental conditions, including the measurement temperature range, the heating and cooling rate and the gas environment during measurements.

Prior to the measurements of the LAST and LASTT materials, the TMA equipment was calibrated with an alumina specimen (3.85 g/cm^3, PN 8459K24, McMaster Carr Supply Company, Chicago, IL). The alumina specimen was cycled once from room temperature to 1273 K in air, with a heating and cooling rate of 10 K/min. The dimensional change, ΔL, increased nearly linearly as a function of temperature (Figure 3.9.1). In addition, the heating data agreed very well with the cooling data without significant hysteresis (Figure 3.9.1). The linear least-squares fitting of heating data to Eq. (1) yielded an average CTE of 8.6×10^{-6}/K between room temperature and 1273 K with an r^2 of 0.99, while the α_{avg} of the cooling cycle was 8.7×10^{-6}/K with an r^2 of 0.99. The average CTE for the polycrystalline alumina obtained in this study compares well with a mean CTE value of 8.8×10^{-6}/K for alumina given by Kingery [Kingery 1976] and the CTE range between 7.2×10^{-6}/K and 8.8×10^{-6}/K for α-alumina cited by Barsoum [Barsoum 1997] (Table 3.9.2).

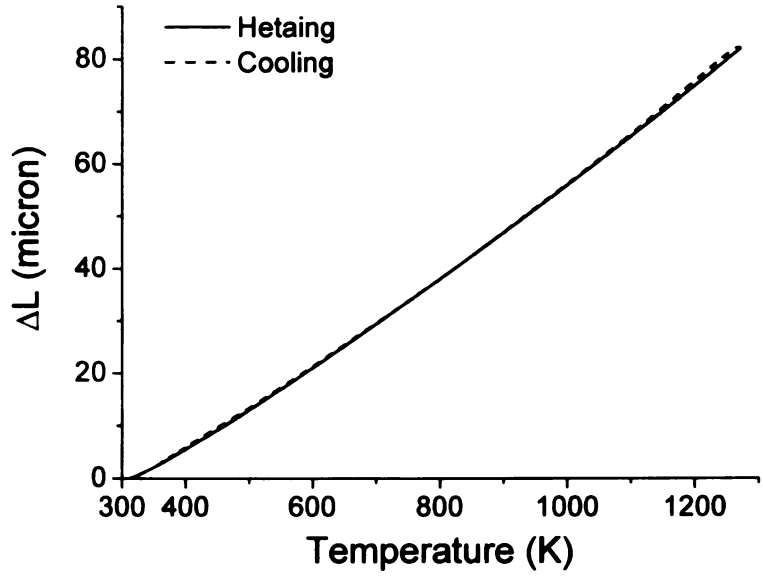

Figure1. Dimension change as a function of temperature as determined by TMA for a pure polycrystalline alumina specimen.

Table 3.9.2. Comparison of coefficient of thermal expansion values for pure alumina between this study and literature.

Source	Temp. range	CTE (x 10^{-6}/K)
Heating cycle in this study	298 – 1273 K	8.6
Cooling cycle in this study	298 – 1273 K	8.7
[Kingery 1976]	298 – 1300 K	8.8
[Barsoum 1997]	273 – 1900 K	7.2 – 8.8

The dimension of the ingot LAST specimen N155 increased nearly linearly with increasing temperature between room temperature and 673 K (Figure 3.9.2). The average CTE calculated from Eq. (1) between room temperature and 673 K was about 22 x 10^{-6}/K for each of the four heating and cooling cycles (Table 3.9.3). However, a small hysteresis between the heating and cooling data was observed for each of the four cycles (Figure 3.9.2), such that the difference in $\Delta L(T)$ at room temperature between the first heating cycle and the fourth cooling cycle was approximately 1.5 microns.

The original length of specimen N155 in the direction parallel to the TMA probe was 2.56 mm. Thus the permanent strain after the TMA measurement was approximately -0.058 percent. Assuming a uniform dimensional change in all directions, then a 0.058 percent reduction in one direction corresponded to a -0.17 percent volumetric change, which implies a 0.174 percent mass loss during the TMA measurement. In fact, the mass loss due to sublimation during the TG-MS analysis for ingot specimen N174 was about 0.17 percent at 973 K (Table 3.8.1 in **Chapter 8**), which agrees well with the 0.174 percent loss observed in the TMA measurement. Thus the hysteresis observed via the TMA (Figure 3.9.2) was likely due to sublimation of the LAST material.

For the hot pressed specimen MSUHP6, $\Delta L(T)$ and T had an approximately linear relationship between room temperature and 623 K (Figure 3.9.3). The original length of MSUHP6 was 2.25 mm and the dimensional change after four cycles was about -2 microns (Figure 3.9.3), which in turn yields a permanent strain of about -0.089 percent.

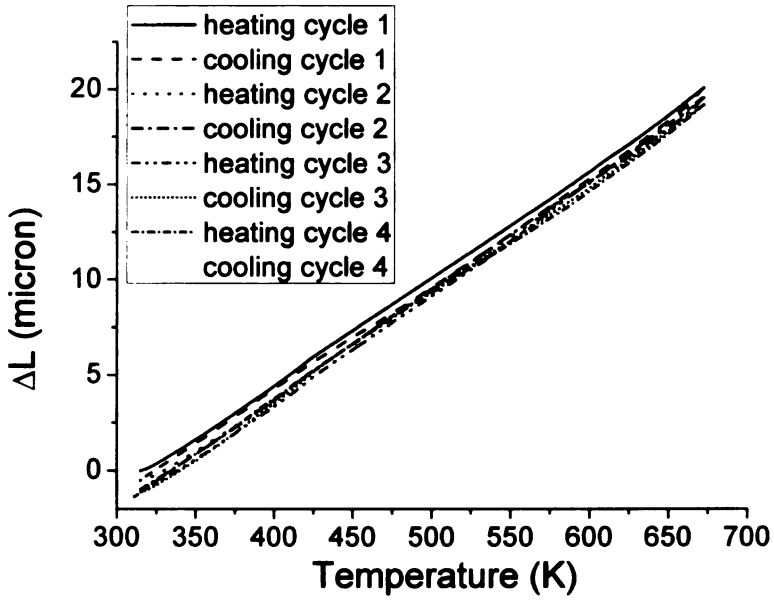

Figure 3.9.2. Dimensional change as a function of temperature as determined by TMA for the n-type ingot specimen N155.

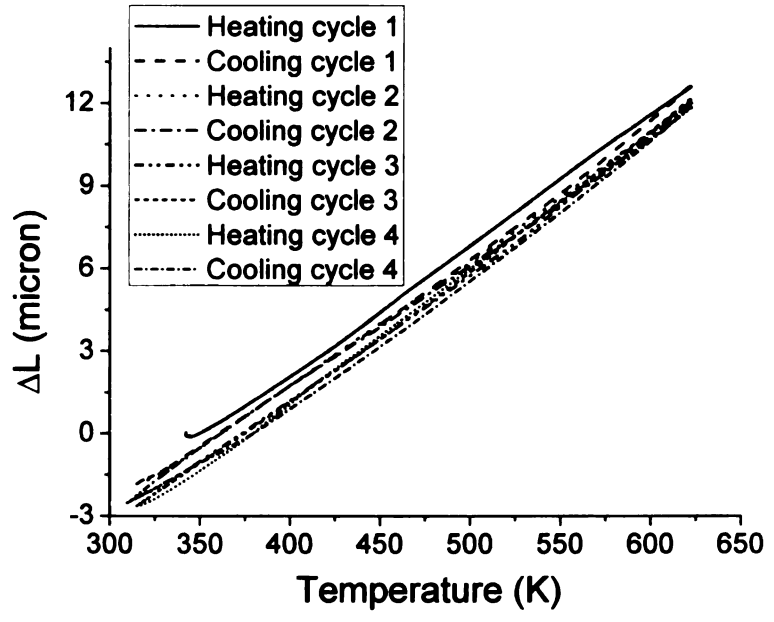

Figure 3.9.3. Dimensional change as a function of temperature as determined by TMA for the n-type hot pressed specimen MSUHP6.

Then the corresponding mass loss was about -0.267 percent, which was consistent with the mass loss of 0.28 percent due to sublimation for specimen MSUHP10 at 973 K as determined via TG-MS (Table 3.8.1 in **Chapter 8**). The average CTE ranged between about 20 x 10^{-6}/K and 21.5 x 10^{-6}/K (Table 3.9.3).

The p-type ingot specimen P45 exhibited a large hysteresis during cycling, where the difference in $\Delta L(T)$ between the first heating cycle and the fourth cooling cycle was as large as 6 microns at 523 K (Figure 3.9.4). At room temperature, the dimensional change after four cycles was about -4 microns, which corresponds to a permanent strain of approximately -0.16 percent giving the original length was 2.42 mm. Assuming a uniform dimensional change in all directions occurred during the TMA measurement, the volumetric change can be approximated as 0.48 percent, which implies a mass loss of 0.48 percent.

However, the mass loss due to sublimation during the TG-MS measurement was 0.36 percent for the ingot LASTT specimen P40 (Table 3.8.1 in **Chapter 8**). In addition, the mass of the specimen P45 before and after TMA measurement were 1.193 gram and 1.190 gram, respectively, which indicates a mass loss of 0.25 percent due to sublimation. Thus for specimen P45, the 0.48-percent mass loss that was derived from the dimensional change measured via TMA was over estimated. In fact, there was a small discontinuity at about 630 K in the ΔL versus temperature curve in first heating cycle (indicated by an arrow in Figure 3.9.4), which corresponded to a 1-micron reduction in length. The fact that the discontinuity only appeared in the first heating cycle implies that this was not a

material response but an artifact.

Thus the actual dimensional change was like about -3 microns at room temperature. Then the corresponding mass loss was about 0.37 percent, which was consistent with the TG-MS data (Table 3.8.1 in **Chapter 8**).

Since there was a significant amount of dimensional change observed in specimen P45 (Figure 3.9.4), the α_{avg} was only calculated between 133 K and about 573 K for the first heating cycle, which was approximately 21.7 x 10^{-6}/K (Table 3.9.3) by a linear least-squares fitting to Eq. (1).

For the p-type hot pressed specimen MSUHP18, an abnormal increase ("jump") in $\Delta L(T)$ near 623 K for each of the four heating and cooling cycles (Figure 3.9.5). The α_{avg} between room temperature and 573 K was approximately 22.7 x 10^{-6}/K for the first heating cycle (Table 3.9.3).

The amplitude of the "jumps" in $\Delta L(T)$ decreased as the thermal cycle increased. The dimensional changes at room temperature with respect to the original length, 7.62 mm, were approximately 150 microns after the first cycle, 190 microns after the second cycle, 210 microns after the third cycle, and 225 microns after the fourth cycle (Table 3.9.4). The permanent strain after each cycle increased from 1.97 percent after the first cycle to about 2.95 after the fourth cycle (Table 3.9.4), while the relative strain accumulated during each cycle range between 1.96 percent in the first cycle and 0.20 percent in the fourth cycle (Table 3.9.4).

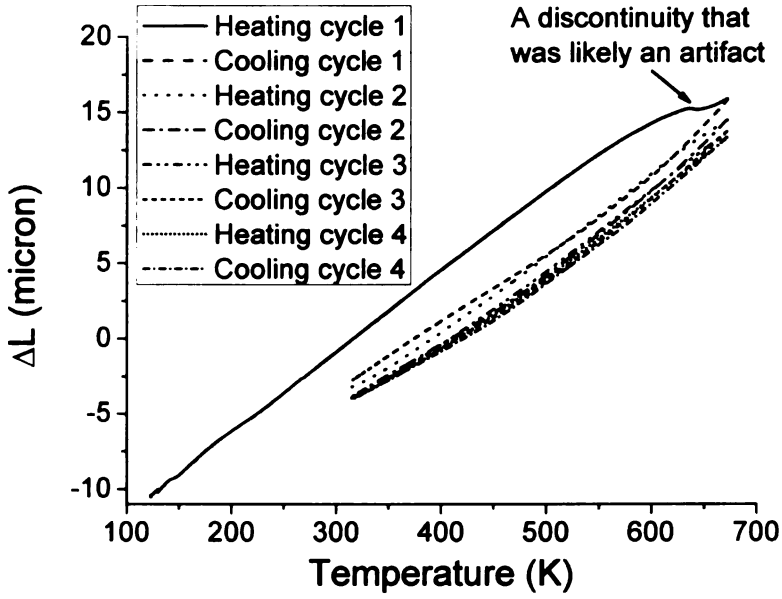

Figure 3.9.4. Dimensional change as a function of temperature as determined by TMA for the p-type ingot specimen P45. Note the specimen length decreases after the first cycle, which may indicate mass loss due to sublimation. A discontinuity occurred at about 630 K during the first heating cycle, which was likely an artifact.

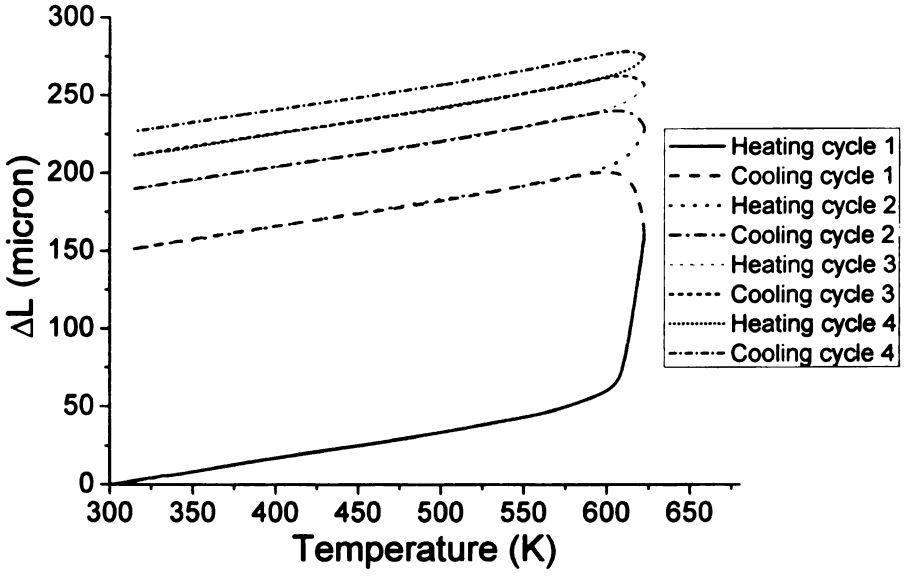

Figure 3.9.5. Dimensional change as a function of temperature as determined by TMA for the p-type hot pressed specimen MSUHP18.

Again, assuming a homogeneous dimensional change in all directions, the volumetric increases were 5.90 percent, 7.48 percent, 8.27 percent, and 8.86 percent after each of the four thermal cycles (Table 3.9.4). The mass change of specimen MSUHP18 after four cycles was only -0.001 gram compared to the original mass of 1.258 gram, which was less than 0.1 percent. The dimensional change in turn resulted in a volumetric porosity increase, where the relative porosities with respect to the specimen prior to the TMA measurement were 5.57 percent, 6.96 percent, 7.64 percent, and 8.14 percent after each of the four cycles (Table 3.9.4). The development of porosity due to thermal cycling in the p-type hot pressed LASTT specimen MSUHP18 was consistent with the bloating phenomenon observed in both n-type and p-type hot pressed specimens (see **Chapter 8**).

The mass loss for specimen MSUHP18 after four cycles was only about 0.08 percent. In contrast, the mass loss due to sublimation during the thermogravity-mass spectroscopy experiment for specimen MSUHP4 was 0.63 percent at 973 K (Table 3.8.1 in **Chapter 8**). However, the fact that the porosity was greater than 8 percent in specimen MSUHP18 after the thermal cycling suggested that MSUHP18 developed an open microstructure where the internal grains were in contact with the testing atmosphere. In contrast, for specimens N155, MSUHP6, and P45 only the outer surfaces were in contact with the testing atmosphere. It is worthwhile to note that although the TMA measurements were conducted in inert atmospheres, the TMA system is not an enclosed system. Thus, it was possible that MSUHP18 gained weight from some reactions with the gas molecules present in the testing environment during thermal cycling.

Table 3.9.3a. Coefficient of thermal expansion obtained by linear least-squares fitting of the TMA data to Eq. (1).

Specimen	Cycle	Temp. Range	Avg. CTE (10^{-6}/K)	r^2
N155	first heating	RT to 673 K	21.9	0.999
	first cooling	673 K to 323 K	21.7	0.999
	2nd heating	323 K to 673 K	22.0	0.999
	2nd cooling	673 K to 323 K	22.2	0.999
	3rd heating	323 K to 673 K	22.7	0.999
	3rd cooling	673 K to 323 K	22.2	0.999
	fourth heating	323 K to 673 K	22.2	0.999
	fourth cooling	673 K to 323 K	21.7	0.999
	Mean	RT to 673 K	22.1 ± 0.3	
MSUHP6	first heating	RT to 623 K	20.2	0.999
	first cooling	623 K to 323 K	20.7	0.999
	2nd heating	323 K to 623 K	20.2	0.999
	2nd cooling	623 K to 323 K	20.0	0.999
	3rd heating	323 K to 623 K	20.9	0.999
	3rd cooling	623 K to 323 K	21.2	0.999
	fourth heating	323 K to 623 K	21.4	0.999
	fourth cooling	623 K to 323 K	20.2	0.998
	Mean	RT to 623 K	20.6 ± 0.5	
P45	first heating	133 K to 573 K	21.7	0.999
MSUHP18	first heating	RT to 573 K	22.7	0.999

Table 3.9.3b. Coefficient of thermal expansion obtained by linear least-squares fitting of the temperature dependent lattice parameter (determined by high temperature X-ray diffraction) to Eq. (1).

Specimen	Temp. Range	Avg. CTE (10^{-6}/K)	r^2
N155	RT to 623 K	23.4	0.997
MSUHP6	RT to 623 K	20.8	0.996

Table 3.9.4. For specimen MSUHP18, the dimensional change with respect to the original length, ΔL, the accumulated permanent strain, ε_{perm}, the relative strain with respect to the previous thermal cycle, ε_{rel}, the accumulated relative volumetric change with respect to the original volume which was calculated from the permanent strain, $\Delta V/V_{orig}$, and the accumulated volumetric porosity, P, as a function of thermal cycle number during the TMA measurement.

Cycle	ΔL (micron)	ε_{perm} (percent)	ε_{rel} (percent)	$\Delta V/V_{orig}$ (percent)	P (percent)
First	150	1.97	1.97	5.90	5.58
Second	190	2.49	0.52	7.48	6.96
Third	210	2.76	0.26	8.27	7.64
Fourth	225	2.95	0.20	8.86	8.14

For all the linear least-squares regression included in Table 3.9.3, the coefficient of determination, r^2, was greater than 0.998 (Table 3.9.3). For the n-type ingot specimen N155 and the n-type hot pressed specimen MSUHP6, the temperature dependent CTE, $\alpha(T)$, was also evaluated using:

$$\alpha(T) = \frac{1}{L(T)}\frac{dL(T)}{dT} \approx \frac{1}{L_{RT} + \Delta L(T)}\frac{\Delta L(T+\delta T) - \Delta L(T-\delta T)}{2\delta T} \qquad (2)$$

where a δT of 10 K was used for all the thermal cycles for both N155 and MSUHP6.

The temperature dependent CTE of N155 increased nearly linearly from 20 x 10^{-6}/K at room temperature to about 24 x 10^{-6}/K at 423 K, and then dropped to 22 x 10^{-6}/K at around 450 K (Figure 3.9.6). The CTE values remained relatively constant at 22 x 10^{-6}/K between 450 K and 570 K. Beyond 570 K the CTE of N155 increased monotonically to 26 x 10^{-6}/K at 673 K (Figure 3.9.6).

The decrease in CTE between about 423 K and 450 K (Figure 3.9.6) may imply some relaxation process occurring in the specimen. In addition, the temperature range of 423 K and 450 K may be related to the "kink" observed in the Young's modulus versus T relationship at about 470 K for the same specimen (see **Part III, Chapter 6**).

Compared to the ingot LAST specimen N155, the CTE of the hot pressed LAST specimen MSUHP6 increased monotonically from about 16 x 10^{-6}/K to 21 x 10^{-6}/K when the temperature increased from room temperature to 623 K (Figure 3.9.7). It appeared that a kink might exist around 420 K, but no conclusions can be drawn at present due to the scatter in the data (Figure 3.9.7).

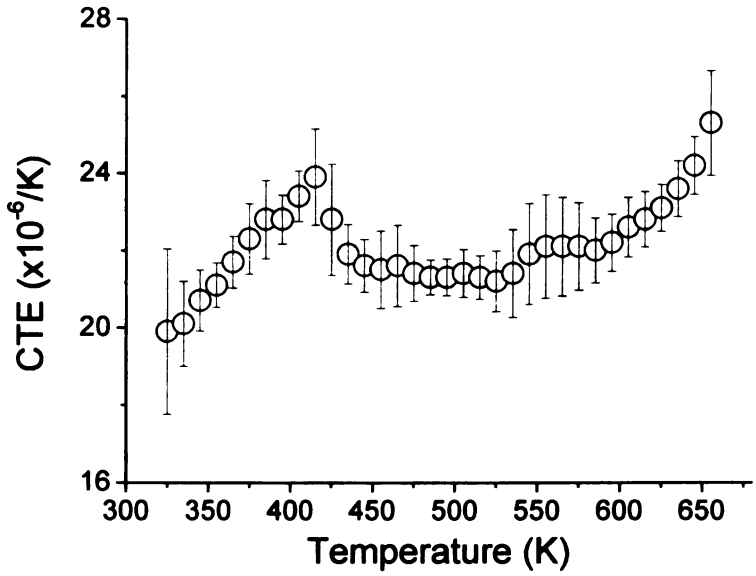

Figure 3.9.6. Temperature dependent CTE of n-type ingot LAST specimen N155 calculated from Eq. (2). The open symbols represent the mean CTE values from the four heating and cooling cycles, while the error bars indicates the standard deviation among the heating and cooling cycles.

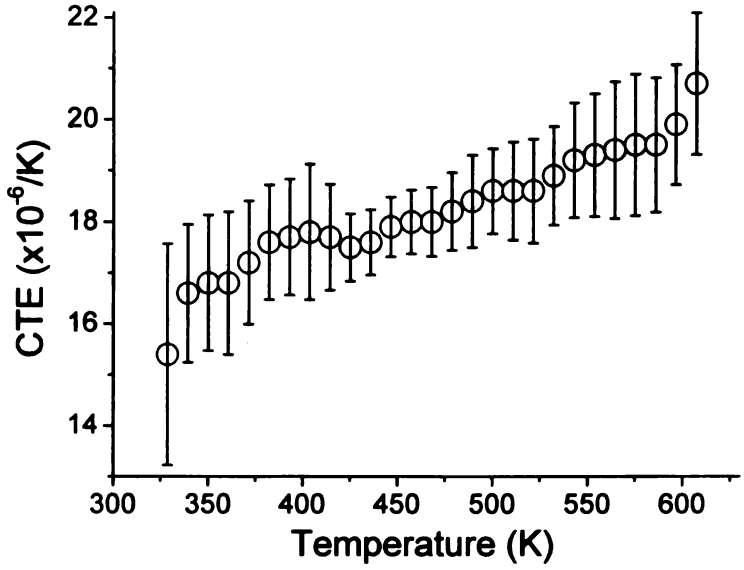

Figure 3.9.7. Temperature dependent CTE of n-type hot pressed LAST specimen MSUHP6 calculated from Eq. (2). The open symbols represent the mean CTE values from the four heating and cooling cycles, while the error bars indicates the standard deviation among the heating and cooling cycles.

1.2. High temperature X-ray diffraction of ingot and hot pressed LAST specimens

In addition to TMA study, the coefficient of thermal expansion was obtained from the lattice parameter as a function of temperature using the high temperature X-ray diffraction (XRD) facility at the High Temperature Materials Laboratory of Oak Ridge National Laboratory. The bulk hot pressed LAST specimen MSUHP6 and a powder specimen of ingot N155 were measured between room temperature and 623 K (**Part II, section 6.1.3**). (The thermal expansion of the same MSUHP6 specimen also was measured by TMA). The high temperature XRD experiments also were designed to examine for possible phase changes in LAST materials, since an abnormal slope change and a hysteresis were observed in the Young's modulus versus temperature relationship of the ingot specimen N155 (see **Chapter 6**). However, the XRD patterns obtained between room temperature and 623 K did not show phase evolution for either N155 or MSUHP6 (Figure 3.9.8).

Using a commercial software (X'Pert HighScore, PANalytical, Netherlands), the lattice parameters at each measurement temperature were calculated by Rietveld refinement of the XRD patterns to the PbTe structure, since LAST and LASTT are essentially doped PbTe materials. The lattice parameters as a function of temperature showed a monotonic increase with temperature for both N155 and MSUHP6 (Figure 3.9.9).

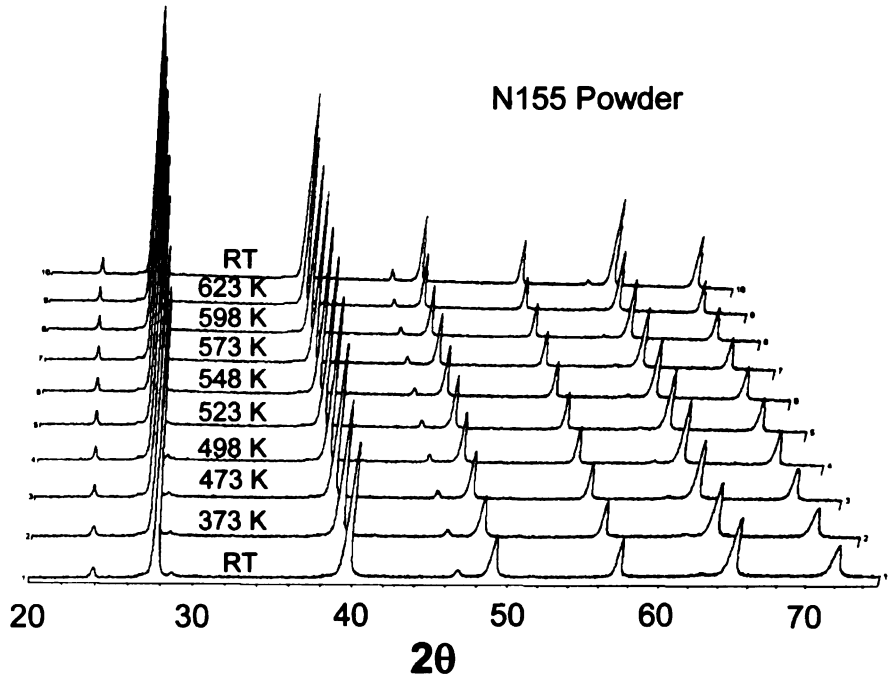

(a)

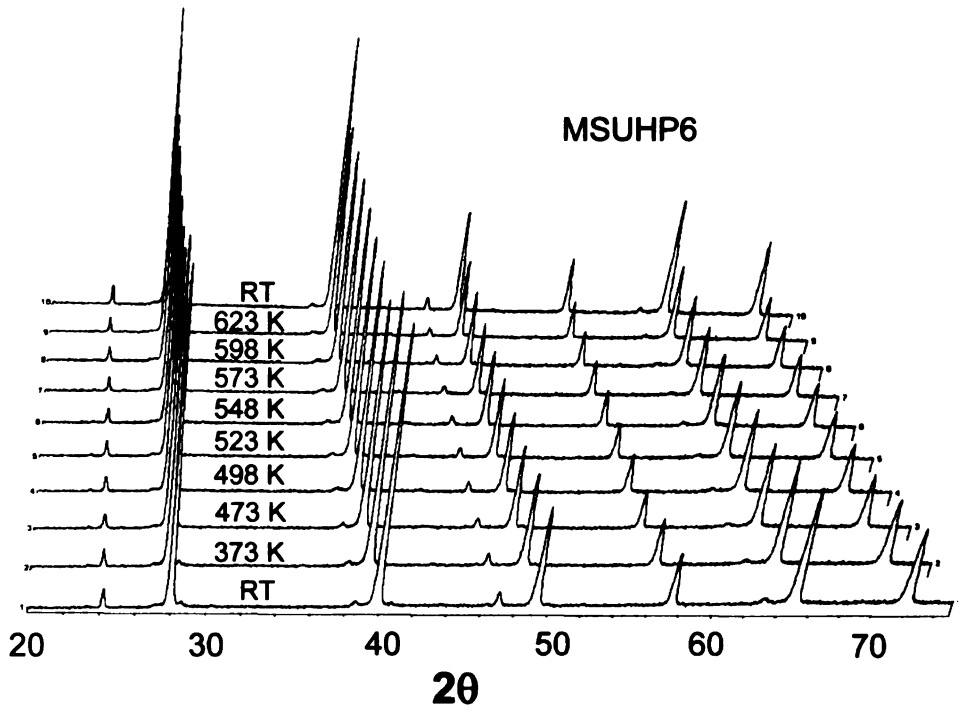

(b)

Figure 3.9.8. Series of high temperature X-ray diffraction patterns as a function of temperature for (a) N155 and (b) MSUHP6 between room temperature and 623 K.

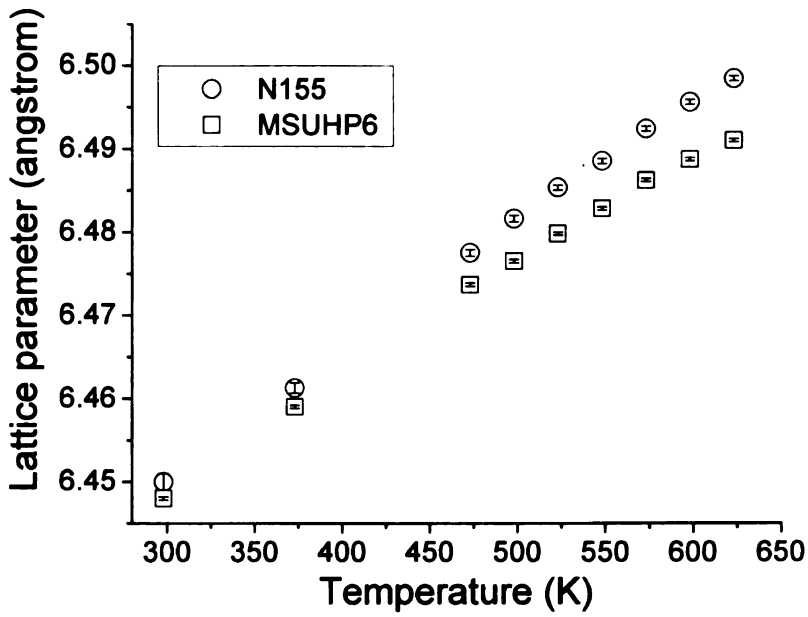

Figure 3.9.9. Temperature dependent lattice parameter as calculated from high temperature XRD patterns for n-type specimens N155 and MSUHP6.

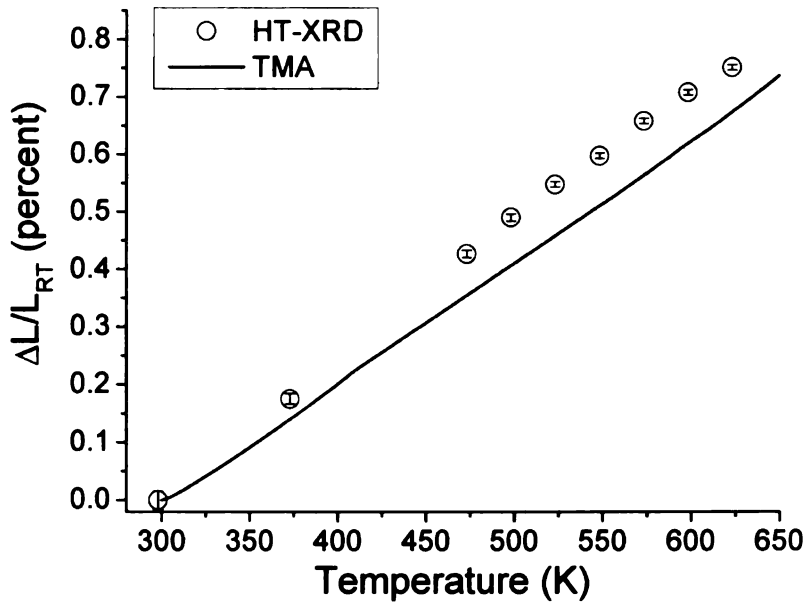

(a)

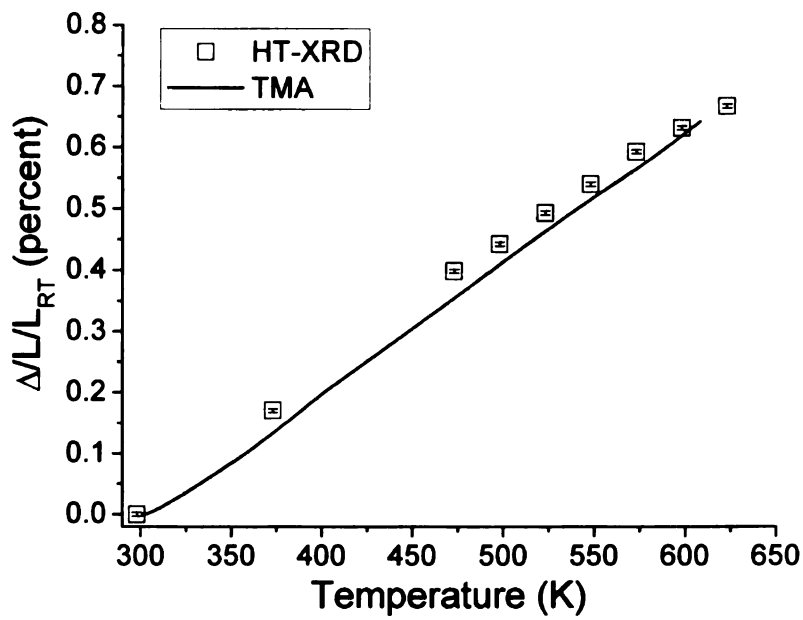

(b)

Figure 3.9.10. Comparison of relative dimensional change with respect to the room temperature value between high temperature XRD measurements and TMA measurements for (a) specimen N155, and (b) specimen MSUHP6.

For specimen MSUHP6, the relative dimensional change with respect to room temperature dimension, $\Delta L/L_{RM}$, agrees well between the high temperature XRD measurement and the TMA measurement (Figure 3.9.10b). However, a slight difference in $\Delta L/L_{RM}$ is observed for the ingot specimen N155 (Figure 3.9.10a), such that $\Delta L/L_{RM}$ values are approximately 0.75 percent for the high temperature XRD measurement and 0.67 percent for the TMA measurement (Figure 3.9.10a).

The same bulk MSUHP6 specimen was used in both the TMA and the high temperature (XRD) measurements. In contrast, the N155 specimen used in the TMA measurement was a bulk specimen, while that used in high temperature XRD measurement was a powder specimen. The composition of the slow-cooled ingot specimens ($Ag_{0.86}Pb_{19}Sb_{1.0}Te_{20}$) is inhomogeneous with inclusions up to 100 microns in diameter (**Part III, Chapter 6**). Thus it is likely that the compositions of the bulk N155 specimen examined by the TMA and the powder specimen (about 1 gram) examined by the high temperature XRD are different, which in turn yield a small difference in $\Delta L/L_{RM}$ values.

The average CTE between room temperature and 623 K was obtained by linear least-squares fitting of lattice parameter data to Eq. (1). For MSUHP6, the average CTE was about 20.8 x 10^{-6}/K, which agrees well with the mean CTE value of 20.6 ± 0.5 x 10^{-6}/K obtained from the TMA measurement (Table 3.9.3). For N155, the CTE value of 23.4 x 10^{-6}/K obtained from temperature dependent lattice parameter is about 5.8 percent

higher than the average CTE value of $22.1 \pm 0.3 \times 10^{-6}$/K determined by TMA (Table 3.9.3), which is due to the difference in the relative dimensional change between the bulk specimen and the powder specimen (Figure 3.9.10).

The room temperature lattice parameter of the ingot specimen N155 (6.450 ± 0.001 angstrom) was about 0.03 percent higher than the lattice parameter of the hot pressed specimen MSUHP6 (6.448 ± 0.0002 angstrom), while the lattice parameter of N155 at 623 K (6.4984 ± 0.0003 angstrom) was about 0.11 percent higher than MSUHP6 (6.4910 ± 0.0001 angstrom) (Figure 3.9.9). The difference in lattice parameter between N155 ($Ag_{0.86}Pb_{19}Sb_{1.0}Te_{20}$) and MSUHP6 ($Ag_{0.43}Pb_{18}Sb_{1.2}Te_{20}$) is likely due to the composition difference (Table 3.9.1), which is in consistence of the observation by Quarez *et al.* [Quarez 2005]. For example, the room temperature lattice parameter of $AgPb_mSbTe_{m+2}$ increased from 6.435 ± 0.005 angstrom for m = 12 to 6.443 ± 0.003 angstrom for m = 18 [Quarez 2005].

2. Room temperature thermal diffusivity

A preliminary study of thermal diffusivity of LAST materials was performed at room temperature using a flash system located at the High Temperature Materials Laboratory of Oak Ridge National Laboratory (see **Part II, section 6.2**). For each specimen included in this study (Table 3.9.5), the thermal diffusivity was calculated from the mean of three measurements.

The room temperature thermal diffusivity of the ingot specimen N155 was 16.2 ± 0.2

x 10^{-3} cm^2/sec, while the thermal diffusivities of the hot pressed specimens ranged from approximately 10.5 x 10^{-3} to 13 x 10^{-3} cm^2/sec (Table 3.9.5). Several studies have indicated thermal diffusivity increases with increasing grain size [Collins 1990, Fayette 2000, Vassen 1999, Wu 1996]. For example, the room temperature thermal diffusivity of SiC thin film increased from about 0.5 cm^2/sec to 0.9 cm^2/sec when the average grain size increased from 6.8 microns to 17.2 microns [Collins 1990]. The grain size of the ingot LAST specimens ranged between approximately 500 to 700 microns [Ren 2007], while the grain size of the hot pressed specimen MSUHP6 is about 50 microns. Thus, the higher thermal diffusivity value of ingot specimen N155 is consistent with the higher thermal diffusivity expected with increasing grain size [Collins 1990, Fayette 2000, Vassen 1999, Wu 1996]. Also, compositional differences among N155 ($Ag_{0.86}Pb_{19}Sb_{1.0}Te_{20}$) and MSUHP5, -6, -7 ($Ag_{0.43}Pb_{18}Sb_{1.2}Te_{20}$) (Table 3.9.5) may also contribute to the difference in thermal diffusivity.

In addition to LAST materials, a pure PbTe specimen and an $AgSbTe_2$ specimen were also included in this study, since the LAST materials are solid solutions between PbTe and $AgSbTe_2$ [Hsu 2004]. The thermal diffusivities of the PbTe specimen and the $AgSbTe_2$ specimen are 8.4 ± 0.1 x 10^{-3} cm^2/sec and 5.1 ± 0.1 x 10^{-3} cm^2/sec, respectively (Table 3.9.5).

Table 3.9.5. Room temperature thermal diffusivity values for n-type ingot and hot pressed LAST specimens, as well as a PbTe specimen and an $AgSbTe_2$ specimen included in this study.

Specimen	Composition	Processing	Thickness (mm)	Thermal diffusivity ($x10^{-3}$ cm^2/sec)
$AgSbTe_2$	$AgSbTe_2$	Bridgman*	1.988	5.1 ± 0.1
PbTe	PbTe	Bridgman*	2.809	8.4 ± 0.1
N155	$Ag_{0.86}Pb_{19}Sb_{1.0}Te_{20}$	Casting	2.556	16.2 ± 0.2
MSUHP3	$Ag_{0.43}Pb_{18}Sb_{1.2}Te_{20}$	Hot pressing	0.805	12.7 ± 0.2
MSUHP6	$Ag_{0.43}Pb_{18}Sb_{1.2}Te_{20}$	Hot pressing	2.258	10.7 ± 0.2
MSUHP7	$Ag_{0.43}Pb_{18}Sb_{1.2}Te_{20}$	Hot pressing	3.284	10.9 ± 0.2

* Polycrystalline materials fabricated by Bridgman method.

3. Thermal fatigue study

A preliminary thermal fatigue study was conducted using the infrared (IR) heating system at the High Temperature Materials Laboratory of Oak Ridge National Laboratory (see **Part II, section 3.5.2**). Two types of heating/cooling profiles were used: (1) slow heating with natural cooling, and (2) fast heating with natural cooling (Figure 3.9.11). The average heating rate in the fast heating/natural cooling profile was about 190 K/min between room temperature and 573 K, while the heating rate in the slow heating/natural cooling profile was less that 25 K/min (Table 3.9.6). The elastic moduli (Young's modulus and Poisson's ratio) were measured as a function of thermal cycle number using resonant ultrasound spectroscopy (see **Part II, section 3.4**).

Three specimens were thermally cycled using the IR apparatus: (i) an ingot LAST specimen N138, (ii) a hot pressed LASTT specimen P20-HP1, and (iii) a Sn- and S-doped PbTe specimen L145 (Table 3.9.6). No significant change in Young's modulus or Poisson's ratio was observed for specimen N138 after two fast cycles, such that the Young's modulus prior to and after cycling were 51.52 ± 0.24 GPa and 51.12 ± 0.22 GPa, while the Poisson's ratio values were 0.278 ± 0.004 prior to cycling and 0.274 ± 0.003 after cycling (Table 3.9.6). For specimen L145, the Young's modulus and the Poisson's ratio of specimen L145 did not show significant change after 12 slow cycles and two fast cycles (Table 3.9.6).

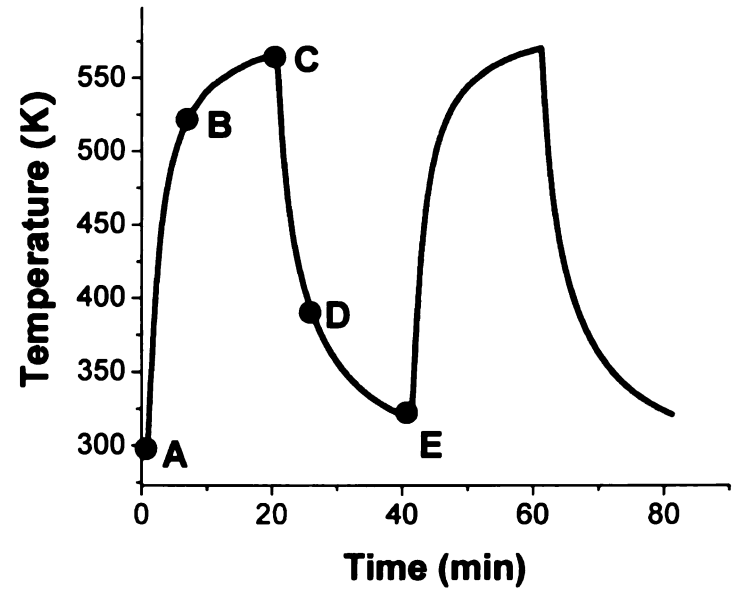

(a)

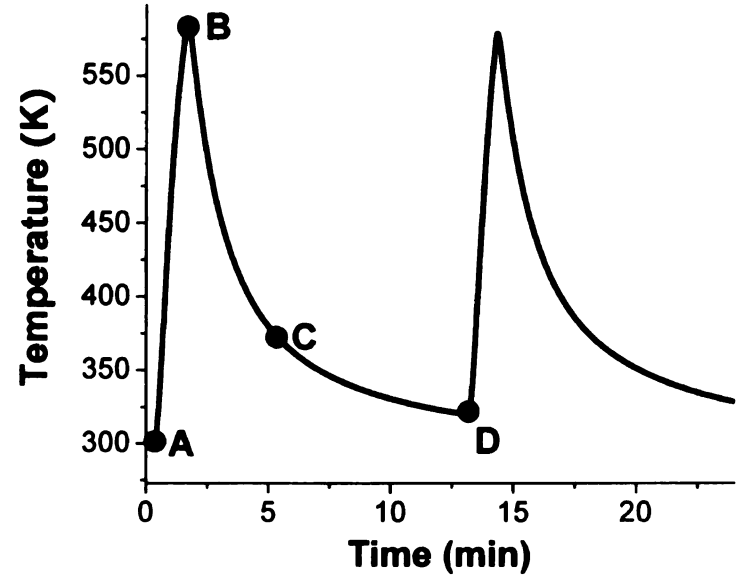

(b)

Figure 3.9.11. Temperature profiles during thermal fatigue cycling for (a) the slow heating/natural cooling thermal cycles, and (b) the fast heating/natural cooling thermal cycles.

Table 3.9.6. For the thermal fatigue experiments performed at ORNL, the average cooling rates during heating and cooling segments for the slow heating/natural cooling profile and the fast heating/natural cooling profile.

Temperature profile	Average heating or cooling rate (K/min)			
	AB	BC	CD	DE
Slow heating/natural cooling	24.4	2.2	-31.8	-3.8
Fast heating/natural cooling	190	-54.8	-6.93	

Table 3.9.7. Young's modulus and Poisson's ratio as a function of thermal cycling for specimens L145, N138, and P20-HP1. The temperature change as a function of time is illustrated in Figure 3.9.11 and summarized in Table 3.9.6.

Specimen/ Composition/ Processing	Thermal cycles	Young's modulus (GPa)	Poisson's ratio
L145 $Pb_{0.95}Sn_{0.05}Te_{0.92}S_{0.08}$ Casting	No cycling	54.14±0.18	0.269±0.002
	2 slow cycles	54.13±0.19	0.269±0.002
	12 slow cycles	54.18±0.19	0.269±0.002
	12 slow cycles + 2 fast cycles	54.20±0.19	0.269±0.002
N138 $Ag_{0.43}Pb_{18}Sb_{1.2}Te_{20}$ Casting	No cycling	51.51±0.24	0.278±0.004
	2 fast cycles	51.12±0.22	0.274±0.003
P20-HP1 $Ag_{0.5}Pb_6Sn_2Sb_{0.2}Te_{10}$ Hot pressing	No cycling	53.20±0.36	0.277±0.007
	2 fast cycles	51.14±0.24	0.279±0.005

For the hot pressed specimen P20-HP1, the undamaged Young's modulus was 53.20 $\pm$0.36 GPa, which decreased to 51.24$\pm$0.24 GPa after five fast cycles (Table 3.9.3). The Poisson's ratio of P20-HP1 did not change significantly, which were 0.277$\pm$0.007 and 0.279$\pm$0.005 prior to and after thermal cycling (Table 3.9.6).

The reduction in the Young's modulus is proportional to the damage state, ε, such that [Case 2002]:

$$\frac{E_{un} - E(\varepsilon)}{E_{un}} = f(\upsilon)\varepsilon \qquad (3)$$

where E_{un} and $E(\varepsilon)$ are the Young's modulus of the un-damaged and damaged materials, while the function f(ν) depends on the microcrack orientation and Poisson's ratio (see **Part I, section 2.3.3**). Thus, the reduction in Young's modulus of specimen P21-HP1 (Table 3.9.6) may indicate damage in the specimen introduced by thermal cycling.

For the hot pressed specimen P20-HP1, the reduction in Young's modulus after five fast cycles is approximately 3.68 percent. The Poisson's ratio of LAST and LASTT materials are approximately between 0.25 and 0.30 (Chapter 2 and Chapter 4). However, the function f(ν) is a relatively weak function of the Poisson's ratio, ν, and the crack shape [Case 2002]. For randomly oriented penny-shaped cracks, f(ν) ranged between 1.692 and 1.794 in the Poisson's range of 0.15 to 0.35, while for the same Poisson's ratio range (0.15 to 0.35), f(ν) varies between 1.598 and 1.665 for slit-shaped cracks [Case 2002]. Assuming f(ν) = 1.7 for the thermal fatigue study of P20-HP1, then from Eq. (3), we can estimate an ε value of about 0.022.

For planar or circular cracks with a radius of a, the damage state, ε, can be approximated as [Case 2002]:

$$\varepsilon = N\langle a^3 \rangle \tag{4}$$

where N is the volumetric crack number density [Case 2002]. If the average crack radius in specimen P20-HP1 is approximately 1/10 of the smallest dimension of the specimen which is 5 mm, then a is about 0.5 mm. Thus the volumetric crack number density, N, for specimen P20-HP1 calculated from Eq. (4) is roughly 1.76×10^{8} m^{-3}.

4. Summary

The coefficient of thermal expansion as a function of temperature for ingot and hot pressed LAST and LASTT materials ranged from about 20 to 23 x 10^{-6}/K (Table 3.9.3, Figs. 6 and 7). The n-type ingot specimen N155, n-type hot pressed specimen MSUHP10, and the p-type ingot specimen P45 showed hysteresis between heating and cooling (Figures 2 – 4). The mass loss derived from the dimensional change for these three specimens agreed well with the mass loss due to sublimation determined via TG-MS (**Chapter 8**), which suggested that the hysteresis was due to the sublimation of LAST and LASTT materials during the TMA experiment.

In contrast, permanent strain was accumulated in the p-type hot pressed specimen MSUHP18 (Figure 3.9.5) during the TMA experiment as a result of bloating. The permanent strain increased from 1.97 percent after the first heating/cooling cycle to about 2.95 percent after the fourth cycle, which corresponded to the development of the

volumetric porosity that increased from 5.57 percent after the first cycle to 8.14 after the fourth cycle (Table 3.9.4).

The hot pressed LAST specimens had a lower thermal diffusivity than the ingot LAST specimen N155 at room temperature (Table 3.9.5), which may be due to differences in grain size and/or composition.

A preliminary thermal fatigue study of a hot pressed specimen P20-HP1 indicated a slight decrease in Young's modulus after five fast cycles. For the ingot specimens L145 and N138 after slow cycling and fast cycling, no significant change in Young's modulus and Poisson's ratio were observed, considering the error bars in the measurements (Table 3.9.7).

Thermal expansion, thermal diffusivity, and thermal fatigue property are important in the thermal-mechanical characterization of thermoelectric devices. Thermal expansion values are required to calculate the thermal stresses. Thermal diffusivity is important for the details of the temperature distribution in the specimen and on the specimen surface as a function of time [Case 2002]. Thermal fatigue damage may affect the mechanical integrity as well as the thermoelectric properties.

Reference

[Barsoum 1997] M. W. Barsoum, *Fundamentals of ceramics*, (McGraw-Hill Co., Inc., New York, 1997), pp. 103.

[Case 2002] E. D. Case, "The Saturation of Thermomechanical Fatigue in Brittle

Materials", in *Thermo-Mechanical Fatigue and Fracture*, edited by M. H. Alibadi (WIT Press, Southampton, UK, 2002), 137-208.

[Collins 1990] A. K. Collins, M. A. Pickering and R. L. Taylor, "Grain-Size Dependence of the Thermal-Conductivity of Polycrystalline Chemical Vapor-Deposited Beta-Sic at Low-Temperatures", *Journal of Applied Physics*, **68**: 6510-6512 (1990).

[Fayette 2000] S. Fayette, D. S. Smith, A. Smith and C. Martin, "Influence of grain size on the thermal conductivity of tin oxide ceramics", *Journal of the European Ceramic Society*, **20**: 297-302 (2000).

[Hsu 2004] K. F. Hsu, S. Loo, F. Guo, W. Chen, J. S. Dyck, C. Uher, T. Hogan, E. K. Polychroniadis and M. G. Kanatzidis, "Cubic AgPbmSbTe2+m: Bulk thermoelectric materials with high figure of merit", *Science*, **303**: 818-821 (2004).

[Kingery 1976] W. D. Kingery, H. K. Bowen and D. R. Uhlmann, *Introduction to ceramics (2nd edition)*, (Wiley-Interscience, New York, 1976), pp. 595.

[Quarez 2005] E. Quarez, K. F. Hsu, R. Pcionek, N. Frangis, E. K. Polychroniadis and M. G. Kanatzidis, "Nanostructuring, compositional fluctuations, and atomic ordering in the thermoelectric materials AgPbmSbTe2+m. The myth of solid solutions", *Journal of the American Chemical Society*, **127**: 9177-9190 (2005).

[Ren 2007] F. Ren, E. D. Case, E. J. Timm and H. Schock, "Hardness as a function of composition for n-type LAST thermoelectric material", *Journal of Alloys and Compounds*, available online at doi:10.1016/j.jallcom.2007.01.086 (2007).

[Vassen 1999] R. Vassen and D. Stover, "Processing and properties of nanograin silicon carbide", *Journal of the American Ceramic Society*, **82**: 2585-2593 (1999).

[Wu 1996] B. M. Wu, Y. L. Du, H. X. Tang, P. Du, X. Y. Qin and L. D. Zhang, "Reduced thermal diffusivity of nanostructured silver", *Journal of Physics and Chemistry of Solids*, **57**: 1211-1213 (1996).

CONCLUSIONS

In this study, mechanical and thermal properties of PbTe-based thermoelectric (TE) materials, including pure PbTe, LAST (Pb-Sb-Ag-Te), and LASTT (Pb-Sb-Ag-Te-Sn) were characterized at both room temperature and as a function of temperature, while the microstructures and compositions were examined for both ingot and hot pressed specimens. In addition, a powder processing procedure for the LAST materials was developed, including pre-milling treatment, planetary ball milling, and hot pressing of milled powders.

For 14 different LAST compositions, the room temperature hardness was measured via Vickers microindentation and nanoindentation (**Chapter 1**), while the room temperature Young's modulus was obtained from microindentation (Vickers indentation and Knoop indentation) and nanoindentation (**Chapter 2**). For both hardness and Young's modulus of a given composition, measured values via microindentation and nanoindentation agreed well (**Chapter 1** and **Chapter 2**) except for specimen N58, whose Young's modulus measured by microindentation was about half of that measured by nanoindentation due to cracks induced by biaxial loading (**Chapter 2**). Both the hardness and the Young's modulus as a function of composition can be expressed as parabolic functions of the molar fraction of the composing elements (Pb, Sb, Ag, Te) (**Chapter 1** and **Chapter 2**).

Biaxial flexure testing was performed to measure the fracture strength for 15 LASTT

ingot specimens (**Chapter 3**). A Weibull analysis of the fracture strength yielded a characteristic strength of about 15 MPa and a Weibull modulus of approximately 3. The 15-MPa characteristic strength agrees with the fracture strength values of other ingot TE materials reported in literature. However the Weibull modulus of 3 implies a large scatter in the fracture strength, which can be problematic in TE device fabrication (**Chapter 3**).

Resonant ultrasound spectroscopy (RUS) was utilized to measure the elastic moduli as a function of temperature, including Young's modulus, shear modulus, and Poisson's ratio, for pure and lightly doped PbTe (**Chapter 5**), S- and Sn-doped PbTe (**Chapter 4**), ingot LAST specimens (**Chapter 4** and **Chapter 6**), and hot pressed LAST specimens (**Chapter 4**).

For the pure PbTe and PbI_2-doped PbTe, both Young's modulus and shear modulus decreased linearly as a function of temperature between room temperature and about 800 K (**Chapter 5**). The Poisson's ratio of the pure PbTe specimen decreases monotonically from about 0.3 at room temperature to about 0.25 near 800 K, while the Poisson's ratio of the PbI_2-doped PbTe increased from approximately 0.255 to 0.30 as the temperature increased from room temperature to about 700 K (**Chapter 5**). For the S- and Sn-doped PbTe specimen, Young's modulus decreased linearly between room temperature and about 800 K, while the Poisson's ratio data showed some scatter near a value of 0.27 at the temperature between room temperature and about 800 K (**Chapter 4**).

For the LAST ingot specimen N138 ($Ag_{0.43}Pb_{18}Sb_{1.2}Te_{20}$), the Young's modulus decreased linearly between room temperature and about 750 K, while the Poisson's ratio

increased from about 0.26 at room temperature to 0.29 near 750 K (**Chapter 4**). For a slow-cooled ingot specimen N155 ($Ag_{0.86}Pb_{19}Sb_{1.0}Te_{20}$), the Young's modulus decreased monotonically from room temperature to about 800K (**Chapter 6**). However, for slow cooled specimen N155 a "kink" (slope change) in the Young's modulus versus temperature was observed near 500 K (**Chapter 6**). In addition, a hysteresis between heating and cooling was observed between about 400 K and 600 K, when the heating and cooling rate during the RUS measurement was 5 K/min (**Chapter 6**). When the heating and cooling rates were decreased to 2 K/min, the hysteresis disappeared, but the kink was still present (**Chapter 6**). The kink and the hysteresis may be due to phase change(s), the electron-deformation coupling, or the point defect relaxation process (**Chapter 6**).

For hot pressed LAST specimens, room temperature Young's modulus decreased exponentially with increasing porosity for a given composition of $Ag_{0.43}Pb_{18}Sb_{1.2}Te_{20}$ in agreement with the modulus versus porosity behavior observed in many materials (**Chapter 4**). For the 94.2 percent dense hot pressed specimen MSUHP6, the Young's modulus decreased linearly between room temperature and about 550 K, while above 550 K a rapid decrease in Young's modulus was observed that is likely due to grain boundary sliding (**Chapter 4**). For specimen UMHP6 which was about 85% dense, the Young's modulus decreased monotonically with increasing temperature although a kink was observed in the Young's modulus versus temperature near 470 K (**Chapter 4**).

Hot pressed specimens included in this study were processed using powders that were crushed, ground, and milled in a planetary mill. The mean particle size of powders

milled after 180 minutes was about 6 microns with equiaxed particle shape. No amorphous phase and no phases other than the parent phase (LAST or LASTT) were observed in any the milled powders (**Chapter 7**). In addition, high temperature X-ray diffraction (HT-XRD) analysis on a hot pressed specimen MSUHP6 showed no phase change between room temperature and 523 K (**Chapter 9**).

Bloating of hot pressed specimens was observed when as-hot-pressed specimens were annealed. The gas evolved from both n-type and p-type hot pressed specimens during annealing was CO_2 as determined from thermogravity-mass spectroscopy (**Chapter 8**). The evolution of CO_2 may be due to the reaction between oxygen and the carbon contamination in the specimens. The carbon contamination may originate from the powder processing (**Chapter 8**). A significant amount of carbon was observed on the fresh fracture surface of specimen MSUHP6 via Auger electron spectroscopy (AES) (**Chapter 8**). From Auger microscopy, needle shaped inclusions also were observed, which are rich in Sb and Te in contrast to the Pb- and Te- rich matrix (**Chapter 8**). In addition, needle-shaped, spherical, and plate-like inclusions were observed by scanning electron microscopy in slow-cooled ingot specimens. Each of these inclusion types was also rich in Sb and Te as determined by energy dispersive X-ray spectroscopy (**Chapter 6**). The bloating problem will affect the high temperature performance of TE devices. Possible solutions to eliminate the carbon contamination in the hot pressed materials are (1) reducing the carbon content in the glove box atmosphere, (2) performing powder milling in an inert atmosphere, and (3) utilizing non-graphite dies during hot pressing.

In addition to mechanical properties, the coefficient of thermal expansion (CTE) was measured as a function of temperature for both ingot and hot pressed LAST and LASTT specimens using a thermomechanical analyzer (TMA) and high temperature X-ray diffraction (HT-XRD) (**Chapter 9**). The average CTE values ranged from about 20 x $10^{-6}/K^{-1}$ to 23.4 x $10^{-6}/K^{-1}$ among ingot and hot pressed LAST and LASTT materials. The room temperature thermal diffusivity of hot pressed specimens was lower than that of the ingot specimen. The differences in thermal diffusivities between hot pressed and ingot specimens may be due to the reduced grain size for the hot pressed specimens and or different composition (**Chapter 9**).

Preliminary study of thermal fatigue showed no significant change in Young's modulus for ingot specimens after thermal cycling. However, a small decrease in Young's modulus was observed in the hot pressed specimen ETP20-HP1, which implies that hot pressed specimens may be more susceptible to thermal fatigue damage, but more research must be done to clarify this point (**Chapter 9**).

The mechanical and thermal property data obtained in this study are important information needed to characterize the thermo-mechanical behavior of LAST and LASTT materials. The SEM, EDS, and AES studies revealed microstructural and compositional features that have not been discovered before. The powder processing procedure developed in this study is effective for the fabrication of TE elements used in TE devices.

BIBLIOGRAPHY

[Agosta 2002] D. S. Agosta, J. E. Hightower, K. Foster, R. G. Leisure and Z. Gavra, "Elastic moduli of polycrystalline ZrCo as a function of temperature", *Journal of Alloys and Compounds*, **346**: 1-5 (2002).

[Ali Omar 1975] M. Ali Omar, *Elementary Solid State Physics*, (Addison-Wesley Publishing Company, Inc., Reading, Massachusetts, 1975), pp. 84.

[Almer 2001] J. Almer, M. Oden and G. Hakansson, "Microstructure, stress and mechanical properties of arc-evaporated Cr-C-N coatings", *Thin Solid Films*, **385**: 190-197 (2001).

[Anderson 1966] O. L. Anderson, "Derivation of Wachtmans Equation for Temperature Dependence of Elastic Moduli of Oxide Compounds", *Physical Review*, **144**: 553-557 (1966).

[Androulakis 2006] J. Androulakis, K. F. Hsu, R. Pcionek, H. Kong, C. Uher, J. J. DAngelo, A. Downey, T. Hogan and M. G. Kanatzidis, "Nanostructuring and high thermoelectric efficiency in p-type Ag(Pb1-ySny)(m)SbTe2+m", *Advanced Materials*, **18**: 1170-1173 (2006).

[Androulakis 2007] J. Androulakis, C. H. Lin, H. Kong, C. Uher, C. I. Wu, T. Hogan, B. A. Cook, T. Caillat and M. G. Kanatzidis, "Spinodal Decomposition and Nucleation and Growth as a Means to Bulk Nanostructured Thermoelectrics: Enhanced Performance in Pb1-xSnxTe-PbS", *Journal of the American Chemical Society*, **129**: 9780-9788 (2007).

[Asthana 1996] C. D. Asthana and A. K. Shrivastava, "Hardness variation in undoped and doped mixed NaCl-NaBr single crystal", in *Disordered Materials - Current Developments* -, edited by (Transtec Publications Ltd, Zurich-Uetikon, 1996), 453-455.

[Atteberry 2004] J. E. Atteberry, D. S. Agosta, C. E. Nattrass, R. G. Leisure, I. Jacob, R. C. Bowman and O. Yeheskel, "Temperature dependence of the elastic moduli of polycrystalline LaAlxNi5-(x) and LaSnxNi5-x", *Journal of Alloys and Compounds*, **376**: 139-144 (2004).

[Baker 2005] M. A. Baker, P. J. Kench, C. Tsotsos, P. N. Gibson, A. Leyland and A. Matthews, "Investigation of the nanostructure and wear properties of physical vapor deposited CrCuN nanocomposite coatings", *Journal of Vacuum Science & Technology A*, **23**: 423-433 (2005).

[Barsoum 1997] M. W. Barsoum, *Fundamentals of ceramics*, (McGraw-Hill Co., Inc., New York, 1997), pp. 70-71, 410-415.

[Bellaiche 1996] L. Bellaiche, S. H. Wei and A. Zunger, "Localization and percolation in semiconductor alloys: GaAsN vs GaAsP", *Physical Review B*, **54**: 17568-17576 (1996).

[Bennett 1995] G. L. Bennett, "Space applications", in *CRC handbook of thermoelectrics*, edited by D. M. Rowe (CRC Press, Inc., New York, 1995), 515-537.

[Bernard 1986] J. E. Bernard and A. Zunger, "Optical Bowing in Zinc Chalcogenide Semiconductor Alloys", *Physical Review B*, **34**: 5992-5995 (1986).

[Bhagavat 2005] S. Bhagavat and I. Kao, "Nanoindentation of lithium niobate: hardness anisotropy and pop-in phenomenon", *Materials Science and Engineering a-Structural Materials Properties Microstructure and Processing*, **393**: 327-331 (2005).

[Bilc 2004] D. Bilc, S. D. Mahanti, E. Quarez, K. F. Hsu, R. Pcionek and M. G. Kanatzidis, "Resonant states in the electronic structure of the high performance thermoelectrics AgPbmSbTe2+m: The role of Ag-Sb microstructures", *Physical Review Letters*, **93**: - (2004).

[Borisova 1984] L. Borisova, "Density-of-States Effective Mass in Solid-Solutions of the (Agx/2Pb1-xSbx/2)Te Type", *Physica Status Solidi B-Basic Research*, **126**: K155-K158 (1984).

[Bottner 2006] H. Bottner, G. Chen and R. Venkatasubramanian, "Aspects of thin-film superlattice thermoelectric materials, devices, and applications", *MRS Bulletin*, **31**: 211-217 (2006).

[Bouad 2003] N. Bouad, R. M. Marin-Ayral, G. Nabias and J. C. Tedenac, "Phase transformation study of Pb-Te powders during mechanical alloying", *Journal of Alloys*

and Compounds, **353**: 184-188 (2003).

[Bouarissa 2003] N. Bouarissa, "Compositional dependence of the elastic constants and the Poisson ratio of GaxI1-xSb", *Materials Science and Engineering B-Solid State Materials for Advanced Technology*, **100**: 280-285 (2003).

[Bridgman 1924] P. W. Bridgman, "Some properties of single metal crystals", *Proceedings of the National Academy of Sciences of the United States of America*, **10**: 411-415 (1924).

[Briscoe 1957] C. V. Briscoe and C. F. Squire, "Elastic Constants of Lif from 4.2-Degrees-K to 300-Degrees-K by Ultrasonic Methods", *Physical Review*, **106**: 1175-1177 (1957).

[Budiansky 1976] B. Budiansky and R. J. Oconnell, "Elastic-Moduli of a Cracked Solid", *International Journal of Solids and Structures*, **12**: 81-97 (1976).

[Buyanov 1999] Y. I. Buyanov, L. V. Goncharuk and V. R. Sidorko, "Phase composition and thermodynamic properties of alloys of the Te-PbTe-Sb2Te3 system", *Powder Metallurgy and Metal Ceramics*, **38**: 270-273 (1999).

[Caillat 1996] T. Caillat, J. Kulleck, A. Borshchevsky and J. P. Fleurial, "Preparation and thermoelectric properties of the skutterudite-related phase Ru0.5Pd0.5Sb3", *Journal of Applied Physics*, **79**: 8419-8426 (1996).

[Caillat 1997] T. Caillat, J. P. Fleurial and A. Borshchevsky, "Preparation and thermoelectric properties of semiconducting Zn4Sb3", *Journal of Physics and Chemistry of Solids*, **58**: 1119-1125 (1997).

[Case 1980] E. D. Case, J. R. Smyth and O. Hunter, "Grain-Size Dependence of Microcrack Initiation in Brittle Materials", *Journal of Materials Science*, **15**: 149-153 (1980).

[Case 1981] E. D. Case, J. R. Smyth and O. Hunter, "Microcracking in large grain Al2O3", *Mater. Sci. and Eng.*, **51**: 175-179 (1981).

[Case 1983] E. D. Case, J. R. Smyth and O. Hunter, "Microcrack healing during temperature cycling of single phase ceramics", in *Fracture Mechanics of Ceramics, Vol.5*, edited by R. C. Bradt, A. G. Evans, D. P. H. Hasselman and F. F. Lange (Plenum Press, New York, 1983), pp. 507-530.

[Case 1993a] E. D. Case and Y. Kim, "The Effect of Surface-Limited Microcracks on the Effective Youngs Modulus of Ceramics .1. Analysis", *Journal of Materials Science*, **28**: 1885-1900 (1993a).

[Case 1993b] E. D. Case, Y. Kim and W. J. Lee, "Cyclic thermal shock in SiC whisker reinforced alumina and in other ceramic systems", in *Proceedings of the Thermal Shock Behavior and Thermal Fatigue of Advanced Ceramics*, edited by G. A. Schneider and G. Petzow (Kluwer Academic Publishers, the Nederlands, 1993b), pp. 393-406.

[Case 2002a] E. D. Case, "Microwave processing of structural ceramics and bioceramics", in *6th International Conference On Joining Ceramics, Glass and Metal*, edited by H. T. Lin and M. Singh (Deutsche Kermaische Gesellschaft, Cologne, Germany, 2002a), pp. 9-16.

[Case 2002b] E. D. Case, "The Saturation of Thermomechanical Fatigue in Brittle Materials", in *Thermo-Mechanical Fatigue and Fracture*, edited by M. H. Alibadi (WIT Press, Southampton, UK, 2002b), pp. 137-208.

[Case 2005] E. D. Case, I. O. Smith and M. J. Baumann, "Microcracking and porosity in calcium phosphates and the implications for bone tissue engineering", *Materials Science and Engineering a-Structural Materials Properties Microstructure and Processing*, **390**: 246-254 (2005).

[Castillo 1988] E. Castillo, *Extreme value theory in engineering*, (Academic Press, Inc., Boston, 1988), pp. 24, 198-203.

[Chao 1991] L. Y. Chao and D. K. Shetty, "Reliability-Analysis of Structural Ceramics Subjected to Biaxial Flexure", *Journal of the American Ceramic Society*, **74**: 333-344 (1991).

[Chao 2002] J. Chao and J. L. Gonzalez-Carrasco, "The influence of processing on the 475 degrees C hardening of MA 956 alloy", *Scripta Materialia*, **47**: 423-428 (2002).

[Chappell 1986] J. S. Chappell, T. A. Ring and J. D. Birchall, "Particle-Size Distribution Effects on Sintering Rates", *Journal of Applied Physics*, **60**: 383-391 (1986).

[Chen 2004] H. Y. Chen, X. B. Zhao, E. Mueller, Y. F. Lu, C. Drasar and A. Mrotzek, "Microstructures of FeSi2 based thermoelectric materials prepared by rapid solidification and hot pressing", *Journal of University of Science and Technology Beijing*, **11**: 67-70 (2004).

[Chen 2003] G. Chen, M. S. Dresselhaus, G. Dresselhaus, J. P. Fleurial and T. Caillat, "Recent developments in thermoelectric materials", *International Materials Reviews*, **48**: 45-66 (2003).

[Chen 2001] K. C. Chen, F. M. Chu, P. G. Kotula and D. Thoma, "HfCo2 Laves phase intermetallics - part II: elastic and mechanical properties as a function of composition", *Intermetallics*, **9**: 785-798 (2001).

[Cheng 1951] C. M. Cheng, "Resistance to thermal shock", *J. Am. Rocket Soc.*, **21**: 147-153 (1951).

[Chiang 1982] S. S. Chiang, D. B. Marshall and A. G. Evans, "The Response of Solids to Elastic Plastic Indentation .1. Stresses and Residual-Stresses", *Journal of Applied Physics*, **53**: 298-311 (1982).

[Childs 1995] K. D. Childs, B. A. Carlson, L. A. La Vanier, J. F. Moudler, D. F. Paul, W. F. Stickle and D. G. Waston, *Handbook of Auger electron spectroscopy*, 3, (Physical Electronics, Inc., Eden Priarie, MN, 1995), pp. 6-7.

[Choa 1999] Y. H. Choa, N. Bamba, H. Hayashi, H. Kondo, T. Sekino and K. Niihara, "Effect of pure-solvents without deflocculants for finer SiC particle dispersed MgO based composite", *Journal of Materials Science*, **34**: 3789-3793 (1999).

[Chouanine 2005] L. Chouanine, M. Takano, O. Kamiya and M. Nishida, "Nanomechanical characterization of thin Ti-Pt-Au multilayers deposited on top of LiNbO3 wafer", *Composites Science and Technology*, **65**: 1414-1420 (2005).

[Chudoba 2004] T. Chudoba, M. Griepentrog, A. Duck, D. Schneider and F. Richter,

"Young's modulus measurements on ultra-thin coatings", *Journal of Materials Research*, **19**: 301-314 (2004).

[Cleveland 1978] J. J. Cleveland and R. C. Bradt, "Grain Size Microcracking Relations for Pseudo-Brookite Oxides", *Journal of the American Ceramic Society*, **61**: 478-481 (1978).

[Collins 1990] A. K. Collins, M. A. Pickering and R. L. Taylor, "Grain-Size Dependence of the Thermal-Conductivity of Polycrystalline Chemical Vapor-Deposited Beta-Sic at Low-Temperatures", *Journal of Applied Physics*, **68**: 6510-6512 (1990).

[Cui 2003] J. L. Cui, X. Qian and X. B. Zhao, "Mechanical and transport properties of pseudo-binary alloys (PbTe)(1-x)-(SnTe)(x) by pressureless sintering", *Journal of Alloys and Compounds*, **358**: 228-234 (2003).

[Cullity 2001] B. D. Cullity and S. R. Stock, *Elements of X-Ray Diffraction*, (Prentice Hall, Upper Saddle River, NJ, 2001), pp. 182-183.

[Darrow 1969] M. S. Darrow, W. B. White and R. Roy, "Micro-Indentation Hardness Variation as a Function of Composition for Polycrystalline Solutions in Systems Pbs/Pbte Pbse/Pbte and Pbs/Pbse", *Journal of Materials Science*, **4**: 313-317 (1969).

[de Graaf 2004] D. de Graaf, M. Braciszewicz, H. T. Hintzen, M. Sopicka-Lizer and G. de With, "The influence of the composition on (the load-dependence of) the microhardness of Y-Si-Al-O-N glasses as measured by Vickers indentation", *Journal of Materials Science*, **39**: 2145-2149 (2004).

[Dhere 1970] N. G. Dhere and A. Goswami, "Growth of Vapour Phase Deposits of Ag2Se and Ag2Te on Single Crystals", *Thin Solid Films*, **5**: 137-144 (1970).

[Doi 2000] Y. Doi, H. Akimoto, K. Matsuki, T. Aida and S. Ochiai, "Production of fine-microstructural nickel aluminides by wet mechanical alloying process", *Journal of the Japan Institute of Metals*, **64**: 518-526 (2000).

[Dole 1983] S. L. Dole and O. Hunter, "Elastic Properties of Hafnium and Zirconium-Oxides Stabilized with Praseodymium or Terbium Oxide", *Journal of the*

American Ceramic Society, **66**: C47-C49 (1983).

[Dowling 1999] N. E. Dowling, *Mechanical Behavior of Materials*, 2nd edition, (Prentice Hall, Upper Saddle River, New Jersey, 1999), pp. 185-188.

[Dresselhaus 2006] M. S. Dresselhaus and J. P. Heremans, "Recent developments in low-dimensional thermoelectric materials", in *Thermoelectric handbook: macro to nano*, edited by D. M. Rowe (Taylor and Francis, New York, 2006), 39/1- 39/24.

[Dulikravich 1999] G. S. Dulikravich, T. J. Martin and B. H. Dennis, "Multidisciplinary inverse problems", in *Inverse problems in engineering: theory and practice*, edited by K. A. Woodbury (The American society of mechanical engineers, New York, 1999), 1-8.

[Einspruch 1963] N. G. Einspruch and R. J. Manning, "Elastic Constants of Compound Semiconductors Zns, Pbte, Gasb", *Journal of the Acoustical Society of America*, **35**: 215-216 (1963).

[Epstein 1965] S. Epstein and Debrette.Ap, "Elastic Constants of and Wave Propagation in Antimony and Bismuth", *Physical Review*, **138**: A771-& (1965).

[Fano 1995] V. Fano, "Lead telluride and its alloys", in *CRC handbook of thermoelectrics*, edited by D. M. Rowe (CRC Press, Inc., New York, 1995), 257-266.

[Fayette 2000] S. Fayette, D. S. Smith, A. Smith and C. Martin, "Influence of grain size on the thermal conductivity of tin oxide ceramics", *Journal of the European Ceramic Society*, **20**: 297-302 (2000).

[Ferber 2005] M. K. Ferber and H. T. Lin, "Environmental characterization of monolithic ceramics for gas turbine applications", in *Advanced Si-Based Ceramics and Composites*, edited by (Trans Tech Publications Ltd, Zurich-Uetikon, 2005), 367-380.

[Filio 1994] J. M. Filio, K. Sugiyama, F. Saito and Y. Waseda, "A Study on Talc Ground by Tumbling and Planetary Ball Mills", *Powder Technology*, **78**: 121-127 (1994).

[Flegler 1995] S. L. Flegler, J. W. Heckman and K. L. Klomparens, *Scanning and Transmission Electron Microscopy: An Introduction* (Oxford University Press, New York,

1995), pp. 74-75.

[Freund 1987] J. E. Freund and R. E. Walpole, *Mathematical Statistics*, (Prentice Hall, Englewood Cliffs, NJ, 1987), pp. 289-295.

[Gates 1977] R. S. Gates and C. A. P. Horton, "Grain-Boundary Sliding in Type-316 Austenitic Steels .1. Grain-Size Dependence", *Materials Science and Engineering*, **27**: 105-114 (1977).

[Gehrsitz 1999] S. Gehrsitz, H. Sigg, N. Herres, K. Bachem, K. Kohler and F. K. Reinhart, "Compositional dependence of the elastic constants and the lattice parameter of AlxGa1-xAs", *Physical Review B*, **60**: 11601-11610 (1999).

[German 1994] R. M. German, *Powder Metallurgy Science*, 2nd edition, (Metal Powder Industries Federation, New Jersey, 1994),

[Giannakopoulos 1994] A. E. Giannakopoulos, P. L. Larsson and R. Vestergaard, "Analysis of Vickers Indentation", *International Journal of Solids and Structures*, **31**: 2679-2708 (1994).

[Gifkins 1977] R. C. Gifkins, "Effect of Grain-Size and Stress Upon Grain-Boundary Sliding", *Metallurgical Transactions a-Physical Metallurgy and Materials Science*, **8**: 1507-1516 (1977).

[Gnanadurai 2006] P. Gnanadurai, N. Soundararajan and C. E. Sooriamoorthy, "Effect of heating rate on the hysteresis in the phase transition in silver telluride thin films", *Vacuum*, **81**: 1-7 (2006).

[Goldsmid 1960] H. J. Goldsmid, *Applications of thermoelectricity*, (John Wiley and Sons, Inc., New York, 1960), pp. 23-39.

[Goldsmid 1995] H. J. Goldsmid, "Applications of thermoelectric cooling", in *CRC handbook of thermoelectrics*, edited by D. M. Rowe (CRC Press, Inc., New York, 1995), 617-619.

[Grant 1953] N. J. Grant, I. S. Servi and A. Chaudhuri, "Slip and Grain Boundary Sliding

as Affected by Grain Size", *Transactions of the American Institute of Mining and Metallurgical Engineers*, **197**: 217-218 (1953).

[Guelorget 2007] B. Guelorget, M. Francois and J. Lu, "Microindentation as a local damage measurement technique", *Materials Letters*, **61**: 34-36 (2007).

[Hall 1995] W. C. Hall, "Terrestrial applications of thermoelectric generators", in *CRC handbook of thermoelectrics*, edited by D. M. Rowe (CRC Press, Inc., New York, 1995), 503-513.

[Harman 2002] T. C. Harman, P. J. Taylor, M. P. Walsh and B. E. LaForge, "Quantum dot superlattice thermoelectric materials and devices", *Science*, **297**: 2229-2232 (2002).

[Hashin 1962a] Z. Hashin and S. Shtrikman, "On Some Variational Principles in Anisotropic and Nonhomogeneous Elasticity", *Journal of the Mechanics and Physics of Solids*, **10**: 335-342 (1962a).

[Hashin 1962b] Z. Hashin and S. Shtrikman, "A Variational Approach to the Theory of the Elastic Behaviour of Polycrystals", *Journal of the Mechanics and Physics of Solids*, **10**: 343-352 (1962b).

[Hassan 2005a] F. E. Hassan, "First-principles study of BNxSb1-x, BPxSb1-x, and BAsxSb1-x, alloys", *Physica Status Solidi B-Basic Solid State Physics*, **242**: 3129-3137 (2005a).

[Hassan 2005b] F. E. Hassan and H. Akbarzadeh, "First-principles investigation of BNxP1-x, BNxAs1-x and BPxAs1-x ternary alloys", *Materials Science and Engineering B-Solid State Materials for Advanced Technology*, **121**: 170-177 (2005b).

[Heremans 2004] J. P. Heremans, C. M. Thrush and D. T. Morelli, "Thermopower enhancement in lead telluride nanostructures", *Physical Review B*, **70**: (2004).

[Heremans 2005] J. P. Heremans, C. M. Thrush and D. T. Morelli, "Thermopower enhancement in PbTe with pb precipitates", *Journal of Applied Physics*, **98**: (2005).

[Hill 1952] R. Hill, "The Elastic Behaviour of a Crystalline Aggregate", *Proceedings of*

the Physical Society of London Section A, **65**: 349-355 (1952).

[Hoepfner 2004] T. P. Hoepfner and E. D. Case, "An estimate of the critical grain size for microcracks induced in hydroxyapatite by thermal expansion anisotropy", *Materials Letters*, **58**: 489-492 (2004).

[Horio 2004] Y. Horio, H. Yamashita and T. Hayashi, "Microstructure and thermoelectric properties of hot-pressed p-type Bi0.5Sb1.5Te3 alloys prepared by rapid solidification technique", *Materials Transactions*, **45**: 3309-3313 (2004).

[Houston 1968] B. Houston, R. E. Strakna and H. S. Belson, "Elastic Constants Thermal Expansion and Debye Temperature of Lead Telluride", *Journal of Applied Physics*, **39**: 3913-3916 (1968).

[Hsu 2004] K. F. Hsu, S. Loo, F. Guo, W. Chen, J. S. Dyck, C. Uher, T. Hogan, E. K. Polychroniadis and M. G. Kanatzidis, "Cubic AgPbmSbTe2+m: Bulk thermoelectric materials with high figure of merit", *Science*, **303**: 818-821 (2004).

[Hsueh 2005] C. H. Hsueh, M. J. Lance and M. K. Ferber, "Stress distributions in thin bilayer discs subjected to ball-on-ring tests", *Journal of the American Ceramic Society*, **88**: 1687-1690 (2005).

[Ikeda 2007] T. Ikeda, S. M. Haile, V. A. Ravi, H. Azizgolshani, F. Gascoin and G. J. Snyder, "Solidification processing of alloys in the pseudo-binary PbTe-Sb2Te3 system", *Acta Materialia*, **55**: 1227-1239 (2007).

[Incropera 1985] F. P. Incropera and D. P. Dewitt, *Introduction to Heat Transfer*, (John Wiley and Sons, New York, 1985), pp. 431.

[Jiang 2005a] J. Jiang, L. D. Chen, S. Q. Bai, Q. Yao and Q. Wang, "Fabrication and thermoelectric performance of textured n-type Bi-2(Te,Se)(3) by spark plasma sintering", *Materials Science and Engineering B-Solid State Materials for Advanced Technology*, **117**: 334-338 (2005a).

[Jiang 2005b] J. Jiang, L. D. Chen, S. Q. Bai, Q. Yao and Q. Wang, "Thermoelectric properties of textured p-type (Bi,Sb)(2)Te-3 fabricated by spark plasma sintering",

Scripta Materialia, **52**: 347-351 (2005b).

[Kac 1966] M. Kac, "Can One Hear the Shape of a Drum?" *American Mathematical Monthly*, **73**: 1-23 (1966).

[Kajikawa 2006] T. Kajikawa, "Thermoelectric power generation system recovering industrial waste heat", in *Thermoelectric handbook: macro to nano*, edited by D. M. Rowe (Taylor and Francis, New York, 2006), 50/1-50/28.

[Kaliakin 2002] V. N. Kaliakin, *Introduction to Approximate Solution Techniques, Numerical Modeling, and Finite Element Methods*, (Marcel Dekker, Inc., New York, 2002), Chapter 12.

[Kamboj 2003] R. K. Kamboj, S. Dhara and P. Bhargava, "Machining behaviour of green gelcast ceramics", *Journal of the European Ceramic Society*, **23**: 1005-1011 (2003).

[Kano 2001] J. Kano, S. Saeki, M. Tanjo and F. Saito, "Reduction in alpha-transformation temperature of gibbsite and boehmite by powder mixing with seed", *Journal of Chemical Engineering of Japan*, **34**: 595-599 (2001).

[Kanoun 2005] M. B. Kanoun, S. Goumri-Said, A. E. Merad and H. Mariette, "Ab initio study of structural parameters and gap bowing in zinc-blende AlxGa1-xN and AlxIn1-xN alloys", *Journal of Applied Physics*, **98**: 5 (2005).

[Karan 2005] S. Karan and S. P. Sen Gupta, "Vickers microhardness studies on solution-grown single crystals of magnesium sulphate hepta-hydrate", *Materials Science and Engineering a-Structural Materials Properties Microstructure and Processing*, **398**: 198-203 (2005).

[Keyes 1961] R. W. Keyes, "The electron contribution to the elastic properties of germanium", *IBM Journal of Research*, **5**: 266-278 (1961).

[Khvostantsev 1980] L. G. Khvostantsev, A. I. Orlov, N. K. Abrikosov and L. D. Ivanova, "Thermoelectric Properties and Phase-Transition in Sb2te3 under Hydrostatic-Pressure up to 9 Gpa", *Physica Status Solidi a-Applied Research*, **58**: 37-40 (1980).

[Khvostantsev 1985] L. G. Khvostantsev, A. I. Orlov, N. K. Abrikosov and L. D. Ivanova, "Kinetic-Properties and Phase-Transitions in Sb2te3 under Hydrostatic-Pressure up to 9-Gpa", *Physica Status Solidi a-Applied Research*, **89**: 301-309 (1985).

[Kim 1991] Y. Kim, W. J. Lee and E. D. Case, "The measurement of the surface heat transfer coefficient of ceramics quenched into a water bath", *Mater. Sci. and Eng. A*, **145**: L7-L11 (1991).

[Kim 1993a] Y. Kim and E. D. Case, "The Effect of Surface-Limited Microcracks on the Effective Youngs Modulus of Ceramics .2. Application of Analysis to Particular Microcrack Geometries", *Journal of Materials Science*, **28**: 1901-1909 (1993a).

[Kim 1993b] Y. Kim, E. D. Case and S. Gaynor, "The Effect of Surface-Limited Microcracks on the Effective Youngs Modulus of Ceramics .3. Experiments", *Journal of Materials Science*, **28**: 1910-1918 (1993b).

[Kim 2004] S. S. Kim, S. Yamamoto and T. Aizawa, "Thermoelectric properties of anisotropy-controlled p-type Bi-Te-Sb system via bulk mechanical alloying and shear extrusion", *Journal of Alloys and Compounds*, **375**: 107-113 (2004).

[Kingery 1976] W. D. Kingery, H. K. Bowen and D. R. Uhlmann, *Introduction to ceramics (2nd edition)*, (Wiley-Interscience, New York, 1976), pp. 816-819.

[Kishimoto 2002] K. Kishimoto and T. Koyanagi, "Preparation of sintered degenerate n-type PbTe with a small grain size and its thermoelectric properties", *Journal of Applied Physics*, **92**: 2544-2549 (2002).

[Korsukova 1996] M. M. Korsukova, V. N. Gurin, S. Otani and Y. Ishizawa, "Solid solution hardening and atomic displacement parameters in La1-xCexB6 crystals", *Solid State Communications*, **99**: 215-219 (1996).

[Kosuga 2005] A. Kosuga, M. Uno, K. Kurosaki and S. Yamanaka, "Thermoelectric properties of Ag1-xPb18SbTe20 (x = 0, 0.1, 0.3)", *Journal of Alloys and Compounds*, **387**: 52-55 (2005).

[Krakhmalev 2006] P. V. Krakhmalev and J. Bergstrom, "Tribological behavior and wear

mechanismsOf MOSi2-base composites sliding against AA6063 alloy at elevated temperature", *Wear*, **260**: 450-457 (2006).

[Kroner 1958] E. Kroner, "Berechnung Der Elastischen Konstanten Des Vielkristalls Aus Den Konstanten Des Einkristalls", *Zeitschrift Fur Physik*, **151**: 504-518 (1958).

[Kuo 2004] Y. K. Kuo, B. T. Liou, S. H. Yen and H. Y. Chu, "Vegard's law deviation in lattice constant and band gap bowing parameter of zincblende InxGa1-xN", *Optics Communications*, **237**: 363-369 (2004).

[Lambrinou 2007] K. Lambrinou, T. Lauwagie, F. Chalvet, G. de Portu, N. Tassini, S. Patsias, T. Lube and O. Van der Biest, "Elastic properties and damping behaviour of alumina-alumina/zirconia laminates", *Journal of the European Ceramic Society*, **27**: 1307-1311 (2007).

[Larsson 1996] P. L. Larsson, A. E. Giannakopoulos, E. Soderlund, D. J. Rowcliffe and R. Vestergaard, "Analysis of Berkovich indentation", *International Journal of Solids and Structures*, **33**: 221-& (1996).

[Lawn 1993] B. R. Lawn, *Fracture of Brittle Solids*, 2nd edition, (Cambridge University Press, New York, 1993), pp. 258-263.

[Laws 1987] N. Laws and J. R. Brockenbrough, "The Effect of Micro-Crack Systems on the Loss of Stiffness of Brittle Solids", *International Journal of Solids and Structures*, **23**: 1247-1268 (1987).

[Lee 1989] W. J. Lee and E. D. Case, "Cyclic Thermal-Shock in Sic-Whisker-Reinforced Alumina Composite", *Materials Science and Engineering a-Structural Materials Properties Microstructure and Processing*, **119**: 113-126 (1989).

[Lee 1990] W. J. Lee and E. D. Case, "Thermal Fatigue in Polycrystalline Alumina", *Journal of Materials Science*, **25**: 5043-5054 (1990).

[Lee 1993] W. J. Lee, Y. Kim and E. D. Case, "The effect of quenching media on the heat transfer coefficient of polycrystalline alumina", *J. Mater. Sci.*, **31**: 2079-2083 (1993).

[Lee 1996] K. Y. Lee, E. D. Case, J. Asmussen and M. Siegel, "Binder burn-out in a controlled single-mode microwave cavity", *Scripta Materialia*, **35**: 107-111 (1996).

[Lee 1997] K. Y. Lee, E. D. Case and J. Asmussen, "Binder Burnout for ceramics and ceramic matrix composites using a single-mode microwave cavity", in *Microwaves: Theory and Applications in Materials Processing IV*, edited by D. E. Clark, W. H. Sutton and D. A. Lewis (American Ceramics Society, Inc, Westerville, OH, 1997), pp. 539-546.

[Lee 1999] K. Y. Lee and E. D. Case, "Microwave sintering of alumina matrix zirconia composites using a single-mode microwave cavity", *Journal of Materials Science Letters*, **18**: 201-203 (1999).

[Leisure 1997] R. G. Leisure and F. A. Willis, "Resonant ultrasound spectroscopy", *Journal of Physics-Condensed Matter*, **9**: 6001-6029 (1997).

[Li 2006] X. F. Li, "Effects of an elastic substrate on the interfacial adhesion of thin films", *Surface & Coatings Technology*, **200**: 5003-5008 (2006).

[Liu 1999] Y. J. Liu, A. Rosidian and R. O. Claus, "Mechanical properties of electrostatically self-assembled Al2O3-ZrO2 nanocomposites prepared at room temperature", *Journal of Cluster Science*, **10**: 421-428 (1999).

[Low 2004] I. M. Low, "Depth-profiling of crystal structure, texture, and microhardness in a functionally graded tooth enamel", *Journal of the American Ceramic Society*, **87**: 2125-2131 (2004).

[Lu 1998] T. J. Lu and N. A. Fleck, "The thermal shock resistance of solids", *Acta Mater.*, **46**: 4755-4768 (1998).

[Ma 2002] J. Ma and L. C. Lim, "Effect of particle size distribution on sintering of agglomerate-free submicron alumina powder compacts", *Journal of the European Ceramic Society*, **22**: 2197-2208 (2002).

[Maeva 2004] E. Maeva, I. Severina, S. Bondarenko, G. Chapman, B. O'Neill, F. Severin and R. G. Maev, "Acoustical methods for the investigation of adhesively bonded structures: A review", *Canadian Journal of Physics*, **82**: 981-1025 (2004).

[Maier 1963] R. G. Maier, "Zur Kenntnis Des Systems Pbte-Agsbte2", *Zeitschrift Fur Metallkunde*, **54**: 311-312 (1963).

[Mandel 1964] J. Mandel, *Statistical Analysis of Experimental Data*, (Interscience publishers, New York, 1964),

[Mandrus 1995] D. Mandrus, J. L. Sarrao, A. Migliori, J. D. Thompson and Z. Fisk, "Thermodynamics of Fesi", *Physical Review B*, **51**: 4763-4767 (1995).

[Mann 1974] N. R. Mann, R. E. Schafer and N. D. Singpurwall, *Methods for Statistical Analysis of Reliability and Life Data*, (Wiley and Sons, New York, 1974), pp. 103-111, 184-188.

[Manson 1966] S. S. Manson, *Thermal Stress and Low Cycle Fatigue*, (McGraw-Hill, New York, 1966), Chapter 7.

[Marshall 1982] D. B. Marshall, T. Noma and A. G. Evans, "A Simple Method for Determining Elastic-Modulus-to-Hardness Ratios Using Knoop Indentation Measurements", *Journal of the American Ceramic Society*, **65**: C175-C176 (1982).

[Martin 1973] H. C. Martin and G. F. Carey, *Introduction to Finite Element Analysis*, (McGraw-Hill, New York, 1973), Chapter 9.

[Matsubara 2006] K. Matsubara and M. Matsuura, "A thermoelectric application to vehicles", in *Thermoelectric handbook: macro to nano*, edited by D. M. Rowe (Taylor and Francis, New York, 2006), 52/1-52/11.

[Matsushita 1984] K. Matsushita, S. Kuratani, T. Okamoto and M. Shimada, "Young Modulus and Internal-Friction in Alumina Subjected to Thermal-Shock", *Journal of Materials Science Letters*, **3**: 345-348 (1984).

[Matsushita 2004] H. Matsushita, E. Hagiwara and A. Katsui, "Phase diagram and thermoelectric properties of Ag3-xSb1+xTe4 system", *Journal of Materials Science*, **39**: 6299-6301 (2004).

[Mayrhofer 2003] P. H. Mayrhofer, A. Horling, L. Karlsson, J. Sjolen, T. Larsson, C.

Mitterer and L. Hultman, "Self-organized nanostructures in the Ti-Al-N system", *Applied Physics Letters*, **83**: 2049-2051 (2003).

[Migliori 1993] A. Migliori, J. L. Sarrao, W. M. Visscher, T. M. Bell, M. Lei, Z. Fisk and R. G. Leisure, "Resonant Ultrasound Spectroscopic Techniques for Measurement of the Elastic-Moduli of Solids", *Physica B*, **183**: 1-24 (1993).

[Migliori 1997] A. Migliori and J. L. Sarrao, *Resonant Ultrasound Spectroscopy: Applications to Physics, Materials Measurements, and Nondestructive Evaluation*, (Academic Press, New York, 1997),

[Miller 1969] R. A. Miller and D. E. Schuele, "Pressure Derivatives of Elastic Constants of Lead", *Journal of Physics and Chemistry of Solids*, **30**: 589-& (1969).

[Mokhtari 2004] A. Mokhtari and H. Akbarzadeh, "First principles investigation of the electronic and structural properties of Mg3xBe3-3xN2 ternary alloy", *Journal of Physics-Condensed Matter*, **16**: 6063-6074 (2004).

[Moore 1995] D. S. Moore, *The Basic Practice of Statistics*, (W. H. Freeman, Inc., New York, 1995), pp. 442-443.

[Morita 1993] K. Morita, A. Umezawa, S. Yamato and A. Makishima, "Surface-Roughness of Yttria-Containing Aluminosilicate Glass-Ceramics as Indicative of Their Machinability", *Journal of the American Ceramic Society*, **76**: 1861-1864 (1993).

[Murnaghan 1944] F. D. Murnaghan, "The compressibility of media under extreme pressures", *Proceedings of the National Academy of Sciences of the United States of America*, **30**: 244-247 (1944).

[Neighbours 1958] J. R. Neighbours and G. A. Alers, "Elastic Constants of Silver and Gold", *Physical Review*, **111**: 707-712 (1958).

[Nolas 2001] G. S. Nolas, J. Sharp and H. J. Goldsmid, *Thermoelectrics: basic principles and new materials developments*, (Springer, Berlin; New York, 2001), pp. 28-57, 151-159, 178-207.

[Nolas 2006] G. S. Nolas, "Structure, thermal conductivity, and thermoelectric properties of clathrate compounds", in *Thermoelectric handbook: macro to nano*, edited by D. M. Rowe (Taylor and Francis, New York, 2006), 33/1- 33/8.

[Nowick 1972] S. Nowick and B. S. Berry, *Anelastic Relaxation in Crystalline Solids* (Academic Press, New York, 1972), pp. 176-221.

[Nye 1967] J. F. Nye, *Physical Properties of Crystals* (Oxford University Press, London, 1967).

[Oliveira 2002] M. Oliveira, K. X. Chen and J. M. F. Ferreira, "Influence of the deagglomeration procedure on aqueous dispersion, slip casting and sintering of Si3N4-based ceramics", *Journal of the European Ceramic Society*, **22**: 1601-1607 (2002).

[Oliver 1992] W. C. Oliver and G. M. Pharr, "An Improved Technique for Determining Hardness and Elastic-Modulus Using Load and Displacement Sensing Indentation Experiments", *Journal of Materials Research*, **7**: 1564-1583 (1992).

[Ono 1962] T. Ono, T. Irie and T. Taahama, "Thermoelectric Properties of AgSbTe2-AgBiTe2, -PbTe and -SnTe Systems", *Journal of the Physical Society of Japan*, **17**: 1070-1071 (1962).

[Overton 1955] W. C. Overton and J. Gaffney, "Temperature Variation of the Elastic Constants of Cubic Elements .1. Copper", *Physical Review*, **98**: 969-977 (1955).

[Ozcan 2005] S. Ozcan, B. Kaynar, M. M. Can and T. Firat, "Synthesis of ZnFe2O4 from metallic zinc and iron by wet-milling process", *Materials Science and Engineering B-Solid State Materials for Advanced Technology*, **121**: 278-281 (2005).

[Ozisik 1985] M. N. Ozisik, *Heat Transfer*, (McGraw-Hill, New York, 1985), Chapter 10.

[Pabi 1996] S. K. Pabi, J. Joardar and B. S. Murty, "Formation of nanocrystalline phases in the Cu-Zn system during mechanical alloying", *Journal of Materials Science*, **31**: 3207-3211 (1996).

[Patel 1965] C. K. N. Patel, "Efficient Phase-Matched Harmonic Generation in Tellurium with a Co2 Laser at 10.6 Amu", *Physical Review Letters*, **15**: 1027-& (1965).

[Peng 2004] J. Y. Peng, J. Y. Yang, T. J. Zhang, X. L. Song and Y. H. Chen, "Preparation and characterization of Fe substituted CoSb3 skutterudite by mechanical alloying and annealing", *Journal of Alloys and Compounds*, **381**: 313-316 (2004).

[Pilchak 2007] A. L. Pilchak, F. Ren, E. D. Case, E. J. Timm, H. J. Schock, C. I. Wu and T. Hogan, "Particle size reduction by planetary ball milling and powder characterization of LAST (Lead-Antimony-Silver-Tellurium) thermoelectric material", *Philosophical Magazine*, **87**: 4567-4591 (2007).

[Porter 1990] W. D. Porter and K. E. Easterlin, *Phase transformation in metals and alloys*, (Campman and Hill, New York, 1990), pp. 1-4, 208-222, 308-314.

[Press 1992] W. H. Press, *Numerical recipes in FORTRAN 77: the art of scientific computing*, (Cambridge University Press, Cambridge, England, 1992), pp. 53, 111.

[Quarez 2005] E. Quarez, K. F. Hsu, R. Pcionek, N. Frangis, E. K. Polychroniadis and M. G. Kanatzidis, "Nanostructuring, compositional fluctuations, and atomic ordering in the thermoelectric materials AgPbmSbTe2+m. The myth of solid solutions", *Journal of the American Chemical Society*, **127**: 9177-9190 (2005).

[Radovic 2004] M. Radovic, E. Lara-Curzio and L. Riester, "Comparison of different experimental techniques for determination of elastic properties of solids", *Materials Science and Engineering a-Structural Materials Properties Microstructure and Processing*, **368**: 56-70 (2004).

[Rahaman 2003] M. N. Rahaman, *Ceramic Processing and Sintering*, 2nd edition, (Marcel Dekker, Inc., New York, 2003), pp. 50-56, 136-137, 343-344, 693-696.

[Ramos 2006] A. S. Ramos, S. P. Taguchi, E. C. T. Ramos, V. L. Arantes and S. Ribeiro, "High-energy ball milling of powder B-C mixtures", *Materials Science and Engineering a-Structural Materials Properties Microstructure and Processing*, **422**: 184-188 (2006).

[Rao 2003] S. S. Rao and D. Ravinder, "Composition dependence of elastic moduli of

gadolinium-substituted nickel-zinc ferrites", *Materials Letters*, **57**: 3802-3804 (2003).

[Rao 2006] A. M. Rao, X. H. Ji and T. M. Tritt, "Properties of nanostructured one-dimensional and composite thermoelectric materials", *MRS Bulletin*, **31**: 218-223 (2006).

[Ravinder 2001] D. Ravinder and T. Alivelumanga, "Room temperature elastic behaviour of cadmium substituted manganese ferrites", *Materials Letters*, **49**: 1-6 (2001).

[Reason 2005] M. Reason, X. Weng, W. Ye, D. Dettling, S. Hanson, G. Obeidi and R. S. Goldman, "Stress evolution in GaAsN alloy films", *Journal of Applied Physics*, **97**: 7 (2005).

[Ren 2006] F. Ren, E. D. Case, E. J. Timm, M. D. Jacobs and H. J. Schock, "Weibull analysis of the biaxial fracture strength of a cast p-type LAST-T thermoelectric material", *Philosophical Magazine Letters*, **86**: 673-682 (2006).

[Ren 2007a] F. Ren, E. D. Case, E. J. Timm and H. Schock, "Hardness as a function of composition for n-type LAST thermoelectric material", *Journal of Alloys and Compounds*, available online at doi:10.1016/j.jallcom.2007.01.086 (2007a).

[Ren 2007b] F. Ren, E. D. Case, E. J. Timm and H. Schock, "Young's modulus as a function of composition for an n-type lead-antimony-silver-telluride (LAST) thermoelectric material", *Philosophical Magazine*, **87**: 4907-4934 (2007b).

[Rice 1998] R. W. Rice, *Porosity of Ceramics*, (Marcel Dekker, Inc., New York, 1998), pp. 100-131.

[Rice 2000] R. W. Rice, *Mechanical Properties of Ceramics and Composites*, (Marcel Dekker, New York, 2000), pp. 308-312.

[Richerson 2006] D. W. Richerson, *Modern Ceramic Engineering: Properties, Processing and Use in Design*, (Taylor and Francis, New York, 2006), pp. 379-383.

[Riffat 2003] S. B. Riffat and X. L. Ma, "Thermoelectrics: a review of present and potential applications", *Applied Thermal Engineering*, **23**: 913-935 (2003).

[Robozerov 2000] V. V. Robozerov, V. A. Zykov and T. A. Gavrikova, "Chemical etching of lead chalcogenides", *Inorganic Materials*, **36**: 127-131 (2000).

[Rossing 1982] T. D. Rossing, "Chladni's law for vibrating plates", *American Journal of Physics*, **50**: 271-274 (1982).

[Rowe 1995] D. M. Rowe, *CRC handbook of thermoelectrics*, (CRC Press, Boca Raton, FL, 1995).

[Royer 1979] D. Royer and E. Dieulesaint, "Elastic and Piezoelectric Constants of Trigonal Selenium and Tellurium Crystals", *Journal of Applied Physics*, **50**: 4042-4045 (1979).

[Saha 2002] R. Saha and W. D. Nix, "Effects of the substrate on the determination of thin film mechanical properties by nanoindentation", *Acta Materialia*, **50**: 23-38 (2002).

[Sakai 1981] N. Sakai, T. Kajiwara, K. Takemura, S. Minomura and Y. Fujii, "Pressure-Induced Phase-Transition in Sb2Te3", *Solid State Communications*, **40**: 1045-1047 (1981).

[Salamov 2006] B. G. Salamov, O. I. Davarashvili, T. S. Mamedov, G. S. Darsavelidze, M. I. Enukashvili and N. D. Akhmedzade, "Investigation of the temperature dependence of the internal friction in PbTe crystals", *Physica Status Solidi a-Applications and Materials Science*, **203**: 3679-3684 (2006).

[Sarrao 1994] J. L. Sarrao, D. Mandrus, A. Migliori, Z. Fisk and E. Bucher, "Elastic Properties of Fesi", *Physica B*, **199**: 478-479 (1994).

[Schenk 1998a] M. Schenk and T. H. D. Le, "Solid-solution hardening of Cd1-xZnxTe bulk crystals", *Semiconductor Science and Technology*, **13**: 335-339 (1998a).

[Schenk 1998b] M. Schenk and C. Silber, "Lattice parameter and microhardness investigations on CdTe1-xSex", *Journal of Materials Science-Materials in Electronics*, **9**: 295-300 (1998b).

[Scherrer 1995] H. Scherrer and S. Scherrer, "Bismuth telluride, antimony telluride, and their solid solutions", in *CRC handbook of thermoelectrics*, edited by D. M. Rowe (CRC Press, Inc., New York, 1995), 211-237.

[Schreiber 1973] E. Schreiber, O. L. Anderson and N. Soga, *Elastic constants and their measurement*, (McGraw-Hill Book Company, New York, 1973),

[Sharma 1963] S. K. Sharma, "Transformation of Structure in Silver - Tellurium Alloy Films", *Nature*, **198**: 280-281 (1963).

[Sharma 1969] S. K. Sharma, "Structural Transformation in Thin Films of Binary Alloys", *Journal of Materials Science*, **4**: 189-194 (1969).

[Sharma 2003] P. Sharma and S. Ganti, "On the grain-size-dependent elastic modulus of nanocrystalline materials with and without grain-boundary sliding", *Journal of Materials Research*, **18**: 1823-1826 (2003).

[Sharp 2006] J. Sharp, J. Bierschenk and H. B. Lyon, "Overview of solid-state thermoelectric refrigerators and possible applications to on-chip thermal management", *Proceedings of the Ieee*, **94**: 1602-1612 (2006).

[Shchennikov 2003] V. V. Shchennikov, S. V. Ovsyannikov and N. Y. Frolova, "High-pressure study of ternary mercury chalcogenides: phase transitions, mechanical and electrical properties", *Journal of Physics D-Applied Physics*, **36**: 2021-2026 (2003).

[Shetty 1980] D. K. Shetty, A. R. Rosenfield, P. McGuire, G. K. Bansal and W. H. Duckworth, "Biaxial Flexure Tests for Ceramics", *American Ceramic Society Bulletin*, **59**: 1193-1197 (1980).

[Shiau 1998] F. S. Shiau, T. T. Fang and T. H. Leu, "Effects of milling and particle size distribution on the sintering behavior and the evolution of the microstructure in sintering powder compacts", *Materials Chemistry and Physics*, **57**: 33-40 (1998).

[Sieborger 2001] D. Sieborger, H. Knake and U. Glatzel, "Temperature dependence of the elastic moduli of the nickel-base superalloy CMSX-4 and its isolated phases", *Materials Science and Engineering a-Structural Materials Properties Microstructure and*

Processing, **298**: 26-33 (2001).

[Simmons 1971] G. Simmons and H. Wang, *Single Crystal Elastic Constants and Calculated Aggregate Properties: a Handbook* (the MIT Press, Cambridge, MA, 1971), pp. ix-x, 200.

[Sinha 1994] A. Sinha, K. Kokini and K. J. Bowman, "Elastic-Constant Degradation from Microcracking in Ceramic-Ceramic Composites Cycled by Slow Thermal Loading", *Materials Science and Engineering a-Structural Materials Properties Microstructure and Processing*, **188**: 317-325 (1994).

[Slater 1950] J. C. Slater, "The Lorentz correction in barium titanate", *Phys. Rev.*, **78**: 748-761 (1950).

[Sreedhar 1972] A. K. Sreedhar and S. C. Gupta, "Electronic effects in elastic constants of PbTe", *Phys. Rev. B*, **5**: 3160-3164 (1972).

[Suess 1961] C. Suess, "Measurement of the elastic constants of LiF and MgO as a function of temperature and pressure", *J. des Recherches du C.N.R.S.*, **54**: 23-59 (1961).

[Suryanarayana 2001] C. Suryanarayana, "Mechanical alloying and milling", *Progress in Materials Science*, **46**: 1-184 (2001).

[Tani 2001] K. Tani, N. Yiwata, M. Harigaya, S. Emura and Y. Nakata, "EXAFS study of Sb-Te alloy films", *Journal of Synchrotron Radiation*, **8**: 749-751 (2001).

[Taylor 1999] P. J. Taylor, J. R. Maddux, W. A. Jesser and F. D. Rosi, "Room-temperature anisotropic, thermoelectric, and electrical properties of n-type (Bi2Te3)(90) (Sb2Te3)(5)(Sb-2 Se-3)(5) and compensated p-type (Sb2Te3)(72)(Bi2Te3)(25)(Sb-2 Se-3)(3) semiconductor alloys", *Journal of Applied Physics*, **85**: 7807-7813 (1999).

[Temuujin 2005] J. Temuujin, M. Aoyama, M. Senna, T. Masuko, C. Ando and H. Kishi, "Benefits of mild wet milling of the intermediates for the synthesis of phase-pure Z-type hexaferrite", *Journal of Materials Research*, **20**: 1939-1942 (2005).

[Ting 1995] J. M. Ting and R. Y. Lin, "Effect of Particle-Size Distribution on Sintering .2.

Sintering of Alumina", *Journal of Materials Science*, **30**: 2382-2389 (1995).

[Tokiai 1995] T. Tokiai, T. Uesugi and K. Koumoto, "Relationship between Thermoelectric Properties and Microstructure on P-Type (Bi2Te3)(0.25)(Sb2Te3)(0.75) System Using Milled Powder", *Journal of the Ceramic Society of Japan*, **103**: 1182-1187 (1995).

[Toprak 2004] M. S. Toprak, C. Stiewe, D. Platzek, S. Williams, L. Bertini, E. C. Muller, C. Gatti, Y. Zhang, M. Rowe and M. Muhammed, "The impact of nanostructuring on the thermal conductivity of thermoelectric CoSb3", *Advanced Functional Materials*, **14**: 1189-1196 (2004).

[Tritt 2006] T. M. Tritt and M. A. Subramanian, "Thermoelectric materials, phenomena, and applications: A bird's eye view", *MRS Bulletin*, **31**: 188-194 (2006).

[Ueno 2005] K. Ueno, A. Yamamoto, T. Noguchi, T. Inoue, S. Sodeoka and H. Obara, "Optimization of hot-press conditions of Zn4Sb3 for high thermoelectric performance. II. Mechanical properties", *Journal of Alloys and Compounds*, **388**: 118-121 (2005).

[Uher 2006] C. Uher, "Skutterudite-based thermoelectrics", in *Thermoelectric handbook: macro to nano*, edited by D. M. Rowe (Taylor and Francis, New York, 2006), 34/1-34/17.

[Ulrich 2002] T. J. Ulrich, K. R. McCall and R. A. Guyer, "Determination of elastic moduli of rock samples using resonant ultrasound spectroscopy", *Journal of the Acoustical Society of America*, **111**: 1667-1674 (2002).

[van Pieterson 2005] L. van Pieterson, M. H. R. Lankhorst, M. van Schijndel, A. E. T. Kuiper and J. H. J. Roosen, "Phase-change recording materials with a growth-dominated crystallization mechanism: A materials overview", *Journal of Applied Physics*, **97**: Art. No. 083520 (2005).

[Varshni 1970] Y. P. Varshni, "Temperature dependence of the elastic constants", *Physical Review B-Solid State*, **2**: 3952-3958 (1970).

[Vassen 1999] R. Vassen and D. Stover, "Processing and properties of nanograin silicon

carbide", *Journal of the American Ceramic Society*, **82**: 2585-2593 (1999).

[Venkatasubramanian 2001] R. Venkatasubramanian, E. Siivola, T. Colpitts and B. O'Quinn, "Thin-film thermoelectric devices with high room-temperature figures of merit", *Nature*, **413**: 597-602 (2001).

[Vining 1995] C. B. Vining, "Silicon germanium", in *CRC handbook of thermoelectrics*, edited by D. M. Rowe (CRC Press, Inc., New York, 1995), pp. 329-337.

[Vurgaftman 2003] I. Vurgaftman and J. R. Meyer, "Band parameters for nitrogen-containing semiconductors", *Journal of Applied Physics*, **94**: 3675-3696 (2003).

[Wachtman 1959] J. B. Wachtman and D. G. Lam, "Young Modulus of Various Refractory Materials as a Function of Temperature", *Journal of the American Ceramic Society*, **42**: 254-260 (1959).

[Wachtman 1961] J. B. Wachtman, W. E. Tefft, D. G. Lam and C. S. Apstein, "Exponential Temperature Dependence of Youngs Modulus for Several Oxides", *Physical Review*, **122**: 1754-& (1961).

[Wachtman 1963a] J. B. Wachtman, "Mechanical and Electrical Relaxation in Tho2 Containing CaO", *Physical Review*, **131**: 517-527 (1963a).

[Wachtman 1963b] J. B. Wachtman, E. P. Levine and H. S. Peiser, "Symmetry Splitting of Equivalent Sites in Oxide Crystals and Related Mechanical Effects", *Journal of Research of the National Bureau of Standards Section a-Physics and Chemistry*, **A 67**: 281-289 (1963b).

[Wachtman 1996] J. B. Wachtman, *Mechanical Properties of Ceramics*, (Wiley Interscience, New York, 1996), pp. 33-35, 72-80, 92-100.

[Wang 2002] R. G. Wang, W. Pan, M. N. Jiang, J. Chen and Y. M. Luo, "Investigation of the physical and mechanical properties of hot-pressed machinable Si3N4/h-BN composites and FGM", *Materials Science and Engineering B-Solid State Materials for Advanced Technology*, **90**: 261-268 (2002).

[Wang 2003] H. Wang and R. B. Dinwiddie, "Development of a LabView based portable thermal diffusivity system", *Proceedings of The 27th International Thermal Conductivity Conference and the 15th International Thermal Expansion Symposium*, edited by H. Wang and W. D. Porter, DEStech Publichations, Inc., pp 484-492, (2003).

[Wang 2006] H. Wang, J. F. Li, C. W. Nan, M. Zhou, W. S. Liu, B. P. Zhang and T. Kita, "High-performance Ag0.8Pb18+xSbTe20 thermoelectric bulk materials fabricated by mechanical alloying and spark plasma sintering", *Applied Physics Letters*, **88**: (2006).

[Watanabe 2001] T. Watanabe, K. Muratsubaki, Y. Benino, H. Saitoh and T. Komatsu, "Hardness and elastic properties of Bi2O3-based glasses", *Journal of Materials Science*, **36**: 2427-2433 (2001).

[Weiss 2003] T. Weiss, S. Siegesmund and E. R. Fuller, "Thermal degradation of marble: indications from finite-element modelling", *Building and Environment*, **38**: 1251-1260 (2003).

[Whittaker 1944] E. T. Whittaker, *Analytical dynamics of particles and rigid bodies*, (Dover Publications, New York, 1944), pp. 38-39.

[Wongmaneerung 2006] R. Wongmaneerung, T. Sarkonsri, R. Yimnirun and S. Ananta, "Effects of milling method and calcination condition on phase and morphology characteristics Of Mg4Nb2O9 powders", *Materials Science and Engineering B-Solid State Materials for Advanced Technology*, **130**: 246-253 (2006).

[Wu 1996] B. M. Wu, Y. L. Du, H. X. Tang, P. Du, X. Y. Qin and L. D. Zhang, "Reduced thermal diffusivity of nanostructured silver", *Journal of Physics and Chemistry of Solids*, **57**: 1211-1213 (1996).

[Wu 2003] D. F. Wu and H. Jiang, "Comment on "A new probability index for estimating Weibull modulus for ceramics with the least-square method"", *Journal of Materials Science Letters*, **22**: 1745-1746 (2003).

[Wylie 1982] C. R. Wylie and L. C. Barrett, *Advanced engineering mathematics*, 4th edition, (McGraw-Hill, Inc., New York, 1982), pp. 934-938.

[Xia 2000] Y. Xia, S. Bhattacharya, V. Ponnambalam, A. L. Pope, S. J. Poon and T. M. Tritt, "Thermoelectric properties of semimetallic (Zr, Hf)CoSb half-Heusler phases", *Journal of Applied Physics*, **88**: 1952-1955 (2000).

[Yang 2004] J. Y. Yang, Y. H. Chen, J. Y. Peng, X. L. Song, W. Zhu, J. F. Su and R. G. Chen, "Synthesis of CoSb3 skutterudite by mechanical alloying", *Journal of Alloys and Compounds*, **375**: 229-232 (2004).

[Yang 2006] J. H. Yang and T. Caillat, "Thermoelectric materials for space and automotive power generation", *MRS Bulletin*, **31**: 224-229 (2006).

[Yashima 1997] I. Yashima, R. Tsukuda, T. Sato and Y. Tochio, "Particle-size effects on bending strength and thermoelectric properties of p-type Bi-Te materials prepared by hot press method", *Journal of the Ceramic Society of Japan*, **105**: 1018-1021 (1997).

[Yavuz 1998] M. Yavuz, H. Maeda, L. Vance, H. K. Liu and S. X. Dou, "Effect of ball milling materials and methods on powder processing of Bi2223 superconductors", *Superconductor Science & Technology*, **11**: 1153-1159 (1998).

[Yousef 2005] S. G. Yousef, J. Rodel, E. R. Fuller, A. Zimmermann and B. S. El-Dasher, "Microcrack evolution in alumina ceramics: Experiment and simulation", *Journal of the American Ceramic Society*, **88**: 2809-2816 (2005).

[Yu 2004] B. L. Yu, X. F. Tang, Q. Qi and Q. J. Zhang, "Preparation and thermal transport properties of CoSb3 nano-compounds", *Acta Physica Sinica*, **53**: 3130-3135 (2004).

[Zadler 2004] B. J. Zadler, J. H. L. Le Rousseau, J. A. Scales and M. L. Smith, "Resonant Ultrasound Spectroscopy: theory and application", *Geophysical Journal International*, **156**: 154-169 (2004).

[Zajickova 2003] L. Zajickova, V. Bursikova, V. Perina, A. Mackova and J. Janca, "Correlation between SiOx content and properties of DLC : SiOx films prepared by PECVD", *Surface & Coatings Technology*, **174**: 281-285 (2003).

[Zeng 2005] J. Y. Zeng, Y. Sato, C. Ohkubo and T. Hosoi, "In vitro wear resistance of three types of composite resin denture teeth", *Journal of Prosthetic Dentistry*, **94**:

453-457 (2005).

[Zhao 2000] L. T. Zhao, T. J. Lu and N. A. Fleck, "Crack channeling and spalling in a plate due to thermal shock loading", *J. Mech. Phys. Solids*, **48**: 867-897 (2000).

[Zhao 2005] D. H. Zhao, M. Wilson and B. E. Borders, "Modeling response curves and testing treatment effects in repeated measures experiments: a multilevel nonlinear mixed-effects model approach", *Canadian Journal of Forest Research-Revue Canadienne De Recherche Forestiere*, **35**: 122-132 (2005).

[Ziman 1979] J. M. Ziman, *Electrons and phonons*, (Oxford University Press, London, 1979), pp. 258, 396-403.

MICHIGAN STATE UNIVERSITY
3 1293 02956